ASPECTS OF SERRATED FLOW IN ALUMINIUM ALLOYS

A THESIS

SUBMITTED TO THE DEPARTMENT OF MATERIALS ENGINEERING

AND THE FACULTY OF ENGINEERING

OF THE UNIVERSITY OF CAPE TOWN

IN FULFILLMENT OF THE REQUIREMENTS

FOR THE DEGREE OF

DOCTOR OF PHILOSOPHY

By

Jonathan Mark Robinson

February 1992

Abstract

Uniaxial tensile testing has been undertaken on a range of aluminium base alloys. Material investigated included commercial binary Al–Mg (5182), ternary Al–Mg–Si (6061) and quaternary Al–Cu–Mn–Si (2014) as well as experimental alloys containing 2at.% additions of Ag, Mg and Zn to commercially pure Al (1070). In addition, composite materials based on both alloys 2014 and 6061, containing 10%, 15% and 20% additions of Al_2O_3 particulate, as well as 20% SiC particulate in the case of 6061, were also tested. Microstructures of materials were varied by prior heat treatments but, for comparison, all materials, were initially tested in the solution treated and quenched condition.

Mechanical testing was undertaken at room temperature throughout the course of the work, and at strain rates such that serrated tensile test curves were manifest. The evolution of microstructural features of the deformation was evaluated utilising both optical and electron microscopy. Surface deformation features, including the formation of both type A and type B deformation markings, was examined on pre–polished specimen gauge lengths at various levels of tensile strain. The planarity of slip line traces was correlated with the evolution of related deformation structures in dynamic experiments in a high voltage transmission electron microscope (HVEM). In addition, the formation of slip lines on the surface of the HVEM microtensile specimens compared favourably with those formed on the surfaces of macroscopic tensile specimens.

Microscale heterogeneities in the deformation observed during in–situ dynamic HVEM experiments on polycrystalline material correlated with the extent of serrated flow manifest in bulk specimens. All materials deformed in the HVEM displayed inhomogeneous dislocation motion consistent with the macroscopically observable discontinuities. The alloys tested were microstructurally distinguishable during dynamic experiments depending primarily on whether or not they had been deliberately alloyed with magnesium. The alloys containing Mg exhibited the activation of parallel slip traces together with minimal

cross–slip in any single microyield event. In contrast, the alloys which did not contain Mg exhibited the simultaneous activation of various intersecting slip systems and were characterised by extensive cross–slip during similar yield events. On the basis of these observations, the magnitude of serrations and extent of serrated flow in the alloys has been discussed.

The extent to which the different alloys were able to undergo dynamic recovery affected both the evolution of the dislocation structure observed in the conventional transmission electron microscope (CTEM) as well as the final fracture mode. The existence of a characteristic shear fracture mode was consistently observed to follow tensile deformation which had been dominated by unstable plastic flow. The ready occurrence of dynamic recovery and the associated formation of dislocation cell structures allowed for more fully developed plastic instability during the final stages of tensile deformation and a lower likelihood of final failure by premature shear.

Finally, the addition of particulate reinforcement to 2014 and 6061 had different effects that were accounted for by the difference in strength between the two monolithic materials. In the case of the weaker 6061, all particulate additions had a strengthening effect whereas in 2014, increasing the volume percent of reinforcement progressively weakened the composite. Serrated flow properties of both alloys were affected by the addition of the particulate reinforcement. The homogeneity of particle distribution as well as the size of the particulate inclusions affected both the tensile properties and final fracture of the composites.

Acknowledgements

I would like to thank the following:

- My supervisor Prof. M P Shaw for consistent support and patience.
- Mr B Greeves and Mr J Peterson for photographic expertise and assistance.
- Mr N A J Dreze, Mr G Newins and Mr R Hendricks for diverse and irreplaceable technical advice and assistance.
- My colleagues, as well as the secretarial staff in the Department of Materials Engineering, University of Cape Town for varied support and assistance during the period in which this work was undertaken.
- Mr D A Gerneke and the staff of the Electron Microscope Unit, University of Cape Town for preparation and maintainance of the TEM.
- Prof. G De Jager and his research students in the Department of Electrical Engineering, University of Cape Town for assistance in the production of digitised images from video material.
- Dr C D Mercer and Mr H Bohl of CERECAM at the University of Cape Town for their assistance with the finite element analysis of tensile test specimens.
- The staff at the NCEM, University of California, Berkeley for assistance and advice in the preparation and execution of the HVEM experiments.
- Dr T J Hurd and Hulett Aluminium (Pty) Ltd for the supply of materials as well as for chemical analysis and partial financial support for the research undertaken at the NCEM.

This thesis is dedicated to a new South Africa and all those in the universities who have spent a long time struggling for the ideals we may yet see realised.

Glossary of Technical Terms and Abbreviations

T Temperature (^{o}K)

RT Room Temperature

$\mathbf{T_M}$ Melting temperature (^{o}K)

$\mathbf{T_m}$ Homologous temperature (T_m=T/T_M)

FCC Face centred cubic

SFE Stacking fault energy

SRO Short range order

GP zone Guinier–Preston zone

$\mathbf{E_A}$ Activation energy

1070 99.7% minimum purity aluminium

2014 Al–Cu–Mn–Si alloy with composition according to specifications detailed in table 2

5182 Al–Mg alloy with composition according to specifications detailed in table 2

6061 Al–Mg–Si alloy with composition according to specifications detailed in table 2

VF615 Experimental binary Al–2at%Mg alloy

VF617 Experimental binary Al–2at%Zn alloy

VF619 Experimental binary Al–2at%Ag alloy

MMC Metal matrix composite

SiC_P Silicon carbide particulate

at% Atomic percent

wt% Weight percent[1]

CR Cold rolling reduction

WQ Water quench

AC Air cooled

T6 Commercial heat treatment designation, referring to solution heat treatment followed by artificial ageing to maximum hardness.

T4 Commercial heat treatment designation, referring to solution heat treatment followed by natural (room temperature) ageing to maximum hardness.

H_V Vickers pyramid number

UTS Ultimate tensile strength

σ Stress

ε Strain

$\dot{\varepsilon}$ Strain rate

%El Percentage elongation

θ Work hardening rate

K_ε Hall–Petch slope

σ^* Thermal component of the flow stress

σ_μ Athermal component of the flow stress

PLC effect Portevin–Le Chatelier effect

DSA Dynamic strain ageing

[1]All compositions given are in wt% unless explicitly specified in the text

$\triangle\sigma$ Stress amplitude of a single serration

ε_c Critical (incubation) strain

ε_L Lüders strain

A, B, C, C_A, C_B, D and E Serration types defined in section 2.3.1

a.e. Acoustic emission

t_w Waiting time

SRS Strain rate sensitivity

C_v Vacancy concentration

TEM Transmission electron microscope

SEM Scanning electron microscope

CTEM Conventional transmission electron microscope

HVEM High voltage electron microscope

EDS Energy Dispersive Spectroscopy

PC Personal computer

Contents

List of Tables

List of Figures

Chapter 1

Introduction

"In discussions with sensible professional men, I have not infrequently encountered the opinion expressed that it would be wasting vain efforts to develop a theory on which the strength of materials could be based scientifically. Homogeneous bodies of materials–I was told–do not exist, homogeneous states of stress are not encountered. It seems, therefore, utterly impossible to deduce a law of nature from experience. Since the existing irregularities furthermore are of such a nature that they nearly completely obscure any orderly behaviour, it has little interest to track the half–blurred traces of such laws. Under these circumstances nothing else remains than to make special tests in every important case and to pay no heed to a physical interpretation of the results. I had to admit in each case that nothing could be said against such reasoning; and yet for more than one hundred years, there have been attempts again and again to establish order within the confusing abundance of the experiences. If one should succeed in finding a few rules under which many experiences could be subordinated–of course rules in which some confidence could be placed–no law of nature would have been derived, but some means found for judging the probability of new results of experience."

Otto Mohr, Z. Ver. deut. Ing., p.740, 1901.

1.1 General

1.1.1 Serrated Plastic Flow

The dynamic interaction between a diffusing solute species and mobile dislocations is commonly referred to as dynamic strain ageing (DSA) [1]. A common, and probably the most familiar, manifestation of DSA is non–uniform plastic deformation which results in discontinuities (serrations) in the record of deformation. Serrated or jerky plastic flow occurs within a specific regime of strain, strain rate and temperature for any specific alloy [2]. Other common manifestations of DSA include a peak or plateau in the variation with temperature of the flow stress, work–hardening rate and Hall–Petch slope. Also, a negative macroscopic measured strain rate sensitivity is frequently concurrent with the existence of serrated plastic flow and is often seen as a prerequisite for such deformation characteristics.

In substitutional alloys of aluminium, discontinuities are commonly observed in the flow stress of alloys deformed at room temperature. The development of such discontinuities is referred to as the Portevin–Le Chatelier (PLC) effect. Concurrent with the occurrence of serrations in the deformation record, is the frequently observed appearance of surface markings similar to Lüders bands, known as PLC deformation bands. In addition, prior to the onset of PLC type deformation, random or flamboyant surface markings may appear at stress concentrations on the surface of deforming specimens.

1.1.2 Practical Consequences

Most commercially used metals include the deliberate addition of several alloying elements in order to produce the desired mechanical properties. The consequence of such additions is that many commercial aluminium alloys exhibit serrated plastic flow during room temperature plastic deformation. This, in turn, may have a direct deleterious effect in mechanical forming operations, specifically cold forming.

A minimum in elongation to fracture has been associated with the occurrence of the

PLC effect [3]. This is similar to the blue–brittleness observed during elevated temperature deformation of steels [4] and results in a reduced room temperature formability of aluminium alloys. In addition, such alloys frequently exhibit flamboyant surface markings, known as stretcher–strain markings, during commercial cold forming operations. Such markings are aesthetically undesirable and the associated surface roughness persists, even after subsequent painting of the formed product.

1.2 Aims of this Research

The aim of this thesis is to correlate the mechanical behaviour of a range of aluminium base alloys with the observation of microstructural features. Observation of deformation features was undertaken on the pre–polished surfaces of the materials as well as utilising both CTEM and in–situ deformation of some of the alloys within an HVEM.

1.3 Approach

All materials tested within the course of this work have been mechanically tested in tension, at room temperature and at a set strain rate ($\dot{\varepsilon} \approx 2.5\times10^{-4}s^{-1}$) except where explicitly indicated.

Limited variation of the mechanical test parameters allowed for direct comparison of all the materials tested, within a regime of deformation, which is known to correspond to the characteristic inhomogeneous plastic flow. The advantage of the approach taken was that it allowed for evaluation of the deformation characteristics and associated microstructural features of a broad range of materials with directly comparable results. In contrast to this, a common feature of work presented in the literature is that the variation of small experimental variables often interferes with the possibility of directly comparing the results of the work.

In addition to the above, a further facet of the approach taken was that it allowed for examination of a full range of deformation features, from a microstructural level through

to typical macroscale features, readily visible to the naked eye. The inhomogeneous deformation of aluminium alloys is ideally suited to such an approach, because the effect consists of macroscale deformation inhomogeneities which are manifestations of corresponding microscale heterogeneities. Although HVEM studies of aluminium alloys have been carried out in the past, these have been confined to single crystals, alloyed only with magnesium.[1] The *coordination* of microscale aspects of the deformation into resultant macroscopic manifestations has not, therefore, been well clarified.

1.4 Validity of the Approach

Verification of the results was achieved by comparing the microstructures produced by in-situ deformation in the HVEM with those of macroscopically deformed specimens observed in the CTEM. In addition, the surface deformation features of HVEM specimens were critically compared with those observed on the surfaces of standard tensile test specimens.

[1]The reader is referred to section 2.6.3, page 48 for a full discussion of prior HVEM work on Al alloys.

Chapter 2

Literature Review

2.1 Introduction

This chapter serves to review a broad range of existing literature covering prior research on dynamic strain ageing in aluminium alloys and related material. The scope of the experimental work to be presented in Chapter 4 is such that the literature reviewed in this chapter necessarily covers a range of published work, including the fundamental microprocesses of dynamic strain ageing, the resultant deformation process modelling and the macroscopic manifestations of the microscopic phenomena.

2.2 Dynamic Strain Ageing

2.2.1 Basic Concepts

The repeated appearance of discontinuities in the stress–strain curve of a deforming alloy is known as serrated or jerky flow. The appearance of a serrated stress–strain record of deformation may occur during tensile [5], compressive [6, 7] or torsional plastic deformation [8] and is characteristic of deformation during a specific regime of temperature (T), strain (ε) and strain rate ($\dot{\varepsilon}$) [2]. Serrated plastic flow can well be described as a resonance effect, which belongs to a particular class of instabilities known as relaxation oscillations [9]. An accurate analogy to describe the effect is the phenomenon of stick–slip

type behaviour often observed under dry sliding friction conditions.

Serrated flow was first observed by Le Chatelier in 1909 in mild steels deformed at elevated temperature [10]. Portevin and Le Chatelier investigated the similar properties of "Duralumin" deformed at room temperature [11, 12] and the phenomenon of serrated flow has subsequently been referred to as the PLC effect.[1] The flow stress discontinuities constituting the PLC effect are now widely accepted to originate on a dislocation scale from interactions between solutes and mobile dislocations, known as dynamic strain ageing (DSA) [14].

DSA refers to the attractive interaction between diffusing solute species in the alloy and mobile dislocations, during the deformation test. Originally, the solute clouds were considered to interact with dislocations during a quasi–viscous type of motion [15, 16]. More recent theories have acknowledged the fundamentally jerky nature of dislocation motion [17, 18, 19]. Ageing has been proposed to occur, not during the free flight motion of dislocations, but rather during the period when the dislocations are temporarily held up at local obstacles in the glide plane, known as the waiting time (t_w). A possible mechanism is the draining of solutes from the forest dislocations by pipe diffusion [20, 6]. Theoretical and modelling aspects of the PLC effect are discussed in section 2.7.

2.2.2 Breadth of Occurrence

Serrated flow curves attributable to DSA are observed to occur in a broad range alloys, where interstitial [21] and substitutional solutes have been considered responsible [22]. The well known phenomenon of "blue–brittleness" in iron [4][2], where serrations occur in the stress–strain curve of material deformed at elevated temperatures, was first attributed to DSA by Nabarro [23].

Materials reported to produce discontinuities in deformation related to DSA micro-processes include FCC alloys of Ni [24, 25] (Also H charged Ni [26] and C doped Ni [27]), Cu [28, 29, 30, 31, 32, 33, 34], Al (eg. [35, 36]), Au [37, 5, 38] and V [39]. The effect is

[1] "Duralumin" refers to a commercial alloy, manufactured following the work of Alfred Wilm, with composition Al–3.5Cu–0.5Mg–0.5Mn [13].

[2] See page 261 of [4].

also manifest in BCC alloys of iron [40]. Both interstitial (C) [41, 42] and substitutional solutes (O, Si, Mn, Ni, Ru, Rh, Re, Ir and Pt) [40] have been considered responsible for serrated flow in iron alloys. Finally, materials with a hexagonal crystal structure have also been observed to deform with serrated flow attributable to DSA microprocesses [43].

2.2.3 Manifestations of DSA

While serrated flow curves are the most commonly observed macroscopic manifestations of the DSA process, there are various other concurrent phenomena. Other anomalies associated with DSA microprocesses have recently been described by Rodriguez [44], and are illustrated [3] schematically in figure 1. A peak or plateau is observed in the variation with temperature of the flow stress, the work hardening rate ($\theta = \Delta\sigma / \Delta\varepsilon$) and the Hall–Petch slope (K_ε). In addition, minima occur in the variation of ductility and strain rate sensitivity ($\gamma = \Delta\sigma / \Delta \ln\dot{\varepsilon}$) with temperature.

Bands of localised deformation (PLC bands) are frequently observed to appear on the surface of a deforming specimen which is producing a serrated flow curve, at apparently random locations on the specimen [45]. Deformation bands are discussed in detail in section 2.3.3.

The occurrence of intensified acoustic emission (a.e.) concurrent with DSA deformation has also been noted in the literature (eg. [46]). Generally, a.e. is the phenomenon of high frequency elastic wave generation during deformation and fracture [47], which has been reasonably well developed as a technique for the study of plastic deformation [48, 49]. During deformation under DSA conditions, high frequency a.e. is regularly emitted and attempts have been made to correlate with this with dislocation multiplication events [50, 51]. In addition to high frequency a.e., audible a.e. bursts have been reported to occur during PLC deformation [46].

[3] Note: Various serration types are illustrated in figure 1. The classification of these is discussed in section 2.3.1.

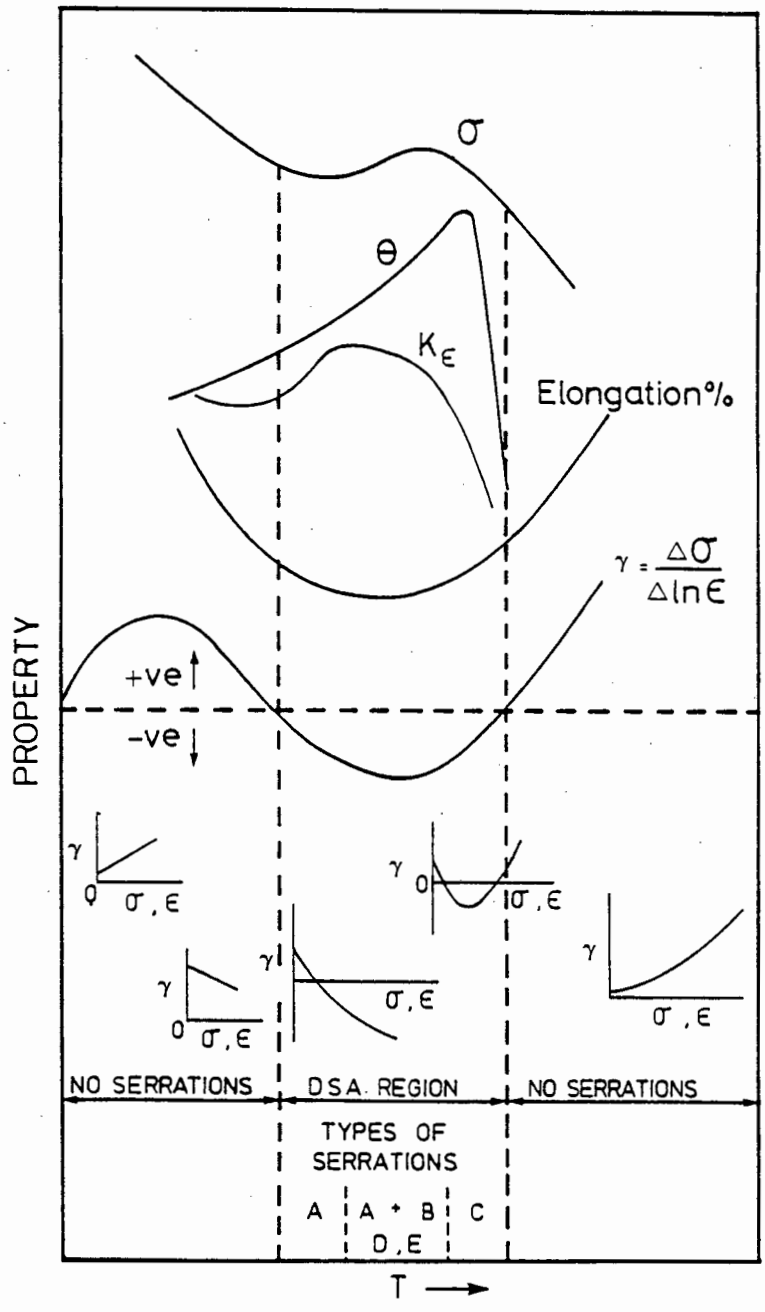

Figure 1: Schematic illustration of the various manifestations of DSA. After Rodriguez [44].

Two features discussed above serve as the most potent indicators of underlying DSA processes, the peak in flow stress variation with temperature and the negative macroscopic[4] strain rate sensitivity (SRS) of the flow stress. The peak in flow stress is generally observed to occur at temperatures of approximately 0.3 T_m (T_m = homologous melting temperature) [53]. The generalised flow stress–deformation temperature curve for a pure metal is illustrated in figure 2 below [54] and the corresponding curve for an alloy, where significant DSA occurs is shown in figure 3 [54]. It must be noted, however, that the domain of DSA is generally broader than that of the *PLC effect [6, 55] and thus the "hump" in the flow stress variation with temperature is an indicator of the proximity of the PLC effect [56] not the exact limits as suggested by figure 1.

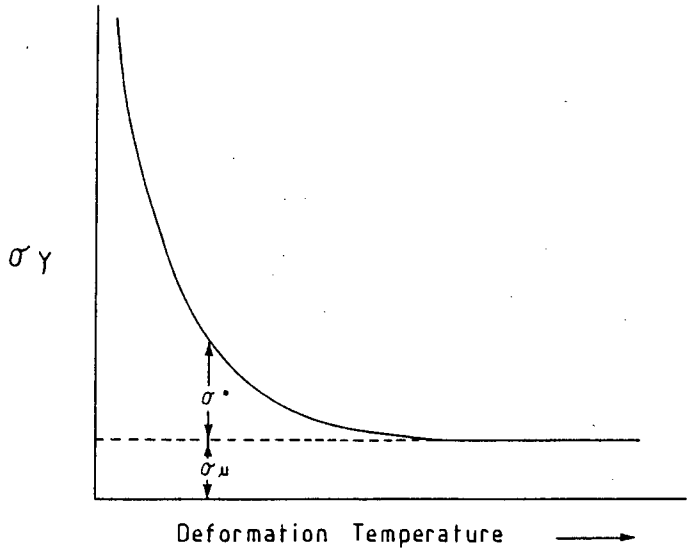

Figure 2: The generalised flow stress vs. deformation temperature curve for a pure metal. The thermal (σ^*) and athermal (σ_μ) flow stress components are indicated. After Morris [54].

The negative macroscopic SRS is also a strong indicator of DSA and the associated proximity of the PLC effect [57]. A direct consequence of a negative SRS is that spontaneous strain localisation may occur. Any fluctuation in the strain rate will necessarily increase in amplitude such that uniform plastic deformation is no longer stable [58]. The negative SRS, as a necessary condition for strain localisation, was one of the basic tenets

[4]A distinction is made here between the macroscopic (measured) SRS and the microscopic (intrinsic) SRS which results from a domain of inaccessible dislocation states. For a full discussion the reader is referred to reference [52].

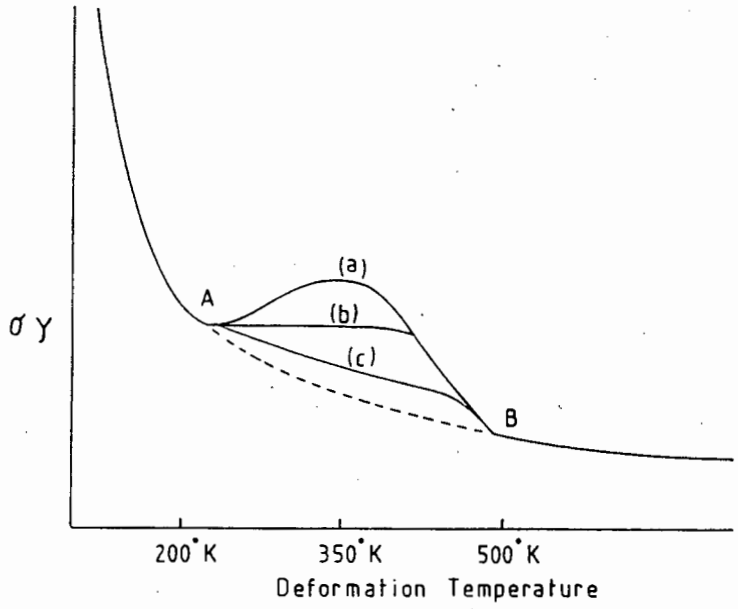

Figure 3: The generalised flow stress vs. deformation temperature curves for an alloy. In (a) the effects of DSA are dominant, whereas in (c), dynamic recovery and softening remain the dominant processes. After Morris [54].

of Pennings mathematical model [59], which has since served as the foundation for several more recent models of PLC processes (eg. [17, 60]). Figure 4 from Pennings paper is reproduced in figure 4, to illustrate the effect of a negative SRS. Theoretical modelling is discussed in more detail in section 2.7.

2.3 Serrated Flow and the Formation of Deformation Bands

2.3.1 Classification of Serration Types

Serrations in the flow curve of an alloy, which are caused by interstitial elements, are reported to be irregular and not easily systematically analysed [61]. In the case of serrations caused by the interaction of substitutional elements and dislocations, however, a systematic analysis has been applied. The serration types are termed A, B, C, D and E (eg. [62]).

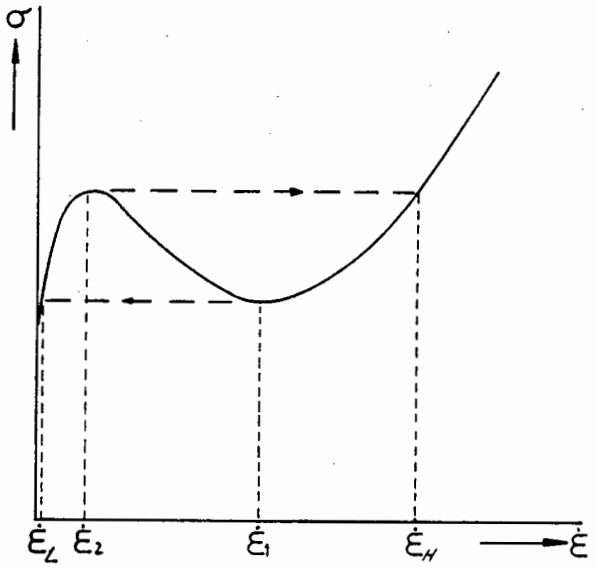

Figure 4: Figure illustrating the possible strain rate jumps associated with a single value of applied stress. After Penning [59].

Classification of the serration types is made according to their appearance on the deformation record and their associated deformation characteristics. An illustration of the serration types is reproduced in figure 5. Types A, B and C are well recognised and their characteristics are well documented [22, 44]. Recently D and E type serrations have also been identified [62].

The characteristics of the individual serration types and the experimental conditions which produce them have been recently summarised [44, 1].

1. Type A serrations are periodic serrations arising from repeated deformation band initiation at the same end of the specimen and propagation of the bands along the gauge length. They are considered to be locking serrations, characterised by an abrupt rise of the flow stress followed by a drop to below the general level of the stress–strain curve. They occur in the low temperature (high strain rate) region of the DSA regime.

2. Type B serrations are oscillations above and below the general level of the stress–strain curve, that occur in quick succession and are due to discontinuous band propagation. The bands corresponding to type B serrations contrast with the smooth propagation of the band that succeeds a type A load drop, with the discontinuities

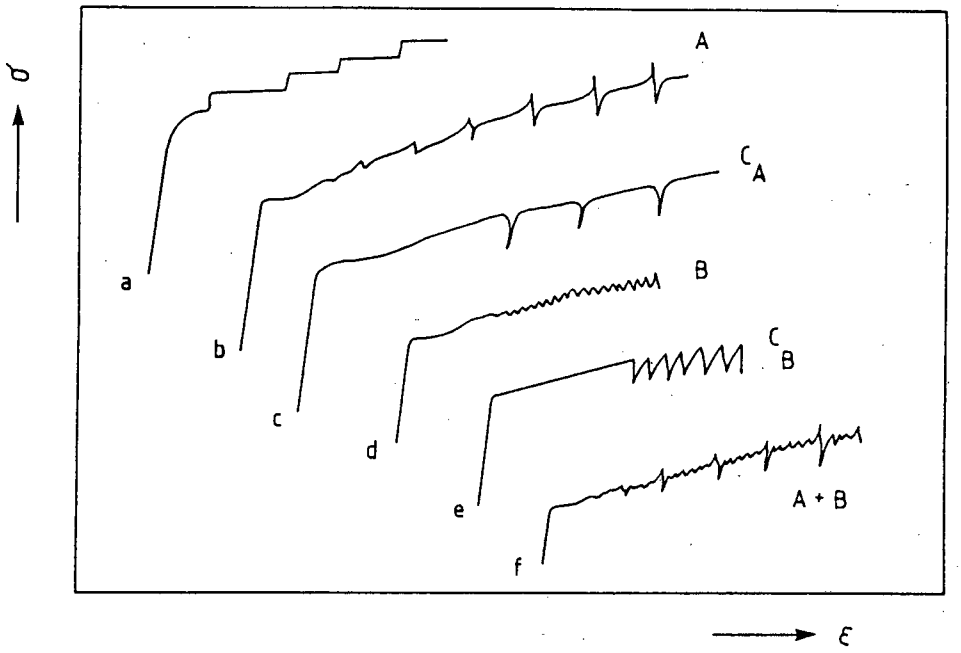

Figure 5: Schematic curves illustrating the various serration types commonly observed in the deformation of substitutional solid solution alloys. After Rodriguez [44].

being thought to arise from the DSA of moving dislocations within the band. Type B serrations often develop from those of type A or alternatively appear at the onset of serrated flow during high temperature deformation, or at slow applied strain rates.

3. Type C serrations are yield drops that fall below the general level of the stress–strain curve and are often considered to be due to dislocation unlocking. They occur at higher temperatures and lower strain rates than types A and B serrations.

4. Type D serrations are plateaus in the stress–strain curve due to band propagation similar to that observed in Lüders deformation, where there is no work hardening or strain gradient ahead of the band. As in the case of type A, type D serrations may occur alone, or together with type B serrations during the band propagation.

5. Type E serrations result from type A serrations at high strains. They are similar to type A serrations, but with little or no work hardening during band propagation.

It can be noted from the above and from figure 5 that more than one serration type

may occur simultaneously. Type E serrations generally appear at high strains, or near the maximum load. If they are preceded by type A, then type E serrations generally cancel out the type A serration [62]. Type B serrations are expected to be accompanied by type A or D, both of which can occur alone. An example of the domain of existence of various serration types in an 0.03%C steel, a ferritic stainless steel and an Al–5%Mg alloy is taken from the work of Pink [61] and presented in figure 8.

2.3.2 The Critical Strain

A significant and controversial feature of serrated deformation curves is the commonly observed occurrence of an incubation strain prior to the onset of serrated flow (eg. [63]). The incubation period, consisting of homogeneous plastic flow, is commonly referred to as the critical strain (ε_c). ε_c was necessarily incorporated into Cottrell's 1953 theoretical treatment, in order to explain the discrepancies between the measured diffusion coefficient and that required for DSA of *moving* dislocations [15]. A critical concentration of vacancies was proposed to be created by plastic deformation, resulting in a substantially enhanced diffusion coefficient of the solute species responsible for DSA of the moving dislocations. The concentration of vacancies (C_v) is classically considered to increase according to $C_v=10^{-4}\varepsilon$ [4][5].

ε_c is observed to be influenced by both strain rate and temperature [17]. The value of ε_c increases with increasing strain rate and decreasing temperature at high strain rates [64], where the first serrations are generally observed to be of type A or B [44]. Where type C serrations are observed, at high temperature and low strain rates, ε_c is reported to increase with increasing temperature and decreasing strain rate. These properties are summarised in figure 6 below. It has also been observed that ε_c generally increases with increasing grain size (eg. [22, 65]).

An effect where ε_c is observed to increase with an increase in temperature or decreasing strain rate [66] has been referred to as the "inverse PLC effect". King et al recently observed this inverse effect of strain rate on ε_c in Al alloys [43], but still concluded that the underlying mechanism was one of dislocation pinning. King et al concluded that

[5]See page 261 of [4].

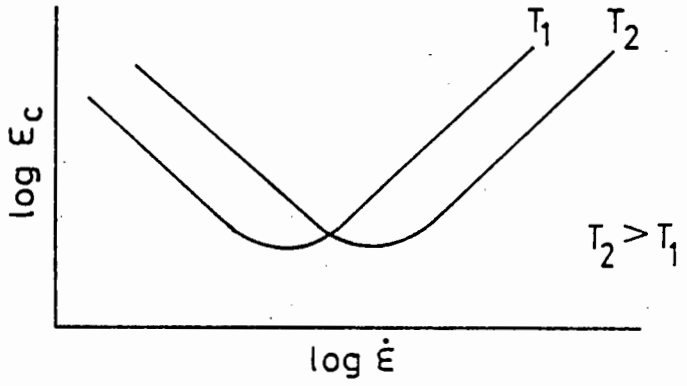

Figure 6: The variation of critical strain with strain rate and temperature. After Rodriguez [44].

solute diffusion through the lattice was responsible for DSA, not pipe–diffusion as has been recently proposed by Mulford and Kocks [6].

ε_c, then, is the critical strain, at which point stress instabilities are evident on the deformation record. The most accurate interpretation of ε_c, however, is that ε_c is the value of strain at which point the SRS becomes negative (eg. [52]). General agreement about how the SRS becomes negative, has yet to be reached.

2.3.3 Deformation Band Formation

Surface markings, frequently in the form of regularly spaced parallel bands, have often been observed in conjunction with serrated deformation curves [45]. Parallel bands form one of the two types of surface markings commonly observed under tensile deformation conditions. The surface markings are generally classified as type A or B, depending on their morphology, after Eborall [67]. Originally, both types were generically referred to as stretcher–strain markings [68].

Type A

Type A surface markings, also referred to as flamboyant or random markings, because of their flame–like or wedge shape, occur after a low strain [61]. Their arrangement is

reported to be identical on both sides of the specimen. The initiation of type A markings is the result of heterogeneous stress distribution and (hence strain distribution) in a deforming specimen [45, 69]. The boundaries of type A markings, formed primarily by shear are associated with kinking of the metal surface by angles up to 50′ [70]. Figure 7 illustrates typical type A surface markings. Two common occurrences of type A markings are in Al–Mg alloys deformed at room temperature or a mild steel deformed in the "blue–brittle" temperature range (approx. 175°C) [69].

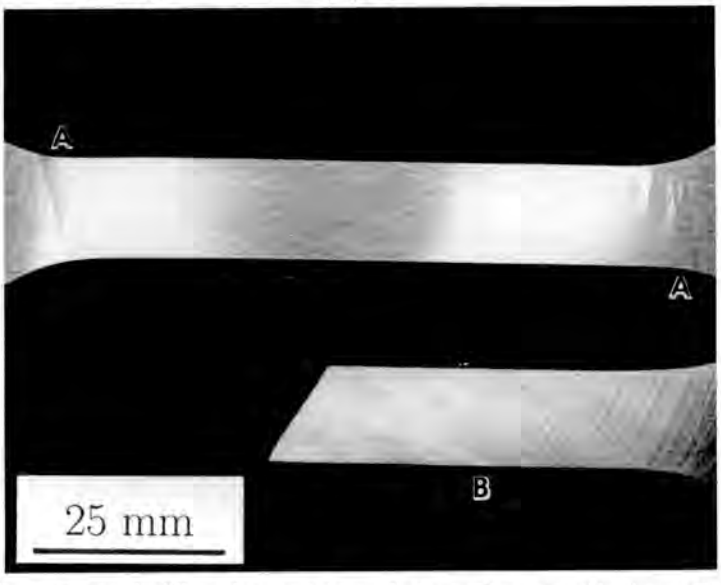

Figure 7: Typical type A (flamboyant) and type B (parallel) surface markings.

Type B

Type B surface markings refer to the regular parallel bands, commonly observed on the surface of a specimen deforming under serrated flow conditions. Type B flow markings, also referred to as Lüders[71] or PLC bands [46], occur at a characteristic angle to the specimen tensile axis (eg. [68]).

The deformation producing type B markings has been recognised as a succession of localised necks along the gauge length of a deforming specimen, which may be continuous or discontinuous [61]. The angle of inclination of the necks is predicted theoretically to occur at 54°44′, by mathematically modelling the formation of localised necks in sheet material deformed under plane stress conditions [72]. Recent research indicates, however, that this angle may be influenced by the rolling texture [73]. Webernig et al [73] found a

variation in the angle of the bands to the tensile axis, depending on the relative orientation of the tensile axis to the rolling direction of the material. The band angle varied from 52° to 66°, where the 66° maximum was associated with the tensile axis being perpendicular to the prior rolling direction

Type A markings generally form first, at strains of up to 2.5%, and are then followed by type B [69]. The fact that type B bands can form at strains as low as 0.5% [69] and yet continue to form until fracture is of interest when considering the micromechanisms of their formation. Recent work considers type B bands (PLC bands) as concurrent with serrated flow, and their occurrence is attributed to DSA microprocesses [56]. The distinction between those bands which propagate during a stress plateau [5] and those forming during overall work hardening [45, 74] has not been explicitly dealt with.

An interesting phenomenon is the disappearance of type B markings under conditions of equibiaxial straining [75] which also reduces the tendency for serrated flow [76]. Tests in which a ball was pressed against a clamped test piece, similar to those used to determine formability, were used to deform sheet aluminium. The material was observed to develop type B flow markings only outside of the central contact area, where deformation was not equiaxed.

2.3.4 The Relationship of PLC Deformation with Lüders Bands

The sudden, localised propagation of slip across a crystal at the onset of plastic deformation is the result of rapid dislocation multiplication and may cause a large yield drop. The initial region of deformation is called the Lüders band, and the boundary between deformed and undeformed regions, the Lüders front [77]. This type of behaviour is commonly observed in the deformation of mild steels (eg. [78]) and similar behaviour may be observed in the case of slowly cooled Al–Mg alloys [79]. The Lüders strain ε_L conventionally refers to the strain increment associated with the passage of a single deformation band (growth of a deforming region) axially along the gauge length of a deforming tensile specimen [4][6]. ε_L is then, the strain produced, at constant stress, immediately after the yield point, which generally produces a uniformly strained total gauge length.

[6]See pages 260–261 of [4]

Although Hall [80] refers to all banding in Al alloys as type A or type B Lüders markings, and ε_L as the initial Lüders extension, a slight correction to this terminology will avoid ambiguity. Type A and B are best suited to describing the two types of deformation markings commonly observed, as described in section 2.3.3. ε_L and Lüders bands refer to the initial passage of a band (and the associated strain increment) into previously undeformed material with no work hardening. PLC bands refer to the persistent formation, and possible propagation, of bands coincident with a serrated deformation record, which may continue until the point of specimen failure.

It must be noted, however, that the DSA of dislocations at a Lüders front may also occur. The result of DSA during ε_L is that the stress oscillates around a constant level and the stress plateau is serrated [42]. Chihab et al [45] reported intermediate strain rate ($\dot{\varepsilon}$=10^{-4} - 10^{-3} s^{-1}) deformation of an Al–5% Mg alloy to occur by discontinuous, but orderly and periodic, deformation, with each band initiated immediately adjacent to the next. DSA at a moving band front may be strong enough to halt its passage, and force yielding to occur in another part of the specimen.

2.3.5 Effects of Specimen Geometry

No obvious systematic work has been undertaken on the effects of specimen geometry on PLC band deformation. Most work has produced results with PLC bands oriented at 55–60° to the tensile axis (eg. [81]), i.e. the angle of bands associated with deformation conditions approximating plane stress. Some testing has been performed using specimens of circular cross–section, where banding has been reported to occur at 45° and 60° [43, 61].

Direct consideration of the orientation of propagating Lüders band fronts, as a function of specimen geometry, was undertaken by Delwiche and Moon [82]. They studied the orientation of a slowly propagating Lüders band front in mild steel by using a two surface trace analysis and standard stereographic projection techniques [83]. Prior to the work of Delwiche and Moon, angles of between 45° and 76° were reported for the angle between a single surface trace of the Lüders band front and the tensile axis [84, 85, 86, 87, 88, 89, 90]. Angles of approx. 55° were consistently reported for specimens of rectangular section cross–section.

Delwiche and Moon experimented on parallelogram cross–section specimen geometries by varying the angles of the parallelograms between 30 and 90°. Trace angles of the Lüders bands were measured on the specimen surfaces and then the angle (θ) between the plane of deformation and the tensile axis was calculated. θ was consistently 44°–46°, except in the case of multiple band nucleation and complex band front development. They concluded that in a low carbon steel;

1) Lüders deformation is produced by shear induced slip. The Lüders front is consistently at 45° to the tensile axis in an axially loaded specimen.

2) Nucleation of the band occurs at a point of stress intensification [91] and spreads on the plane of maximum shear.

2.4 Variables Affecting the Nature of Serrated Flow

2.4.1 Microstructural Variables

Solute Concentration

Since DSA entails interaction between mobile solutes and dislocations, the solute concentration of the alloy can be expected to influence serrated flow characteristics. DSA is generally a phenomenon observed in dilute solid solutions [56] but has been reported to occur in alloys of solute content of 20% or higher [92]. The concentration of solutes trapped in solid solution, affected by prior solution and precipitation treatments, will then have a direct effect on DSA related deformation properties. Precipitation hardening is generally observed to suppress serrated flow [93, 94]. The effects of precipitation processes on serrated flow in Al alloys are explicitly dealt with in section 2.5.3.

The effect of different solute contents has been examined in the cases of commercial purity polycrystalline material [79], experimental high purity polycrystalline material [95, 96] and high purity single crystals [96]. In all cases the stress amplitude ($\triangle\sigma$) of serrations was observed to increase with increasing solute content. Further, for a specific grain size,

the regularity of serrations was observed to increase with increasing Mg content in Al–Mg polycrystals [96].

By plotting $\log \dot{\varepsilon} T$ against 1/T, Miura [95] was able to determine the activation energy E_A for the onset of serrated flow in various Al–Mg alloys. E_A for Alloys with between 0.55at.% and 3.0at.% Mg, with more than one grain size in each case, was consistently calculated to be 0.60±0.02 eV i.e. independent of solute content and grain size.

Grain Size

Variations in grain size are observed to affect both the surface flaws formed on a deformed specimen [68] and the serrated flow characteristics of the flow curve [65].

Stretcher–strain markings are known to be most intense in materials with a fine grain size [97, 98], which has been attributed to the $1/\sqrt{d}$ dependence [79] of ε_L [99]. Where the grain size exceeds ~50 μm, stretcher strain markings are replaced by "orange–peel" type surface markings [61]. Orange peel type deformation refers to the surface roughening produced in the deformation of coarse grained aluminium alloys as a result of orientation dependent glide [61]. The disappearance of stretcher–strain markings for coarse grain sizes suggests, therefore, the co–operative nature of the deformation of multiple grains necessary for their formation. Fujita and Tabata [96] suggest the need for trigger grains (those with a maximum Schmidt factor) to advance deformation localisation to a few grains surrounding the trigger. Importantly, they conclude that each step yield (serration) in a polycrystal consists of deformation amongst a limited group of grains, but not necessarily to heterogeneous deformation within each individual grain.

Two other noteworthy features with regard to the effect of grain size on the nature of serrated flow have been presented in the literature. Firstly, serrations are observed to persist until higher strains in fine grained material [3] and secondly, some consideration has been given to the fact that DSA may occur preferentially at grain boundaries [44]. If DSA does occur preferentially at the grain boundaries, then that would provide a reasonable rationalisation for why small grained material has enhanced DSA properties.

Prior Deformation

Materials tested for DSA properties are usually tested in the cold–rolled, annealed or solution treated and quenched condition. Some work exists on the effect of precipitation hardening on serrated flow (eg. [100]), which is discussed in section 2.5.3.

Original considerations given to the effect of pre–treatments on yielding discontinuities were aimed at suppressing the occurrence of stretcher–strain markings. Because of the deleterious effect of surface markings on the appearance of cold pressings, commercial treatments were devised to minimise their occurrence [61, 4]. An example is the German designation for pre–treated alloys, "ffa" (flieBfigurnarm), implying low stretcher–strain. The methods devised were largely developed empirically, without a clear understanding of the micro–mechanisms involved.

Methods to minimise markings are largely effective in terms of type A markings, which are the more harmful in press forming operations. A very light rolling of the material, known as "skin passing" or "pinch rolling" is effective for restricting the subsequent formation of type A markings in a press forming operation [3]. The dislocations are assumed to be torn away from their solute clouds by the rolling operation, and hence subsequent dislocation motion is less sudden. Another method is to increase the grain size of the material being formed [61], but caution has to be exercised that an "orange–peel" type effect doesn't replace the type A markings [101]. A similarly effective method to minimise the appearance of type A markings is to solution–treat and quench the material prior to forming, but this is known to enhance the possibility of formation of type B markings. The only really effective method of removing type B markings is to deform the material outside the PLC ($\dot{\varepsilon}$, T) regime.

The tensile characteristics of an Al–5Mg–0.8Mn alloy have been considered as a function of prior cold–rolling deformation [102]. The maximum serration amplitude ($\triangle\sigma_{max}$) increases with the percentage of prior cold–rolling deformation. In the case of annealed material, a distinct work hardening was observed in conjunction with a steadily increasing $\triangle\sigma$ until failure. In the case of the cold–rolled material, serrations were observed to occur in a series of successive plateaus of constant stress (minimal work hardening), with increasing $\triangle\sigma$.

Roopchand and Morris [103] tested a 5086 commercial Al-Mg alloy[7] for the effects of 0%, 30%, 60% and 80% prior cold–rolling reduction on serrated flow properties. The observed increase in $\triangle\sigma$ with prior cold work was attributed to enhanced solute diffusivity as a result of deformation induced vacancies. The macroscopic SRS was also observed to become more negative with increasing amounts of prior cold work.

Other workers [104], however, found that initial homogeneous yielding occurred in Al–Mn–Mg, in spite of sufficient time having elapsed for ageing to have occurred. Prior cold work of greater than 20% deformation was observed to entirely suppress serrated flow, and it was argued that strong dislocation interactions may have been dominating over DSA effects. Pink [105], working on the effect of cold–rolling on serrated flow, found similar features, in that the domain of serrated flow was observed to decrease in the cold worked state. In binary Al-Mg, serrations were equally well pronounced for thickness reductions of 0%, 50% and 75%. A difference was observed in the case of Al–5%Zn–1%Mg, in that 25% reduction was observed to reduce serrations to "mere discontinuities", which were barely visible in testing following 50% rolling reduction. In the case of Al–Mg and Al–Zn–Mg, the disappearance of serrated flow in the second alloy after cold–rolling, was attributed to the occurrence of deformation induced precipitation.

It is likely that the disappearance of serrated flow with cold–rolling reported by Saha et al [104] was the result of a similar phenomenon to that suggested by Pink [105] for the case of Al–Zn–Mg. The results, where serrated flow is enhanced by prior cold–rolling deformation, are in line with models which consider the development of glide plane obstacles as fundamental to the DSA affected deformation process [106].

2.4.2 Test Parameters

Test Temperature

Serrated flow occurs within a specific regime of temperature, i.e. within the regime where DSA of dislocations readily occurs. Indications of the temperature regime include the

[7]The four digit coding of commercial Al alloys is detailed in section 2.5.2.

negative SRS of the flow stress and the "hump" in flow stress variation with temperature.[8] The specific effect of varying the test temperature, on serrated flow properties, is best summarised by the diagrams in figure 8. The domains of serrated flow and range of existence of the various serration types is clearly illustrated by the three examples of variations with test temperature.

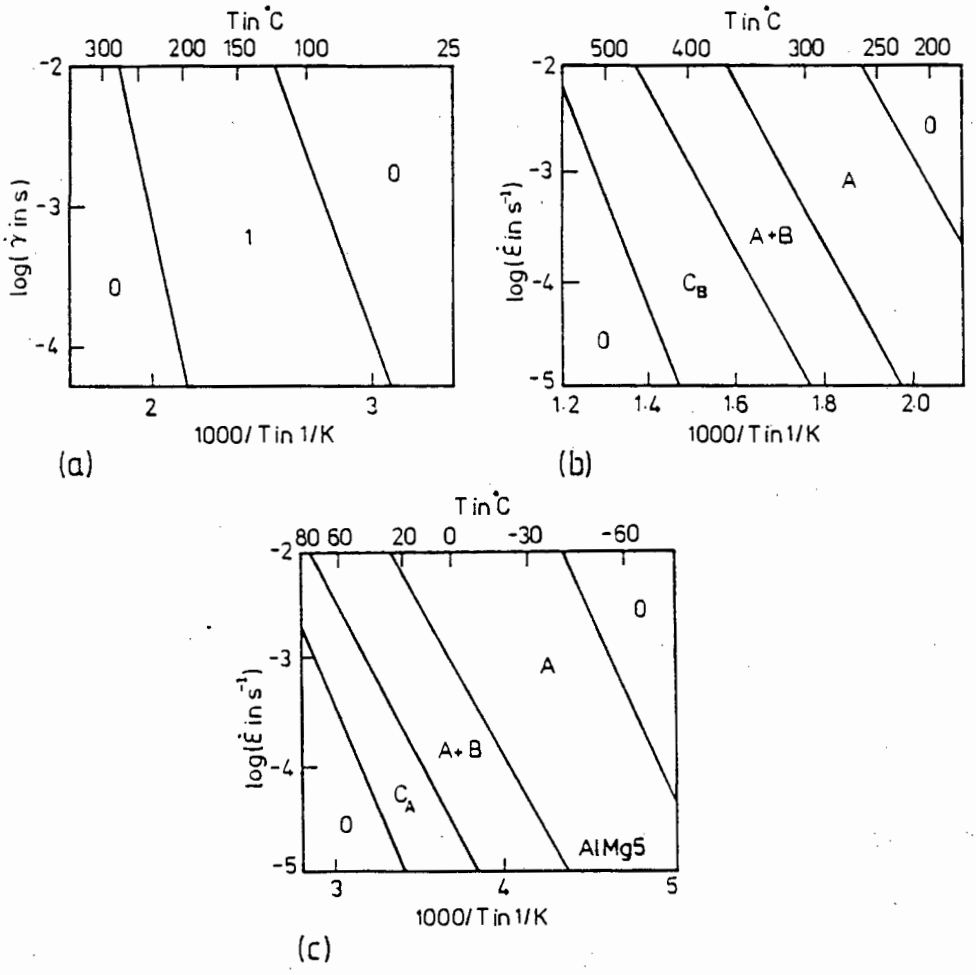

Figure 8: The domains of serrated flow and the range of existence of the various serration types illustrated by the three examples of variations with test temperature i.e. (a) 0.03%C stteel (b) Ferritic stainless steel (c) Al–5%Mg. After Pink [61].

Serrated flow in Al–Mg has been observed to disappear (revert to homogeneous deformation) at lower strains as the temperature was raised [107]. The disappearance of serrated flow at an upper critical strain was also observed in Ni alloys [24] and Fe alloys

[8]See also section 2.2.3.

[108] and resulted in a model proposed by Hayes and Hayes [108]. The most recent attempts at modelling PLC type deformation include the possible occurrence of more than one critical strain, and hence the dissappearance of serrated flow at high strains [109]. Modelling and theoretical aspects are discussed further in section 2.7.

Strain

Serrated flow is associated with both a ductility minimum and a peak in the work–hardening rate [44]. The high work hardening rate is at least partially due to the rapid accumulation of a dense dislocation structure [42], further discussed in section 2.6.3. The observed abnormally high rate of dislocation accumulation is probably due partly to the high production rate of dislocations associated with repeated yielding [42, 54], but also due to the solute restricted dynamic recovery processes (and associated dislocation annihilation) [54].

With direct reference to serrated flow, the most obvious influence of plastic strain accumulation is the progressive increase in serration amplitude ($\triangle\sigma$) which is often observed (eg. [96, 81]). The first possible reason why DSA is more effective at higher strains, is that one could expect more effective dislocation pinning by mobile solutes on account of a higher solute diffusivity, itself associated with the increased vacancy population produced by plastic deformation. A second plausible reason for the increase in ($\triangle\sigma$) is that, at higher strains, the greater density of forest dislocations in any single glide plane would imply enhanced obstacle strength, and therefore an increased waiting time (t_w) allowing for more effective dislocation pinning.

Strain Rate

The characteristic negative SRS of the flow stress of an alloy deforming in the DSA regime has been introduced in section 2.2.3. A similar effect is the negative SRS of $\triangle\sigma$. A decrease in the serration amplitude at increased applied strain rates has been observed by Korbel and Dybiec [35] and others [40, 45, 110]. In terms of the theory proposed by Korbel and Dybiec, the decrease in $\triangle\sigma$ was rationalised by considering stress relaxation in the vicinity

of a band. The time available for stress relaxation, and hence for maintaining the stress concentration at the band front required for its easier propagation, was considered to be lessened by testing at higher strain rates. If t_w is considered, then the time for ageing (t_w) of temporarily arrested mobile dislocations is lessened by increased strain rate testing. A decrease in t_w means decreased strength of the forest/mobile dislocation junction, and therefore a decrease in ($\triangle\sigma$). The applied strain rate may also affect the ε_c, as has been discussed in section 2.3.2.

Straining Conditions

Serrated plastic flow has been regularly observed in specimens subjected to uniaxial tension, but has also been observed to occur under compression (eg. [6]) and torsional (eg. [8]) loading.

Unstable plastic flow of Al alloys, during torsion testing, has been observed in both AL–Mg–Si [111, 8] and Al–Zn–Mg [112]. Inhomogeneous deformation in Al–Mg–Si was not by repeated discontinuous yielding, but rather by the initiation of one or more high strain bands, which propagated slowly over the gauge length [8]. Typical Lüders stress plateaus occurred on the deformation record, with two modes of discontinuous yield observed depending on the initial state of the specimen. For quenched specimens and short ageing times, strain localisation was attributed to DSA phenomena. For long ageing times, strain softening, associated with dislocation shear of precipitates [113, 114], was the proposed mechanism [111].

Essentially similar deformation to that observed in Al–Mg–Si, was observed in Al–Zn–Mg tested in torsion [112]. Again two deformation modes, depending on the extent to which solutes were precipitated from solution, were observed.

2.5 Serrated Flow in Aluminium Alloys

2.5.1 History

As is evident from the preceding information, aluminium alloys have a substantial history of being researched for DSA related properties. The initial work by Portevin and Le Chatelier examined two aluminium alloys, ternary Al–Mg–Si and Al–Cu ("Duralumin") [11, 12]. Two major features of the inhomogeneous deformation of Al alloys conspire to make them particularly suitable for investigation into DSA related phenomena;

1. The classic deformation features exhibited by substitutional Al alloys during deformation in the DSA regime, especially in the case of Al–Mg.
2. The occurrence of the phenomena during deformation close to room temperature.

2.5.2 Solutes Responsible for Serrated Flow in Al Alloys

Serrated flow properties in classic binary and ternary Al alloys were reviewed by Hall in 1971 [80]. Solutes to which serrated flow could be attributed to included Cu, Mgand Mn. Since Hall's work, serrated flow during room temperature deformation has been ascribed to Si [115], Ag [116] and Zn [55, 117]. Further, high temperature deformation has revealed the probability of Fe as solute producing serrated flow, outside of the standard regime of room temperature testing [58].

Binary Alloys

- Aluminium–copper

Early work on binary Al–Cu utilised soft tensile testing machines[9], which produced stepped as opposed to serrated curves [80][10]. Characteristic features of the deformation included a smooth rounded initial yield point, followed by serrations after a clear ε_c, the length of steps (magnitude of serrations) increasing with strain and the presence of type A and/or type B deformation markings under favourable conditions.

Type A markings observed by Hooper were, however, found in a commercial material containing Mg, Mn and Si [118]. Krupnik and Ford [119] tested material of varying Cu content and observed similar behaviour in 1.35%Cu, 3.83%Cu and a commercial material containing 4%Cu as well as Mg, Mn, Fe and Si. No type A markings were observed but persistent type B markings were reported, unless the sample had been heavily aged or overaged. Hooper [118] produced similar results to Kruprik and Ford, but with a suggestion of type A yielding in annealed samples. Static ageing tests confirmed the relationship between serrations and capacity to age.

Various investigations into the deformation properties of Al–Cu single crystals, have revealed no serrated flow in air cooled, fully aged and overaged conditions [80][11]. Different rates of strain hardening were observed and static strain ageing occurred in an interrupted tensile test. Two possible rationalisations for the lack of serrated flow were suggested, either an essential impurity was missing in the single crystal material, or grain boundary effects are fundamentally important.

More recent research on Al–Cu polycrystals has been interpreted to confirm the role of Cu in DSA related deformation inhomogeneities [94, 120]. Commercial polycrystalline Al–Cu containing Mg and Mn was found to produce a serrated deformation curve in the solution heat treated (SHT) condition (490°C, 1hr, WQ) as well as when fully annealed (490°C, 1hr, 2°C min^{-1} furnace cool) [94]. SHT material deformation records showed predominantly type C serrations and a consistently negative macroscopic SRS of the flow stress. Annealed material deformed with type B serrations at much lower loads (UTS$\approx$540kg, $\dot{\varepsilon}$=1.5$\times 10^{-4}$) in comparison to the SHT material (UTS$\approx$840kg, $\dot{\varepsilon}$=1.5$\times 10^{-4}$), but also had a negative SRS of the flow stress. The

[9] "soft" tensile machines rely on a stepwise or continuously increased load. Modern tensile machines are usually "hard" i.e. with a spring constant $K \geq 10000 N/mm$ and deformation is usually specified by a rate of cross–head change.

[10] See page 181 of [80]

[11] See page 184 of [80]

negative SRS in the annealed material was attributed to DSA by mobile Cu atoms, but in the case of the quenched solution treated material, was attributed to time dependent natural ageing (age hardening) phenomena. Aged material (490°C 1hr, WQ, 3 days at room temperature) deformed with smooth tensile curves and exhibited a positive to zero SRS. No comment was made on band formation or surface markings.

Directly comparable testing to that using commercial material (above) was undertaken on three high purity, binary Al–Cu experimental melts containing 1%, 3% and 4.5% Cu [120]. Alloys were heat treated at 345°C, 485°C and 535°C for two hours followed by slow cooling to deliberately avoid natural ageing (precipitation) phenomena during tensile testing. All material had a negative SRS in the strain rate regime 10^{-5} $s^{-1} \leq \dot{\varepsilon} \leq 10^{-2}$ s^{-1}, and the associated tensile deformation curves were serrated. Serration amplitude was dependent on solute content (Cu content $\uparrow \Longrightarrow \Delta\sigma \uparrow$) and heat treatment temperature. The 1% alloy had a constant serration amplitude for all three heat treatment temperatures, whereas the 3% and 4.5% Cu had a peak $\Delta\sigma$ after treatment at 485°C.

- Aluminium–magnesium

  As is clearly apparent from the preceding sections, Al–Mg forms the definitive substitutional alloy system investigated for serrated flow properties. The surface markings are of concern in industrial forming processes, and the profound serrations (and other concurrent DSA related manifestations) provide model examples of generally occurring phenomena.

  Examples of the deformation behaviour of Al–Mg alloys, presented earlier in this chapter, have illustrated many of the DSA related manifestations, which are summarised below. Serrated flow in Al–Mg exists over a $\dot{\varepsilon}$–T regime defined from $\dot{\varepsilon} \approx 10^{-6} \rightarrow 10^{-2}$ and T $\approx -80°C \rightarrow 80°C$ [62]. At higher temperatures serrations persist until higher strain rates and, conversely, lower strain rates are required to induce serrations at the lower end of the temperature regime. Serration types[12] A, B, C, C_A and C_B have been observed to occur and their appearance depends on the strain, strain rate and temperature of testing.

[12]Classification of serration types is discussed in section 2.3.1, page 10.

ε_c has frequently been observed to precede serrated flow in Al–Mg (eg. [74]) but is reportedly not absolutely necessary prior to the onset of serrations of type A or B [62]. ε_c is observed to increase with increasing $\dot{\varepsilon}$ and may increase or decrease with increasing temperature depending on the serration type [95]. ε_c decreases with increasing temperature in the case of type A serrations but shows the opposite tendency in the case of type B and C serrations. Serrations in Al–Mg (as well as other materials [108]) have been observed to occur with an upper critical strain [107]. The upper ε_c is the strain at which deformation again becomes homogeneous, i.e. the serrated tensile curve becomes smooth. In Al–Mg, the upper ε_c is observed to occur at lower strains, as the deformation temperature is increased [107].

Each stress drop is observed to coincide with the formation of deformation bands on the specimen surface, which may form consecutively or at apparently random points on the gauge length [45]. The formation these surface markings has been discussed, with particular reference to Al–Mg in section 2.3.3. $\triangle\sigma$ is observed to increase with accumulated ε and decrease with increasing $\dot{\varepsilon}$ [81].

Serrated flow has been observed in single crystals of Al–Mg tested in conjunction with polycrystals of the same material [96]. Single crystals were observed to show a significant decrease in $\triangle\sigma$ in relation to polycrystals and the serrations are far less regular. $\triangle\sigma$ increases with strain until the transition between stage II and stage III, after which it gradually decreased towards a constant value. The heterogeneity of deformation bands was maximised at the end of stage II. Serrations were observed at both 293 and 77 K, at which point solute diffusion becomes very limited [121]. The authors therefore concluded that the cause of serrated flow exists, even under conditions where solute diffusion hardly exists. It is possible, however, that another factor, such as localised deformation due to adiabatic heating [122], may have influenced the deformation properties at 77 K. Alternatively, the fundamentally jerky motion of dislocations between thermally surmountable obstacles in the glide plane [19] may have been enhanced to different degrees, by solute–dislocation interactions, at the two test temperatures.

More recently, Tabata et al considered the deformation of three different orientations of Al–Mg single crystals [123]. The three specimens were oriented for single (S), double (D) and multiple (M) slip from the onset of plastic deformation. In all cases, serration amplitude increased to a maximum at the end of stage II, and

then gradually decreased to a constant value. In the case of specimen M, a sharp large amplitude serration was observed to correspond with large local strain in the specimen. For specimens S and D, broad serrations of small amplitude were observed. The authors concluded that the shape and magnitude of the serrations in Al–Mg single crystals is strongly related to the nature of the obstacles formed by the interactions between dislocations. This result, therefore, lends support to the proposition that the ageing of dislocations during DSA occurs mainly during the waiting time (t_w), during which the dislocations are temporarily held up at local obstacles in the glide plane [38]. The obstacles are likely to be forest dislocations, from which rapid draining of solutes may occur, by "pipe diffusion" [6, 20].

- Aluminium–iron

  Two papers by Chossat in 1950, not directly dealing with serrated flow, show Al–Fe to exhibit steps during deformation by a soft tensile machine, after annealing at 350°C or above [124, 125]. Fe has a very low equilibrium solubility in Al, from 0% at 400°C to 0.05% at 650°C (immediately prior to melting) [80].

  Recent work on a rapidly solidified Al–Fe–V–Si [126] alloy, showed both a small anomaly in the flow stress vs. temperature and a dip in the SRS at ~400 K. This unusually high temperature for the appearance of DSA effects (in Al alloys) was attributed to the mobility of dissolved Fe. The reason suggested for the high temperature occurrence of the effect was that Fe is a transition element whose diffusivity in Al is much lower than "normal" elements.[13]

- Aluminium–manganese

  Phillips et al originally reported testing a Al–1.52%Mn alloy where they found little evidence of strain ageing and type B yielding was rarely observed [68]. In a later study by Hinesly and Morris [122], a commercial Al–Mn alloy (3003) containing 1.04%Mn, 0.68%Fe and 0.48%Si was tested and the authors found the SRS to be dependent on the initial microstructure of the alloy.

  Hinesly and Morris [122] tested the 3003 commercial alloy after subjecting it to various heat treatments i.e. solid solution (1125°F, 4.5 hrs, WQ), dispersion hardened (as for solid solution plus 4.5 hrs at 950°F, WQ) or pre strained and aged (solution

[13]Rapid solidification can be expected to have increased the maximum solubility of Fe in Al. In addition, it is not clear how V and Si may have modified the phase boundaries.

treated, strained to 15% and aged 11 days at room temperature). Although no gross instabilities were observed, a negative SRS was noted for solution treated material tested at 25°C and a zero SRS was observed for the dispersion as well as the pre–strained and aged conditions tested at 25°C. All conditions showed a positive SRS for testing at -196°C. Constitutional instability [103] and localised adiabatic heating were considered to be the main influences on the SRS. The authors argued that the more unstable the initial structure is, the greater the resulting strain rate independence of the flow stress is likely to be.

- Aluminium–silicon

  Chossat, testing two Al–Si alloys containing 0.5 and 0.7%, reported tensile deformation with slight steps [124, 125]. Much more recently, the PLC effect was examined directly in Al–Si containing 0.2%, 3.03%, 6.80%, 11.75% and 19.90% Si [115]. The PLC effect was present in the 0.2% and 3.03% alloys tested in the as cast, annealed and solution treated conditions. In 6.8% and 11.75% Si alloys, the PLC effect was present only in the solution treated condition and the effect was not observed at all in the 19.90% Si alloy. Niimoni et al [115] considered the effects of the various heat treatments and compositions on ε_c. The effects of quenched in vacancies were proposed as the main explanation for the observed characteristics, the mechanisms were not dealt with.

- Aluminium–silver

  Al–Ag is a unique alloy system amongst aluminium alloys, in that the size difference between aluminium and silver atoms is minimal (0.7%) [80, 92, 116]. In the Cotterell theory, interaction between dislocations and solute atoms is mainly attributed to a size (Goldschmidt radius) effect [80, 127].

  Price and Kelly [128] observed a sharp initial yield point in Al–Ag, heat treated to produce GP zones. Samples containing γ', however had a smooth yield point. The yield point in material containing GP zones was attributed to dislocation cutting through the zones, and no mention was made of the occurrence serrated flow.

  Recent work on a variety of alloys proposed an alternative theory (the cluster theory[14]) for the PLC effect and reported the "persistent" occurrence (as opposed

[14]The possibility of solute clustering influencing serrated flow had been previously introduced by Cuddy and Leslie [40].

to "limited" or "non–occurrence") of the PLC effect in binary Al–Ag [92]. The relationship was considered between the PLC effect and solid solubility in various binary alloys, including aluminium alloys containing separately Ag, Cu, Mg and Zn. In considering that one cannot predict a relationship between the concentration of solute and the occurrence of the PLC effect, Onodera et al [92] showed a correlation between the capacity to form precipitates or short range ordered (SRO) regions and the PLC effect.

Binary Al–Ag of concentrations 0.5at.% and 1.4at.% was both water quenched and furnace cooled from 723 K and then tensile tested at 283 K. Al–Ag was reported to deform with persistent occurrence of the PLC effect at both concentrations tested. The "size–effect" was considered by the Onodera et al to be insufficient to explain the occurrence of the PLC effect in an alloy with less than 1at.% Ag in Al. The crux of the theory proposed, to consistently explain the PLC effect in all the alloys examined, was that precipitation or SRO regions will be readily formed from super–saturated solid solutions during deformation. Dislocations temporarily arrested at precipitates or SRO regions, may cut through them and so diminish their ability to act as obstacles. Accordingly, resistance to dislocation motion on a specific slip plane will decrease and result in localised deformation.

In a second paper, specifically examining the PLC effect in Al–Ag alloys, Onodera et al [116] again adopted the cluster theory to explain their results. Materials tested, in this case, were high purity binary melts of 0.5at.%, 1.0at.%, 1.5at.%, 2.5at.% and 4at.% Ag. Specimens were quenched, furnace cooled, slow cooled or quenched and aged from 723 K followed by tensile testing and evaluation of the SRS of the flow stress. The PLC effect, comprising irregular serrations in the flow stress curve, was observed to occur in all alloys, but only for specific prior heat treatments. In 0.5at.% and 1.0at.% material, the PLC effect was only observed in the furnace cooled material. In the 2.5at.% and 4at.% material, the effect was only observed to occur in quenched or quenched and aged material. The main contradiction with Cottrell type dislocation locking was that more solute in solid solution did not necessarily imply an easier occurrence of the PLC effect. The observed effects were rationalised by considering following:

The 0.5at.% and 1.0at.% material had insufficient solute to form clusters, during quenching, which could act as effective dislocation barriers. In the case of the

higher solute content alloys tested (2.5at.% and 4.0at.%), clusters were proposed to form just after quenching. For slow cooling, the lower solute content (0.5at.% and 1.0at.%) alloys would be able to form clusters, whereas in the higher solute content alloys, some of the readily formed clusters would tend to Ostwald ripen at the expense of others.

In all of the cases examined by Onodera et al above, the PLC effect occurred concurrent with a negative macroscopic (measured) SRS.

- Aluminium–zinc

  Zn in Al was initially shown to be effective in producing serrated flow by Chossat [125]. Price and Kelly also observed serrated flow in single crystals of binary Al–Zn tensile tested at room temperature [128].

  Two recent papers reporting on serrated flow in binary Al–Zn have been published [55, 117], although various reports of ternary alloys containing Zn as a primary solute have also been published [100, 129, 130]. Pink and Krol [55] comprehensively tested an Al–10.5%Zn alloy following a report which excluded Zn as a solute capable of producing serrated flow in Al alloys [92]. Onodera et al reported the "non–occurrence" of the PLC effect in 1.2at.% and 5.4at.%Zn alloys,[15] quenched from 723 K. Initial testing on the 10.5%Zn alloy, quenched from single phase (~723 K), confirmed that no serrated flow occurred at test temperatures of -100°C to 100°C. Low $\triangle\sigma$ serrations were, however, observed when the material was quenched from a homogenisation temperature of 275°C. This result is contrary to conventional observations, where quenching from a higher temperature would be expected to enhance the intensity of serrations, due to a higher concentration of vacancies being retained in solid solution. The unconventional result presented by Pink and Krol was only for the case of binary Al–Zn containing more than 6%Zn (2.6at.%).

  Previous results on quenched microstructures of Al–Zn, which contained prismatic vacancy loops (dislocation loops) when the material was quenched from 400°C but not when it was quenched from 275°C [131], prompted Pink and Krol [55] to reconsider the homogenisation temperature. Their assumption was that the loops observed (in the material quenched from higher temperature) would act as sinks

[15] 1.2at.% and 5.4at.%Zn in Al correspond to 2.2wt.% and 15.5wt.%Zn respectively

for excess vacancies. Sufficient vacancies would, therefore, not be available for assisting the diffusion of zinc atoms. The common argument of the need for excess vacancies being necessary to enable adequate substitutional solute diffusion, and associated initiation of serrated flow, was considered invalid. In the above case it was argued that an excess of vacancies would allow for the rapid precipitation of Zn, thereby depleting dislocations of Zn atoms which would have otherwise obstructed the dislocations.

Subsequent to the paper by Pink and Krol [55], experiments on high purity 6% and 10%Zn alloys have produced serrated flow from both [117]. Specimens were annealed at 365°C, water quenched and immediately tested at temperatures between -64°C and 26°C. Other testing included annealing at 365°C as well as water quenching (after solution treatment) followed by ageing at room temperature for 1, 2 and 5 hours. Both alloys were reported to exhibit types A and B serrations, with type B only appearing at low strain during room temperature testing. ε_c was measured at a variety of strain rates in order to derive the activation energy (E_A) for the process. At the higher temperatures, E_A compared favourably with the energy of exchange between a zinc atom and a vacancy, while at the lower temperatures E_A was similar to that for divacancy motion in pure Al. The importance of vacancies was confirmed by quenching and ageing experiments, where ε_c was observed to decrease with increasing temperature in the range 380–440°C. ε_c was also observed to increase with ageing time.

The contradiction between the work of Pink and Krol [55] and the more conventional results for Al–Zn presented in this section is not easily resolved. Single crystal tests support the more conventional results of Jovanovic [117]. The testing of single crystals of Al–15%Zn showed serrated flow in samples quenched from 550°C but not when the samples were quenched from 220°C, or only after considerable strain in the latter [128]. The retention of vacancies from high temperature was used as an explanation to rationalise the effects found in single crystals.

Commercial Aluminium Alloys

The international classification of wrought aluminium alloys is based on a four digit system, in which the first digit represents the major alloying addition [132]. The common recognised systems are:

1. Aluminium (99% minimum).....1XXX
2. Copper.....2XXX
3. Mangenese.....3XXX
4. Silicon.....4XXX
5. Magesium.....5XXX
6. Magnesium and Silicon.....6XXX
7. Zinc.....7XXX
8. Other (eg. Al-Li).....8XXX

In the 1XXX system the last two digits represent the minimum purity. These two digits are the same as the two digits to the right of the decimal point in the percentage purity of the Al, expressed to the nearest 0.01%. The second digit refers to the special control of specific impurities. If the second digit is zero, then the alloy has "natural" impurity limits.

For 2XXX – 8XXX, the last two digits have no significance other than to identify the specific alloy. The second digit is zero, if it is the original alloy, with the numbers 1–9 indicating consecutive modifications.

Specific designations for the temper of the alloys are

1. For wrought alloys:
   (a) F: As fabricated (i.e. as rolled, extruded or forged)

(b) 0: Annealed, recrystallised

(c) HX: Strain hardened (X = 2, 4, 6 or 8 indicating the amount of prior cold work)

(d) H9 : Extra hard (Indicates more rolling deformation than "full hard" H8 temper)

2. For heat treatable alloys

(a) TX : Thermally treated.

(b) T4 : Specific temper i.e. solution treated and naturally aged.

(c) T6 : Specific temper i.e. solution treated and artificially aged.

- 1XXX Alloys

  McReynolds [133] reported a stepped stress strain curve resulting from the tensile testing of an air cooled 2S commercially pure aluminium[16] with the discontinuities evident between -10 and 50°C. The major impurities present were 0.14%Cu, 0.48%Fe and 0.11%Si. Subsequent work produced confirmation that stepped curves could be produced in commercially pure material [80]. No attempt was made to isolate a specific element responsible, but it is conceivable that the net effect of numerous impurities may have been responsible.

- 2XXX Alloys

  Aluminium–Copper–Magnesium wrought alloys containing 2.4%–6.3% Cu, 0.35%–1.5%Mg as well as possibly 0.3%–0.8%Mn and 0.18%–0.8%Si. Silicon additions produce an alloy (2014) which is more responsive to artificial ageing. 2024, is a strong structural alloy, where the hardening is accomplished by a complex aluminium, copper and magnesium phase rather than the original Al–Cu phase of the binary alloy [134].[17]

  Serrated flow in 2024 was observed by Rosen and Bodner [94] and has been partially discussed in section 2.5.2. The 2024 alloy tested contained 4.4%Cu, 1.4%Mg,

[16] 2S is the old British designation for a commercially pure aluminium. 2S is equivalent to the modern alloy designated 1200.

[17] See page 365 of [134].

0.7%Mn, 0.27%Fe and 0.17%Si. Serration amplitude at $\dot{\varepsilon} = 1.5\times10^{-4}$ s^{-1} was observed to peak ($\Delta\sigma_{max}$) at 20 MPa with $\sigma \approx 400$MPa i.e. $(\Delta\sigma_{max}/\sigma) \approx 5\%$. A direct comparison with pure binary Al–Cu tested at $\dot{\varepsilon} = 1.6\times10^{-4}$ s^{-1} shows $\Delta\sigma_{max} \approx 4.2$ MPa at $\sigma \approx 238$ MPa i.e. $(\Delta\sigma_{max}/\sigma) \approx 1.8\%$.

The difference in $\Delta\sigma$ observed above is likely to be accounted for by the other alloy additions, specifically magnesium, which alone is already sufficient to produce serrations at 1.4%. Fujita and Tabata [96] observed $\Delta\sigma_{max} \approx 1$ MPa at $\sigma \approx 125$ MPa in Al–1%Mg polycrystals i.e. $(\Delta\sigma_{max}/\sigma) \approx 0.8\%$.

- 5XXX Alloys

  5000 series alloys conventionally contain 0.8%–6%Mg, 0.12%–0.8%Mn and 0.12%–0.25%Cr [134].[18] Cr or Mn are added to form grain growth stabilisers [134][19] in combination with other elements. In addition, Mn has the effect producing a stronger alloy for a given Mg content as well as stabilising the alloy against age softening. Direct investigations of commercial materials, with regard to inhomogeneities in plastic deformation has been undertaken by a number of authors [74, 122, 79, 35, 62, 135, 136]. In general, the plastic deformation properties of 5XXX alloys are dominated by Mg and therefore strong similarities exist between the deformation properties of the commercial materials and the binary Al–Mg alloys discussed in section 2.5.2.

  Lloyd tested three commercial alloys 5052, 5154 and 5083 containing 2.34%, 3.31% and 4.46% Mg respectively. All material tested was deformed in the zero temper.[20] The yield stress was observed to exhibit a positive SRS in all cases, while the UTS exhibited a negative SRS. This probably reflects the delayed development of DSA processes with strain. Lüders strain was observed to be grain size dependent, decreasing with increasing grain size. Grain size effects dominated over Mg content variations in determining the Lüders strain. Alternative explanations for the negative SRS of the UTS (but not the yield stress) are that the development of a dense forest dislocation substructure [18], or the creation of excess vacancies, may have been necessary.

- 6XXX Alloys

[18] See page 353 of [134].
[19] See page 353 of [134].
[20] The reader is referred to section 2.5.2, for a full description of commercial heat treatment designations.

6000 series alloys contain both Mg and Si which are used to precipitate Mg_2Si in the heat treated and aged (T6) condition [134].[21] Mg and Si are added in balanced proportions to nominally combine as Mg_2Si. Excess Si may also be added for increased strength to the detriment of corrosion resistance. The Mg content ranges from 0.6% to 1.2% with Si ranging from 0.35% to 1.3%. Deliberate additions of Mn, Cu and Cr may also be included in the alloy composition.

The occurrence of serrated flow in six series alloys tested under torsional and tensile deformation conditions has been regularly reported [2, 8, 57, 64, 93, 111, 137, 138]. Typical features of the deformation include the formation of both type A and B deformation markings and the appearance of type A and B serrations on the flow curve [137]. Type C serrations have also been observed to occur during tensile deformation of an Al–Mg–Si alloy [2].

Precipitation has been observed to suppress serrated flow (see also section 2.5.3) in material aged for longer than 6 hrs at 180°C [93]. In addition, the SRS was observed to decrease with increasing strain, becoming negative at a strain which increased with increasing prior ageing time [138]. For ageing times longer than 4hrs at 160°C, the SRS was observed to remain positive at all strains.

The measurement of an activation energy of 0.6 eV for the onset of serrated flow in a 6061 alloy [2] compares favourably with values measured on a binary Al–Mg alloy [95] (see section 2.4.1), and suggests that a similar mechanism must be operative. In the 6061 alloy the authors concluded, after considering various alternatives, including the interaction of dislocations with precipitates, that the 0.6 eV E_A corresponded most favourably to the cutting of forest dislocations by temporarily halted mobile dislocations [2]. The stress to cut forest dislocations was suggested to include a component required by the mobile dislocations to breakaway from the solute cloud. The solute cloud itself was proposed to form preferentially at the junction between the mobile and forest dislocations, during t_w via a pipe–diffusion mechanism.

Finally, two causes of flow stress instability have been suggested for this class of alloy [111]. Firstly, serrated yielding arising from the diffusion of solutes to dislocations temporarily arrested at local obstacles, as discussed above and elsewhere in this chapter. Secondly, slip localisation may occur as a result of the shearing and

[21] See page 365 of [134].

consequent destruction of precipitate particles. The shearing of precipitates results in a negative strain hardening while serrated yielding itself arises from a negative strain rate dependence of the flow stress. Both of the above mechanisms have been proposed to account for localised tensile shear failures in precipitation hardened Al alloys [139, 140, 141]. The latter mechanism (shearing of precipitates) was suggested to dominate over DSA effects in Al–Mg–Si tested in torsion, where the full extent of strain softening was able to be observed.

2.5.3 Effects of Precipitation Processes

Two main effects of precipitation processes on serrated plastic flow have been mentioned in this chapter. The first, precipitation prior to deformation, is more easily checked for and controlled. Precipitation from a saturated solid solution by natural or artificial ageing, prior to deformation, denudes the matrix of one or more solutes, which may be responsible for the DSA of dislocations during subsequent deformation. The second possibility, precipitation during deformation, is difficult to place in the chronological series of microstructural events but examples of this are covered in this section.

Examples of precipitation prior to deformation generally indicate that the longer the ageing time after quenching, the more the SRS tends to positive values and the less likely serrated plastic flow is [2]. Generally, the effect of decreasing the solute concentration in the matrix or altering the pre–deformation microstructure by precipitation is expected to reduce the likelihood of the PLC effect occurring [55, 93, 108, 138, 142, 143, 144], but there are exceptions [92, 116, 145].

Precipitation during the deformation of 2024 was considered responsible for a negative SRS observed when the data from stress–strain curves was replotted as a stress–strain rate relation [94] at constant strain. The effect of altering the imposed deformation rate on solution treated 2024 (precipitation hardenable) was to produce the time dependent effect of a negative SRS. A slow strain rate allows for natural ageing (precipitation hardening) during the test, strengthening the alloy and thereby creating the impression of a negative SRS (i.e. the alloy is stronger when tested at slower strain rates). The anomaly

arises from not varying the strain rate during a test, and thereby measuring the instantaneous macroscopic SRS, which may indeed be positive at the stress where the original measurement was made.

A connection has been made between the formation of clusters or precipitates and the cause of the PLC effect [40, 92, 145]. Pink and co–workers [100] considered that previous work (discussed above) on how ageing affects the occurrence of serrated flow, may not have varied the ageing conditions adequately. Pink et al therefore varied the ageing conditions of a commercial 7020 alloy (Al–5%Zn–1.2%Mg) in order to determine how the size and type of precipitates influenced serrated flow [100, 105, 129, 130]. Pink thoroughly investigated the effect of annealing time (t_A) and temperature (max T_A=400°C) on the characteristics of serrated flow exhibited by solution treated 7020 [100]. He found a maximum ε_c for $T_A \approx 70°C$, i.e. the temperature where the maximum density of GP zones is formed. These results refuted earlier work, which had correlated the formation of GP zones formation with the appearance of serrations [129]. The work presented by Pink involved examining the effect of varying both t_A and T_A, as well as varying the test temperature, on serration type and amplitude. Varied conclusions were drawn from the work, but in general, precipitates were observed to decrease the tendency towards serrated flow. G.P. zone formation was observed to affect ε_c more dramatically than $\Delta\sigma$. The increase in ε_c observed was ascribed to the depleted vacancy concentration associated with GP zone formation. The formation of a stable coherent phase was observed to decrease $\Delta\sigma$, which was attributed to a decrease in the lattice solute population available for DSA. Deformation induced precipitation, probably of GP zones, was observed to increase ε_c for high temperature deformation, in contrast to the model of vacancy assisted diffusion (eg. [15]). Straightforward application of the Cotterell model [15] was therefore rendered impossible by the assumed diffusion of solute atoms occurring less readily due to the precipitated phases present.

2.5.4 Modern Aluminium Alloys

Aluminum–Lithium

Aluminium lithium alloys offer a good combination of low density and high elastic modulus. Li has significant solubility in Al (5.2% max) and has the capacity to produce precipitation hardening effects with the metastable, ordered δ' phase (Al_3Li) [134].[22]

Post yield serrated flow has been observed in Al–Li based polycrystals deformed in both tension [146, 147, 148] and compression [7]. Tamura et al initially reported serrated flow in the high strain deformation of Al–Li single crystals, which was attributed to work softening associated with dislocation cutting of δ' particles [149]. Similar polycrystals did not produce the same effect, an anomaly which was attributed to the interference of the primary slip system by grain boundaries or the operation of multiple slip systems. Wert and Wycliffe [146], testing an Al–2.5%Li–1.2%Cu–0.7%Mg alloy in tension, observed the precipitation of S′ (a precursor to Al_2CuMg) coincident with the disappearance of serrated flow. They concluded that Cu and Mg were the solutes responsible for serrated flow.

Although the unpinning stresses in Al–Li are an order of magnitude smaller than for Al–Mg [80], Evans [147] observed jerky flow in binary Al–9.6at.%Li, as well developed as for Al–Mg. Evans considered that the combined interaction between dislocation pinning and strain hardening may have been responsible, as has been previously suggested [6, 18]. Other possibilities considered by Evans, were the combination of SRO and solute redistribution or alternatively the precipitation of δ' on glide dislocations temporarily held up by forest dislocations.

Gregson et al investigated the tensile deformation of various commercial Al–Li–Cu and Al–Cu–Li alloys and found regions of no work hardening to occur concurrently with pronounced serrated flow [148]. The serrated flow observed was attributed to the rapid release of dislocations after pinning by atmospheres of Li atoms (and their associated vacancies). Natural ageing was found to suppress serrated flow, due to the decreased concentration of Li in solid solution associated with the formation of δ' (Al_3Li) particles. The

[22]See page 47 of [134].

regions of zero work hardening were associated with the activation of a single slip system in unrecrystallised and textured material, at which point work hardening commenced via the activation of planar slip on a second slip plane.

Haung and Gray [7] have also reported the classical effects of DSA, negative SRS, serrated flow and the formation of localised bands of deformation in Al–2.90%Li–1.00%Cu and Al–2.30%Li–2.85%Cu. Although the activation energy for the onset of serrated flow was determined to be ~51kJ/mol, nearly 1/3 of that required for Li diffusion in the matrix (~130kJ/mol), Li was considered to be the responsible solute. DSA via pipe (dislocation core) diffusion was proposed as the most likely dislocation–solute atom interaction process.

Metal Matrix Composites

Metal matrix composite (MMC) materials with a light alloy matrix are of extensive current interest because of their potential to combine strength, stiffness and wear resistance of ceramics with the formability and toughness of metals. Commercial production of MMC material is well developed and they are therefore readily available in the USA and Europe.

In spite of the availability of literature on the deformation properties of 2XXX, 5XXX, 6XXX and 7XXX based composites (eg. [150, 151, 152, 153]), no reports of serrated flow in these materials have appeared. Composites extensively tested for σ–ε, ductility and fracture behaviour were only examined in the F and T6 tempers[23] i.e. not solution treated to achieve the maximum solute content in the matrix [154]. The likely reason for not testing material in the solution treated condition is that commercial application would be in the stable F or T6 tempers. A further consideration is the commonly observed high dislocation density in composite material in comparison to the monolithic alloy [155]. The high dislocation density promotes rapid natural ageing [156], and the associated solute depletion of the matrix would make the occurrence of serrated flow more unlikely to occur after shorter periods of natural ageing compared with the corresponding monolithic alloy.

Testing in the course of the present work has produced serrated plastic flow in an Al based MMC, tested in the solution treated condition [157]. 6061 + 20%SiC_P material,

[23]The reader is referred to section 2.5.2 for a description of commercial heat treatment designations.

tensile tested immediately after quenching from the solution temperature was observed to exhibit extensive serrated flow until fracture. Comparison with the monolithic alloy in the same condition, showed similarities in the serration types observed (A and B) superimposed on different rates of work hardening (higher for the composite). Tensile testing of material in the T6 temper produced no serrated flow in either the monolithic material or the composite due to matrix solute depletion by the precipitation of $AlMg_2Si$.

2.6 Microstructural Aspects of Solute Modified Deformation and Strain Localisation

2.6.1 Slip Mode Modification in FCC Substitutional Solid Solutions

FCC metals can be broadly subdivided into two classes, on the basis of whether they deform by predominantly planar or wavy slip. The most definite basis for classifying metals into the above two classes is by direct observation of the deformation dislocation structures [158]. Generally, dislocations are observed either as clusters adjacent to regions of low density or as ladder like planar arrays [159]. The distribution of dislocations on any single plane is more even, in the case of a material exhibiting planar slip. In the past the main criterion applied to determine which slip mode dominates was the measure of separation energy between partial dislocations, i.e. the stacking fault energy (SFE) [158]. A decrease in SFE implies an increase in the separation between partial dislocations and an associated increase in the difficulty of cross–slip.

Recent published work has questioned the validity of applying SFE as the sole determining criterion of the differences in observed slip mode [158, 160]. Suggestions for other primary influences on the planar or wavy nature of the observed slip are:

1. The impediment of dynamic recovery by solutes, for the cases where solute additions do not significantly alter SFE. The association between dynamic recovery and cross

slip is well established [54, 161], therefore restricted dynamic recovery can be taken to imply restricted cross slip [106].

2. A proposal that the slip mode can be characterised by considering the increase in yield stress with alloying. The commonly observed increase in yield stress with the addition of alloy elements means that an effect of alloying on the slip mode can possibly be anticipated [162].

3. The possibility of a glide plane softening effect, as a result of the local destruction of short range order (SRO) by the passage of dislocations, could be expected to initiate planar slip [163, 164].

Gerold and Karnthaler attribute the sole origin of planar slip features to the destruction of SRO or ordered precipitates [160]. SFE and other parameters, such as the value of the yield stress, were considered to play a minor role, possibly supporting the formation of planar dislocation arrays but not, in isolation, leading to distinct planar slip. The authors noted the correspondence between the activation of planar slip and the possible initiation of strain bursts in low cycle fatigue deformation. In the case of glide plane softening, the possibility of collective planar cross slip was considered, as opposed to individual cross slip events, producing wavy slip. Dislocations emitted from a single source could be expected to follow one another, even after a double cross–slip event, as a result of glide plane softening effects. In wavy slip material however, glide is spread over several planes by independent cross–slip events. These features are schematically illustrated in figure 9.

2.6.2 Observations of Surface Slip Line Features

Although the most definite and important classification of slip mode modification is achieved by examining the dislocation structure [158], the observation of surface slip features can provide similarly pertinent information. Examination of deformation band formation as well as the slip line structure in individual grains has the potential to aid in clarifying the operative mechanisms of deformation heterogeneity.

Serrated flow involves successive deformation increments with each step of deformation necessarily corresponding to the collective motion of many dislocations [165]. The

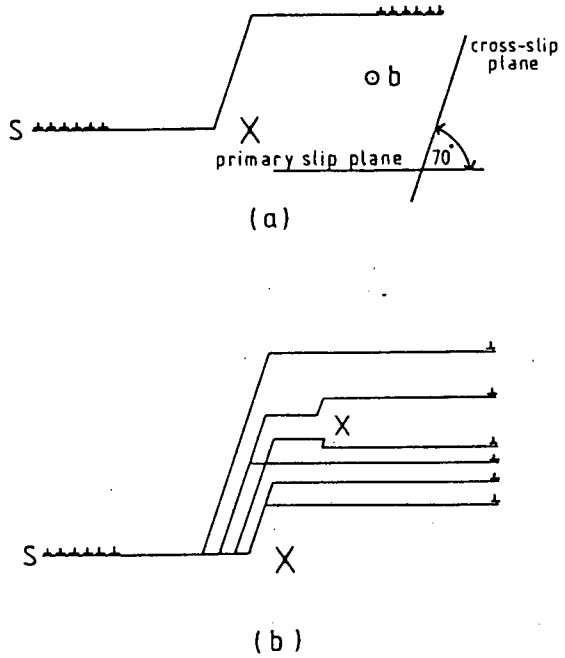

Figure 9: Two possible types of cross–slip event suggested for materials exhibiting either (a) planar or (b) wavy slip. After Gerold and Karnthaler [160].

relationship between collective dislocation processes and the formation of slip band structures has been extensively documented by Neuhauser [166]. Recent work by the same author has considered the relationship between the dynamic formation of slip bands and the details of the microprocesses underlying their formation, with particular reference to the PLC effect [167]. By utilising in–situ deformation in a specially developed light microscope, Neuhauser has been able to simultaneously record macroscopic quantities (σ, $\dot{\varepsilon}$, T) and the evolution of slip bands. Slip bands are characterised according to their number, height and arrangement with their formation and evolution being examined in dark–field utilising a high speed film camera and high intensity illumination [168].

Examination of the early stages of plastic deformation of Al–Cu single crystals was undertaken by Neuhauser [167] on material containing 2at.%, 5at.%, 10at.% and 15at.% Cu. As the deformation temperature was raised, the number of simultaneously active slip band bundles was observed to decrease, until the point was reached where each serration corresponded to the growth of a single slip band bundle.[24] The growth of a single slip band was observed to be achieved by successive addition of slipbands at its margin. The

[24]A slip band bundle refers to a cluster of slip bands in a single unit.

heterogeneity of slip itself was observed to be strongly influenced by alloy content, in that the height of each slip band increases and its width decreases as the solute content is raised. Cross slip between slip traces was observed to occur and the authors suggested that this may be important because of the possible relationship between the propagation of slip at a Lüders band front and cross slip.

In Al–Mg single crystals, surface slip band features were observed to change in correspondence with changing stress amplitude of serrations [96]. Slip bands referred to as "bands of secondary slip" exhibited a maximum heterogeneity at the end of stage II deformation, corresponding to the maximum $\triangle\sigma$ (see also section 2.5.2).

Saunders [169] made an extensive examination of the microstructure and slip distribution in a range of commercial aluminium alloys after uniaxial and biaxial tensile deformation. Optical metallography and TEM were utilised to study the deformation responses of 1100, 3003, 5182, 6009, 6010 and 6061. On the basis of the microstructural strengthening mechanism, a distinction was possible between the tendency towards wavy slip or more localised deformation. The dispersion strengthened alloys (1100–0, 3003–0, 6010–0) displayed wavy slip, high levels of strain hardening and resistance to strain localisation. Precipitation and solution strengthened alloys exhibited more localised deformation and lower capacities for biaxial strain hardening.

2.6.3 Microstructures Observed in Materials Prone to Strain Localisation

General

Schmidt and Miller [170] have compared the initial rates of strain hardening in Al–Mg and Al, based on the data by Scherby et al [171]. The increased rate of strain hardening at $T_m \approx 0.3$ (where $T_m = T/T_M$ and T_M is the melting temperature) is commonly observed in other metals including commercial purity Ti, Fe–Mn, Fe–N and 316 stainless steel. Although substitutional solutes produce a lesser effect on strain hardening than interstitial solutes, the enhancement of strain hardening is generally attributed to four possible

processes.

1. Precipitation during deformation.
2. An increased rate of dislocation multiplication.
3. A decreased rate of recovery.
4. Enhanced effectiveness of dislocation strengthening in the presence of solutes.

Observation of Microstructures Utilising CTEM

The direct correlation between microstructural observations and the occurrence of DSA phenomena has not been well documented in the literature. Recent work by Korbel and co–workers [172, 173] has achieved the successful elucidation of the microstructural aspects of strain localisation during rolling deformation of Al–Mg, but corresponding features of tensile deformation have not been published.

Experiments on the effect of Ni and Mn on the deformation substructure of Fe deformed in tension, showed a direct correlation between increased strain hardening rate and the dislocation structure [174]. A high strain hardening rate was observed during deformation in the "blue–brittleness" temperature regime[25] and this was attributed to rapid dislocation multiplication due to DSA effects. A decreased tendency for cell formation was attributed to solute restricted dynamic recovery. Keh et al [175] showed that the rate of dislocation multiplication in an 0.035%C steel was approximately three times higher under DSA deformation conditions (200°C) than when the material was deformed at room temperature.

The TEM observations presented by Saunders [169] based on his examination of various commercial aluminum alloys (see also preceding section) produced a correlation between the observed slip modes and dislocation configurations, although he did not specifically relate this to DSA. In the alloys displaying wavy slip features, dislocations were

[25] see also section 2.2.2

observed to be arranged in a well defined cell structure. In the alloys exhibiting planar slip traces, however, no evidence of dynamic recovery (cell formation) was observed.

Korbel and co–workers examined the microstructural features associated with strain localisation during the rolling deformation of Al–4.8%Mg [172]. They observed the formation of crystallographic microbands and macroscopic shear bands, both of which formed at lower strains than conventionally observed in Al alloys. The dislocation structure of the microbands was reported to contain regular arrays of dislocations but no evidence of this was shown. The microbands were very localised, and their potential co–ordination into larger scale events was suggested to be dependent on macroscopic loading geometry.

Korbel and Martin [173] examined the same Al–4.8%Mg alloy discussed above, after cross rolling, to ascertain the mechanism of microband organisation into macroscopic shear bands. Macroscopic shear bands resulted directly from the growth of crystallographic microbands, not from the linkage of separate microbands. The mechanism proposed was the nucleation of a microband by the generation of an initial avalanche of dislocations followed by conversion into a shear band when further long distance crystallographic glide was precluded (eg. by a grain boundary).

Further work by the above authors examined the correlation between macroscopic strain localisation and deformation micromechanisms in a low C steel [176]. Tensile deformation at room temperature showed a similar process to that observed in rolled Al–Mg, with macroscopic strain localisation (MSL) clearly preceded by microscopic flow instabilities. Coarse slip bands (CSB) were observed to form early in the deformation and then evolve into micro shear bands (MSB) which in turn lead to MSL. Deformation within the MSL region was composed of both homogeneous and heterogeneous (CSB, MSB) components. No similar work has been published for aluminium alloys, although Korbel et al [172] suggested that tensile testing was effectively a variation in the loading geometry and similar results to those produced by rolling deformation could therefore be expected.

In a general discussion, with an example from Zircalloy, Hong [177] compared the dislocation structures formed in material deformed at different temperatures. The deformation test temperature corresponded to the athermal plateau (of yield stress variation with temperature) and a second deformation temperature was chosen, above the plateau.

He observed a clustering of dislocations for the case of deformation within the athermal plateau and a homogeneous dislocation distribution for deformation temperatures above the athermal plateau. In the former (clustering) case, dislocation velocity was proposed to increase in a field of low internal stress and decrease in field of high internal stress, due to DSA effects. For deformation at higher temperature, dislocations were considered to move at an average velocity regardless of the internal stress fields, and hence a uniform dislocation structure evolves.

Microstructural Evolution Studies Utilising HVEM In–situ Deformation

In–situ deformation of metals within an HVEM has a major advantage in the potential to unambiguously determine the sequence of microstructural events during the deformation process. In–situ straining within an HVEM is generally seen as a complementary examination technique, allowing for dynamic observation in material thicknesses where defect behaviour approximates that in bulk material, subject to limitations [178]. Care has to be taken to allow for surface, size and irradiation effects, specifically by comparing the evolved microstructure to that observed in bulk specimens deformed and then observed in a CTEM. 3 μm thick samples have been observed to produce microstructures which closely resemble those found in bulk materials [179]. The thickness criterion refers to the minimum defect mean free path, which is accepted to be approximately 3 μm [180]. The mean free path of defects is a maximum in the early stages of deformation in materials that have not been predeformed [179].

The PLC effect has been directly investigated by in–situ deformation in the HVEM on single crystals of Al–Mg [53, 181]. Nohara et al [53] investigated the effect of deformation temperature on dislocation behaviour in an Al–3.3at.%Mg alloy. Single crystals were tested at temperatures of 0.26, 0.32, 0.46 and 0.63 T_m corresponding to regions on the variation of CRSS with temperature curve, illustrated in figure 10. The authors attributed the PLC effect to the rapid, simultaneous formation of narrow slip bands at random places with some reoccurrence of slip in the same traces. Below the temperature regime of PLC effects, pinning and bowing of dislocations during their jerky motion was attributed to a random distribution of solutes in the glide plane. Above the PLC temperature regime smooth, viscous and simultaneous motion of dislocations was observed to occur.

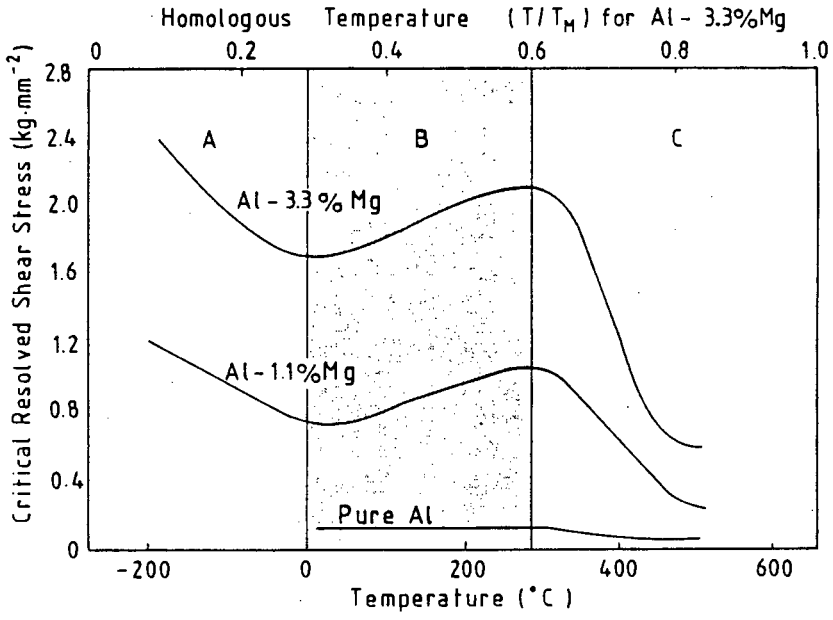

Figure 10: The temperature dependence of the CRSS. After Nohara et al [53].

Tabata et al conducted in–situ deformation experiments in the HVEM on Al–0.3%Mg single crystals at both –80°C and room temperature [181]. They observed retarded motion of mobile dislocations around tangles and dislocations were observed to pile up against the tangles for specific waiting times. The t_w was observed to be markedly prolonged during room temperature deformation compared to –80°C, where t_w was observed to approximate that found in pure aluminum [182]. Stress instabilities were attributed to sudden bursts of dislocation motion upon overcoming obstacles. Dislocations were observed to rapidly form coarse slip bands by abrupt collective cross–slip which included sudden dislocation multiplication. The motion of both edge and screw dislocations was observed to be relatively smooth and homogeneous at –80°C.

Martin [183] has considered the collective properties of dislocations in his review paper, including those presented by Nohara et al in the preceding discussion. An attempt was made to synthesize the original theoretical work of Gilman [184] on dislocation multiplication and the more recent work of Neuhauser [185, 168, 186] on slip line formation as well as in–situ HVEM work [53] and x–ray topographical studies. Martin attributed the macroscopic stress instabilities commonly observed to the collective dislocation motion which occurs no longer monotonically, but in bursts. The principle dislocation properties

referred to were the sudden slowing down of groups of mobile dislocations when their number reached a critical density. In addition, the tendency towards planar flow in specific active planes was considered.

Dislocation motion observed in in–situ deformation HVEM experiments is, then, inherently jerky as can be expected [19]. The major distinction observed between different deformation conditions is the degree to which localised collective dislocation motion occurs i.e. the microscopic heterogeneity. No HVEM in–situ deformation work appears to have been published on the deformation of polycrystalline material in the DSA regime. A significant difference between DSA influenced deformation of polycrystals and the similar deformation of single crystals is the mechanism by which the co–ordination of slip is achieved between several grains. The heterogeneous deformation of polycrystals has been observed to differ from that of single crystals, at least in that the magnitude of individual serrations ($\triangle\sigma$) is markedly higher than that observed in single crystals [96].

2.7 Theoretical and Modelling Aspects of the DSA Microprocesses

2.7.1 General

The theoretical treatment of the PLC effect and its connection with DSA microprocesses has undergone extensive development since the first modified diffusional approach for substitutional alloys was published [15]. Developments include Penning's mathematical approach [59], the possibility of DSA occurring during t_w at local obstacles in the glide plane of mobile dislocations [187], a non-diffusional approach [188], the questionable role of vacancies in the process [17], the strain dependence of DSA effects [18], the role of collective dislocation processes [189] and others [14, 60, 109, 190, 191, 192]. This set of treatments has recently culminated in a consistent explanation of various phenomena associated with the PLC effect by considering the strain dependence of both the mobile and forest dislocation densities [109]. It is interesting to note that Kubin and Estrin's [109] approach does not necessarily assume that diffusion is vacancy assisted.

In addition to the theoretical treatments listed above, simulations and phenomenological approaches have provided some clarification on the mechanism of transition from microscopic to macroscopic instabilities. An electronic model to produce simulated tensile test curves, based on various test conditions, was utilised to provide a ready visualisation of the occurrence of serrations within certain specific $\dot{\epsilon}$ and T bands [193]. McCormick [194] has presented a successful numerical simulation of the PLC effect by utilising a constitutive flow equation to produce results in good agreement with experimental measurements. More general considerations of non-linear phenomena using non–linear stability analysis [195] have also led to successful modelling of the self-organisation and co–operative behaviour of large densities of dislocations [165]. Finally, a classical description of self sustained oscillations, involving second order non–linear differential equations has been used to produce a simple and useful picture of jerky behaviour characterised by negative differential friction, analogous to stick-slip phenomena [9].

2.7.2 Fundamentals of Various Approaches

In a broad sense, theoretical treatments of the PLC effect have emphasised one of two aspects. The discussion which follows is, therefore, divided into two sections covering primarily either the "vacancy hypothesis" with its emphasis on vacancy enhanced diffusion or alternatively the case where the emphasis is placed on strain hardening. The third section following draws heavily on the recent, more complete approach of Kubin and Estrin [56, 109], who have successfully integrated various manifestations of the PLC effect, into their most recent efforts.

At the outset, certain common ground may be delineated between the various approaches. Jerky flow or serrated yielding is now generally accepted to be related to the dynamic interaction between mobile solute atoms and dislocations (DSA) on a microscopic level [106]. As a result of DSA, there is an ageing component contribution to the friction stress of dislocations [196]. This ageing component, then, induces a negative contribution to the SRS of the flow stress of the deforming alloy. The onset of PLC type instabilities (the PLC effect) occurs approximately at the point where the negative contribution to the SRS (resulting from DSA) is sufficient to produce an overall negative SRS. The closed

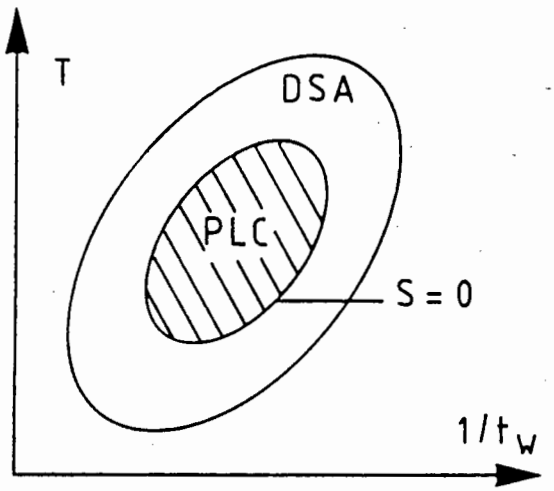

Figure 11: The domain of occurrence of both DSA and the PLC effect shown by closed curves in the T, $1/t_w$ space. After Kubin and Estrin [58].

curve in figure 11, reproduced from the work of Kubin and Estrin [58], delimits the domain of the PLC effect which can be seen to be a sub–domain of the limits of DSA operation. The curve bounding the PLC effect in figure 11 is that for which the value of the SRS is zero. Therefore, as soon as the SRS becomes negative, any fluctuation in $\dot{\varepsilon}$ will tend to increase in amplitude such that uniform plastic deformation is necessarily unstable. Finally, it should be emphasised here that the SRS is a strain dependent quantity, which may only become negative during the course of plastic deformation. The strain at which the SRS becomes negative is, then, the critical strain for the onset of plastic instabilities (ε_c).

Consensus about the mechanism of the strain dependence of the SRS has not yet been reached, but three main possible causes have been presented in the literature:

1. The enhancement of solute atom diffusivity by deformation–induced vacancies.
2. An increase in the mobile dislocation density.
3. Redistribution of solute atoms in the distorted regions of dislocation cores.

The origins of the above concepts are discussed in the following sections.

2.7.3 The "Vacancy" Approach

The origins of this approach stem from the original treatment of DSA in substitutional alloys [197]. Following the suggestion that DSA was responsible for the serrated deformation curves of mild steels [23], where interstitial C and N were proposed to diffuse fast enough to allow for ageing during plastic deformation, Cottrell and Jawson [197] proposed a similar explanation for the serrated curves of substitutional alloys. Considering that the occurrence of serrated flow appears only after a critical strain, and that the calculation of room temperature diffusion rates in Al (extrapolated from high temperature measurements) were far too low to account for DSA, a modification was proposed for substitutional solid solutions. Cottrell [15] suggested that an enhanced diffusion coefficient, resulting from the known increase in vacancy concentration due to plastic deformation, could account for the discrepancy. Dislocations were proposed to alternately drag and break free from solute atmospheres during a quasi viscous type motion through the lattice.

The Cottrell concept of DSA, relying on dislocations moving through the lattice at a steady sub–critical velocity, was able to qualitatively predict the T and $\dot{\varepsilon}$ dependence of serrated yielding. However, McCormick [187] and Wiljer et al [5] showed that ε_c calculated on the basis of the Cottrell model was inaccurate by many orders of magnitude. Van den Beukel [17], therefore proposed a modified "vacancy model" which described DSA as the diffusion of solute atoms to dislocations, temporarily arrested at local obstacle in the glide plane, during the waiting time t_w. The concept of t_w was developed by McCormick [187], following from the ideas of Sleeswyk [20]. McCormick's ideas were based on experiments which suggested the inherent discontinuity of dislocation motion and the fact that, in most cases, the average dislocation velocity was determined primarily by the arrest time at local obstacles.

A key feature of the model forwarded by van den Beukel, was the *bulk* diffusion of solutes to temporarily arrested dislocations, where the diffusion coefficient (D) was enhanced by the production of vacancies during plastic deformation. The concentration (C) of solutes experienced locally by the dislocations was therefore not constant, and is expressed as a function of D and t_w.

$$C = C(Dt_w) \tag{1}$$

where Dt_w can be expressed as a function of ε, $\dot{\varepsilon}$ and T as follows:

$$Dt_w \simeq \frac{\varepsilon^{m+\beta}}{\dot{\varepsilon}} \exp[-\frac{Q_m}{kT}] \tag{2}$$

Q_m is the migration energy for vacancies, with the $m + \beta$ exponent arising from the strain dependence of the mobile dislocation density (ρ_m) and the vacancy concentration (C_v), as expressed in relations 3 and 4 below.

$$\rho_m \propto \varepsilon^{\beta} \tag{3}$$

$$C_v \propto \varepsilon^{m} \tag{4}$$

A range of Dt_w values can then be shown to exist where $\frac{\partial \sigma}{\partial \dot{\varepsilon}} \leq 0$ which correspond to the regime of inhomogeneous deformation which is illustrated in figure 12. Clearly $\frac{\partial \sigma}{\partial \dot{\varepsilon}}$ is negative between the two zero values corresponding to the curve maxima and minima.

The form of the curve in figure 12, derived theoretically by van den Beukel [38] corresponds exactly with that used by Penning [59]. Penning showed that the form of the curve shown was a necessary material characteristic for unstable plastic flow. The effect of ε on the σ vs. $\dot{\varepsilon}$ curve is illustrated in figure 13, where for increasing values of ε, the minimum shifts to higher values of $\dot{\varepsilon}$.

The inclusion of a $\dot{\varepsilon}$ and T dependent critical strain is encompassed by equation 5 below.

$$\varepsilon^{m+\beta} \simeq \dot{\varepsilon} \exp[\frac{Q_m}{kT}] \tag{5}$$

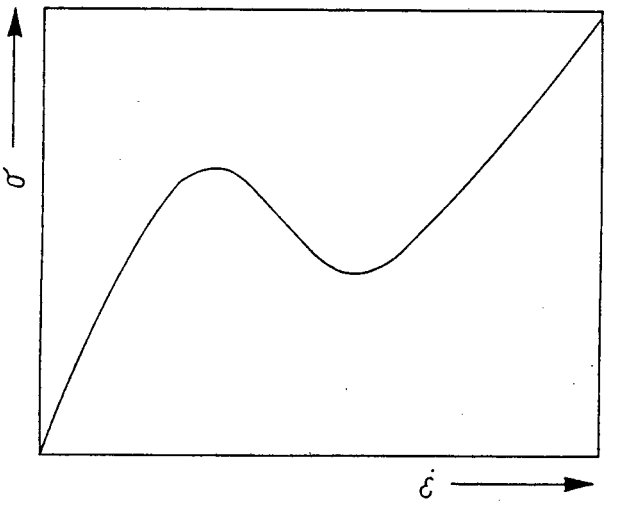

Figure 12: The variation in stress with applied strain rate under DSA conditions. After van den Beukel [198].

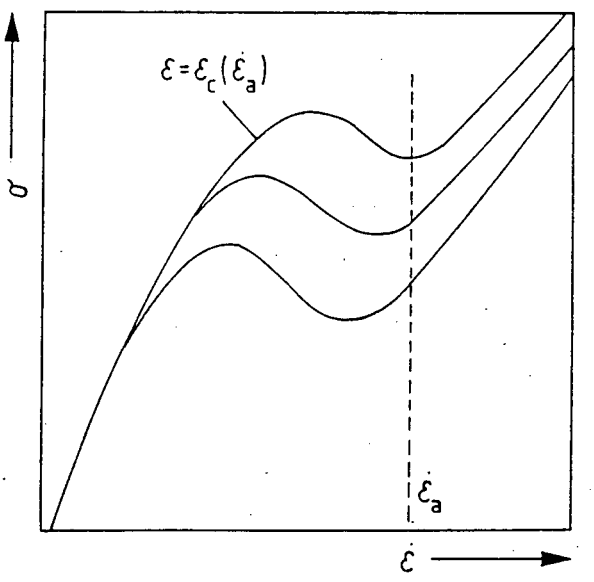

Figure 13: The dependence of stress on applied strain rate at different values of strain. After van den Beukel [198].

In van den Beukels approach [38], he noted that the saturation of dislocations by solutes during t_w, proposed by McCormick [187], was not a necessary condition for serrated yielding. Serrated yielding was proposed to start at much lower concentrations of solutes on dislocations than that predicted by McCormick. Importantly, in both cases, the change in solute concentration locally experienced by dislocations, ΔC, was not predicted to occur instantaneously upon a $\dot{\varepsilon}$ change. The time required for ΔC was of the order of t_w, and this is able to account for the phenomenon of "flow stress transients" observed after a $\dot{\varepsilon}$ change (eg. [36]).

The common features of the "vacancy models" can then be summarised as follows:

At ε_c,

$$\rho_m^{(c)} C_v^{(c)} = K_1 \dot{\varepsilon} e \frac{E_m}{kT} \tag{6}$$

where E_m is the vacancy migration energy and the superscript c refers to the critical strain.

All three models yield different values of K_1 and Cottrell's (K_1) is not reconcilable with experiment [17].

If $\rho_m = A\varepsilon^\beta$ and $C_v = B\varepsilon^m$, then ε_c can be expressed in the form below:

$$\varepsilon_c^{m+\beta} = K_2 \dot{\varepsilon} e \frac{E_m}{kT} \tag{7}$$

where

$$K_2 = \frac{K_1}{AB}$$

For interstitial alloys, equations 6 and 7 are replaced by:

$$\rho_m^{(c)} = K_1' \dot{\varepsilon} e \frac{E_m'}{kT} \tag{8}$$

and

$$\varepsilon_c^{\beta} = K_2' \dot{\varepsilon} e \frac{E_m'}{kT} \tag{9}$$

where E_m' is the migrational energy of the solute element.

In his summary of the "vacancy models", van den Beukel [17] noted the successful features, and adequately countered apparent exceptions to its predictions. Successful results include the intermediate annealing out of vacancies to increase ε_c, after an initial period of straining [107, 199] and the lowering of ε_c due to the excess concentration of vacancies frozen in by rapid cooling (quenching). In addition, the T dependence of ε_c given by equation 7 is found to be in reasonable agreement with experiment and the measured activation energy is observed to correspond with that of vacancy migration. Other examples of the models success were given and it was concluded that satisfactory agreement exists between experiment and the models based on diffusion of solutes to dislocations temporarily arrested at local obstacles in the glide plane

2.7.4 The "Strain Hardening" Approach

Cuddy and Leslie [40] initially considered the empirical relation for $\Delta\sigma$, where;

$$\Delta\sigma = A + B \log Z \tag{10}$$

with A and B as constants.

$$Z = t(\frac{-Q}{RT})$$

with t, the reloading time and T, temperature.

The above authors found the apparent activation energy (Q) for the growth of serrations to be about half that required for the diffusion of substitutional solutes in iron. On

the basis of negative results of vacancy annealing experiments and the failure of the critical strain criterion, Cuddy and Leslie concluded that the pinning of dislocations was not due to a high solute diffusivity resulting from deformation enhanced vacancy production. An alternative explanation proposed was that a redistribution or reorientation of solute atoms or solute atom clusters was occurring in the dislocation cores. The approach considered the mechanism of pipe–diffusion, where enhanced diffusion along dislocation lines occurs, as suggested by Nakada and Keh [21]. An interesting feature of the discussion by Cuddy and Leslie, is that they suggested that dislocation pinning (leading to serrated flow) was unlikely to be effected by an individual substitutional solute, but rather by some solute complex or cluster, possibly including both interstitial and substitutional solutes.

In the approach due to Mulford and Kocks [6], the flow stress is expressed as the total of two additive contributions:

$$\sigma = \sigma_f + \sigma_d \tag{11}$$

where σ_f is the friction imposed on dislocation motion by solutes and σ_d is a result of dislocation-dislocation interactions and the cause of strain hardening.

In a material obeying equation 11, the SRS is also composed of two additive contributions.

$$[\frac{\partial \sigma}{\partial \dot{\varepsilon}}]_T = [\frac{\partial \sigma_f}{\partial \dot{\varepsilon}}]_T + [\frac{\partial \sigma_d}{\partial \dot{\varepsilon}}]_T \tag{12}$$

Considering that only the second term of equation 12 should be influenced by work hardening, specifically:

$$\sigma_d = \alpha(\dot{\varepsilon}, T) \cdot \mu b \sqrt{\rho} \tag{13}$$

where ρ is the dislocation density, which changes with strain, and α describes the dependence of the effective interaction strength on thermal activation, then:

$$[\frac{\partial\sigma}{\partial\dot{\varepsilon}}]_T = [\frac{\partial\sigma_f}{\partial\dot{\varepsilon}}]_T + \frac{\sigma_d}{\alpha}[\frac{\partial\alpha}{\partial\dot{\varepsilon}}]_T \tag{14}$$

or

$$[\frac{\partial\sigma}{\partial\dot{\varepsilon}}]_T = \sigma_f[\frac{\partial\ln\sigma_f}{\partial\ln\dot{\varepsilon}}]_T - [\frac{\partial\ln\alpha}{\partial\ln\dot{\varepsilon}}]_T + \sigma[\frac{\partial\ln\alpha}{\partial\ln\dot{\varepsilon}}]_T \tag{15}$$

Therefore a plot of $[\frac{\partial\sigma}{\partial\ln\dot{\varepsilon}}]$ vs. flow stress (Haasen plot), will produce a straight line whose slope is given by:

$$\frac{1}{m_d} \equiv [\frac{\partial\sigma_d}{\partial\ln\dot{\varepsilon}}]_T = [\frac{\partial\ln\alpha}{\partial\ln\dot{\varepsilon}}]_T \tag{16}$$

with its intercept being the first term on the right of equation 15.

Considering specifically the slope of $[\frac{\Delta\sigma}{\Delta\ln\dot{\varepsilon}}]_T$ vs. flow stress curve, Mulford and Kocks [6] proposed an explanation for serrated flow requiring a combination of solute interaction and strain hardening. The slope of $[\frac{\Delta\sigma}{\Delta\ln\dot{\varepsilon}}]_T$ vs. flow stress was observed to be negative from the beginning of deformation (the total SRS itself being positive), whereas jerky flow begins at a strain where the total SRS becomes negative. The micromechanism resulting in jerky flow was therefore considered to be operating from the onset of plastic deformation, resulting in the negative slope in $[\frac{\Delta\sigma}{\Delta\ln\dot{\varepsilon}}]$ vs. flow stress. As a result, vacancies produced during plastic deformation were considered not to be playing an important role in the process.

The reason given for the observed behaviour, is that the contribution of the σ_f term results in an initial positive total SRS, but sufficient strain accumulation (forest hardening) results in the change to a negative total SRS at ε_c. A summary of these considerations is reproduced in figure 14.

The approach due to Mulford and Kocks, following from the earlier considerations of dislocation arrest by Sleeswyk, suggested that solute atmospheres form on forest dislocations and then subsequently drain by pipe diffusion to enhance the dislocation junction

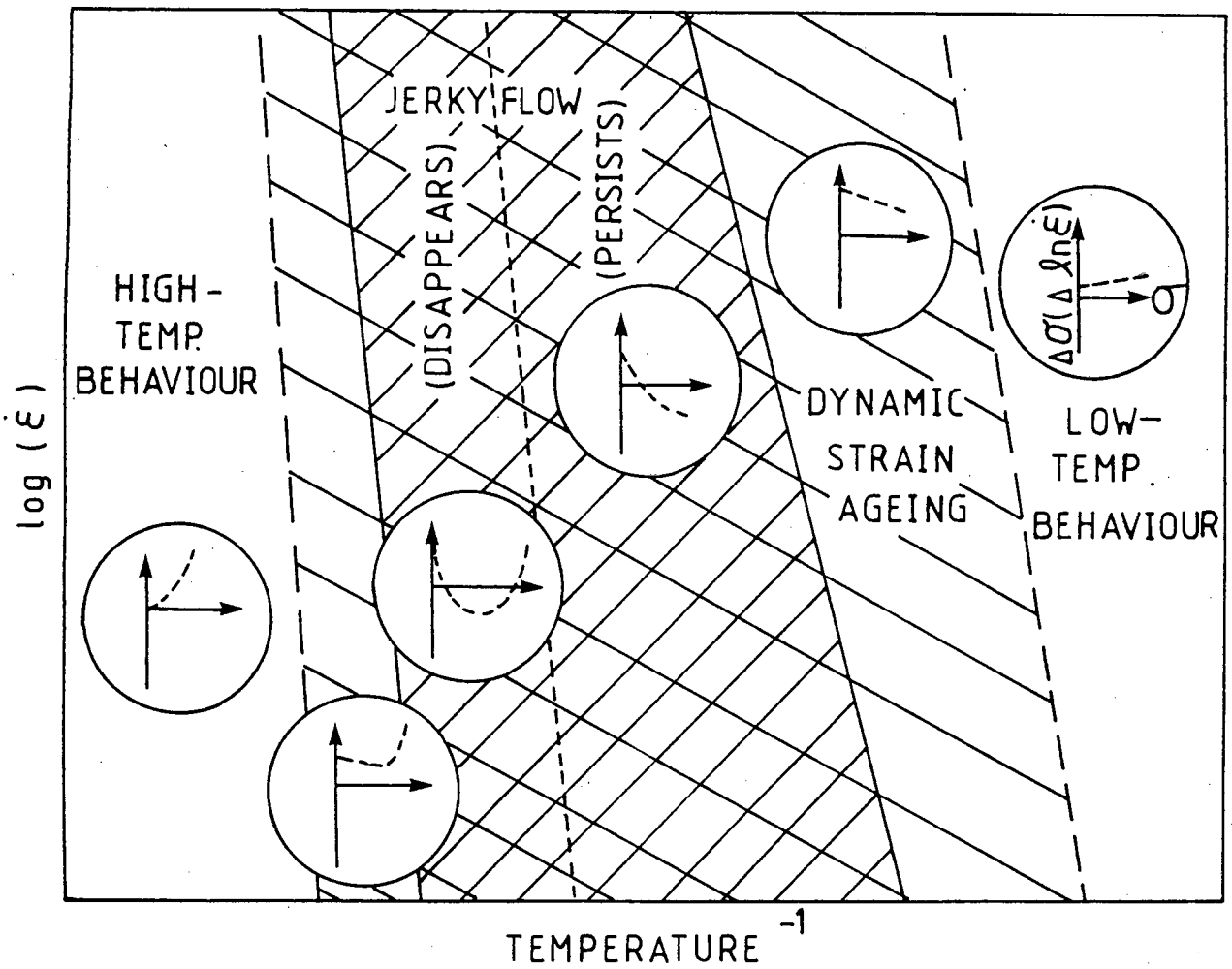

Figure 14: Schematic diagram of the temperature and strain rate regimes of DSA and jerky flow. After Mulford and Kocks [6].

strength. The rapidity of diffusion and the fact that it is not necessary for the whole dislocation segment to be pinned, imply that very little diffusion would be necessary to produce obstacles which increase in strength with t_w. The underlying DSA mechanism was considered to become steadily more effective with the accumulation of strain until the point where a negative total SRS is reached, without the requirement for the bulk diffusion of solutes. The fundamental difference with the approach of van den Beukel is therefore in the interpretation of the strain dependence of the SRS. In both cases it is held that an increase in the effective dislocation glide resistance occurs above a specific temperature due to DSA. The SRS of the flow stress is also crucial in both approaches, where the assertion is that any solute mobility will make a negative contribution to the total SRS. The negative contribution increases with strain until the point where macroscopic deformation is unstable and jerky flow initiates.

Internal friction techniques have been applied to single crystal deformation of Al–Mg and Cu–Al, where three different regimes of solute segregation were observed at different temperatures [2]. At low temperatures, dislocations interacted with fixed solute populations. At intermediate temperatures, solutes segregated to stationary dislocations, mostly from the region surrounding the dislocation core, without the assistance of an excess concentration of vacancies produced by plastic deformation. At higher temperatures, segregation reached a saturation value, because solutes remained in random solution in preference to segregating to dislocations. This work, can the be taken as experimental support for the aspects of the strain hardening approach to DSA described above. Importantly, the segregation of solutes was generally observed to occur in two stages. The dislocation first receives solutes originating from within the dislocation core region followed by relatively slower segregation from the lattice.

2.7.5 Towards a Synthesis

As discussed in the preceding section, common ground exists between the the theoretical approaches of van den Beukel [17, 198] and that of Kocks et al [6, 200]. The major points of agreement are in the need for quasi–static ageing during t_w, the role of the SRS in determining macroscopic behaviour and the negative contribution by any solute mobility

to the total SRS. In conflict, however, was the interpretation of the strain dependence of the flow stress and it is to this end that a joint publication was produced by van den Beukel and Kocks [18]. The idea of a deformation enhanced vacancy population resulting in a strain dependent solute diffusivity was retained by van den Beukel for the case of substitutional alloys. In addition, van den Beukel utilised the concept of a strain dependent mobile dislocation density for the relationship between $\dot{\varepsilon}$ and t_w in all alloys. Mulford and Kocks concluded that solute mobility affects the strain hardening component of the flow stress rather than the friction stress. The latter explanation was considered by the authors to be effective in explaining the observed higher sensitivity of the UTS to DSA when compared with the yield strength.

The essence of the combined approach due to van den Beukel and Kocks, was that it could include the influence of solute mobility on the friction stress and on strain hardening. The former is affected by decreased obstacle spacing along the dislocation line length and the latter by increasing the strength of dislocation junctions. The authors did not agree, however, on the role of deformation produced vacancies.

As suggested in the introduction to this section, the most recent theoretical approach to the PLC effect does not necessarily require a resolution to the debate of van den Beukel and Kocks. Kubin and Estrin [109] have proposed a model for the critical strains associated with the PLC effect in terms of the strain dependence of both the mobile and forest dislocation densities. A consistent explanation of the critical strains for both the onset and termination of jerky flow, the occasional occurrence of two PLC regimes within the same deformation curve and the behaviour of critical strains at high and low temperatures has been proposed.

The model of Kubin and Estrin follows from the approach of van den Beukel [38] and Kocks [196] to assume that the SRS (S) is the sum of two additive contributions. S_0 stems from the activation of dislocation motion in the absence of DSA and S_{ageing} represents the "harder" obstacles in the glide plane of mobile dislocations.

$$S \equiv S_0 + S_{ageing}(\varepsilon) \tag{17}$$

The plastic $\dot{\varepsilon}$ is given by:

$$\dot{\varepsilon} = \frac{b\rho_m \rho_f^{-1/2}}{t_w} = \frac{\Omega}{t_w} \tag{18}$$

where b is the magnitude of the burgers vector, ρ_m the mobile dislocation density and $\rho_f^{-1/2}$ the average spacing between localised obstacles (forest dislocations).

$\Omega = \Omega(\varepsilon)$ is then defined as the elementary incremental strain corresponding to the deformation when all mobile dislocations accomplish a successful activation event at $t = t_w$.

The ageing component of the total SRS is then expressed as:

$$S_{ageing}(\varepsilon) = (\frac{\partial f}{\partial \dot{\varepsilon}})_\varepsilon = -\frac{df}{d\ln t_w} \tag{19}$$

where $f = f(t_w)$, the increase in obstacle strength due to DSA.

The total SRS is therefore:

$$S(\varepsilon) = S_0 - \frac{df}{d\ln[\Omega(\varepsilon)/\dot{\varepsilon}]} \tag{20}$$

S_0 was considered constant, as a simplifying assumption, although in practice it is generally variable.

It can be seen from the equation above, that a similarity exists with the models of van den Beukel and Kocks, in that DSA will make a strain dependent negative contribution to the total SRS. At the strain where the total SRS becomes negative (ε_c), the onset of jerky flow will occur. If, during the course of testing, a point is reached where S again becomes positive, jerky flow will terminate. A second critical strain is therefore defined, ε_c', where the termination of serrated flow occurs, as has been observed experimentally (eg. [107]).

In estimating the critical conditions, Kubin and Estrin made use of a function for f defined by Louat [201].

$$f = f_0\{1 - \exp[-(\frac{t_w}{\tau_0})^{2/3}]\} \tag{21}$$

where f_0 is the maximum stress increase produced by ageing, and τ_0 is the relaxation time.

The function above is able to capture the basic features of the ageing process, *without* ruling out other types of interactions or diffusional processes.

The model of Kubin and Estrin, by considering the evolution of two coupled dislocation densities, is able to account for various experimentally observed features of PLC type deformation. In particular, the strain ranges of existence of the PLC effect are both qualitatively and quantitatively accounted for. While the detail of the preceding summary is necessarily limited, it is apparent that parallels with the strain hardening approach exist. Specifically, the stress dependence of the SRS during DSA conditions is expressed as follows:

$$S = M\sigma_d - K\sigma_d(\frac{D\Omega}{\dot{\varepsilon}})^{2/3} \tag{22}$$

where σ_d is the contribution to the flow stress of the dislocation–dislocation interactions. K incorporates the constants in a deformation test and D is the (constant) effective diffusion coefficient. The SRS in the absence of ageing, $M\sigma_d$, then obeys the Cottrell–Stokes law [4][26] for a substitutional solid solution i.e. a linear increase with stress. An important consideration by the Kubin and Estrin [109], was that an outright rejection of the vacancy approach would entail difficulties in interpreting the observed difference in the ε_c vs. $\dot{\varepsilon}$ behaviour between interstitial and substitutional alloys. Finally, therefore, a suggestion proposed was the possible inclusion of a third term into an extended evolutionary model. The possible coupling of the vacancy concentration as a third structural variable to the mobile and forest dislocation densities could then reconcile the models and

[26]See page 339 of [4]

provide an acceptable solution.

Chapter 3

Experimental Techniques

3.1 Introduction

This chapter describes the experimental procedures utilised in alloy preparation, mechanical testing and microstructural examination of the various aluminium alloys investigated. Materials tested were either commercially produced alloys manufactured by HULAMIN[1] or alternatively, experimental melts produced by alloying commercial purity, 99.7%, aluminium (1070)[2] with various additions, as discussed in section 3.3. Mechanical testing, in all cases, was undertaken using uniaxial tensile testing, before and after which, the material was subjected to microstructural examination using both optical and electron microscope techniques.

3.2 Commercial Alloy Preparation

3.2.1 Commercial Purity Aluminium (1070)

Aluminium of 99.7% minimum purity was received from HULAMIN in the form of a cast billet conforming to the composition specifications outlined in table 2. The actual chemical analysis of the material supplied is shown in table 3.

[1]The reader is referred to Appendix B for a list of proprietary names and products.
[2]The four digit coding of commercial Al alloys is detailed in section 2.5.2, page 34.

The cast material was sectioned into 12 mm slabs and subsequently rolled into sheet by a process similar to that used in the production of commercial Al-Mg (5182) rolled sheet. The process route used for the commercial production of 5182 was used as a standard during the course of this work to aid comparitive examinations between materials. It is detailed in section 3.2.3, page 69. The rolling schedule was carried out using a Dinkel K65E laboratory rolling mill and is detailed in table 1.

Table 1: Rolling reduction sequence for cast 1070.

HOT/COLD	T(°C)	ROLL GAP(mm)	H_{V20}
H	400	9.0	
H	400	7.5	26.2
C	RT	6.0	34.8
C	RT	4.5	34.6
C	RT	3.0	40.7
Interanneal 400°C, 15 minutes, WQ			
C	RT	2.0	
C	RT	1.0	
Interanneal 400°C, 15 minutes, WQ			
C	RT	0.5	
C	RT	0.3	

Specimens for tensile testing were produced according to ASTM B557M (Standard Test method for Al and Mg Alloys) as described and illustrated in appendix A. Full-size specimens were stamped from the ~0.4 mm material, and subsize specimens were machined from the 3 mm plate.

3.2.2 Al–Cu–Mn–Si (2014)

A commercial quarternary Al–Cu–Mn–Si precipitation hardenable alloy (2014) was received from HULAMIN in the form of hot rolled 9 mm thickness plate. 2014 is an alloy hardened by the precipitation of a complex aluminium, copper and magnesium phase

Table 2: Chemical compostion specifications for commercial alloys.

No.	Alloy	Cu	Mg	Si	Fe	Mn	Zn	Ti	Cr
1070	99.7%Al	0.03	0.03	0.20	0.25	0.03	0.07	0.03	
2014	Al–Cu–Mn–Si	3.90 5.00	0.20 0.80	0.50 0.90	0.50	0.40 1.20	0.25	0.15	0.10
5182	Al–Mg	0.15	4.00 5.00	0.20	0.35	0.20 0.50	0.25	0.10	0.10
6061	Al–Mg–Si		1.00	0.60		0.28			0.20

Table 3: Actual chemical compositions of alloys tested.

No.	Alloy	Cu	Mg	Si	Fe	Mn	Zn	Ti	Cr
1070	99.7%Al	0.00	0.003	0.05	0.16	0.000	0.004	0.000	0.003
2014	Al–Cu–Mn–Si	4.65	0.66	0.86	0.31	0.91	0.32	0.24	
5182a	Al–Mg	0.016	4.44	0.14	0.30	0.30	0.01	0.016	0.009
5182b	Al–Mg	0.03	4.34	0.15	0.35	0.41		0.021	0.019
5182c	Al–Mg	0.029	4.62	0.15	0.32	0.34	0.14	0.027	0.017
5182d	Al–Mg	0.040	4.81	0.14	0.27	0.37	0.01	0.004	0.006
6061	Al–Mg–Si	0.22	0.87	0.59	0.32	0.078	0.15	0.031	0.17

rather than the Al–Cu phase of original binary Al-Cu alloys [134].[3] The 2014 material tested during the course of this work was produced by multiple pass hot rolling a $330 \times 1070 \times 2500$ mm^3 billet at 500°C. The alloy conformed to the composition specifications presented in table 2 and the actual chemical composition of the alloy is presented in table 3.

ASTM B557M subsize tensile specimens were prepared, by conventional machining methods, from the plate. The material was tested in the solution treated (505°C, WQ) condition, directly after quenching in order to minimise the effect of natural ageing. In addition, some specimens were allowed to age at room temperature, for one or two hours prior to tensile testing. Finally some material was aged to peak hardness (175°C, 10 hours), referred to as the T6[4] temper, and then tensile tested.

The aim of testing in the naturally aged and T6 condtions was to ascertain the progressive effect of the precipitation of solutes on the serrated flow characteristics exhibited by the alloy. All testing was performed at room temperature. Specimen gauge lengths were mechanically polished prior to tensile testing in order to facilitate subsequent surface deformation observations.

3.2.3 Binary Al–Mg (5182)

The commercial binary Al–Mg (5182) alloy formed the basis of the majority of testing and rolling procedures, because of the profound serrated flow properties exhibited during room temperature testing. Material from four different casts (a–d) was tested during the course of the work, with each cast conforming to the same chemical composition limits. Composition limits for the alloy are given in table 2 and the analyses of the specific casts are given in table 3.

The rolling reduction process route of 5182 is a commercial procedure, from which material was sampled at various points, in order to ascertain the effect of prior rolling deformation on the mechanical properties. From the bulk ingot size of $470 \times 3040 \times 1070$ mm^3,

[3] See page 365 of [134].
[4] Commercial temper designations are detailed in section 2.5.2, page 34.

material was rolled down to 0.35 mm final sheet thickness as follows:

Hot roll to 6.7mm (~21 passes)

1. Cold roll : 6.7mm → 4.4mm

2. Cold roll : 4.4mm → 2.9mm

3. Cold roll : 2.9mm → 1.73mm

INERT GAS ANNEAL (300°C, 2hours)

4. Cold roll : 1.73mm → 0.86mm

5. Cold roll : 0.86mm → 0.50mm

6. Cold roll : 0.50mm → 0.31mm

Although the commercial rolling sequence utilises an inert gas anneal after the third cold pass, material tested in the course of this work was continuously cold–rolled without an anneal. In order to produce a continuous cold–rolling sequence, material was taken after the third pass and cold–rolled in the laboratory for the subsequent reductions. Only commercial 0.35 mm 5182 sheet material was tested after the exact sequence described above in the commercial cold–rolling schedule.

3.2.4 Ternary Al–Mg–Si (6061)

6061 is a commercial ternary alloy, conventionally hardened by a precipitation heat treatment after solution heat treatment. Precipitates used to strengthen the material are an ordered Mg_2Si (β') phase with no direct evidence of coherency [137].

The material tested in the course of this work was produced by HULAMIN in 20×40 mm^2 extrusions. The billet was extruded in the solution temperature range (520°C), quenched upon leaving the die and then aged (175°C, 7 hours) to peak hardness, referred to as the T6 condition. Composition specifications are given in table 2 and the analysed chemical composition of the alloy used for mechanical testing is given in table 3.

3.3 Experimental Alloy Preparation

Three experimental alloys were produced by making 2at.% additions of Zn, Ag and Mg to commercial purity aluminium (1070). Alloys were produced using a medium frequency Leybold–Heraeus vacumn induction melting facilty at MINTEK.[5] Al–Zn and Al–Mg alloys were produced by alloying high purity HULAMIN master alloys with 1070 and the Ag alloy was produced by alloying 99.9% minimum purity Ag with the 1070.

Subsequent homogenisation, as well as hot and cold–rolling of the ingot down to 3 mm plate, was carried out at MINTEK. Rolling sequences utilised the 50 ton two high reversing mill and the procedure followed was similar to the 5182 production route described in section 3.2.3. The production schedule for the experimental melts is outlined below:

1. Homogenisation 500°C for 24 hours
2. Hot roll (400°C) to 7.5mm
3. Cold roll (RT) to 4.5mm

[5]The reader is referred to Appendix B for a list of proprietary names and products.

4. Cold roll (RT) to 3.0mm

Material was then received as 4.5 mm and 3.0 mm thick plate for testing and further cold–rolling. Cold–rolling from 3 mm to ~0.4 mm was achieved using the Dinkel K65E laboratory rolling mill exactly as described for 1070 in section 3.2.1, page 66.

The three melts were coded as follows:

VF 615: Al–Mg
VF 617: Al–Zn
VF 619: Al–Ag

The cast analysis of the base alloy, 1070, as well as the 2at.% alloys is presented in table 4.

Table 4: Composition of experimental alloys tested.

No.	Alloy	Cu	Mg	Si	Fe	Mn	Zn	Ti	Cr
1070	99.7%Al	0.0	0.003	0.05	0.16	0.000	0.004	0.000	0.003
VF615	Al–Mg	0.000	1.54	0.06	0.18	0.000	0.005	0.000	0.003
VF617	Al–Zn	0.002	0.018	0.10	0.25	0.008	4.020	0.000	0.004
VF619	Al–Ag	0.003	0.001	0.05	0.17	0.02	0.052	0.005	0.003

3.4 Metal Matrix Composite Preparation

The materials investigated were commercially produced metal matrix composite (MMC) materials based on the standard commercial alloys 2014 and 6061. Particulate additions, by volume, of either 10%, 15% or 20% Al_2O_3 or SiC were used in the manufacture of the materials. Production of the composite material was achieved by addition of the particles to the molten metal using a DURAL[6] patented mixing unit, which is designed to wet and

[6]The reader is referred to Appendix B for a list of proprietary names and products

distribute the particles uniformly in the matrix. The composite was then cast into an extrusion billet for final fabrication.

Material tested was extruded by HULAMIN in a similar process to the production of 6061 billet discussed in section 3.2.4, page 71. All material tested was extruded in the form of 20×40 mm^2 billet except for the case of 6061 + 10% Al_2O_3, which was extruded in the form of an I-beam section. Material was extruded at solution temperature (520°C), quenched upon leaving the die and then artificially aged to peak hardness. The condition that the material was received in was, therefore, peak aged in all cases, i.e. the T6 condition.

3.5 Tensile Testing

3.5.1 Specimen Geometries

The majority of tensile testing utilised either the ASTM B557M[7] standard rectangular specimen or a proportionately reduced (subsize) specimen of the same geometry. Full sized specimens were stamped from the ~0.35 mm thick sheet by HULAMIN and all other specimens were produced in the Department of Materials Engineering workshop using conventional machining methods. In addition, some circular X-section specimens were produced from 5182c[8] to asses the effect of this geometry on the serrated flow properties.

The effect of the ratio of the width to the thickness of the specimen gauge length was assessed by testing specimens with various gauge length thicknesses. Specimens were machined to different thicknesses from the same initial plate thickness. In addtion, specimens of different thicknesses were also produced from plate of corresponding thickness. The net effect of the above was to enable evaluation of both the effect of specimen geometry, as well as the effect of cold–rolling deformation on the inhomogeneous deformation.

[7]As described in Appendix A.

[8]See section 3.2.3 for descriptions of individual melts

3.5.2 Surface Preparation

Specimens were tested with the surface in four possible conditions; either as machined, as stamped (surface of 0.35 mm rolled material), mechanically polished or electropolished. Polishing of the specimen surfaces was necessary, prior to tensile testing, in order to facilitate later examination of the surface deformation and associated slip line structure.

Standard metallographic polishing of the gauge lengths utilised a jig made with the reverse imprint of the specimen to hold it during grinding and polishing as illustrated in figure 15. Polishing to 0.25 μm was completed prior to the final recrystallisation anneal, to avoid the possibility of inducing mechanical damage in the surface layers, and thereby altering initial yield characteristics.

In the case of the metal matrix composite material, electropolishing using a 25% nitric acid in methanol solution proved to be more effective than mechanical polishing. Mechanical polishing of the composites tended to produce a greying of the surface with no lustre, attributable to the crushing and smearing of the composite particles at the specimen surface.

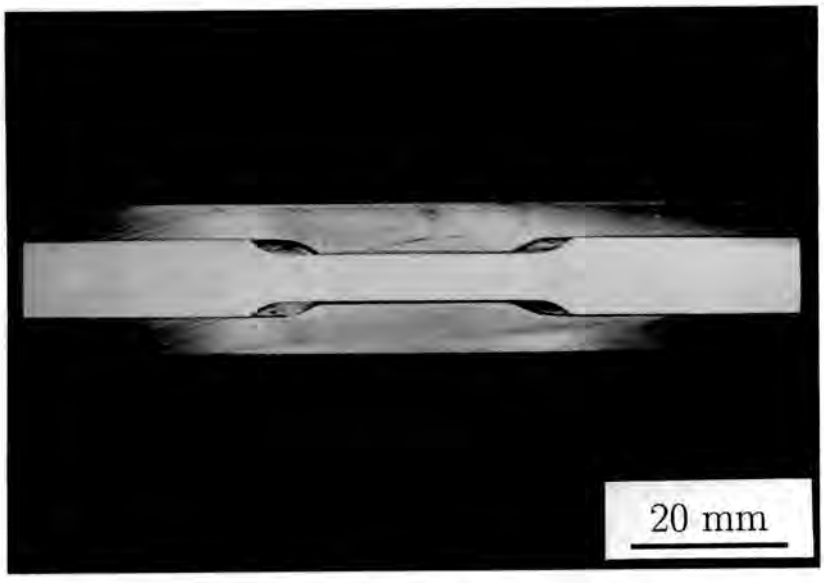

Figure 15: Grinding and polishing holder used in the surface preparation of tensile specimens.

3.5.3 Data Acquisition and Processing

The majority of tensile testing was carried out at a standardardised strain rate of $\dot{\varepsilon} \approx 2.5 \times 10^{-4}s^{-1}$, corresponding to a known regime for room temperature manefestation of serrated flow in aluminium alloys [54]. Testing at strain rates other than $2.5 \times 10^{-4}s^{-1}$ is clearly indicated during the course of Chapter 4. Tensile testing utilised a Zwick[9] 1484 universal testing machine interfaced to a personal computer (PC) for data acquisition and machine control.

The standard rate used for the aquistion of data was 0.01 mm of specimen extension per data point aquired. One hundred data points per mm extension proved to be sufficient to completely resolve individual serrations for qualitative and quantitive examination. The commercially available software used, Zwick 7005, has the capacity to produce an output file format for use by other programs. Final copies of the tensile test records were therefore produced by importing the data captured by the Zwick software into Quattro Pro, a commercial spreadsheet package.

3.6 Observations of Surface Deformation

3.6.1 Macroscopic Tensile Specimens

Use was made of both a Cambridge S200 scanning electron microscope (SEM) and a Reichert Me F2 optical microscope. Tensile specimen gauge lengths were examined at specific strains after premature termination of the tensile test. Specimens were ultrasonically cleaned prior to examination and then clamped in a vice attachment in the SEM. Images were produced by utilising a combinaton signal of both secondary and back scattered electrons.

Normarski interference microscopy proved particularly effective for surface deformation observations in the case of specimens which deformed by the propagation of deformation

[9]The reader is referred to Appendix B for a list of proprietary names and products.

bands. The minimal topographical effect of a band propagating along a tensile specimen gauge length meant that the SEM was not ideally suited to this application.

3.6.2 HVEM Microtensile Specimens

In order to verify that the deformation of the minature tensile specimens,[10] used for in situ deformation in the HVEM, was comparable to the bulk specimens, a small straining stage was built. The straining device used was similar in design to the type of device conventionally employed for in–situ straining in the SEM, and is illustrated in figure 16. The stage was built such that conversion to in–situ SEM straining, using an existing electric motor drive, is a possible future application. For the purposes of this work, specimens were incrementally strained to uncalibrated strain levels in the laboratory, and then subsequently examined at these points in the SEM.

The technique involved initially preparing the microtensile specimens in the jet–polisher, using exactly the same method used to prepare the specimens prior to viewing in the HVEM, as discussed in section 3.8.2. Following jet-polishing, specimens were strained under a stereo optical microscope until the first evidence of plastic deformation was observable. The entire device, illustrated in figure 16, was then loaded into the SEM for examination of the development of the slip line structure. Examination was at accelerating voltages of 25 keV or less, to minimise flaring effects, and the signal used was a combination of secondary electrons and back scattered electrons to maximise slip line contrast. If necessary, the specimen was then removed from the SEM chamber and given a further strain increment while being viewed under the stereo microscope, then examined in the SEM for a second time.

3.7 Conventional TEM

Specimens were prepared by two similar methods, determined by whether or not annealing of the 3 mm disc could take place prior to final thinning, as discussed below.

[10] See also section 3.8, page 78.

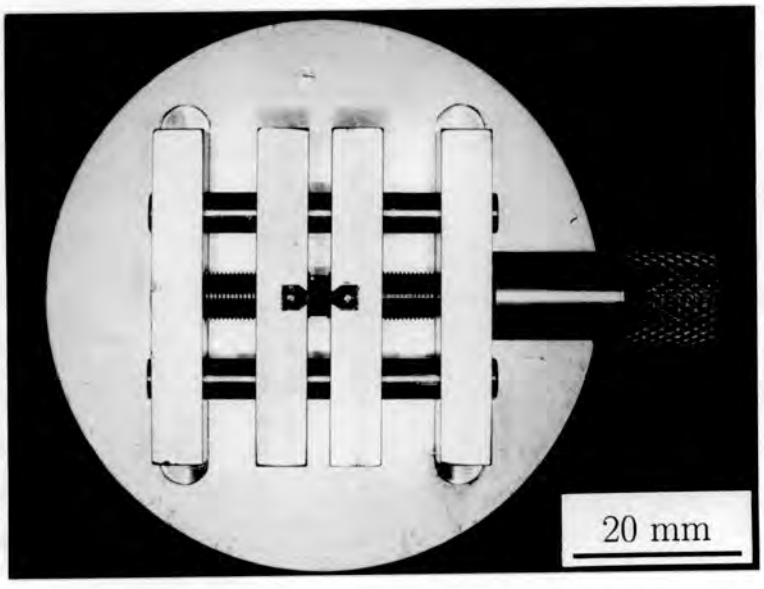

Figure 16: Straining stage used in the Cambridge S200 SEM.

1. In the first case, for examination of recrystallised structures and heavily cold-worked structures, 3mm discs were punched from the ~0.4 mm thick sheet material using a Materials Science (North West)[11] 3 mm disc punch. Final grinding to 0.10 → 0.15 mm was carried out using a 3 mm disc grinding jig manufactured in Department of Materials Engineering. Grinding was against 1000 grit sandpaper and was followed by a recrystallisation anneal.

2. Where preservation of the deformation microstructure was necessary, as in the case of 3 mm discs cut from the guage length of pre–deformed tensile specimens, spark erosion techniques were used. Initial rough grinding of the gauge length from both sides produced a thickness of ~1 mm, from which 3 mm discs were cut at 300V, using the laboratory spark eroder.

Final thinning, in all cases, utilised twin jet polishing techniques with a 25% nitric acid in methanol solution at 0°C and a potential of 15V. Polishing was carried out using a Struers Tenupol automatic twin–jet polishing unit.

An attempt was made to prepare TEM specimens from MMC material by using a two stage technique, initially twin–jet electropolishing, and later, electropolishing followed by

[11]The reader is referred to Appendix B for a list of proprietary names and products.

ion beam thinning. The lack of cold stage facillities and fine control of the ion mill, including automatic termination, severely limited this approach. TEM foils produced contained heavy ion damage (eg. [203][12]) and heating artifacts, even where attempts were made to have a very low angle (less than 15°) of ion beam impingement accelerated through minimum keV (less than 2.5 keV accelerating voltage). Where twin jet electropolishing to transparency was attempted, topograhical restrictions from the unthinned particles hindered any reasonable viewing of the microstructure. Spark erosion cutting of 3 mm discs from the material prior to final thinning showed that the inclusion of particles in the material did not restrict the ease of spark machining.

3.8 High Voltage Electron Microscopy

In–situ deformation studies of microtensile specimens was carried during the period July/August 1990 utilising the KRATOS 1500 keV HVEM at the National Center for Electron Microscopy (NCEM), Lawrence Berkeley Laboratories, Berkeley, California.

3.8.1 Materials and Preparation

Five materials were selected for testing and observation in the HVEM, including the three experimental melts discussed in section 3.3 as well as the base material 1070 and the higher Mg content 5182 alloy. Material in all cases was selected from cold–rolled $\sim$ 0.4 mm thick sheet, from which, the microtensile specimens were punched.

3.8.2 Specimen Preparation

Microtensile specimens were produced in an unconventional manner by utilising a punching tool and die, manufactured by the Division of Production Technology of the CSIR,[13] using spark erosion techniques. The punch and die are illustrated in figure 17 and the

[12]See page 115 of [203]

[13]The reader is referred to Appendix B for a list of proprietary names and products

microtensile specimens produced are illustrated in figure 18. The conventional method of producing the specimens [203] uses a photo–resist technique, known as chemical milling, which was not immmediately available in South Africa. In addition, specimens produced by chemical milling are often of relatively low dimensional tolerance. After stamping, specimens had mounting holes for the straining pins of the straining stage drilled into them, using a specific jig to hold them rigid.

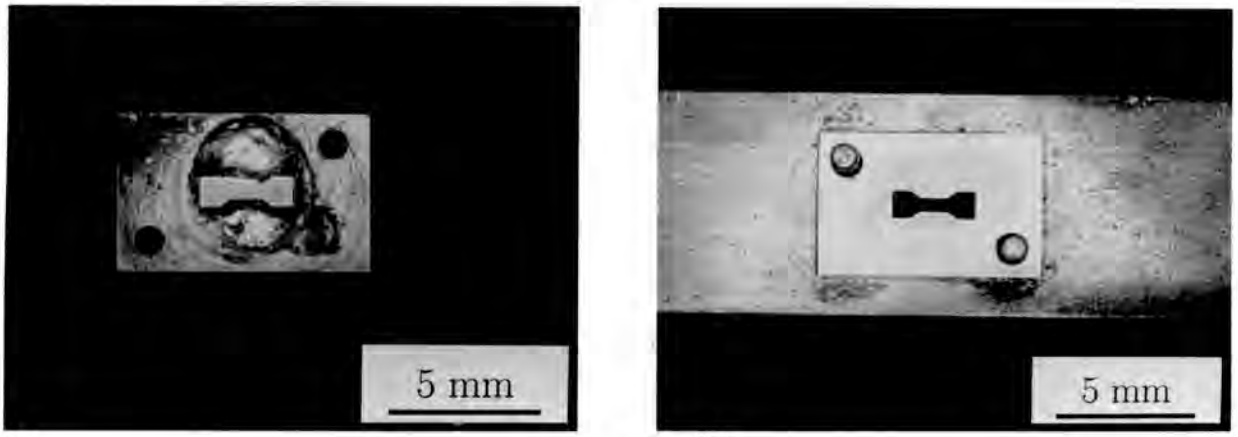

(a) (b)

Figure 17: Punch (a) and dye (b) used to produce microtensile specimens.

Recrystallisation and solution heat treatment annealing was carried out at 400°C (500°C in the case of VF619, to ensure complete solid solution of the silver), in a vertical tube furnace. Annealing (30 mins) was followed immediately by direct quenching into water. Heat treatment was performed directly before electropolishing and viewing in the microscope, in order to minimise any possible effects of natural ageing prior to testing.

Final thinning and electropolishing utilised a similar technique to the preparation of CTEM specimens.[14] Specimens were examined after thinning using one of two preparation methods, detailed below:

1. Based on a suggestion by Clark et al [204], a modified specimen holder was designed and produced in the Department of Materials Engineering workshop for the jet–polishing unit. Figure 19 illustrates the holder design, the key feature of which is the rectangular polishing slot. The effect of having a polishing slot is the production

[14]See section 3.7, page 76.

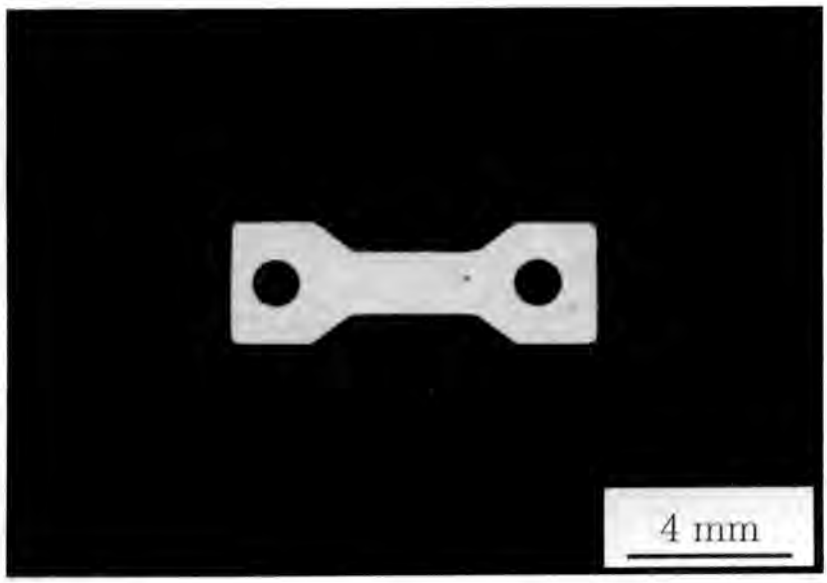

Figure 18: Microtensile specimen with mounting holes drilled.

of an oval penetration in the gauge length of the microtensile specimen, as illustrated in figure 20.

2. Some problem was encountered with exceeding the maximum load (2 kgf) of the HVEM straining stage, in that the specimen holder could not be loaded to above 2 kgf without being damaged. In the case of the stronger 5182 and VF619 (Al–Ag) alloys, a standard (3 mm disc) thinning holder was used, to effectively weaken the specimen by thinning it across the entire gauge width. A specimen thinned by this method is illustrated in figure 21. The technique employed was to manually terminate the thinning process at the first transmission of light, which was observed by removing the photo–sensor for the automatic terminator. The specimens produced had an electron transparent area surrounded by a region of the gauge length, which was thin right across the gauge width, allowing the specimen to plastically deform at very low stresses.

Specimens produced by the above two thinning techniques are illustrated in figures 20 and 21.

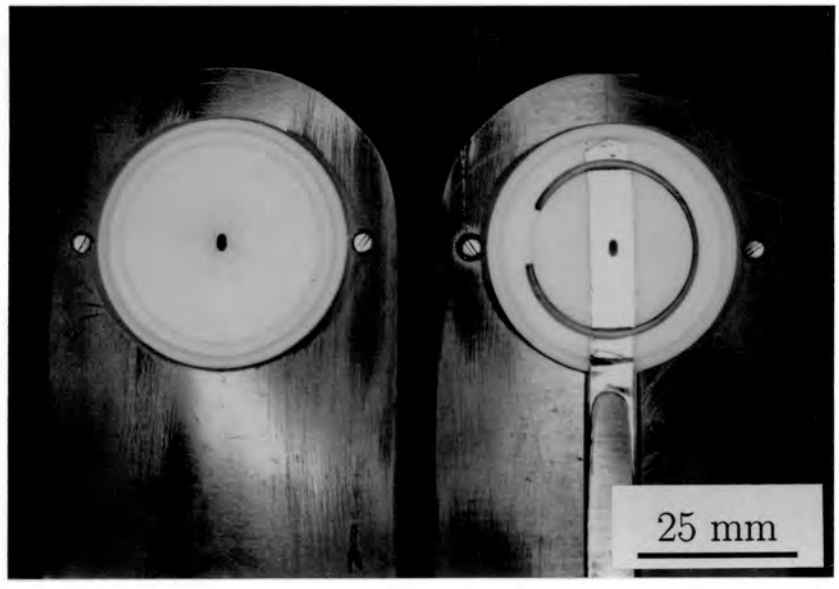

Figure 19: Modified polishing holder for the Struers Tenupol.

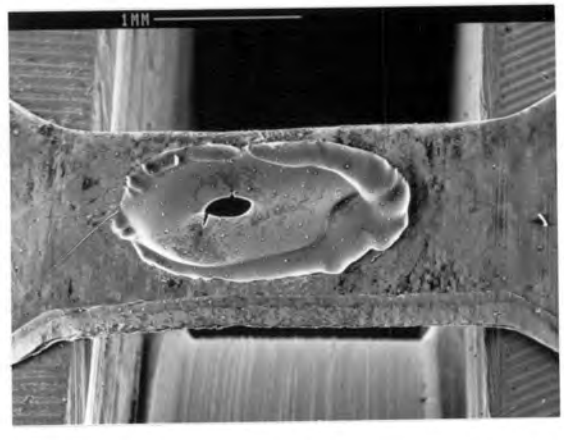

Figure 20: HVEM microtensile specimen, jet polished using the polishing holder illustrated in figure 19.

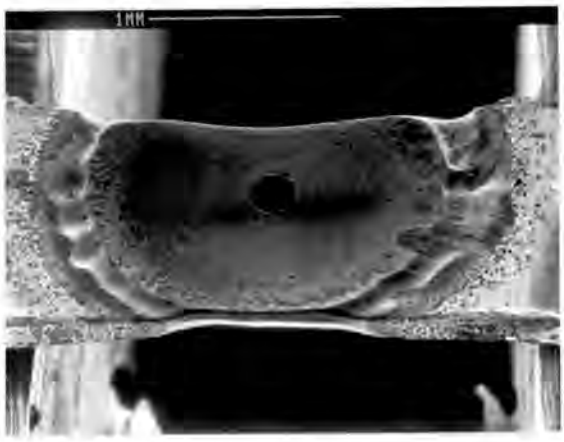

Figure 21: HVEM microtensile specimen, jet polished using the standard (3 mm disc) polishing holder.

3.8.3 HVEM Operating Techniques

In–situ deformation was carried out in all cases at room temperature, in a double tilt dual straining mechanism stage [205]. The specimen was strained by alternate tensioning using a mechanical motor drive followed by straining with piezo–electric crystals [203]. The piezo–electric crystals provide for vibration free straining which could be readily viewed and dynamically recorded at high magnifications.

Selection of an area likely to deform was achieved by assuming that yielding would occur in an area adjacent to the electropolished hole and with the maximum probability of deformation along the long edges of the oval perforation. Mechanical factors i.e. the geometry of the perforation in the specimen were observed to dominate over metallurgical, in that deformation was always initiated at the mechanical stress concentrators, regardless of the orientation of the grain in that area. The process was, therefore, one of initially identifying areas where yielding had just occurred or was imminent and then optimising viewing conditions prior to further straining.

3.8.4 Records of HVEM Deformation

Two processes were utilised to record the images produced during in–situ straining in the HVEM, as follows:

1. By recording on conventional high resolution electron microscope film. Straining was temporarily halted to allow for the recording of conventional images and associated diffraction patterns.

2. By necessarily lower resolution dynamic recording using videotape. The video was run continuously during the application of strain and dynamic evolution of the microstructure recorded. A camera was mounted in the line of the beam, directly below the conventional viewing screen for recording of these images.

Production of hard-copy images from the video source material was achieved using a PC based video digitising card, known as a frame grabbing card. A MATROX[15] card was used in conjunction with high image quality (4 head) VHS video machine. The configuration allowed for frame by frame previewing of the tapes and subsequent "grabbing" (digitising and storing) of these images. Source material was recorded at 30 frames per second.

For final photographic reproductions, the 512×512 byte images of the video (generated by the frame grabbing card) were viewed on a high resolution monitor, and finally phtographed on 35 mm film using a conventional single lens reflex camera.

[15]The reader is referred to Appendix B for a list of proprietary names and products.

Chapter 4

Results

4.1 Introduction

This chapter presents a systematic description of the results of mechanical testing, surface deformation observations, microstructural examination utilising CTEM and dynamic microstructural evolution studies, utilising HVEM. For clarity of presentation, the chapter is divided according to the alloy types tested. In addition, the format of the chapter is such that it allows for ready comparison of the results of similar experimental procedures applied to the different alloys examined.

4.2 General

4.2.1 Finite Element Analysis of Specimen Geometry

As discussed in Chapter 3, tensile testing was carried out according to ASTM B557M[1] and specimens were, in all cases, proportional to the dimensions defined in the test standard. In order to aid in the determination of the effect of rectangular section specimen geometry on PLC band formation, a rudimentary finite element analysis was undertaken. Rectangular cross–section specimens were the only geometry tested which deformed via

[1]The reader is referred to Appendix A for a diagram of ASTM standard specimens used in the course of this work.

the repeated occurrence of visually detectable PLC bands. Circular cross–section specimens produced serrated flow stress curves during deformation (as was the case with the rectangular cross–section specimens), but no deformation band formation was detected.

Utilising a commercial finite element analysis package (ABAQUS[2]), a finite element mesh was imposed on the rectangular section specimen geometry plan. The mesh, illustrated in figure 22, was intentionally finer in the shouldered area of the specimen because initial yielding, in the form of type A (flamboyant) deformation markings, had been observed to occur in this area. [3] The application of uniaxial, *elastic* loading was considered, and its effect on the finite element mesh is illustrated in figure 23. In figure 23, the displaced mesh illustrated is delineated by solid lines in contrast to the original mesh marked by dotted lines. It can be seen from figure 23 that the mesh is more deformed at the gauge length ends than towards the centre of the gauge length.

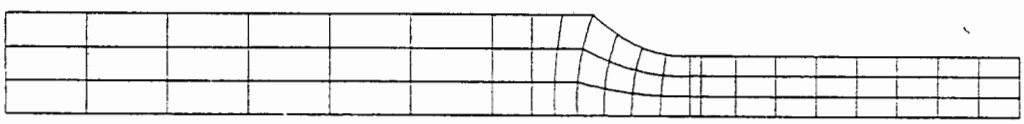

Figure 22: Finite element mesh used to determine the effect of elastic loading on the rectangular section specimen geometry.

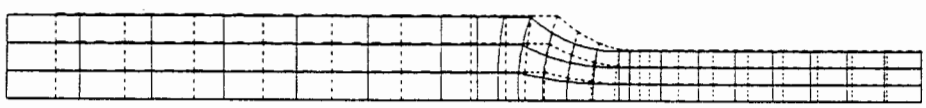

Figure 23: The distorted finite element mesh (solid lines) resulting from the application of tensile loading to the original mesh (dashed lines).

An indication of the stress intensity in the specimen shoulder region is given by the von Mises criterion [206], plotted as shaded yield loci, and illustrated in figure 24. From

[2]The reader is referred to Appendix B for a list of proprietary names and products.
[3]The initial yielding referred to is discussed further in section 4.5.1 pages 106 and 111.

figure 24, it is clear that the stress intensity is maximised at the specimen shoulder and progressively decreases towards the centre of the specimen gauge width. As discussed in section 4.5.1, type A surface markings form in a triangular shape at the specimen shoulders[4] (upon yielding), the position of which correlates directly with the yield loci shown in figure 24.

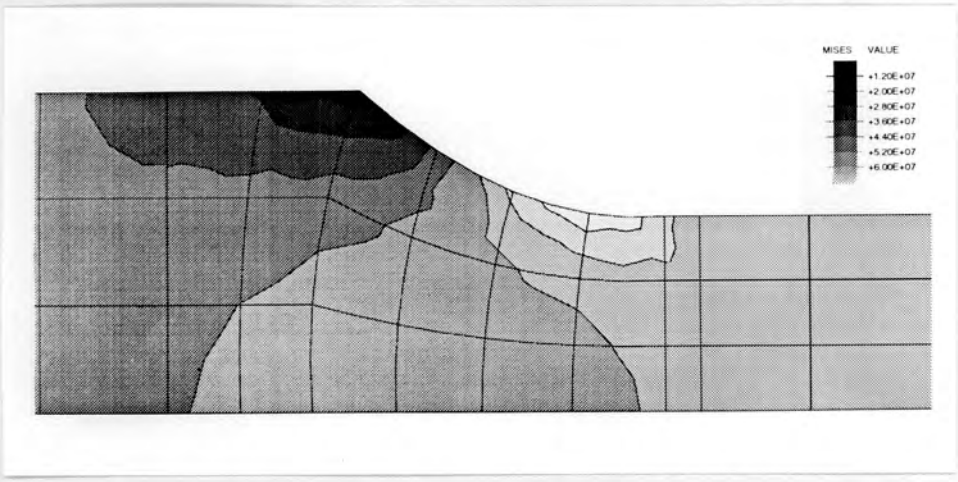

Figure 24: The shaded stress contours, indicating relative stress intensities in an axially loaded specimen (plane stress).

4.2.2 Extension Measurement During Tensile Testing

Two available options were considered for strain measurements of the deforming tensile specimens. The Zwick 1484 tensile test machine used during the course of this project was equipped with both a cross–head extensometer and an external knife–edge type clip–on extensometer. The use of a knife–edge extensometer is generally preferable based on the following considerations:

1. The sensor accuracy of the knife–edge extensometer is 0.001 mm per output pulse as opposed to the 0.01 mm per pulse in the case of the cross–head extensometer.

2. A cross–head extensometer is necessarily more remote from the deforming region of a tensile specimen (gauge length) than a clip–on extensometer. The cross–head

[4]An optical micrograph of typical type A surface markings observed during the course of this work was shown in figure 7, section 2.3.3.

sensor is separated from the specimen gauge length by both the specimen shoulders and the grips.

In the case of inhomogenous deformation, however, the possibility exists for plastic deformation to occur outside of the gauge length defined by the knife edges. The result of using a knife–edge extensometer in this case, where extreme deformation inhomogeneities occur, is that an inaccurate record of the deformation may result. An example of the deformation record from a 5182 specimen, produced using a clip–on extensometer, is presented in figure 25. It is clear from the figure that apparent compression of the tensile specimen is recorded, where for an increase in applied stress, the specimen becomes shorter. The "compression" occurs in the gauge length by elastic contraction of this region when plastic extension of the specimen occurs outside of the region defined by the knife edges.

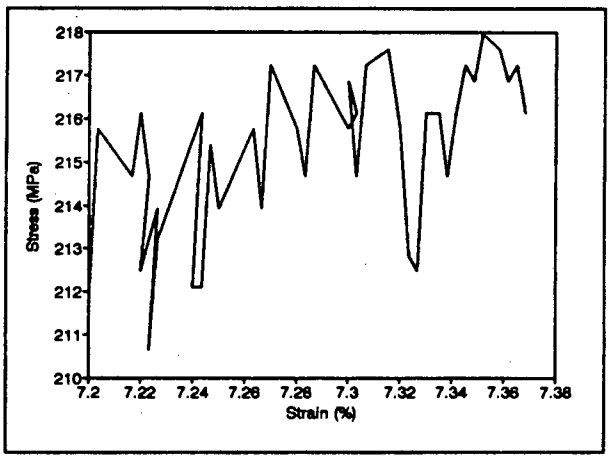

Figure 25: A section of the flow stress curve of commercial Al–Mg alloy (5182) recorded using a clip–on knife–edge type extensometer

For the reasons outlined above, tensile test records during the course of this work were mostly acquired using a cross–head extensometer. Plastic deformation occurs throughout the gauge length of a tensile specimen, defined by the reduced section between the two shoulders and, to a lesser extent, in the shoulders themselves. The deformation recorded by a cross–head extensometer is then, the sum total of this deformation. A section of a flow stress record using data acquired with the cross–head extensometer, comparable to that in figure 25, is reproduced in figure 26 for comparison. It can be seen in figure 26 that the repetitive regular nature of PLC type deformation is clearly recorded by this method.

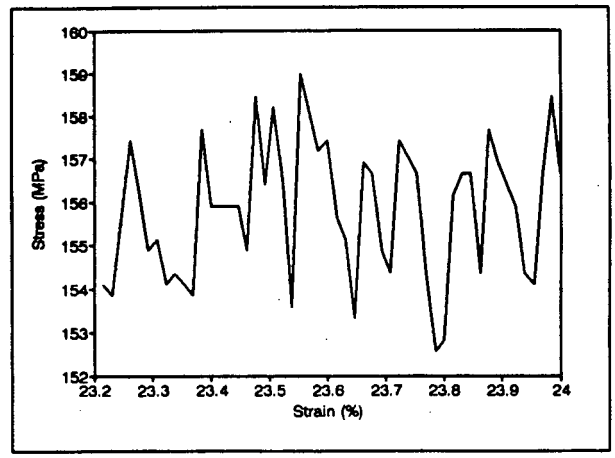

Figure 26: A section of the flow stress curve of commercial Al–Mg (5182) recorded using a cross–head extensometer.

The preceding argument holds true especially for the case of extreme deformation inhomogeneities, typified by the case where deformation bands propagate within the gauge length of a deforming specimen. A knife–edge extensometer was, therefore, only used to acquire data in the situation where deformation bands were observed not to propagate. In testing where the clip–on extensometer was used, the gauge length defined by the knife–edges was maximised, in order to minimise effects of deformation occurring outside of the gauge length (defined by the knife–edges). The specific test results, where a clip–on extensometer was used are clearly marked during the course of this chapter.

4.2.3 Commonly Observed Deformation Band Orientations

For the purposes of clarity of presentation of the results in this chapter, terminology describing deformation band types observed during the course of this work is defined in this section. Three major band orientations were observed to commonly occur and these are illustrated in figure 27.

The orientation of band formation is dependent on the conditions of deformation, specifically whether the specimen is being deformed under conditions approximating plane stress or plane strain.[5] Three situations were regularly observed to develop during testing

[5]The reader is referred to section 2.3.3 where the orientation of deformation bands has been discussed with specific reference to Lüders bands

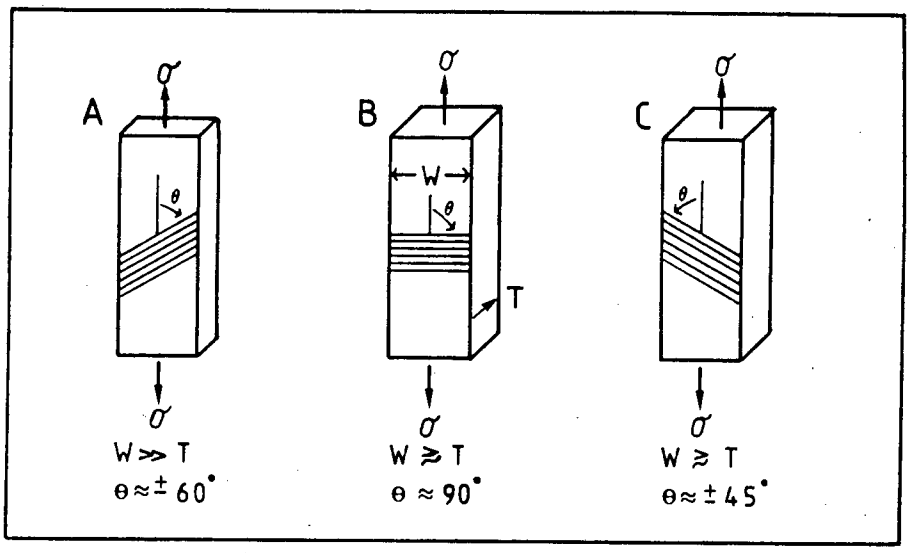

Figure 27: The three common orientations of deformation band formation observed during the course of this work.

in the course of this work, respectively illustrated in figure 27 (A), (B) and (C).

1. Under deformation conditions approximating *plane stress*, where the specimen width (W) far exceeded the thickness (T), deformation bands were observed to form at $\theta \approx 60°$ to the tensile axis. θ was measured on the broad specimen face as indicated in figure 27. This value is in agreement with the theoretical predictions of Hill [72] and the experimental observations of others (eg. [45]).

2. Under deformation conditions approximating *plane strain*, where the specimen width (W) was greater than or equal to the thickness (T), deformation bands were generally observed to occur at 45° to the tensile axis. This angle was not apparent by only measuring θ on the broad specimen face, but the two band types observed can be adequately described by only considering θ. The orientation of the band type illustrated in (B) of figure 27 is referred to (during the course of this work) as 45° to the tensile axis through the specimen thickness. This orientation is, therefore, at 90° to the tensile axis on the broad specimen face. The orientation of the bands illustrated in (C) of figure 27, however, is distinguished from (B) by being described as at 45° to the tensile axis through the specimen width. This orientation is, therefore, at 45° to the tensile axis on the broad specimen face.

4.3 Commercial Purity Aluminium (1070)

4.3.1 Tensile Test Results

In order to facilitate CTEM investigations of deformed microstructure evolution, cold worked material was recrystallised prior to tensile deformation. The recrystallisation heat treatments applied were at temperatures corresponding to the single phase region of the of the binary phase diagram for the alloying element under consideration. In the case of 1070, a temperature of 400°C was employed for recrystallisation. 400°C corresponds to the temperature required to produce single phase solid solutions of Al–2at.%Zn and Al-2at.%Mg, and was therefore selected for solution treating 1070 to aid in comparing the results of tensile tests from these two materials. The recrystallisation anneal was followed by a water quench, again in direct correspondence with the solution treatments applied to other materials tested.

The material was tested in two specimen geometries, as discussed below, both with rectangular cross–sections.

1. Subsize ASTM B557M specimens machined from 3 mm thick plate.
2. Full–size ASTM B557M specimens stamped from ~0.4 mm thick sheet material.

ASTM B557M Subsize Specimens

In the first case, subsize specimens machined from 3 mm thick plate formed the standard for tensile testing with the emphasis on surface deformation and fracture studies. The second case allowed for macroscopic testing of the material used to produce the HVEM microtensile specimens, as discussed in section 3.8.2. In addition, in alloys where the deformation occurred by the repeated formation/propagation of deformation bands, these bands were most readily visualised on the surface of full–size specimens stamped from ~0.4 mm thick material.

The tensile deformation of 3 mm thick cold worked material 1070 was characterised by the onset of plastic deformation without a defined yield point. Post yield deformation occurred with minimal work hardening prior to the onset of plastic instability. Plastic deformation progressed until failure with minor irregularities in the flow stress, the stress amplitude ($\triangle\sigma$) of these serrations being $\sim$0.16 $\rightarrow$ 0.4 MPa. Subsequent recrystallisation (400°C, 30 minutes) of the material resulted in similarly gradual yielding, followed by regular and extended low amplitude type B serrations, as illustrated in figure 28. The serrations, were of a similar magnitude to those exhibited by the cold worked material, with $\triangle\sigma \approx 0.2 \rightarrow 0.4$ MPa.

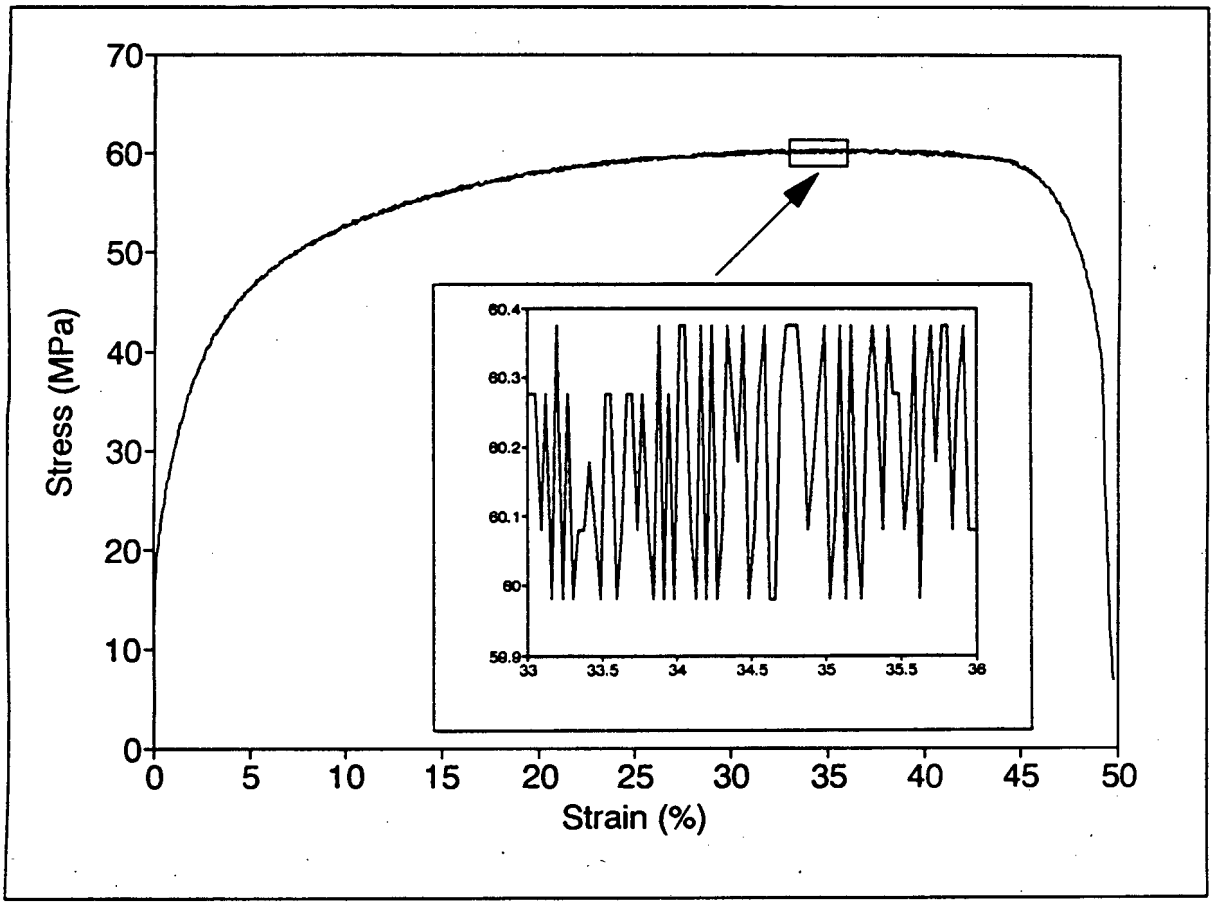

Figure 28: Tensile deformation record of commercial purity aluminium (1070), cold–rolled to 3 mm thickness and annealed (400°C, 30 minutes, WQ). (Knife–edge extensometer)

ASTM B557M Full–size Specimens

Material, cold–rolled to ~0.4 mm final thickness, was used to produce the full–size ASTM B557M specimens. Material was annealed (400°C, 20 mins, WQ) immediately prior to tensile testing, the record of which is presented in figure 29.[6]

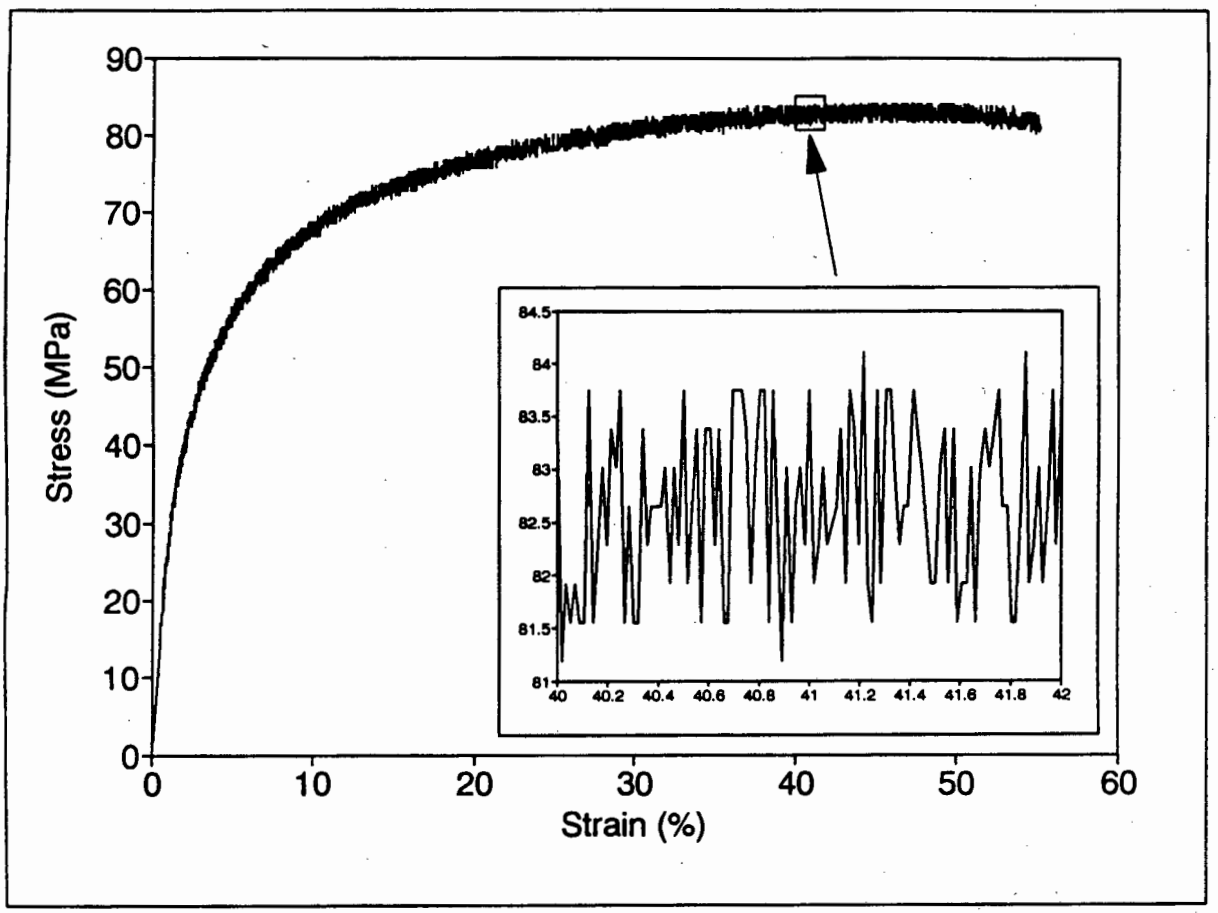

Figure 29: Tensile deformation record of commercial purity aluminium (1070), cold–rolled to ~0.4 mm thickness and annealed (400°C, 20 mins, WQ).

The deformation of the annealed and quenched, ~0.4 mm thick material was characterised by several distinct features:

1. A continuous yield, comprising serrated plastic flow from the onset of plastic deformation.

[6] $\dot{\varepsilon} = 3.95 \times 10^{-4} s^{-1}$.

2. Sustained serrated plastic flow, with $\Delta\sigma \approx 3$ MPa, until final fracture.

3. A substantial portion of plastic deformation approximating ideally plastic straining i.e. accompanied by little or no work–hardening.

4.3.2 Surface Deformation Observations

The surface deformation features associated with tensile straining were examined on pre–polished tensile specimens utilising the SEM. Specimens were mechanically polished to a surface finish of 0.25 μm, following which, final annealing was carried out. Specimen surfaces were examined for deformation features after fracture or alternatively at pre–determined values of strain by premature termination of the tensile test.

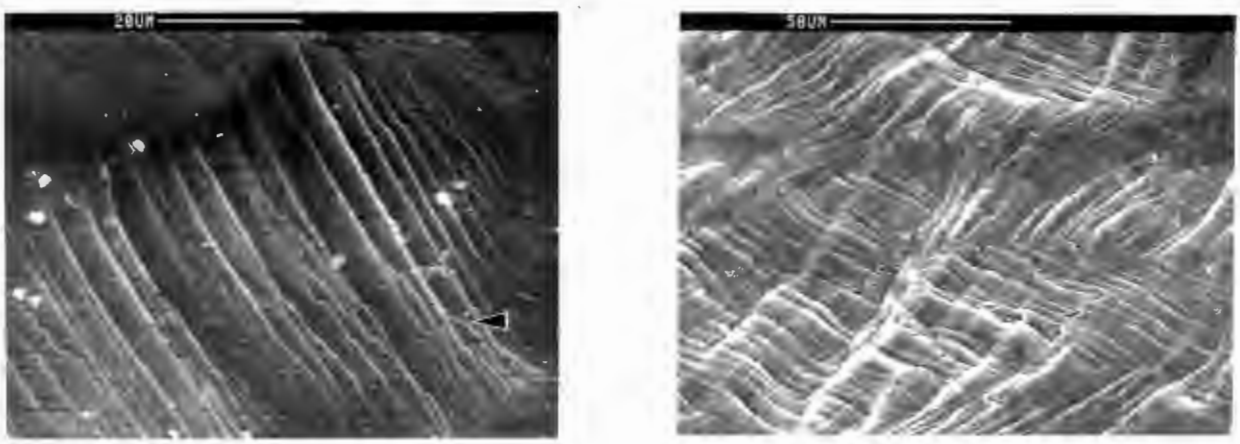

(a) (b)

Figure 30: SEM micrographs illustrating the surface deformation features observed after tensile straining of annealed 1070. (a) illustrates the low strain (~5%) deformation and (b) shows a similar specimen at a higher value (~20%) of total tensile strain

Figure 30 illustrates the characteristic surface deformation features associated with the tensile deformation of annealed 1070. The lower strain deformation, illustrated in (a), is characterised by parallel slip band formation together with features consistent with planar cross–slip (arrowed) [77]. At higher strains, the slip traces exhibited characteristic waviness, resulting from the activation of numerous slip systems.

4.3.3 Microstructural Observations (CTEM)

Figures 31 and 32 illustrate the cold–rolled and annealed microstructures of 3 mm thick 1070 material respectively.

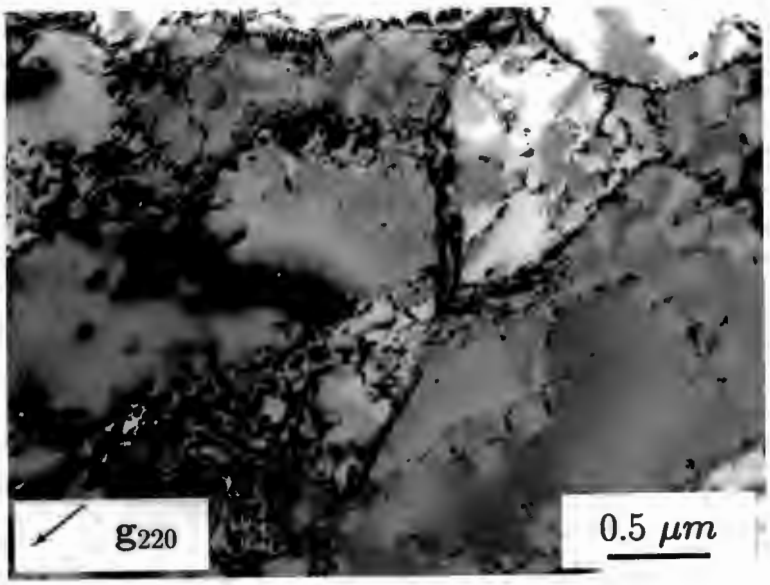

Figure 31: Bright–field TEM micrograph of 3 mm thick cold–rolled 1070 illustrating characteristic dislocation tangles and aligned dislocation arrays surrounding dynamically recovered subgrains.

The microstructural development of the annealed 3 mm thick 1070 during tensile straining is clearly illustrated in figure 33 (a)–(c). The sequence of micrographs illustrated in figure 33 (a)–(c) shows the microstructure of annealed material which has been deformed in tension to levels of 1%, 2% and 5% total strain. The evolution of the microstructure illustrated in figure 33 (a)–(c) corresponds with the deformation record presented in figure 28.

In the case of ~0.4 mm cold–rolled material, a comparison can be made between figure 34 and the microstructure of 3 mm cold–rolled material shown in figure 31. From the two figures it can be seen that the annealed and quenched ~0.4 mm material has a higher quenched in dislocation density when compared with the 3 mm cold rolled material in a similar condition.

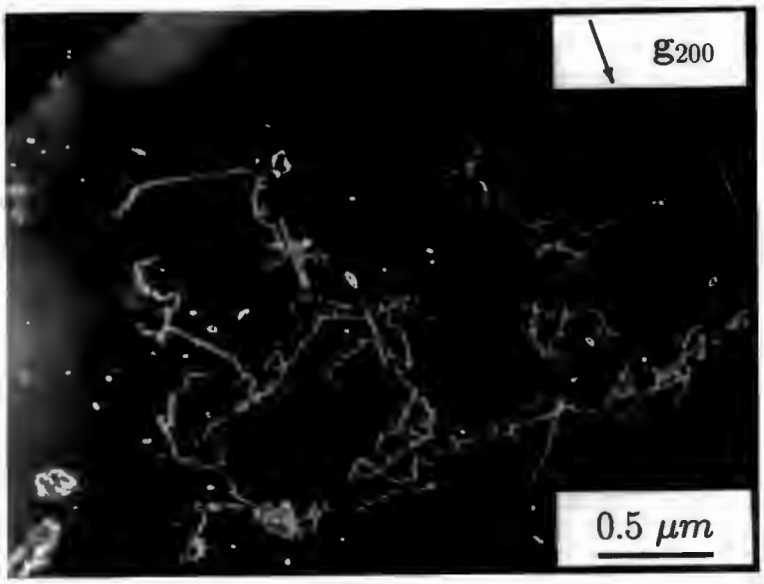

Figure 32: Weak–beam TEM micrograph of annealed 3 mm cold–rolled 1070, characterised by small dislocation loops and a background of dispersed low density dislocation clusters.

4.3.4 Microstructural Evolution (HVEM)

Microtensile specimens stamped from 1070 material were annealed at 400°C for 1/2 hr followed by water quenching immediately prior to deformation in the HVEM. Deformation from the onset of plastic deformation was characterised by sudden collective motion of multiple dislocations. Sudden successive yield events were often associated with the rapid appearance of slip traces on the specimen surface. These yield events frequently occurred on slip planes other than the slip plane on which dislocations were currently being imaged.

Figure 35 illustrates the type of initial yield event described above. Some movement of dislocations on single slip planes was observed to precede the dramatic yield events. Single dislocations were observed to move into the field of view and pile up against pre–existing dislocation tangles or grain boundaries. A sequence of micrographs, illustrating the motion of dislocations on a single slip plane preceding a major yield event, is presented in figure 36.[7]

[7]HVEM micrographs do not have the g–vector indicated on the micrograph due to problems encountered with the diffraction pattern–image rotation calibration of the instrument. All micrographs were, however, recorded at optimum two beam diffracting conditions.

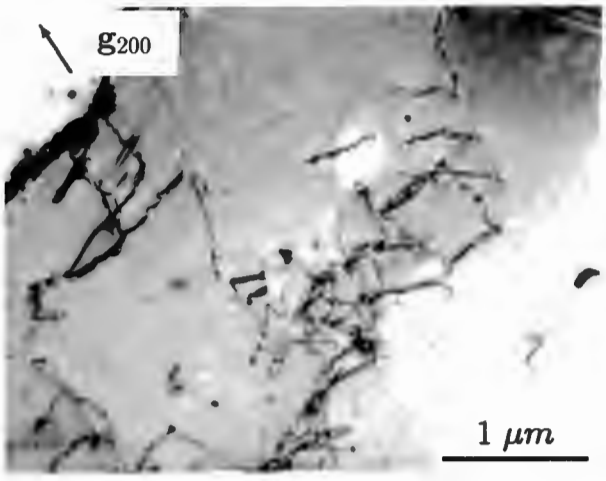

(a) 1% Total tensile strain.

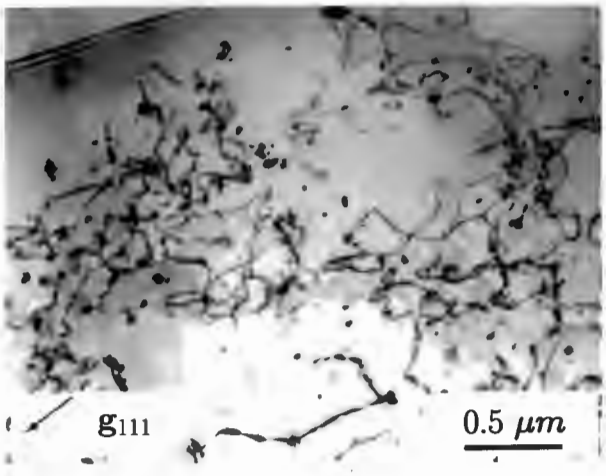

(b) 2% Total tensile strain.

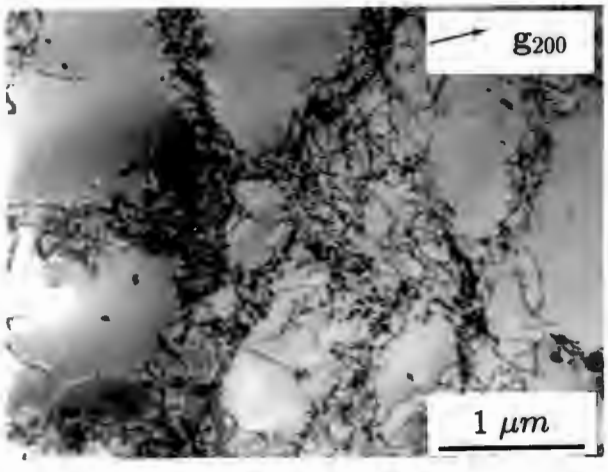

(c) 5% Total tensile strain.

Figure 33: Bright–field TEM micrographs (a)–(c) illustrate the development of the deformation microstructure during tensile straining in 3 mm thick cold rolled 1070, after annealing. (a)–(c) show the material deformed in tension to 1%, 2% and 5% total strain respectively.

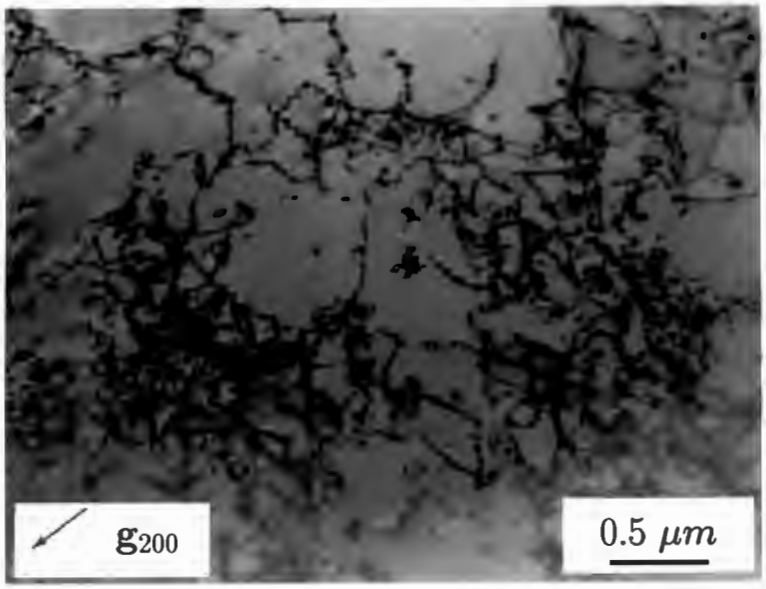

Figure 34: Bright–field TEM micrograph of ~0.4 mm thick cold–rolled and annealed 1070, which exhibits a higher density of dislocations than the 3 mm thick material in a similar condition.

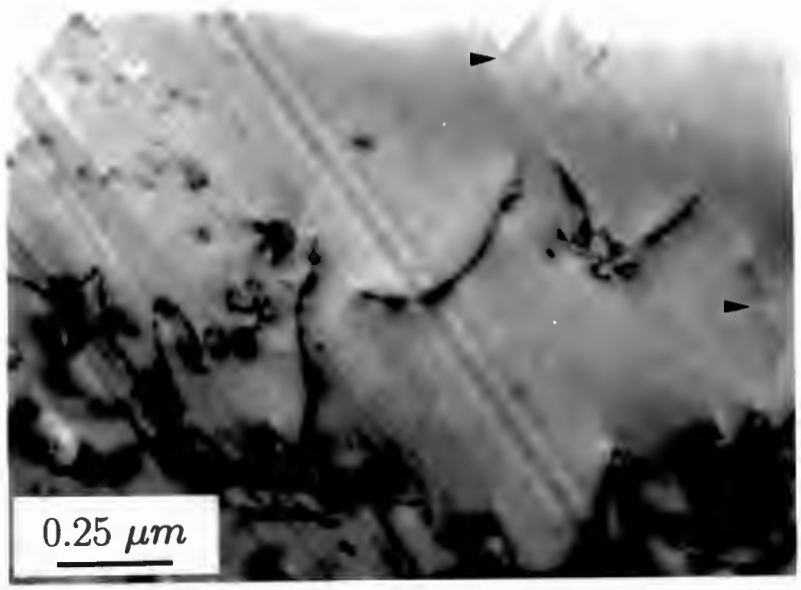

Figure 35: Bright–field HVEM micrograph of annealed 1070, illustrating the rapidly formed slip traces, as well as planar cross–slip features (arrowed).

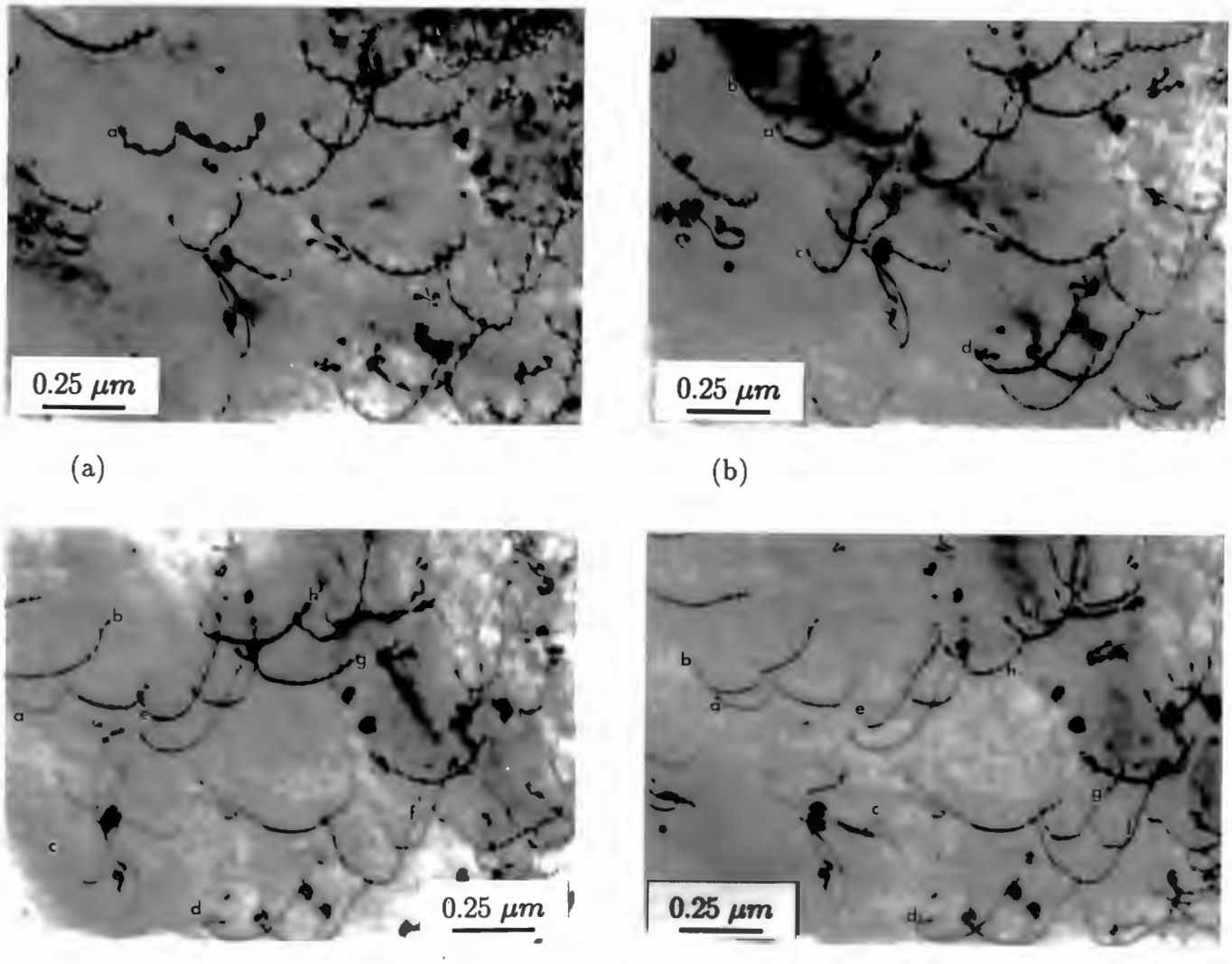

Figure 36: Bright–field HVEM sequence of micrographs (a)–(d) illustrating the motion of dislocations in a single slip plane preceding a major yield event. Markings on the micrographs indicate the successive positions of individual dislocations in the field of view.

As described above, dislocation motion in a single slip plane was often observed to precede the more dramatic multiple slip system yield events. The major yield events were characterised by the sudden activation of slip on various slip planes in the field of view, evidenced by slip traces in the oxide film on the specimen surface. Extensive cross–slip and multiple active planes characterised such yield events. Examples of the result of this sudden yielding, taken from video taped material are illustrated in figure 37.

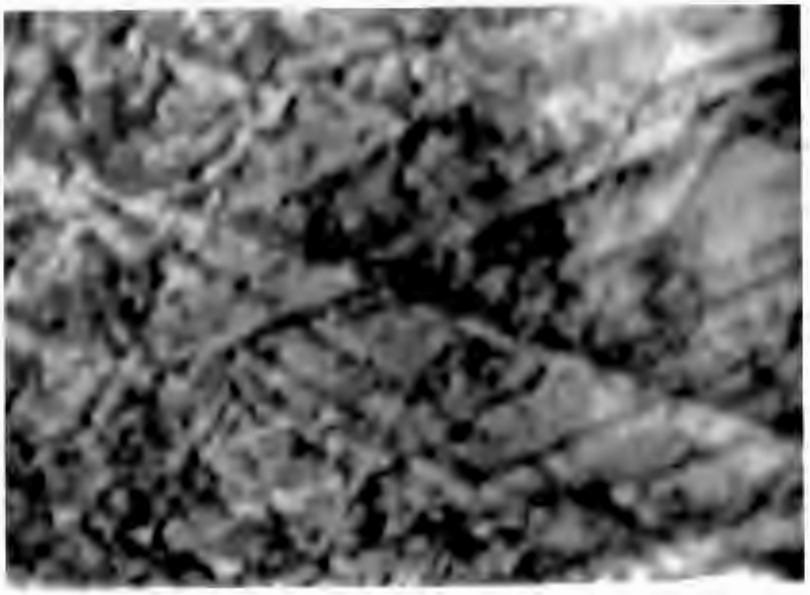

Figure 37: Video tape image of rapidly formed, intersecting slip traces (produced during in–situ deformation) on the surface of alloy 1070.

4.3.5 Comment

Commercial purity 1070 was observed to deform with low amplitude but regular and consistent serrations in all conditions tested. The aim of testing 1070 was to test a material which exhibited homogeneous plastic deformation and then to compare this with the same material alloyed with 2at.% additions of Ag, Zn and Mg. The result was, however, not necessarily unexpected, given other published results on aluminium of comparable purity [133, 80].

The material was characterised by its ease of dynamic recovery deduced from low work hardening rates, wavy slip traces and ready formation of dislocation cell structures. Significantly, however, deformation characteristics observed in the HVEM corresponded

with the macroscopic features, most notably in terms of the discontinuous nature of the deformation at a micro level. Characteristics of the fracture are discussed in conjunction with the experimental alloys based on 1070, in section 4.8.7, page 171.

4.4 Commercial Al–Cu–Mn–Si (2014)

The commercial quaternary precipitation hardenable alloy conforming to the composition specifications given in table 2, page 68 is designated 2014. The alloy is conventionally strengthened by the precipitation of S′ (Al_2CuMg) during artificial ageing at 175°C for 10 hrs. Ageing is carried out after a solution heat treatment (505°C, 2 hrs) followed by quenching in water. In addition, the alloy may be further strengthened by the addition of particulate (or fiber) reinforcement and thus forms a matrix alloy for MMC manufacture.

The 2014 alloy tested during the course of this work was deformed either immediately after solution heat treatment or after a specific period of natural (RT) ageing. The natural ageing response of the alloy is rapid for approximately 3 hrs, after which the material stabilises at a Vickers hardness (H_{V20}) of approximately 125. The natural ageing response of 2014 is presented in figure 38.

4.4.1 Tensile Testing

A typical stress–strain response for alloy 2014 in the freshly solution treated condition is presented in figure 39. Serrated flow develops from the onset of plastic deformation, i.e. without an incubation strain (ε_c), and is characterised by small irregularities in the flow stress ($\triangle\sigma_{max} \approx 1$ MPa). The serrations observed were consistently interspersed with single large flow stress discontinuities, where $\triangle\sigma \approx 10$ MPa. The isolated single stress drops resemble type C serrations, similar in appearance to those occasionally observed in martensitic stainless steels [207, 208]. A distinction can be made between two types of these single stress drops observed i.e. where the deformation resumes at either a lower or higher value of the flow stress subsequent to the stress drop. The two possible situations are clearly visible in the inset of figure 39.

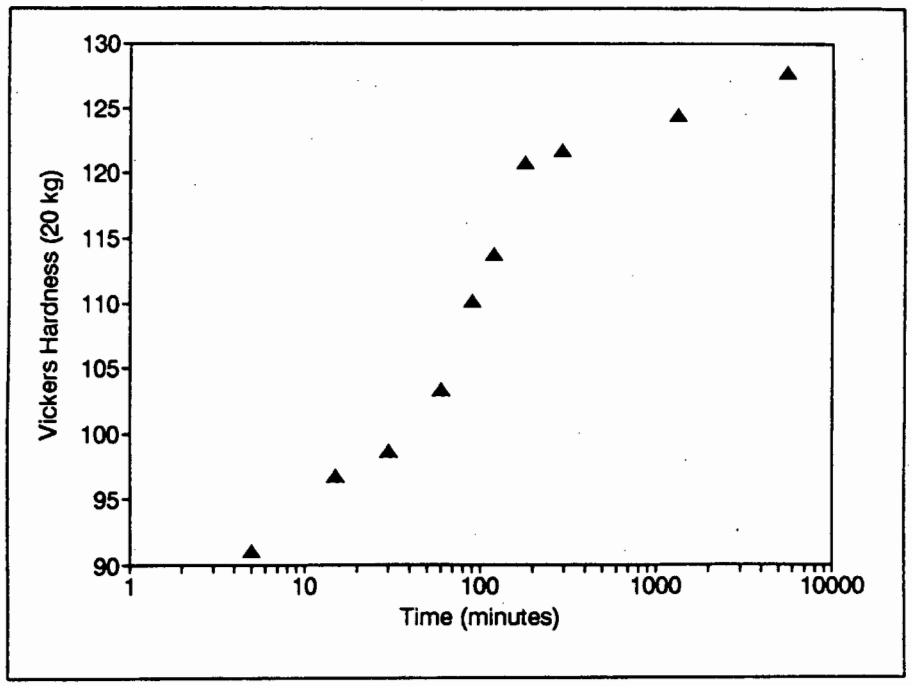

Figure 38: The natural (room temperature) ageing response of alloy 2014 after solution heat treatment (505°C, 2hrs, WQ), measured by the change in Vickers hardness (H_{V20}).

As many as 25 large amplitude single stress drops were observed to occur during the course of any single tensile test. Generally the magnitude of the stress drops were observed to increase from $\Delta\sigma \approx 4$ MPa to $\Delta\sigma \approx 20$ MPa prior to failure. The suddenness of the load drops, meant that they were accompanied by minimal plastic extension, and were therefore not always recorded in the stored record of discrete computer acquired data points. The existence of these single stress drops was, however, always verifiable in the original continuous record[8] of the tensile test. Regular audible acoustic emission was emitted by the specimens, coincident with the formation of the isolated load drops.

Natural ageing of the specimens, for periods up to 3 hrs, was observed to decrease the frequency of occurrence of these single stress drops. It must be noted, however, that even material which had been artificially aged to peak hardness prior to tensile testing (175°C, 10 hrs), exhibited some isolated type C serrations during deformation. In the peak aged condition, however, no smaller serrations were observed to punctuate the single stress drops.

[8]Tensile test records were acquired as a continuum during the course of the test, and subsequently stored as a set of discrete data points.

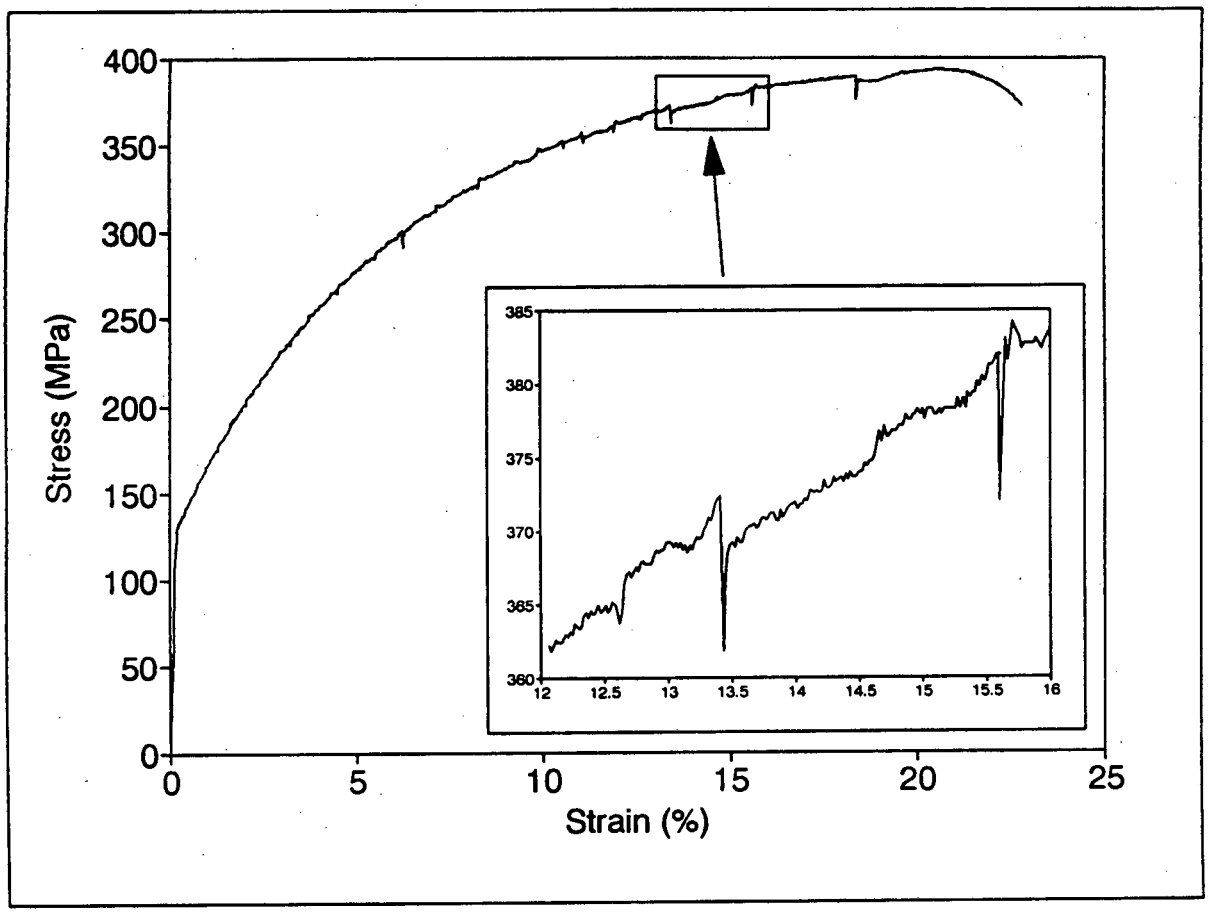

Figure 39: Tensile deformation record of solution treated (505°C, 2hrs, WQ) alloy 2014, tested immediately after quenching. (Knife–edge extensometer)

Figure 40: SEM micrograph illustrating the surface deformation features associated with the single isolated stress drops during tensile deformation of alloy 2014.

4.4.2 Surface Deformation Observations

SEM examination of the pre–polished tensile specimen surfaces, after tensile deformation, revealed features unique to this particular alloy. Surface slip line development was retarded until high values of strain, close to that required for specimen fracture. From values of strain of approximately 5%, however, inclusions in the material were observed to be cracked or fractured. The surfaces of fractured tensile specimens showed the cracking of inclusion particles to be associated with intense slip line formation and associated deformation localisation.

A SEM micrograph illustrating the surface deformation features described above, is shown in figure 40. EDS analysis of the inclusion particles showed them to rich in Cu relative to the matrix, indicating that they are probably undissolved $CuAl_2$ particles. It is noteworthy that there was no indication of macroscopically observable deformation band formation on 2014 specimen surfaces, regardless of the initial microstructural state prior to tensile testing.

4.4.3 Microstructural Observations (CTEM)

The quenched microstructure of 2014 is illustrated in figure 41. The microstructure was characterised by a network of quench associated defects [209], namely helical dislocations

Figure 42: SEM micrograph illustrating the regions of smaller ductile dimples as well as larger shear elongated dimples associated with the sudden ductile failure of alloy 2014 specimens. The direction of shear is vertical.

4.4.5 Comment

2014 exhibited regular serrated flow with serration amplitude ($\Delta\sigma_{max} \approx 1$ MPa), approximately similar to that observed in the previous alloy, 1070. The existence of large isolated stress drops coincident with audible acoustic emission distinguished 2014 from other alloys tested during the course of this work. These isolated stress drops were shown to be associated with inclusion fracture observed under the SEM.

The alloy is used as a matrix material in the manufacture of MMC material, and was therefore tested in its monolithic form in order provide a basis for comparison with tensile characteristics of the composite materials.[9]

4.5 Commercial Al–Mg (5182)

The commercial binary Al–Mg alloy, 5182, was chosen as a basis for comparison with the other alloy systems tested during the course of this work. As is apparent from the discussion in Chapter 2, Mg as a solute in aluminium is generally considered responsible for producing the most profound deformation inhomogeneities commonly observed in aluminium base alloys.

[9]The deformation characteristics of the MMC materials are discussed in section 4.7, page 140.

4.5.1 Tensile Test Results

Figure 43 shows a typical stress–strain curve for cold–rolled 0.35 mm thick 5182 sheet, produced by the tensile deformation of a stamped ASTM B557M full–size specimen. The stress–strain curve is characterised by the following features:

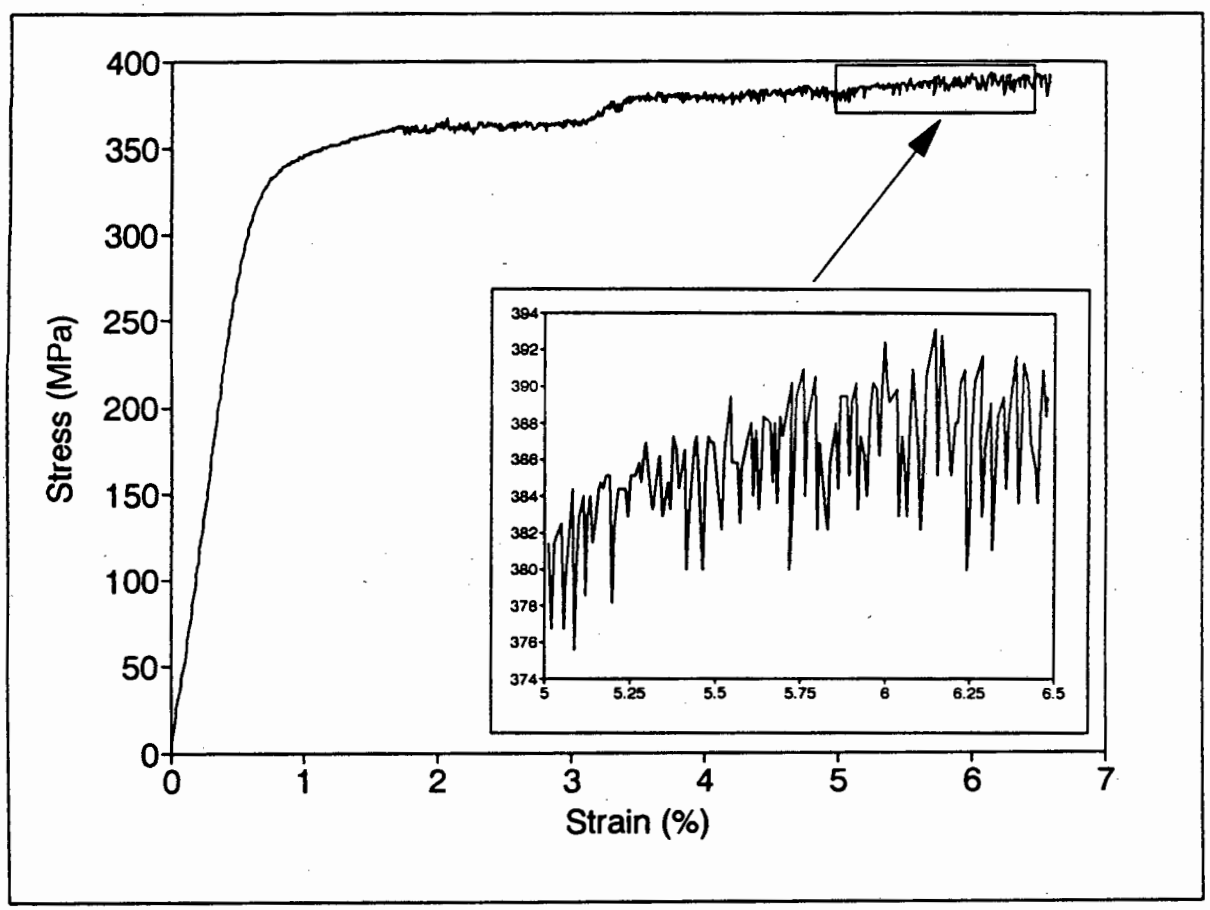

Figure 43: Tensile deformation record of 0.35 mm thick cold–rolled alloy 5182 sheet.

1. An initial region of deformation, ε_c, after the onset of plastic flow, containing irregular low stress amplitude ($\triangle\sigma_{max} \approx 2$ MPa) serrations. No deformation band formation was observed to occur during this period of plastic extension.

2. A plateau of plastic deformation, following ε_c, at approximately constant average stress with $\triangle\sigma \approx 2 \rightarrow 5$ MPa. This region of deformation corresponds to a Lüders type extension associated with the continuous propagation of a single set of discretely resolvable deformation bands from one end to the other of the specimen

gauge length.

3. Following the occurrence of the first stress plateau, a small region of work hardening was observed to occur. The region of work hardening was serrated, and followed by a second stress plateau of serrations. The second stress plateau is distinguished from the first by the occurrence of a steadily increasing $\triangle\sigma$ with increasing strain. $\triangle\sigma$ increased during this region from an initial value of ~5 MPa to ~12 MPa just prior to failure.

4. Deformation during the second stress plateau was observed to be accompanied by the regular repeated formation of deformation bands at apparently random locations in the specimen gauge length. The formation of these bands was consistently coincident with the emission of audible acoustic emission in the form of regular clicking sounds.

Following the tensile testing of purely cold–worked 0.35 mm thick material, two annealing heat treatments were carried out. The first involved heating the material at 300°C (30 mins, AC), simply to produce a recrystallised microstructure and the second was at 450°C (10 mins, WQ). The different times for the two heat treatments were utilised to produce recrystallised material with the same grain size. Both 300°C and 450°C heat treatments take the material into the single phase region of the binary Al–Mg phase diagram. The deformation record of 0.35 mm material, heat treated at 300°Cis presented in figure 44.

From figure 44 the following features can be noted:

1. Plastic deformation is achieved from the yield point via a serrated Lüders extension, the Lüders strain (ε_L).

2. Two definable regions of plastic extension follow the Lüders strain, the first being a small portion of rapid work hardening during serrated plastic flow.

3. The initial period of work hardening is followed by a less rapid and decreasing rate of stress increase with increasing strain (rate of work hardening).

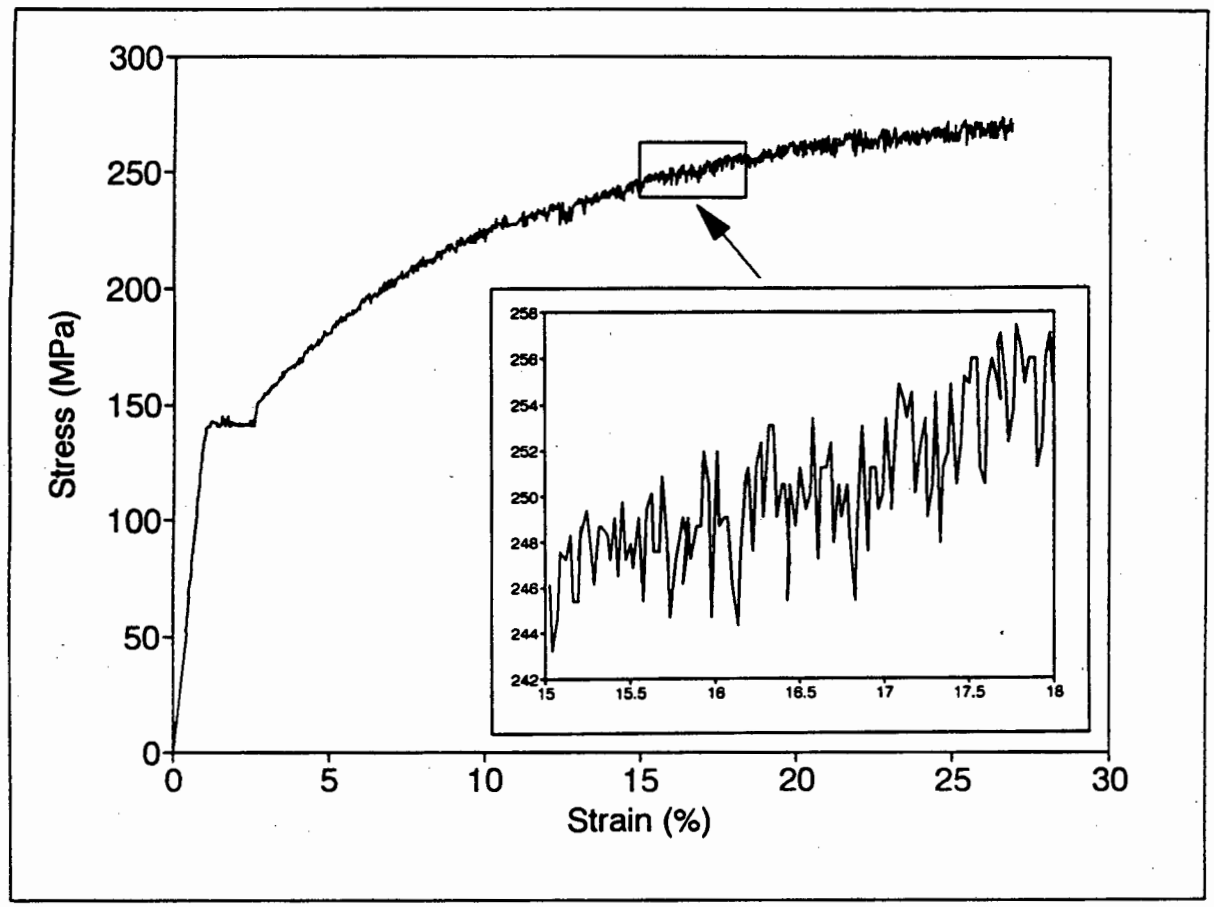

Figure 44: Tensile deformation record of 0.35 mm thick alloy 5182 material, annealed at 300°C (30 mins, AC).

4. The majority of the deformation i.e. all plastic extension beyond the Lüders strain is characterised by a steady increase in $\Delta\sigma$ until final fracture of the specimen. The value of $\Delta\sigma$ ranges from ~2 MPa to a maximum of ~10 MPa.

The deformation of the specimens was physically accomplished by inhomogenous deformation constituting both deformation band propagation (band front motion) and the apparently random occurrence of deformation bands in the gauge length. Yielding was initiated by the formation of type A surface deformation markings at the specimen shoulders. The formation of type A markings was observed to precede the Lüders extension, which in turn was accomplished by the propagation of deformation band fronts along the gauge length in the direction of tensile loading.

Band fronts propagating during ε_L were observed to always initiate at one end of the specimen gauge length directly adjacent to the type A surface markings. The single Lüders band front was observed to either propagate along the specimen gauge length, with its progression occasionally being interrupted or, alternatively, to be completely halted. Where the progression of the Lüders front was completely halted, this caused the initiation of a second band front propagating from the opposite end of the gauge length. The discontinuities in band front propagation corresponded to the serrations observed in the deformation record during the ε_L. On occasions, the second band front, which was propagating from the opposite end of the gauge length, was also halted, necessitating the secondary propagation of the initial band front. The process described in the preceding sentence was observed to occur more than once during some tensile tests, causing successively alternating propagation of the two mutually converging band fronts.

During the deformation of the specimen after ε_L, serrated flow was accomplished in the same manner as with the case of the cold–rolled specimen. Deformation bands continually appeared at random points on the gauge legit, occasionally propagating over sections of the gauge length, until fracture. The occurrence of audible acoustic emission was regularly heard to occur during the period of deformation from the ε_L until specimen fracture, coincident with deformation band formation. The acoustic emission occurred more readily in the recrystallised material at strain levels approaching fracture and coincident with the larger amplitude $\Delta\sigma$ serrations.

Annealing the 5182 at 450°C,[10] followed by water quenching was observed to produce a similar, but notably distinct, deformation record compared with the case of the same material treated at 300°C. An example of the stress–strain curve from 0.35 mm thick 5182 material, solution treated at 450°C, is presented in figure 45. It can be seen that the most notable distinction is the absence of a Lüders extension immediately after the yield point. Plastic deformation following the yield point was immediately discontinuous, with low amplitude serrations ($\triangle\sigma \approx 2$ MPa) of steadily increasing amplitude with increased accumulated strain ($\triangle\sigma_{max} \approx 8$ MPa).

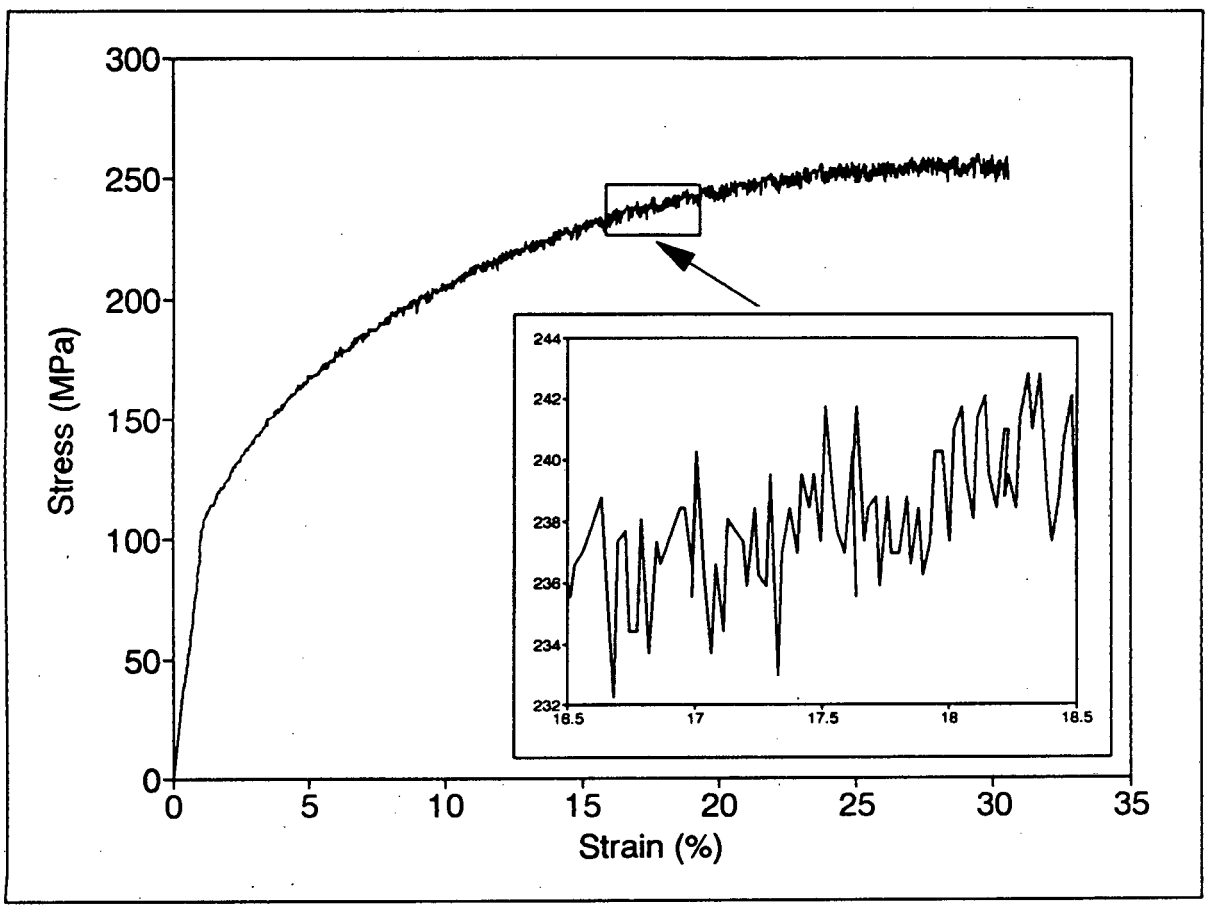

Figure 45: Tensile deformation record of alloy 5182, cold–rolled to 0.35 mm thickness and solution treated (450°C, 10 mins, WQ).

[10]10 minutes was selected to produce a similar grain size to the material annealed at 300°C. Essential features of the deformation were unaltered by annealing times of up to 2 hrs at 450°Cfollowed by a water quench.

The Effect of Specimen Geometry

0.35 mm thick cold–rolled alloy 5182 was consistently observed to deform with the formation and propagation of deformation bands. The deformation bands were oriented at ~60° to the tensile axis when examined on the broad (12.5 mm) specimen surface. The 60° angle corresponds with that commonly observed to occur in both Lüders and PLC band deformation during plane stress deformation [45, 211, 212]. The geometry of the 0.35 mm thickness specimen cross–section was rectangular, with a high ratio of width to thickness. ASTM B557M subsize specimens manufactured from 7.4 mm plate material were, however, observed to deform without any indication of macroscopic surface deformation features (bands) forming. The absence of band formation on the surface during tensile testing occurred in spite of profound serrated flow features evident in the deformation record.

Considering the distinction between the above two cases led to a systematic examination of the circumstances leading to deformation band formation in 5182. The approach taken was to compare both deformation records and surface deformation features evident during and after the deformation of various specimen geometries.

Tensile tests were carried out using specimens with either rectangular or circular cross–sections, either machined or stamped from plate material which had been sampled from various points in the cold–rolling schedule. In addition, some specimens were tested from strip material, without the conventional shoulders, to ascertain the effect of the specimen shoulders on band formation. The rationale for considering unshouldered specimens was based on the observation that type A (flamboyant) surface markings were consistently observed to precede the formation of type B (band) markings in the recrystallised 0.35 mm thick specimens. Type B markings apparently evolved directly from the type A markings formed at the specimen shoulders at the yield stress.

Three types of macroscopically visible deformation features occurred during the course of tensile testing the material sampled from various points in the rolling schedule, detailed as follows:

1. No band formation occurred, regardless of the specimen geometry. This situation

was typical for the 7.4 mm thick hot rolled material, where circular (4 mm diameter), square (6×6 mm^2) and rectangular (6×3 mm^2) cross–section specimens produced virtually identical deformation records. An example of the deformation record from hot–rolled 5182 (7.4 mm) material (6×6 mm^2) is shown in figure 46. Serrated flow occurred throughout the test from the yield point until the strain to fracture was reached. From figure 46, it can be seen that regular small serrations were interspersed with groups of larger amplitude yield drops. Serration amplitude was variable with $\Delta\sigma_{max} \approx 10$ MPa and a consistent amplitude of 3 $\rightarrow$ 6 MPa prior to fracture.

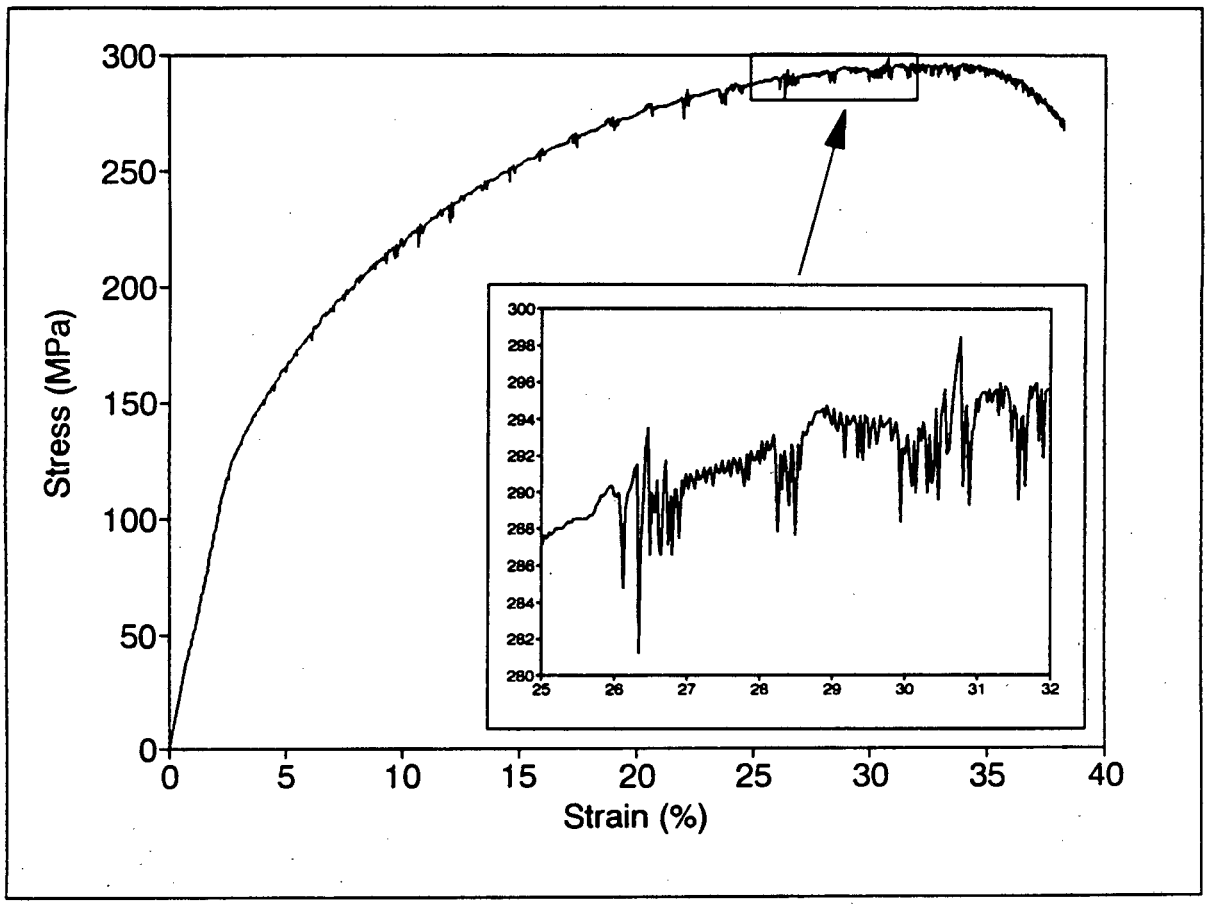

Figure 46: Tensile deformation record of 7.4 mm thick hot–rolled alloy 5182 (6×6 mm^2 cross–section).

2. Band formation occurred at 60° to the tensile axis on the broad face of the rectangular cross–section specimens. The specific cases where 60° band formation occurred were in the 0.35 mm thick cold–rolled and recrystallised material (12.5×0.35 mm^2

cross–section) and 1 mm thick cold–rolled material (6×1 mm^2 cross-section) as well as recrystallised 1 and 2 mm thick cold–rolled material (6×1 and 6×2 mm^2 cross–sections).

3. Band formation occurred at 90° to the tensile axis on the broad specimen face of rectangular cross–section specimens. This occurred in 2 mm and 3 mm thick cold–rolled material (2×6 mm^2 and 3×6 mm^2 cross-sections) as well as 3 mm thick recrystallised material.

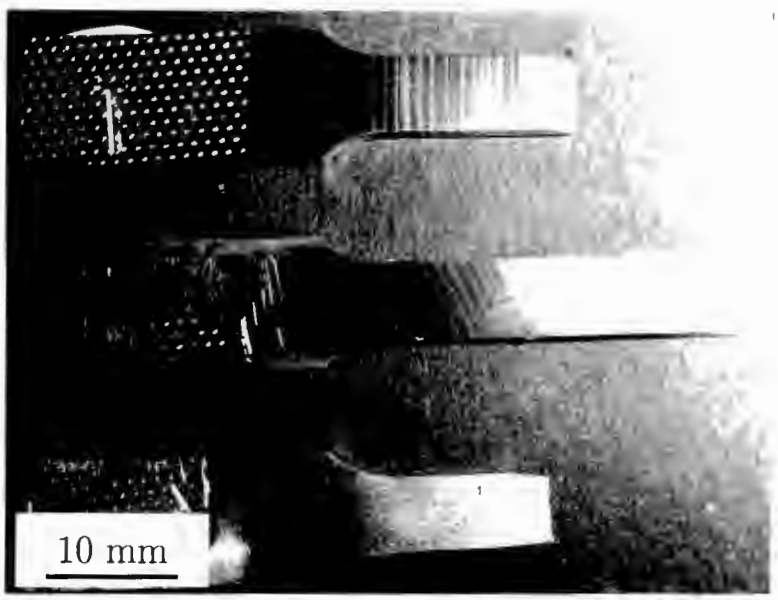

Figure 47: Optical micrograph showing the three types of macroscopically observable surface deformation on alloy 5182 specimens, i.e no band formation or bands oriented at either 90° or 60° to the tensile axis.

An illustration of the three types of macroscopically observable surface deformation is shown in figure 47. A unique situation occurred in the case of 1 mm thick cold–rolled material, in that a mixed mode of inhomogeneity was observed, where bands were oriented at both 60° and 90° to the tensile axis on the same specimen.

In the case of strip specimens, without shoulders at the end of the gauge length, no distinction was observed in the band types which occurred, when these were compared to conventional shouldered tensile specimens. The band orientation was, therefore, a function of the shape of the cross–sectional geometry as well as the microstructural condition of the material, but was not significantly affected by the existence of shoulders at the gauge length ends.

In order to directly assess the effect of specimen geometry on the tensile deformation characteristics, under conditions where ready formation of deformation bands occurred, 3.1 mm thick material was tested with various specimen cross–sections. Material was machined into 3.0 mm, 2.0 mm and 1.0 mm thickness ASTM B557M subsize specimens, as well as circular section specimens with a diameter of 2.8 mm. Cold–rolled material was tested as well as material subsequently annealed at 300°C (30 mins, WQ). The tensile test properties are summarised in table 5.

Table 5: Summary of the tensile test data from 5182, cold–rolled to 3.1 mm, and then machined to various cross–section shapes. (UTS and $\triangle\sigma$ measured in MPa.)

	Cold Rolled (CR)			CR and Recrystallised		
X–section	UTS	$\triangle\sigma_{max} \approx$	% El.	UTS	$\triangle\sigma_{max} \approx$	% El.
3×6 mm^2	394.7	7	6.5	300.0	11	30
2×6 mm^2	411.8	5	8.3	277.9	11	21
1×6 mm^2	397.0	17	6.2	256.2	12	17.5
ϕ=2.8 mm	380.4	5	9.6	290.0	10	24

In the case of the cold worked material, only the 1 mm thick rectangular section specimens exhibited obvious macroscopic band formation at 60° to the tensile axis on the broad specimen face. Some light contrast band formation at 90° to the tensile axis occurred on the surfaces of the 3 mm and 2 mm thick specimens. Fracture, in all cases, was by 45° shear failure through the specimen thickness, except for the 1 mm thick specimens. 1 mm thick specimens were observed to fail by a combined fracture influenced by both 60° and 90° bands, in that sections of the fracture surface were oriented at both 60° and 90° to the tensile axis.

Recrystallised material deformed similarly to the purely cold worked material, with clear band formation only visible on the surface of the 1 mm thick specimen. Both variants[11] of the 60° bands were clearly visible on specimen surface with eventual fracture, by tensile overload, parallel to the band orientation. All other cases, including the circular section specimen, failed by 45° shear through the specimen thickness. No band formation

[11]Band formation at 60° to the tensile axis may have two possible variants i.e at + or - 60° to the tensile axis when examined on the broad specimen surface.

was observed to occur on the surface of the circular section specimen tested either before or after recrystallisation.

The Effect of Cold Rolling Deformation

The development of serrated flow during a tensile test, concurrent with the accumulation of plastic strain, prompted an investigation into the effect of prior cold–rolling on serrated flow properties. Material was sampled from various points in the commercial cold–rolling reduction sequence.[12] Plate material, hot rolled to 7.4 mm, as well as that subsequently cold–rolled to 4.5 mm, 3.1 mm, 2.0 mm and 1.0 mm thicknesses was used to manufacture the tensile specimens. Subsize ASTM B557M specimens, standardised to 3 mm thickness, were machined from the plate, except in the case of 2 mm and 1 mm thick material where specimen thickness corresponded to the plate thickness. Material of thickness 7.4 mm, 4.5 mm and 3.1 mm was sampled directly from the commercial cold–rolling sequence, whereas 2 mm and 1 mm thick material was produced by laboratory rolling 3.1 mm thick material down to 2 mm and 1 mm thicknesses. The effect of cold–rolling the 3.1 mm thick material to 2 mm and 1 mm thicknesses, was to produce a continuous cold–rolling sequence without the commercially applied interanneal at 3.1 mm material thickness.

A summary of the results of tensile testing is produced in table 6 for both cold–rolled material and material which was cold–rolled with a subsequent recrystallisation anneal (300°C, 30 mins, WQ).

In the first set of tests, i.e. material continuously cold–rolled from 7.4 mm $\rightarrow$ 1.0 mm, pertinent features of the deformation can be summarised as follows:

1. Macroscopically visible surface deformation features consisted of surface roughening and dulling in all cases, except for the of 1 mm thick cold–rolled material.

2. Very low contrast deformation band markings were visible on the surfaces of 3.1 mm and 2 mm thick cold–rolled material at 45° to the tensile axis on the broad specimen

[12]The rolling reduction sequences referred to in this section have been detailed section 3.2.3, page 69

Table 6: Summary of mechanical testing data from 5182, cold–rolled to various thicknesses, and then tested either before or after annealing. (UTS and $\triangle\sigma$ measured in MPa.)

	Cold Rolled (CR)			CR and Recrystallised	
Thickness	H_{V20}	UTS	$\triangle\sigma_{max} \approx$	UTS	$\triangle\sigma_{max} \approx$
7.4 mm	75	292.4	7	272.4	7
4.5 mm	104	308.8	6	295.2	9
3.1 mm	110	394.7	/	300.0	11
2.0 mm	124	411.8	4	303.2	15
1.0 mm	131	472.1	20	317.8	17

face. Distinct band markings, oriented at 60° to the tensile axis were visible on the surface of material cold–rolled to 1 mm thickness.

3. Fracture in all cases was by ductile shear at 45° to the tensile axis through the specimen thickness. The edge of the fracture surface was, therefore, at 90° to the tensile axis when the broad specimen face was viewed.

Material, which had been annealed at 300°C prior to tensile deformation, exhibited some distinctly different features to the cold–rolled material:

1. In the case of 7.4 mm thickness material, some surface dulling resulting from tensile deformation occurred prior to plastic instability and 45° tensile overload shear fracture.

2. The 4.5 mm thick material showed similar behaviour to the above case, but was distinguished by the formation of 2 → 5 shear bands in the vicinity of the eventual fracture, prior to specimen failure. Minimal plastic instability occurred prior to failure and the final fracture was directly in one of the shear bands.

3. The 3.1 mm thick material exhibited indistinct deformation bands throughout the deformation, oriented at 45° to the tensile axis when examined on the broad specimen face. Final fracture was not along one of the bands, however, but rather at 45° through the specimen thickness as for 7.4 and 4.5 mm material.

4. The 2 mm thick material exhibited deformation bands oriented at both 45° and 60° to the tensile axis on the broad specimen surface. Final fracture was at 45° through the specimen thickness, and at 90° to the tensile axis when viewed on the broad specimen surface. The fracture surface was notably more macroscopically smooth than for the 7.4 mm thickness material.

5. Finally, in the 1 mm thick material plastic deformation was dominated by the formation of 60° deformation bands, with some evidence of 90° bands having formed. Final fracture was again the same as the preceding cases, i.e. at 45° through the specimen thickness.

In summary, therefore, both specimen geometry effects and prior cold–rolling deformation influence both the band orientation during tensile testing and the final fracture surface orientation. The mode of failure can generally be described as shear influenced tensile overload, regardless of whether the material had been annealed prior to tensile testing. The shear component influence was observed to dominate over direct tensile overload for higher values of prior cold–rolling deformation, indicated by the macroscopically more smooth fracture surface. A clear increase in the value of $\Delta\sigma_{max}$ was observed to occur in the annealed material, as the amount of cold–rolling deformation prior to heat treatment was increased. This increase in $\Delta\sigma_{max}$ was less evident, although still apparent in the case of material which was simply in the cold–rolled condition.

The Effect of Grain Size

Following from the known effects[13] of grain size on ε_L, $\Delta\sigma$ and the occurrence of surface deformation markings, an attempt was made to study the effect of grain size on serrated flow related deformation characteristics. The approach entailed solution treating the material, at temperatures sufficient to cause grain growth (450°C), for a range of times.

Grain growth stabilisation is, however, achieved in 5182 by the addition of Mn, which results in a fine dispersion of $FeMnAl_6$ particles [134]. Long annealing periods at 450°C,

[13]The reader is referred to section 2.4.1, page 19 for a discussion of the effects of grain size on serrated flow and associated surface markings.

therefore produced a dramatically uneven grain size distribution as a result of "abnormal" grain growth or secondary recrystallisation [213]. The net effect of the $FeMnAl_6$ particles was to generally pin grain boundaries, but some grains were observed to grow to significantly larger sizes than the average. Single large grains were observed to occur with diameters orders of magnitude larger than in the majority of the material. An illustration of a specimen with an etched surface, which had been subjected to a long period at 450°C is illustrated in figure 48.

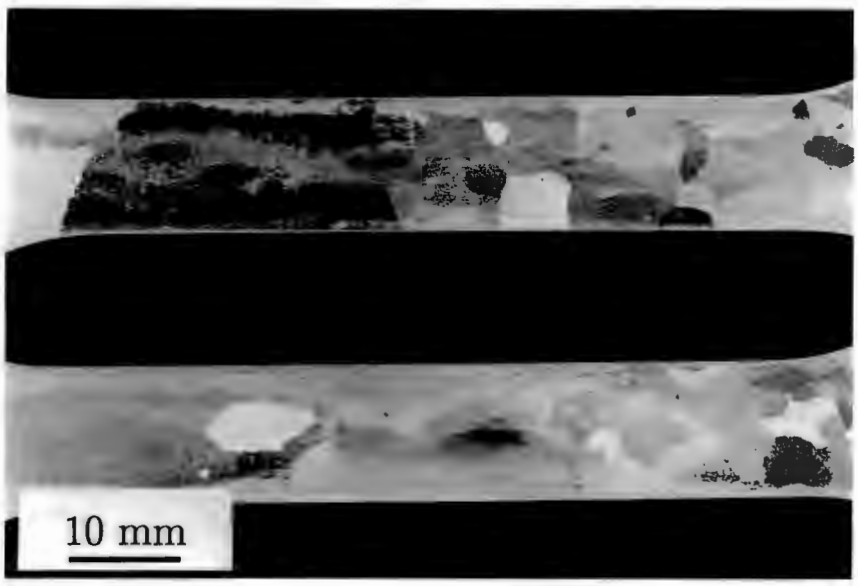

Figure 48: The effect of annealing for 10 hrs at 450°C on the grain size and distribution in an alloy 5182, 0.35 mm thick specimen.

Although a systematically varying range of grain sizes was not achieved, some comment on the effect of increased grain size can be made. A continuous change in the serrated flow properties occurred in conjunction with the increased annealing periods, from $1 \rightarrow 24$ hrs. In all cases, instabilities in the flow stress were evident from the onset of plastic deformation until specimen failure. An initial ε_L was not present in the larger grained material, nor were type A markings apparent on the specimen surface. Type B markings (deformation bands) were, however, observed to persist after longer annealing times than those required for the disappearance of type A markings.

For the very long annealing times (24 hrs), impingement of the "abnormal" grains was observed to occur resulting in a relatively uniform large grain size. The result of deforming this large grained material was to produce continuous low amplitude stress instabilities

which did not alter significantly with the accumulation of plastic strain.

In summary, therefore, three cases occurred. Either the material had a uniform small grain size, or a very large variation in grain size, or a relatively uniform large grain size. Some "orange–peel" type surface roughening, corresponding to deformation differences between individual grains, was observed in the second case. In addition, material with non–uniform grain size showed some indistinct surface banding, probably corresponding to deformation in regions of the gauge length comprised of smaller grains. The range of grain sizes is observed is evident in figure 48.

4.5.2 Surface Deformation Observations

As is apparent from the preceding sections, macroscopically visible surface deformation can be divided into three possible classes. Firstly, the formation of type A (flamboyant) marking can occur at the specimen shoulders immediately after yielding. Secondly, the formation of deformation bands (Lüders or PLC) bands can occur, subsequent to the formation of type A markings or alternatively without their prior formation. Finally, in the absence of type A or B deformation markings the surface was characterised by dulling apparently associated with the independent deformation of individual grains, forming a so called "orange peel" effect. It is important to emphasise, however, that all three of the above cases occurred in conjunction with serrated plastic flow.

The three situations outlined above, have been illustrated in figure 47. In the cases where the pre-deformation condition of the material was conducive to band formation, two dominant situations developed, directly dependent on the particular specimen geometry.

1. Where the specimen width substantially exceeded the thickness, as in the case of the full–size ASTM B557M specimens, band formation regularly occurred at 60° to the tensile axis on the broad specimen surface.

2. Where the specimen width was of a similar dimension to the specimen thickness, band formation regularly occurred at 90° to the tensile axis, observed on the broad specimen surface.

Imaging of the specimen surface, in the cases where band formation occurred, was more easily achieved using Normarski interference optical microscopy as opposed to SEM. A typical band front propagating into undeformed material during the Lüders extension is illustrated in figure 49. The continuity of a polishing scratch across the band front from deformed to undeformed material serves to illustrate the lack of shear associated with the 60° band formation.

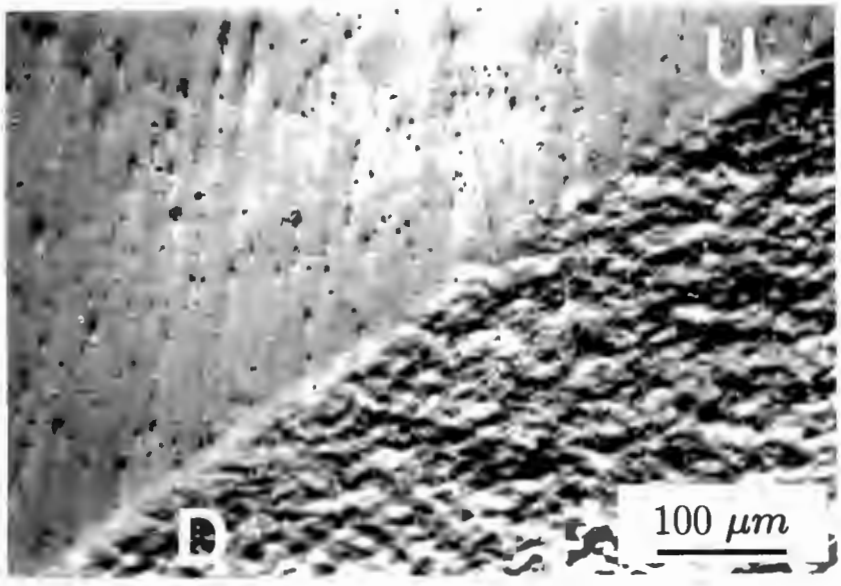

Figure 49: Optical micrograph (Normarski interference contrast) illustrating the surface features associated with the propagation of a Lüders band from deformed (D) into undeformed (U) material.

4.5.3 Microstructural Observations (CTEM)

Microstructures most extensively examined by CTEM were from the 0.35 mm thick cold-rolled material after annealing (300°C, 30 mins, AC) and deformation in tension to a range of strain levels. The reason for examining 0.35 mm thick material in the recrystallised condition was firstly because of the low initial dislocation density and secondly because of the relative simplicity of locating specific deformed regions in the gauge length and then spark machining TEM discs from such an area. The microstructure of the cold worked material, illustrated in figure 50, consisted of a very high density of dislocation tangles and contained no evidence of dynamic recovery processes. Tensile deformation of this material resulted in microstructures which were indistinguishable from the starting

structure. The aim of recrystallisation was therefore to produce a low dislocation density, from which point tensile deformation associated microstructural evolution would be simpler to monitor.

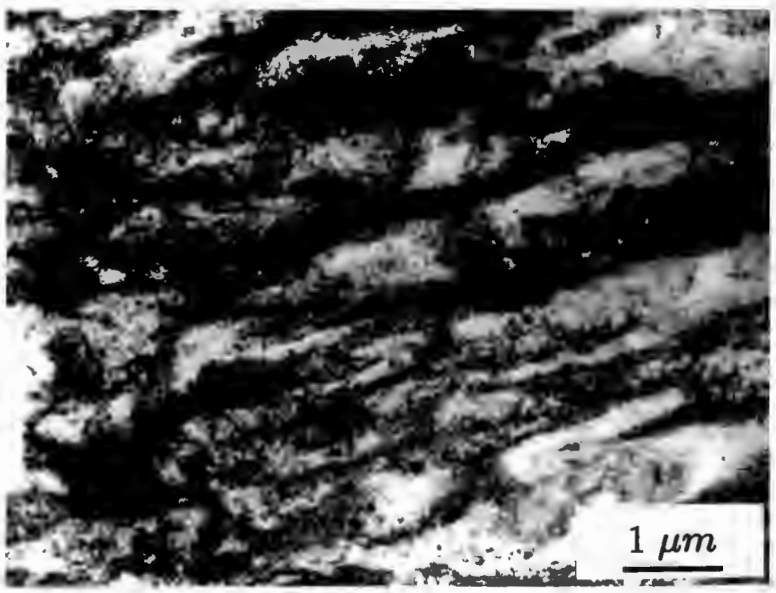

Figure 50: Bright–field TEM micrograph illustrating the cold worked microstructure of alloy 5182 (0.35 mm thick sheet), characterised by dense dislocation clusters with no evidence of dynamic recovery.

The microstructure of alloy 5182 0.35 mm thick material, after annealing (300°C, 30 mins, AC) is illustrated in figure 51, and can be seen to be characterised by an extremely low dislocation density amongst a distribution of inclusion particles (eg. $FeMnAl_6$). Grain boundaries were generally observed to be "clean" except for occasional intersections with inclusions.

The pre–deformation microstructure of 0.35 mm thick material annealed at 300°C (1/2hr, 30 mins, AC) can be directly compared to that from the same material, *waterquenched* from 450°C, as shown in figure 52. The microstructure in figure 52 consists of a significantly higher density of dislocations, associated with the quench from high temperature.

A comparison of the tensile deformation properties of material with the pre–deformation microstructures illustrated in figures 51 and 52 can be made by considering the deformation records in section 4.5.1. Figures 44 (page 108) and 45 (page 110) show the test records of material air cooled from 300°C and water quenched from 450°C respectively.

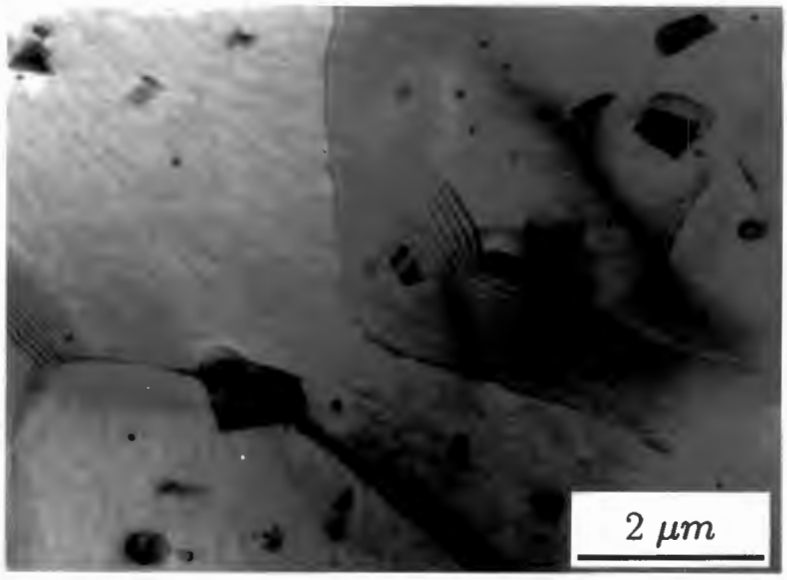

Figure 51: Bright–field micrograph of annealed (300°C, 1/2 hr, AC) 0.35 mm thick alloy 5182, illustrating the low dislocation density, precipitate free grain boundaries and the inclusion particle distribution.

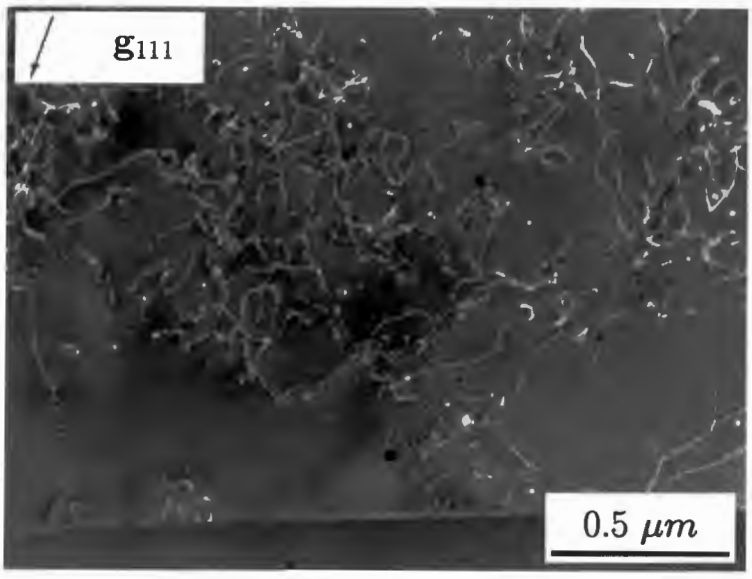

Figure 52: Weak–beam TEM micrograph illustrating the microstructure of annealed (450°C, 10 mins, WQ) 0.35 mm thick alloy 5182 sheet. The micrograph illustrates a significantly higher dislocation density in the material when compared to the same alloy annealed at 300°C.

Tensile deformation of material annealed at 300°C produced, firstly, type A deformation markings at the specimen shoulders. Secondly, this was followed by the single passage of a Lüders band and finally by the appearance, at random points in the gauge length, of single PLC bands. 3 mm diameter TEM discs were spark machined from the gauge lengths of specimens, deformed to the strain levels required to produce the sequence of macroscopically observable features described above. The results of TEM examination of the microstructural development are summarised below:

1. TEM foils machined directly from regions where the formation of type A deformation markings had appeared on the specimen surface displayed a dramatic increase in dislocation density. A micrograph illustrating the change is shown in figure 53. The dislocation activity was dominated by parallel dislocations, consistent with the predominant activation of a single slip system, although distinct planar arrays were not observed.

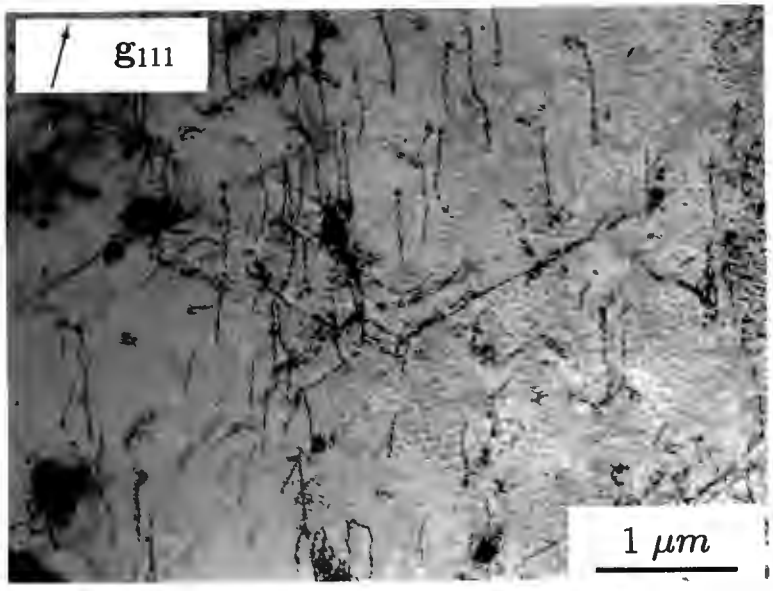

Figure 53: Bright–field TEM micrograph illustrating the increase in dislocation density associated with the formation of type A surface markings.

2. Further deformation produced the passage of a Lüders band and foils cut from this region revealed microstructures equivalent to those cut from the specimen shoulder regions displaying macroscopic type A markings. The microstructure associated with the passage of a Lüders band in the direction of the tensile axis is shown

in figure 54. A noteworthy feature in both of the above cases was the increased density of dislocations in the vicinity of inclusion particles, suggesting the role of the particle/matrix interface as a dislocation source. An illustration of the apparent operation of such a source is illustrated in figure 55.

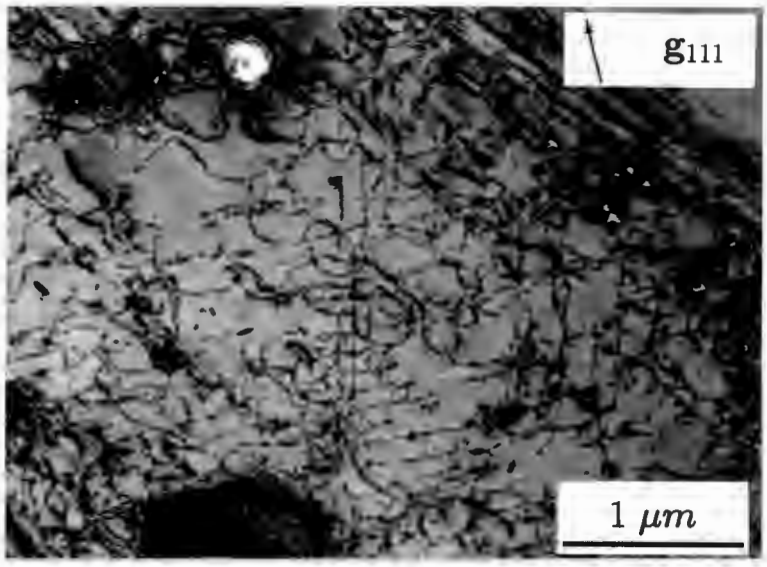

Figure 54: Bright–field TEM micrograph illustrating the microstructure associated with the passage of a single Lüders band front along the gauge length of an annealed 0.35 mm thick alloy 5182 specimen.

3. An interesting feature of the microstructural evolution was revealed by examining TEM foils taken from ahead of a propagating Lüders front or from between two converging Lüders band fronts. Pre–macro yield features consisted of planar dislocation arrays eminating from triple point junctions or grain boundaries, prior to the more dramatic yield events associated with macroscopically observable deformation features. Two such arrays are illustrated in figures 56 and 57.

4. Deformation microstructures produced after the passage of the initial Lüders front were characterised by a continuous rapid increase in dislocation density. The micrograph in figure 58 shows the dislocation configuration from a tensile specimen after $\sim 10\%$ total tensile strain. Dislocation accumulation, with no indication of dynamic recovery associated cell formation, occurred until final fracture of the specimen. The microstructure at fracture closely resembled that produced by rolling deformation as illustrated in figure 50, page 121. No obvious inhomogeneities in the microstructure were observed to occur, in spite of extensive examination for the formation of

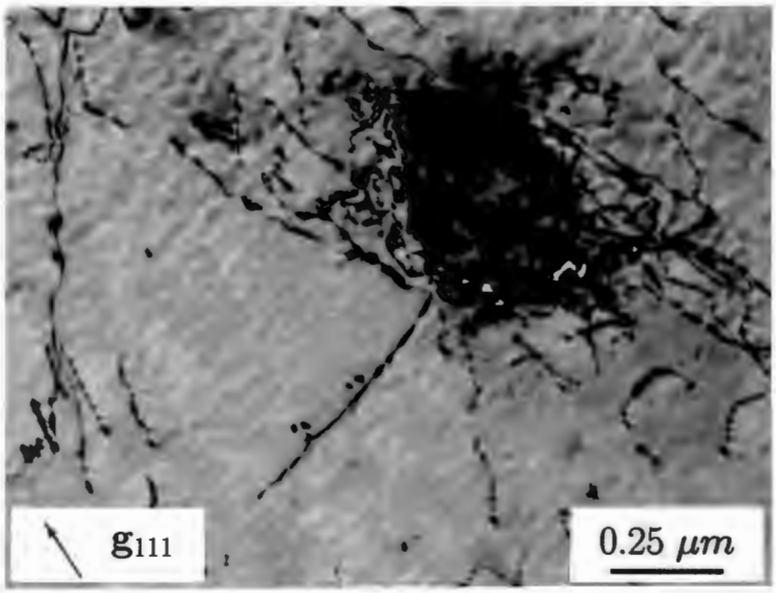

Figure 55: Bright–field TEM micrograph illustrating the apparent operation of an inclusion particle/matrix interface dislocation source associated with the formation of type A surface markings and the passage of a Lüders band front.

Figure 56: Bright–field TEM micrograph collage illustrating the emission of a planar dislocation array from a triple point junction. The foil was machined from a specimen where deformation was interrupted prior to macroscopic yielding in the gauge length.

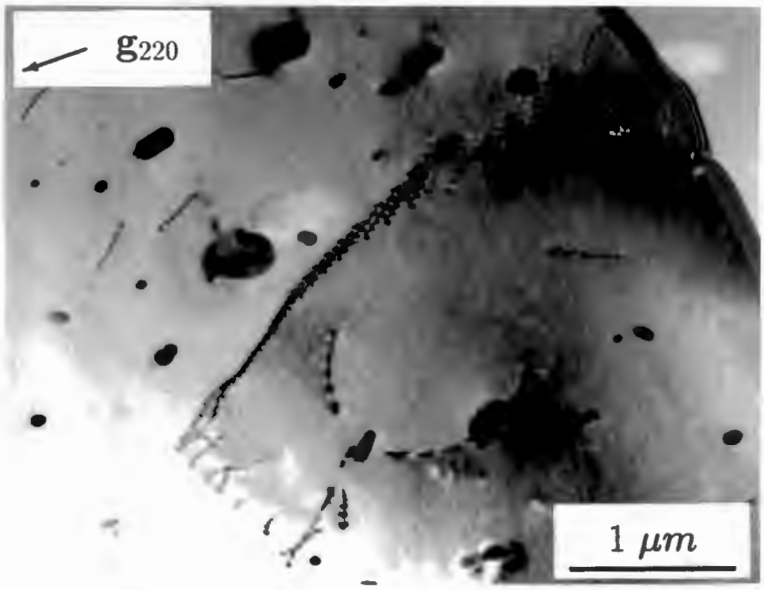

Figure 57: Bright–field TEM micrograph illustrating the emission of a planar dislocation array from a grain boundary, prior to macroscopic yielding in the region of the specimen from which the micrograph was taken.

microbands.

4.5.4 Microstructural Evolution (HVEM)

During in–situ deformation in the HVEM, the alloys containing Mg, VF615 (2at.%Mg) and 5182 (~5at.%Mg), exhibited deformation characteristics which had both similarities to and distinct differences from the other alloys tested. In–situ deformation of 0.35 mm thick alloy 5182, immediately after solution treatment (400°C) and water quenching was characterised as follows:

1. As in the case of 1070, deformation from the initial yield point was typified by sudden yield events and the rapid formation of slip traces in the surface oxide film, caused by the movement of multiple dislocations.

2. The source of yielding described above, was generally either at triple point grain boundary intersections or the grain boundaries themselves. Occasionally, the relatively slow movement of isolated dislocations preceded the more dramatic yield

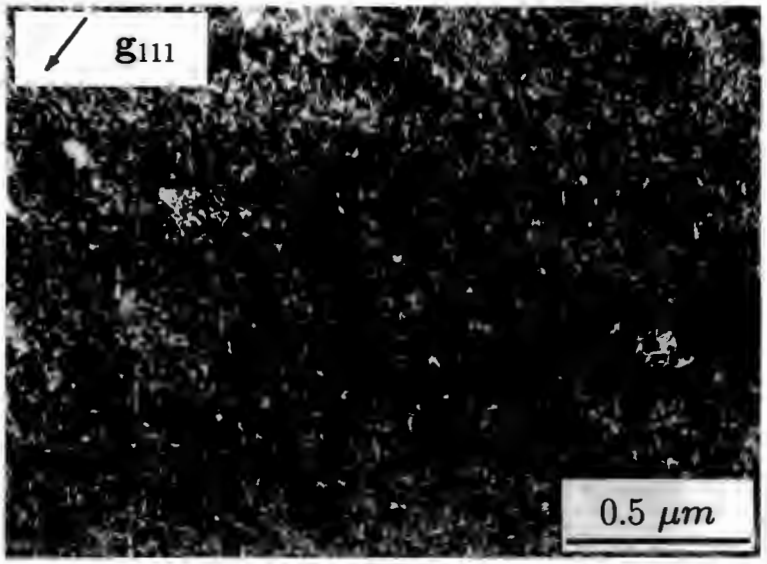

Figure 58: Weak–beam TEM micrograph showing the dislocation configuration from an annealed 0.35 mm thick alloy 5182 specimen deformed to ~10% total tensile strain. Deformation was accomplished by the formation and propagation of macroscopic deformation bands.

events. The origin of slip traces, emanating from a grain boundary source is illustrated in figure 59.

3. Yield events generally comprised the rapid formation of a series of coplanar slip traces, corresponding to the motion of dislocations which were not necessarily on the slip plane being currently imaged. As in the case of CTEM foils examined from bulk specimens previously deformed in tension, concentration of dislocations was observed to occur in the vicinity of inclusion particles and some initiation of slip was observed to occur at these locations. The micrograph in figure 60 illustrates the localised slip trace formation as well as the higher density of dislocation tangling in the vicinity of inclusion particles.

The microstructure of alloy 5182 produced by in–situ deformation in the HVEM could be favourably compared to that produced by the deformation of bulk specimens and subsequently examined in the CTEM (see eg. figure 54). An example of the dislocation configuration produced in–situ in the HVEM, and characterised by parallel dislocations, is shown in figure 61.

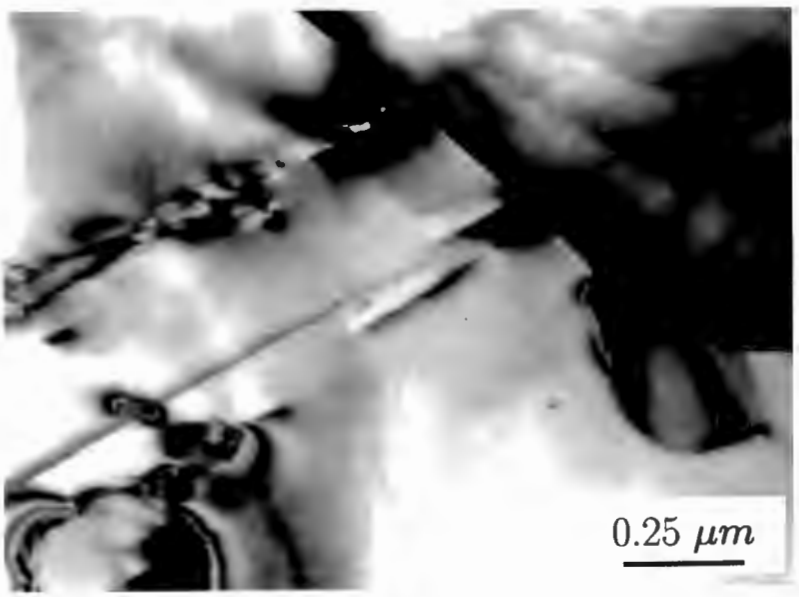

Figure 59: Bright–field HVEM micrograph illustrating initial yielding in alloy 5182, showing planar slip traces originating from a grain boundary dislocation source.

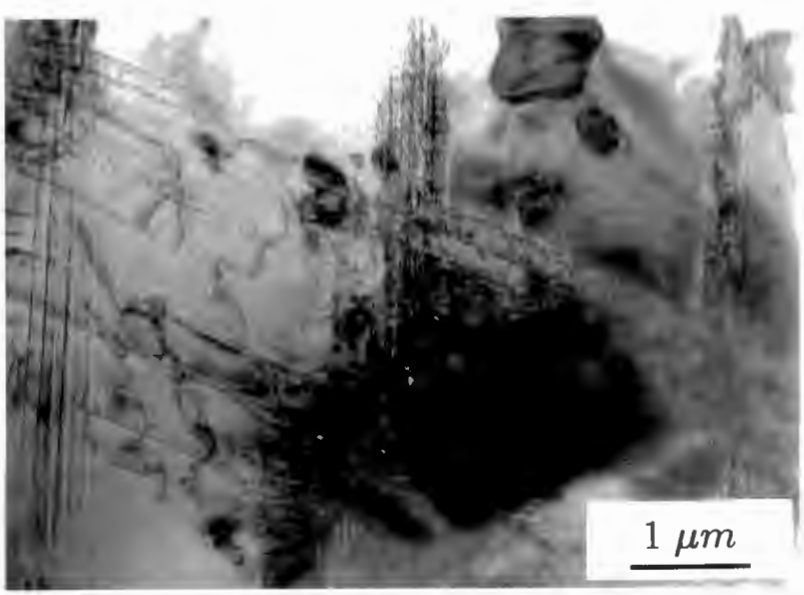

Figure 60: Bright–field HVEM micrograph illustrating localised concentration of slip, as well as the higher density of dislocation tangling in the vicinity of inclusion particles in alloy 5182.

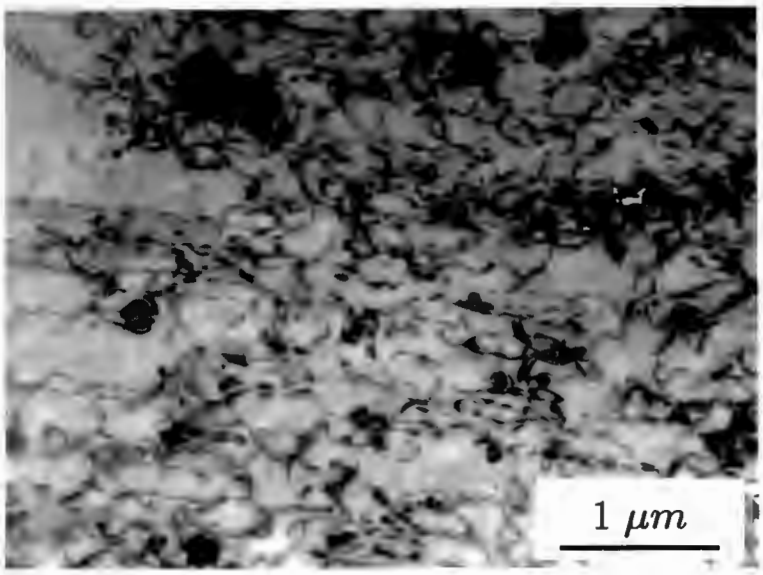

Figure 61: The microstructure of alloy 5182, resulting from rapid yielding during in–situ deformation in the HVEM. This microstructure can be favourably compared to the dislocation configurations, observed in the CTEM, produced by deformation of standard tensile specimens.

Transfer of slip between grains was frequently observed to initiate at the point of dislocation pile–up impingement with the grain boundary of the initially deforming grain. Emphasis must be placed on the rapidity and suddenness of the yield events which comprised the mass collective motion of multiple dislocations. Very little evidence of slower, viscous motion of dislocations was observed to occur, although, such viscous motion occasionally preceded the sudden, collective events. Two sequential images reproduced from video tape are shown in figures 62 and 63, which serve to indicate the rapidity and suddenness of such events. The time delay between the two images is less than 1 second.

The major difference between the Mg containing alloys and the others tested, was in the extent to which deformation was dominated by a single active slip system. All the alloys deformed in–situ in the HVEM displayed rapid, sequential and discontinuous yielding on a microstructural level, but the degree of cross slip and the number of concurrently active slip systems was markedly varied. In the case of VF615 (Mg) and 5182, yield events were largely confined to a single set of parallel slip traces, with minimal, if any, cross slip occurring. Corresponding yield events in 1070 and alloys VF617 (Zn) and VF619 (Ag) comprised of multiple intersecting and concurrently active slip traces, with extensive cross–slip evident. Higher strain deformation in the alloys containing Mg was

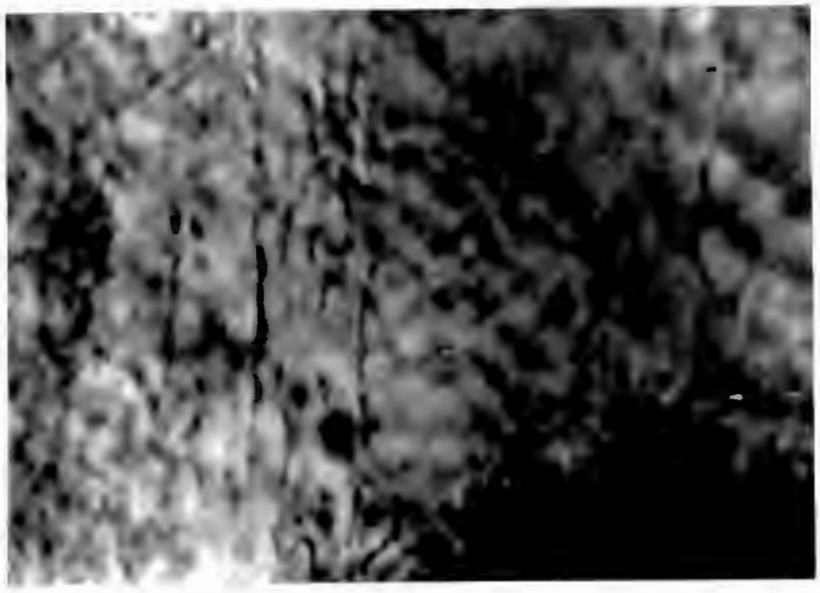

Figure 62: Video tape image illustrating a partially yielded portion of a grain in solution treated and water quenched alloy 5182.

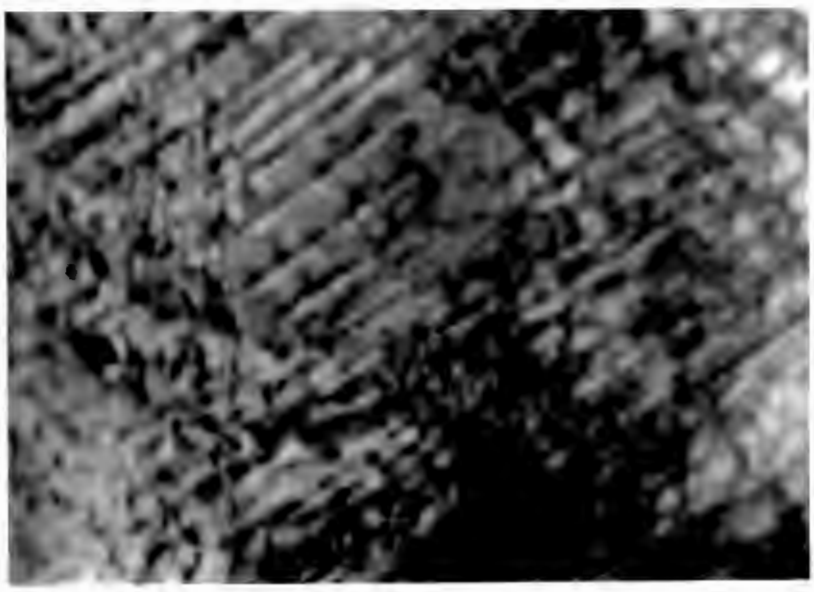

Figure 63: The same region as that shown in the preceding micrograph, with less than one second time delay between micrographs, showing the sudden formation of multiple coplanar slip traces.

similar to the initial yield events i.e. accomplished by the regular formation of coplanar slip traces superimposed on the existing deformation microstructure.

4.5.5 Fracture

As suggested previously, specimen fracture was strongly influenced by the geometry of the specimen being tested. Fracture, in all cases, except where deformation was accomplished by the formation of bands at 60° to the tensile axis, was by tensile overload in conjunction with 45° shear through the specimen thickness. Shear bands were regularly observed to form in the vicinity of the eventual fracture, immediately prior to failure, even in cases where the majority of deformation was not accompanied by macroscopically observable band formation. Shear band formation prior to failure was not, however, a prerequisite for the ultimate failure to be shear influenced.

An example of a fracture surface formed by rapid ductile shear is illustrated in the SEM micrograph presented in figure 64. Figure 64 was taken from the fracture surface of a 2 mm diameter circular cross–section specimen machined from 3 mm cold–rolled 5182. The material was solution treated and water quenched prior to tensile testing and the fracture surface was macroscopically smooth in appearance. The surface can be seen to be characterised by relatively small ductile dimples, slightly elongated in the (vertical) direction of shear. Such regions of ductile dimpling were often interspersed with smoother regions, as well as larger coalesced voids. The smoother regions consisted of detail made up of approximately parallel striation type markings.

In the cases where deformation was accomplished by the formation and propagation of deformation bands, specimen failure was always through such a band. Where the ratio of specimen width to the thickness was high and band formation occurred at an angle of 60° to the tensile axis, eventual fracture was always by direct ductile tensile overload (not accompanied by shear). 60° band formation occurs via the sequential formation of localised necks [72] through the specimen thickness, and fracture of the specimens was observed to occur in the same way. Although the fracture surface of such specimens was characterised by features associated with ductile, tensile overload, minimal plastic instability preceded the fracture. The situation was rather one of sudden ductile failure

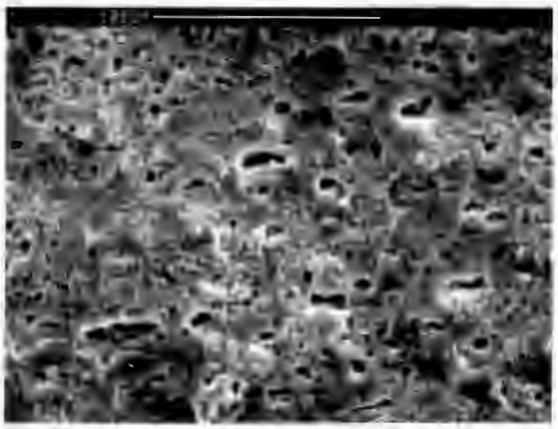

Figure 64: SEM micrograph illustrating the shear fracture of an alloy 5182 circular cross–section specimen machined from 3 mm thick, cold–rolled and annealed material.

through an active deformation band.

4.5.6 Comment

The plastic deformation of 5182 at the strain rates tested was dominated by inhomogeneities of deformation. The preceding section highlights various aspects of this deformation, including the existence of type A and B surface markings, the occurrence and orientation of Lüders and PLC bands and their relationship with the specimen cross–section, as well as the some indication of the influence of grain size.

A clear distinction was observed between the microscale deformation inhomogeneities exhibited by 5182 in comparison to 1070 during HVEM in–situ deformation experiments. Finally, the failure mode and fracture surface orientation of tensile specimens was observed to directly correlate with the deformation characteristics during the course of any single tensile test.

4.6 Commercial Al–Mg–Si (6061)

6061 is commercial ternary Al–Mg–Si alloy, known to exhibit room temperature serrated flow, as discussed in Chapter 2. It is precipitation hardenable by the formation of β',

which allows for substantial strengthening but effectively denudes the matrix of Mg. The equilibrium precipitate β (Mg_2Si) develops directly from β'. 6061 is also a matrix alloy employed in the manufacture of metal matrix composite material.

4.6.1 Tensile Test Results

6061 tested during the course of this work was machined into subsize ASTM B557M specimens, surface polished and then tensile tested. The billet of material received from HULAMIN was in the T6 (peak aged)[14] condition, which necessitated a subsequent solution treatment to redissolve the precipitates. Two microstructural conditions were therefore tested, firstly the peak aged (T6, as received) and secondly the solution treated condition (520°C, 1hr, WQ). The results of testing in both the solution treated and T6 conditions are shown in figures 65 and 66.

From figure 65, it can be seen that the T6 material showed a well defined yield point followed by plastic extension with a low work hardening rate. The post yield extension consisted of serrations of amplitude $\triangle\sigma \approx 0.3$ MPa occurring from approximately $3\% \rightarrow 7.5\%$ strain.

Solution treatment (520°C, 1 hr, WQ) can be clearly seen (figure 66) to have substantially enhanced the serrated flow exhibited by the material. The deformation characteristics were comparable to those exhibited by the hot rolled 5182 (see section 4.5.1). Plastic deformation could be divided into three regions during the course of a single test:

1. Small continuous low amplitude serrations beginning at ~0.7% strain and continuing to ~3.5% strain.
2. From ~3.5% strain to ~7.5% strain, the deformation was characterised by a series of approximately constant stress plateaus at successively higher values of stress. Between the plateau regions were small regions of rapid work hardening.
3. Finally, deformation continued until the onset of localised necking, with continuous

[14]The reader is referred to section 2.5.2, page 34 for a list of commercial heat treatment designations.

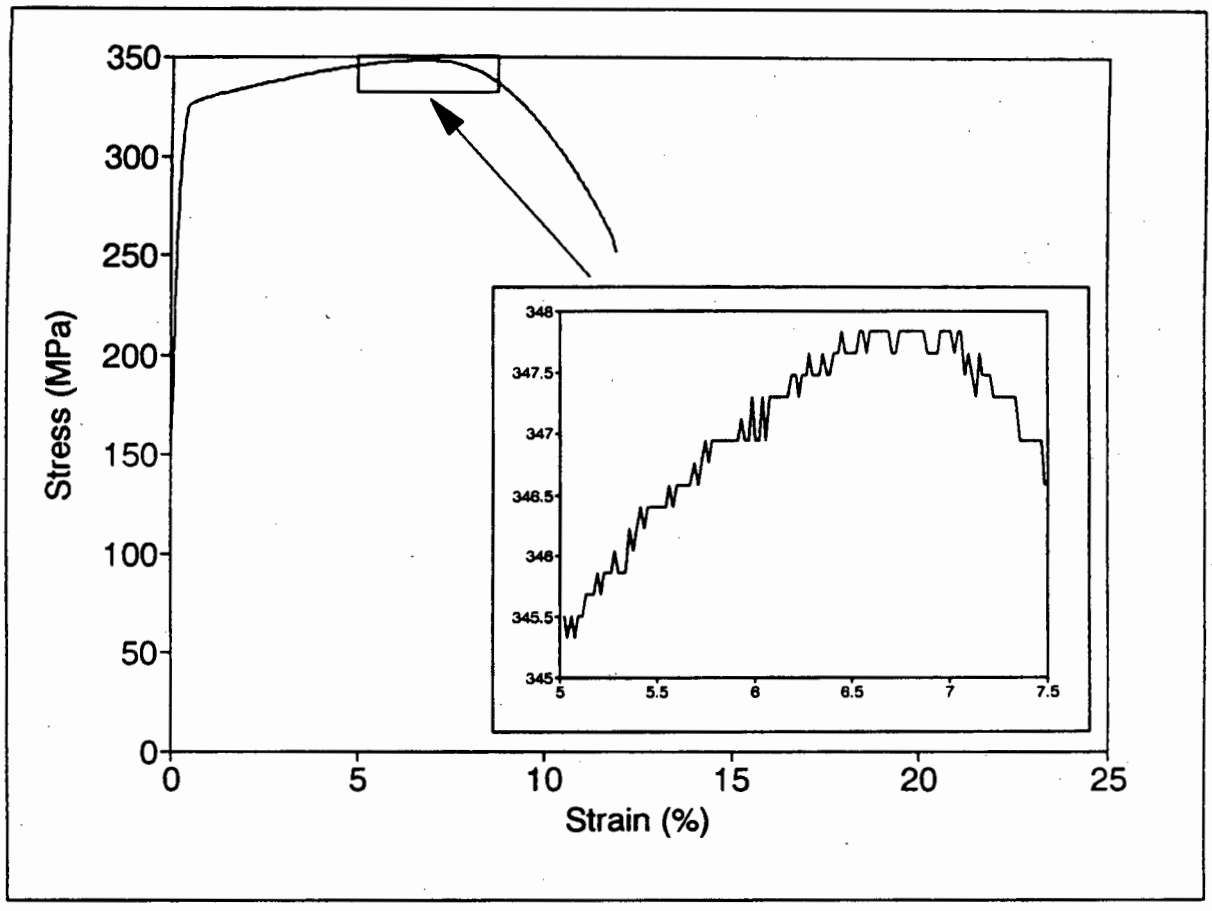

Figure 65: The tensile deformation record of alloy 6061 in the T6 condition. (Knife–edge extensometer)

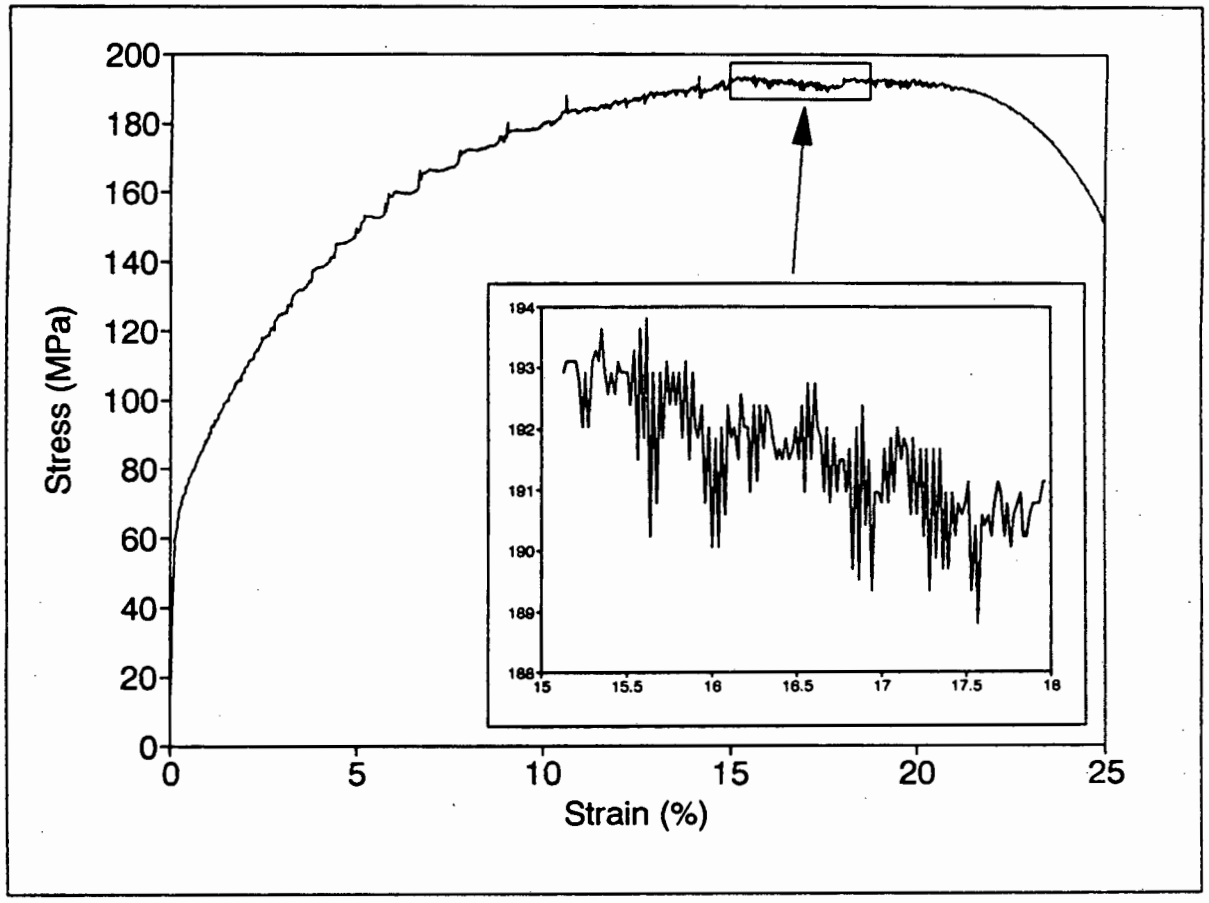

Figure 66: The tensile deformation record of alloy 6061 in the solution treated and water quenched condition.(Knife–edge extensometer)

serrations of similar amplitude. $\Delta\sigma_{max}$ during this third region of extension was ~3.5 MPa.

4.6.2 Surface Deformation Observations

Some very low contrast parallel deformation bands could be observed, under oblique illumination conditions, on the surface of the specimen which was solution treated prior to testing. The deformation bands were oriented, unusually, at 45° to the tensile axis, through the specimen width. The banding was of sufficiently low contrast that it was not resolvable during the course of the test, so the chronology of formation must be speculative. Consideration of prior observations on alloy 5182 during the course of this work, however, leads to the suggestion that the band formation may well have been concurrent with the stress plateaus observed on the tensile test record.

4.6.3 Microstructural Observations (CTEM)

Starting microstructures from material in both the T6 and freshly quenched conditions were examined, and these are presented in figures 67 and 68 respectively. In order to accurately represent the solution treated microstructure, natural ageing time was minimised by examining the material in the TEM as soon as possible after quenching.

4.6.4 Fracture

Fracture of the material showed an interesting distinction between the precipitation hardened and solution treated material. The T6 material failed with very similar characteristics to that observed for most of the 5182 specimens. Fracture was at 45° to the tensile axis through the specimen thickness after limited plastic instability in the gauge length. Fracture was, therefore, again accompanied by shear.

A similar situation was observed in the case of solution treated material, except that

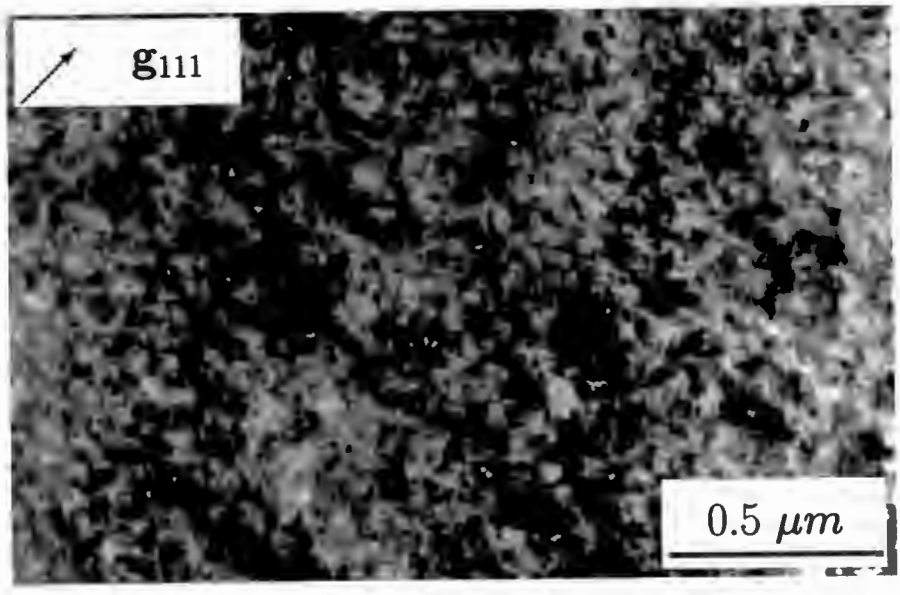

Figure 67: Bright–field TEM micrograph of 6061 (T6) prior to tensile testing.

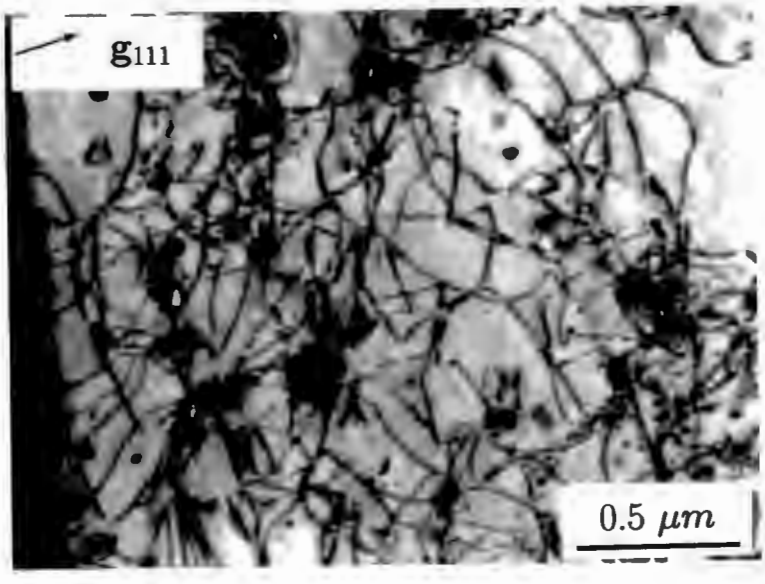

Figure 68: Bright–field TEM micrograph of solution treated (520°C, 1hr, WQ) 6061 prior to tensile testing.

the shear influence was bimodal. The fracture surface orientation was at 45° to the tensile axis through the specimen thickness in the central region of the fracture surface, as for the T6 condition. The outer edges, comprising approximately half the total fracture surface area, were shear lips formed at the same angle as the bands discussed in section 4.6.2. The fracture surface is best illustrated by the micrograph presented in figure 69.

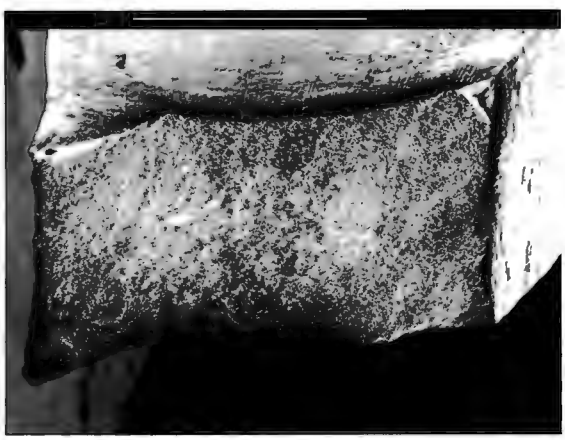

Figure 69: SEM micrograph illustrating the fracture of a solution treated alloy 6061 specimen, illustrating the central shear region as well as outer shear lips.

Details of the three regions of the fracture surface in figure 69 are shown in figure 70 The micrographs (a)–(c) illustrate the microscopically similar shear mechanism operative in all three regions, in spite of differing macroscopic orientations. All three micrographs show elongated ductile dimples in the direction of macroscopic shear.

4.6.5 Comment

As is the case with alloy 2014, 6061 forms the matrix for a range of MMC materials with both particulate and fiber additions. The monolithic alloy therefore serves as a basis for comparison with the MMC materials. The low amplitude serrated flow observed is consistent with the Mg content of the alloy being less than 1% (see table 3, page 68). Similarly, the near continuous deformation curve of the T6 condition is consistent with the solute depletion of the matrix by β' precipitation.

The very low contrast of deformation banding is of interest, specifically in the context of its unusual orientation i.e. shear influenced but not through the specimen thickness

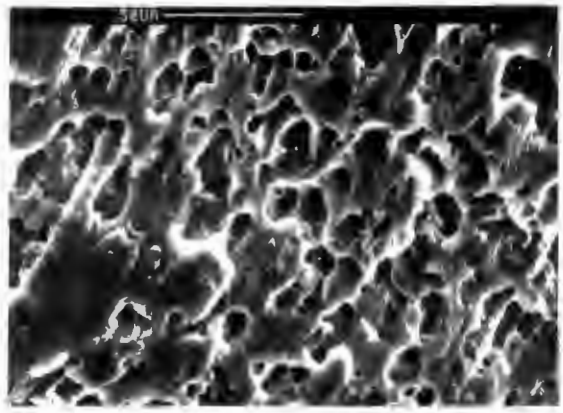

(a)

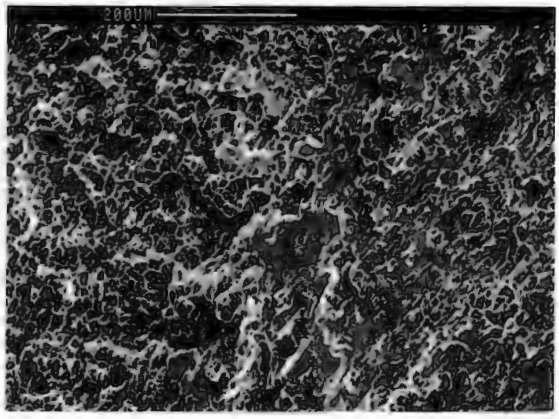

(b)

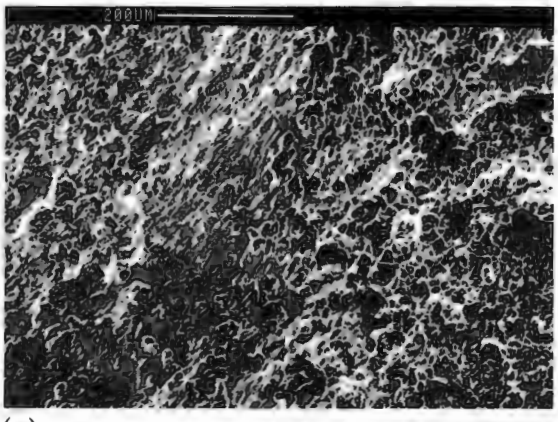

(c)

Figure 70: SEM micrographs (a), (b) and (c) show detail from the three orientations of macroscopic shear (marked a, b and c) evident on the fracture surface of the solution treated 6061 material.

as was commonly observed in the course of this work. The final fracture of the material correlated directly with the preceding deformation inhomogeneity (band formation) by failing in response to bimodal shear influences.

4.7 Metal Matrix Composites

Metal matrix composites containing various volume fractions of Al_2O_3 and SiC were investigated. The materials were based on the matrix alloys of either 2014 or 6061 and contained either 10%, 15% or 20% Al_2O_3, or 20% SiC particulate additions.

4.7.1 Tensile Test Results

6061 Matrix

The four materials were tested immediately after solution treatment (520°C, 1hr, WQ). Alloy 6061 containing 10%, 15% and 20% Al_2O_3 as well as 20% SiC all exhibited serrated flow, but no formation of deformation bands was observed. A summary of the tensile test data is presented in table 7.

Table 7: Summary of tensile test data from 6061 based MMC material tested directly after solution heat treatment.

	UTS (MPa)	% Elongation	$\Delta\sigma_{max} \approx$
Monolithic	193.8	25.0	4 MPa
10%Al_2O_3	200.0	17.6	1 MPa
15%Al_2O_3	223.5	10.9	5 MPa
20%Al_2O_3	228.3	14.6	4 MPa
20%SiC	269.4	9.75	3 MPa

An example of a tensile deformation record from 6061 containing 10% Al_2O_3, is presented in figure 71. It can be seen that the essential characteristics of the deformation

remains unchanged in comparison to the monolithic material. Serrated flow was present from the onset of plastic deformation, without an incubation strain. A series of successive serrated stress plateaus is apparent followed by further inhomogeneous deformation prior to plastic instability and final failure.

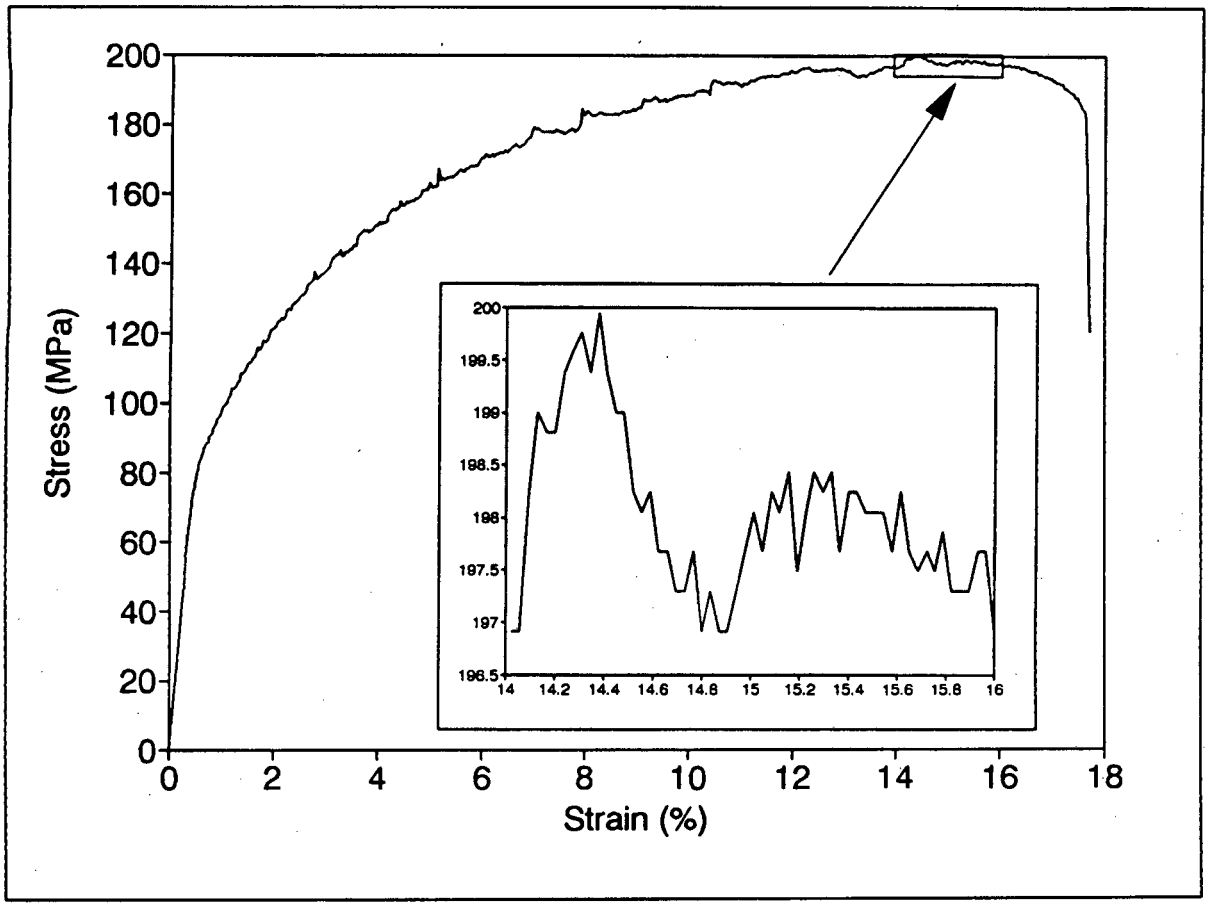

Figure 71: The tensile deformation record of alloy 6061 + 10% Al_2O_3 tested in the solution treated (520°C, 1 hr, WQ) condition.

2014 Matrix

The 2014 matrix MMC specimens were machined to conform with the subsize ASTM B557M specifications, mechanically polished to a 1 μm surface finish and tested in the solution treated condition. Solution treatment was carried out at 505°C for 2 hrs followed by water quenching. A summary of the tensile test results is presented in table 8.

The deformation in all cases was typified by a more gradual yield point, when compared to the monolithic alloy. In addition, discontinuities associated with pre–macro yielding were observed in the upper regions of the elastic deformation region. Macroscopic yielding was accomplished by a gradual transition into (serrated) plastic flow. Serration amplitude was largely unchanged from the onset of plastic deformation until final fracture.

The 10% and 15% Al_2O_3 composites both exhibited single large stress drops (type C) superimposed on the generally low amplitude serrations. The 20% Al_2O_3 composite was an exception, in that the general value of $\Delta\sigma$ was higher than for the comparable materials tested and these serrations were not interspersed with the single large stress drops.

From Table 8, it is clear that the solution treated composites generally displayed inferior mechanical properties in comparison to the monolithic material. The only exception, was the strength increase observed to occur in the case of the 10% Al_2O_3 composite.

4.7.2 Surface Deformation Observations

The surfaces of both sets of composite material tensile specimens were mechanically polished prior to tensile deformation. Final polishing utilised 1 μm alumina paste in preference to diamond paste to minimise crushing of the particulate material. Crushed particulate tended to smear in the specimen surface, producing a dull finish and unrepresentative particle distributions. In addition to mechanical polishing, the 6061 based composites were

Table 8: Summary of tensile test data from 2014 based MMC material tested directly after solution heat treatment.

	UTS (MPa)	% Elongation	$\Delta\sigma$ (MPa)
Monolithic	385.4	26.25	1
10%Al_2O_3	405.6	15.51	1
15%Al_2O_3	292.5	10.97	1
20%Al_2O_3	292.9	7.24	1–2.5

electropolished prior to deformation. Electropolishing resulted in a smoother surface finish of the material between composite particles, but also caused the particles to stand proud of the surface. Due to limited availability of material and specimens, the surface deformation was only observed after specimen failure and not at any intermediate values of strain.

6061 Matrix

Slip line formations were generally planar and parallel within any given grain. There were also various cases of wavy slip line features observed, resulting from the activation of multiple slip systems. A distinct feature was that the predominant direction of slip line formation was at 90° to the tensile axis, often resulting in continuity of the slip line direction across grain boundaries. The surface deformation features are illustrated in figures 72 and 73, which were photographed from the surfaces 20% SiC and 20% Al_2O_3 composite specimens respectively, after straining to fracture.

Figure 72: SEM micrograph illustrating surface slip line features associated with the tensile deformation of alloy 6061 + 20% SiC.

Some particulate fracture was observed to occur in all cases, two examples of which are shown in SEM micrographs of the specimen surfaces from 20% SiC and 15% Al_2O_3 composites in figures 74 and 75 respectively.

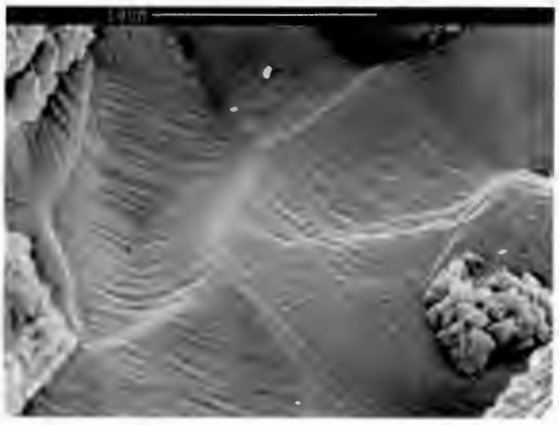

Figure 73: SEM micrograph illustrating surface slip line features associated with the tensile deformation of alloy 6061 + 20% Al_2O_3.

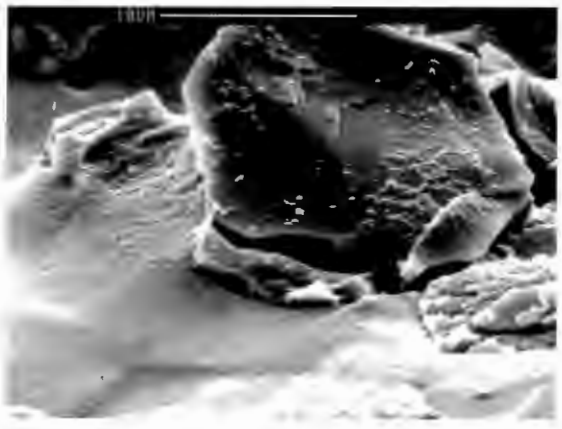

Figure 74: SEM micrograph illustrating particulate fracture from the surface deformation of alloy 6061 + 20% SiC.

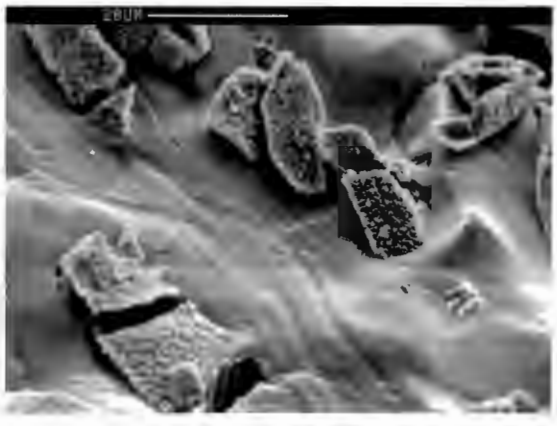

Figure 75: SEM micrograph illustrating particulate fracture and slip line features from the surface deformation of alloy 6061 + 15% Al_2O_3.

2014 Matrix

In the case of 2014, particularly the monolithic material and that containing 10% Al_2O_3, slip lines were predominantly oriented at 90° to the tensile axis, i.e. parallel to the direction of eventual shear fracture. This is clearly illustrated by the micrograph in figure 76, where the tensile axis is vertical. The limited depth of focus in the micrograph is a result of the high tilt angle necessary to clearly image the slip lines.

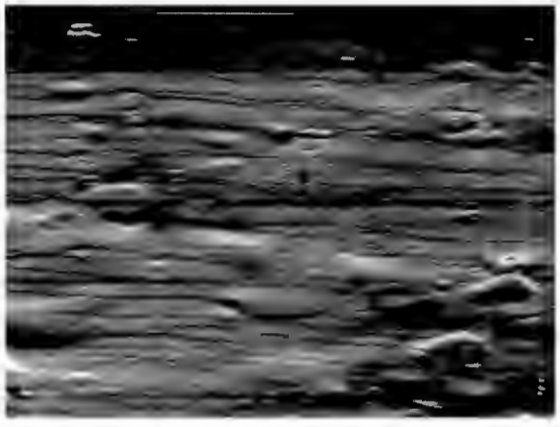

Figure 76: SEM micrograph illustrating the parallel slip line features of the surface deformation of monolithic alloy 2014.

The particle distribution in the composite materials examined was generally uniform except in the case of 10% Al_2O_3. In this case, particles were aligned into clear bands in the extrusion direction. This inconsistency, however, led to some insight into the preferential fracture of these regions as is illustrated by the SEM micrographs in section 4.7.4.

Particle fracture was the dominant feature of the surface observations, but this was occasionally accompanied by interface failure. Either of the above cases accounts for extreme loaclisation of deformation, demonstrated by the concentration of slip lines, particularly in the case of the 20% Al_2O_3 material. These features are illustrated figure 77.

4.7.3 Microstructural Observations (CTEM)

The preparation of CTEM foils from MMC material requires the use of an ion beam thinning apparatus, equipped with a cold stage [156], which was unavailable during the

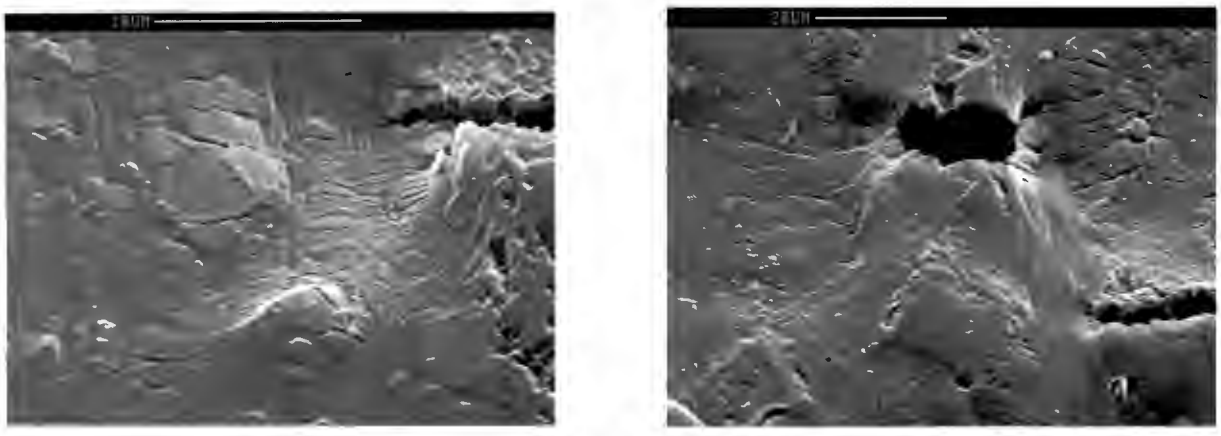

Figure 77: SEM micrographs illustrating particulate fracture, interface failure and slip line features of the surface deformation from alloy 2014 + 20% Al_2O_3.

course of this work. The approach taken was to attempt two stage preparation, by initially utilising conventional jet–polishing techniques followed by ion thinning without using a cold stage. The microstructure observable after this procedure was, however, heavily ion damaged resulting in unrepresentative microstructures.

4.7.4 Fracture

The mode of shear dominated ductile fracture observed in both monolithic 2014 and 6061 was directly affected by the particulate additions in both cases.

6061 Matrix

Three modes of failure were observed to occur:

1. The common mode of ductile shear through the specimen thickness in the case of the monolithic material as well as that with 10% and 20% Al_2O_3 additions. The fracture surface was oriented at 45^o to the tensile axis and failure was preceded by minimal plastic instability (nominally brittle).

2. Nominally brittle failure with the entire fracture surface orthogonal to the tensile axis in the case of the 15% Al_2O_3 composite.

3. Ductile shear at 45° to the tensile axis through the gauge width in the case of material containing 20% SiC.

Micrographs illustrating the details of the three failure modes from MMC materials containing 20% Al_2O_3, 15% Al_2O_3 and 20% SiC are illustrated in figures 78, 79 and 80 respectively.

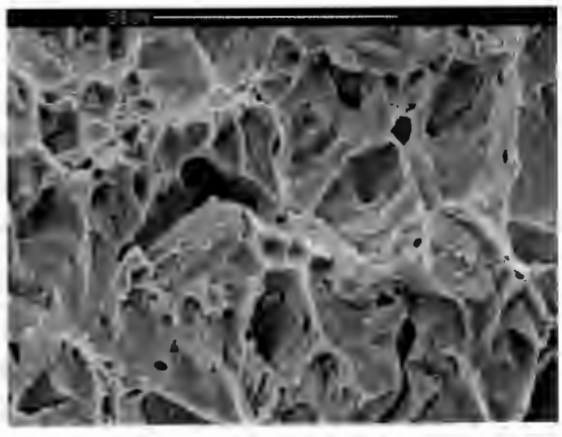

Figure 78: SEM micrograph from the fracture surface of alloy 6061 + 20% Al_2O_3.

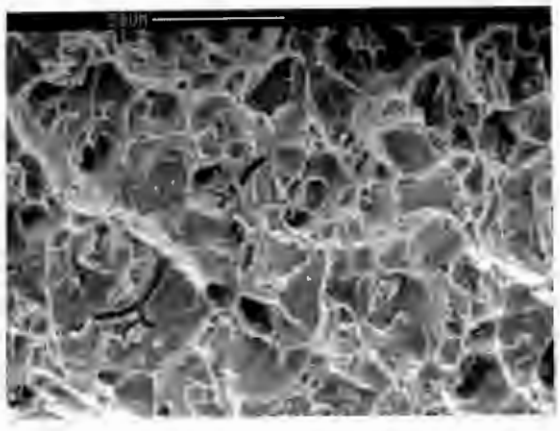

Figure 79: SEM micrograph from the fracture surface of alloy 6061 + 15% Al_2O_3.

2014 Matrix

The same three fracture modes described above were seen to occur in the testing of alloy 2014 based composites.

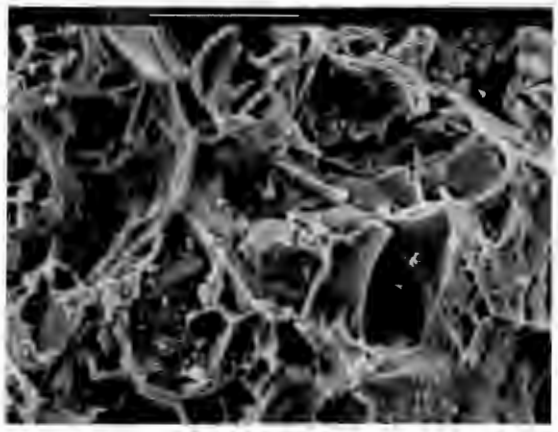

Figure 80: SEM micrograph from the fracture surface of alloy 6061 + 20% SiC.

1. 45° shear through the specimen thickness in the case of the monolithic material as well as the 15% Al_2O_3 composite.

2. Entire fracture surface orthogonal to the tensile axis, accompanied by limited plastic instability, in the case of the 20% Al_2O_3 composite.

3. Ductile shear through the specimen width in the case of the 10% Al_2O_3 composite.

In the case of the 10% Al_2O_3 MMC, the bands of particles aligned in the extrusion direction were observed to play a role in the premature failure of the material. Comparison with particle free regions of the gauge length show that the particle rich regions undergo earlier fracture surface formation. Such a region is shown in figure 81, illustrating the fracture surface within a particle rich band.

Details from the fracture surfaces of 2014 containing 10%, 15% and 20% Al_2O_3 are illustrated in the figures 82, 83 and 84 respectively. The clearest indication of the mode of fracture comes from considering the 10% Al_2O_3, where fine ductile dimples are seen to be separate from regions containing the higher particle density.

4.7.5 Comment

All the MMC material tensile displayed serrated plastic flow, when tested in the solution treated condition. This result, although in direct correspondence with the monolithic

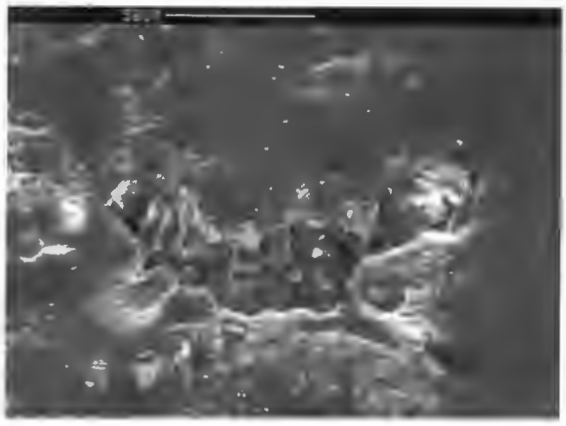

Figure 81: SEM micrograph illustrating the premature fracture surface formation associated with a particle rich band in the alloy 2014 + 10% Al_2O_3 composite.

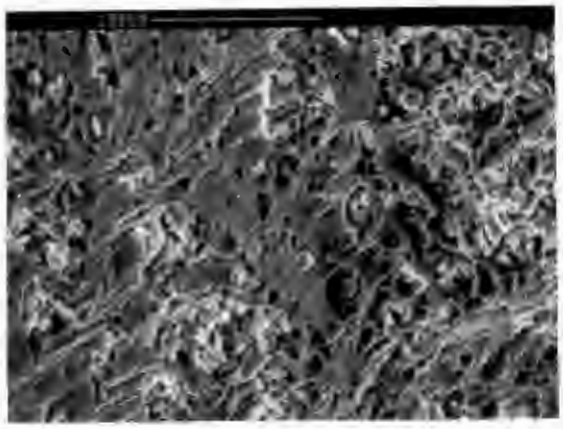

Figure 82: SEM micrograph of the fracture surface features from the alloy 2014 + 10% Al_2O_3 composite.

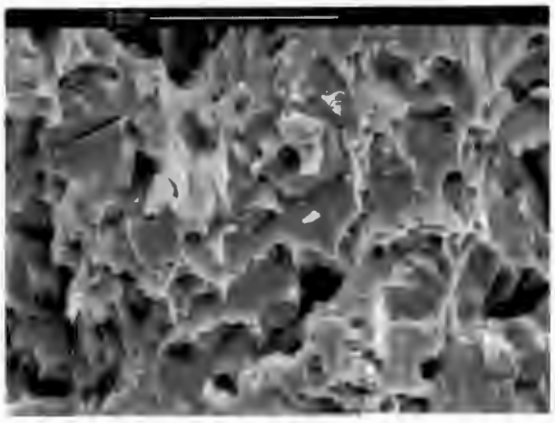

Figure 83: SEM micrograph of the fracture surface features from the alloy 2014 + 15% Al_2O_3 composite.

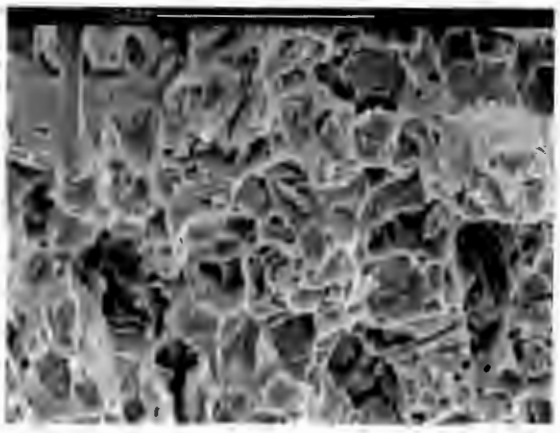

Figure 84: SEM micrograph of the fracture surface features from the alloy 2014 + 20% Al_2O_3 composite.

alloy, was not necessarily predictable, because of the role of the particle inclusions in determining dislocation densities after rapid cooling, as well as during plastic straining. Pre–macro yielding was especially evident in alloy 2014 based MMC's, associated with particle influences on the localised nature of initial yielding. All cases tested suggest some influence of particle cracking on slip localisation. Fracture was largely shear influenced, but the orientation of the fracture surfaces was also influenced by the inclusion of particulates in the material.

4.8 Experimental (2at.%) Alloys

This section covers the tensile deformation and associated microstructural investigation of the three experimental alloys, manufactured by making 2at.% additions of Ag, Mg and Zn to commercial purity Al (1070). Exact atomic percentage additions of each element were chosen in order to directly compare the effect of the same amount of three different solutes on the microstructural development and serrated flow properties of the alloys during tensile testing.

4.8.1 The Response of the Experimental Alloys to Ageing

The three alloys (as well as 1070 for reference), were subjected to Vickers hardness tests, subsequent to solution heat treatment and water quenching. Hardness indentations were made at set intervals for up to 100 hrs natural ageing (RT) and 10 hrs artificial ageing (175°C). Within 100 hrs at room temperature, no significant ($\geq$10%) difference from the post quench hardness for any individual alloy was observed.

Artificial ageing at 175°C after quenching showed 1070, VF615 (Mg) and VF617 (Zn) to be stable at H_{V20} values of approximately 24, 25 and 38 GPa respectively. The H_{V20} value of VF619 (Ag) was, however, observed to increase from 30 to 48 GPa in the first two hours at 175°C, and to 58.5 GPa after a total ageing time of 10 hrs.

4.8.2 Tensile Test Results

Full and subsize ASTM B557M specimens were respectively stamped and machined from 3 mm thick cold–rolled plate and ~0.5 mm thick sheet of all three alloys. Material was tested in both cold–rolled as well as solution treated conditions. Solution treatment was carried out at 400°C followed by water quenching, except in the case of Al–2at.%Ag, where both 450°C and 500°C treatments were also employed to ensure full solid solution of the Ag. 400°C is sufficient to dissolve approximately 2.3at.%Ag, 13.25at.%Mg and 82.8at.%Zn in pure Al [214]. The temperature chosen for solution treatment was, therefore, the minimum necessary to ensure complete solution of the alloying element under consideration, while simultaneously minimising grain growth. A minimum grain size is desirable to emphasise the serrated flow properties (see section 2.4.1 in chapter 2).

Subsize Specimens

Solution treatment at 400°C, followed by water quenching, produced three distinct types of serrated flow. The tensile test curves for VF617 (Zn), VF619 (Ag) and VF615 (Mg) are reproduced in figures 85, 86 and 87.

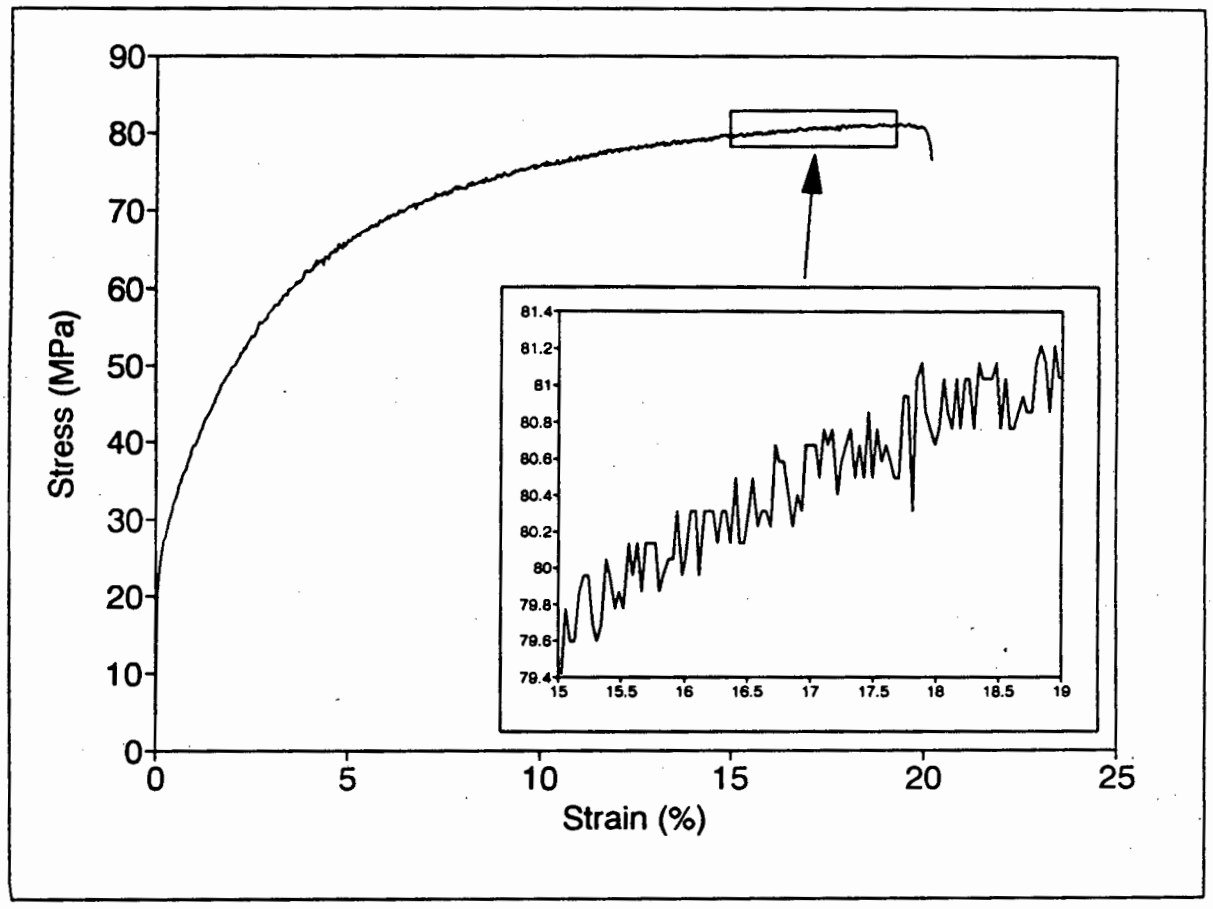

Figure 85: The tensile deformation record of 3 mm thick cold-rolled alloy VF617 (Zn), tested immediately after solution treatment (400°C, 30 mins, WQ).

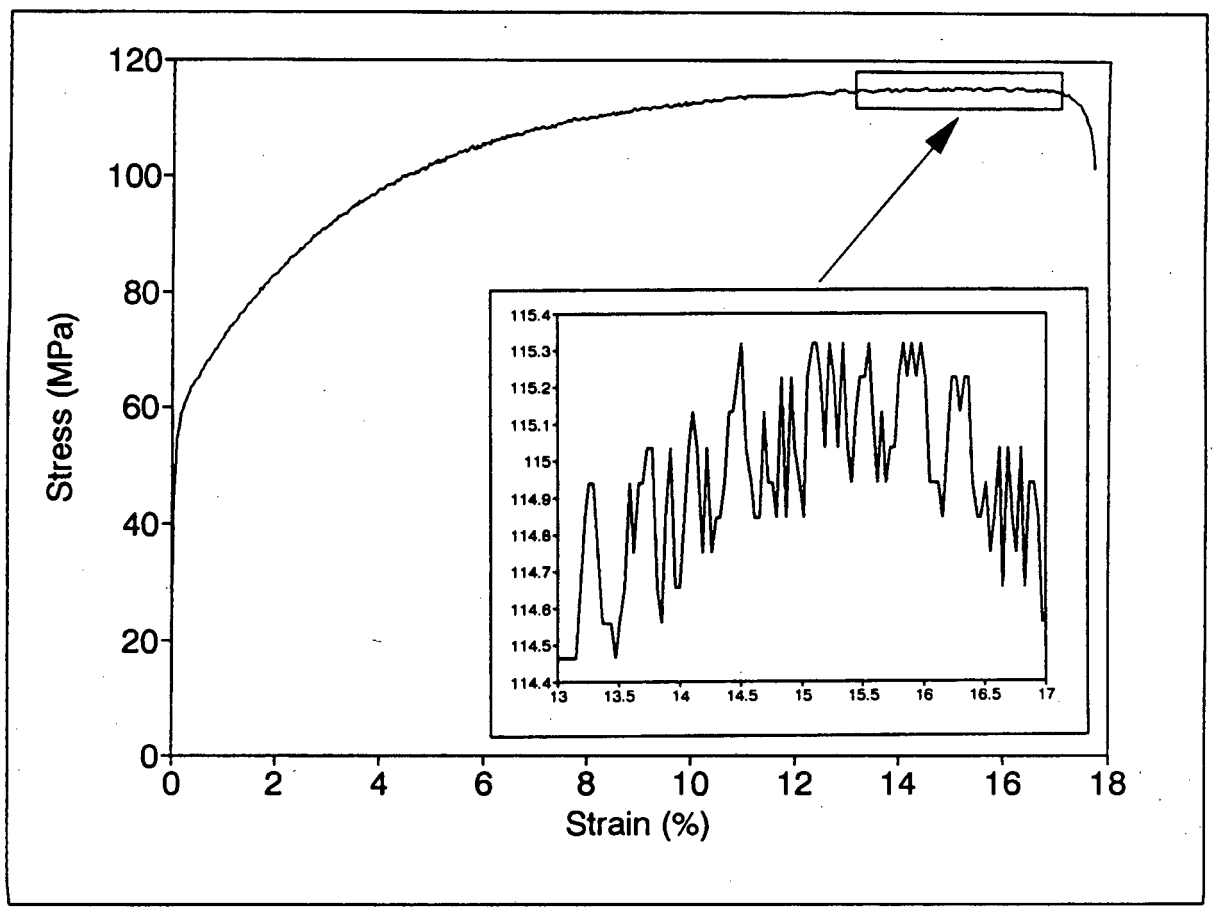

Figure 86: The tensile deformation record of 3 mm thick cold-rolled alloy VF619 (Ag) tested immediately after solution treatment (450°C, 30 mins, WQ).

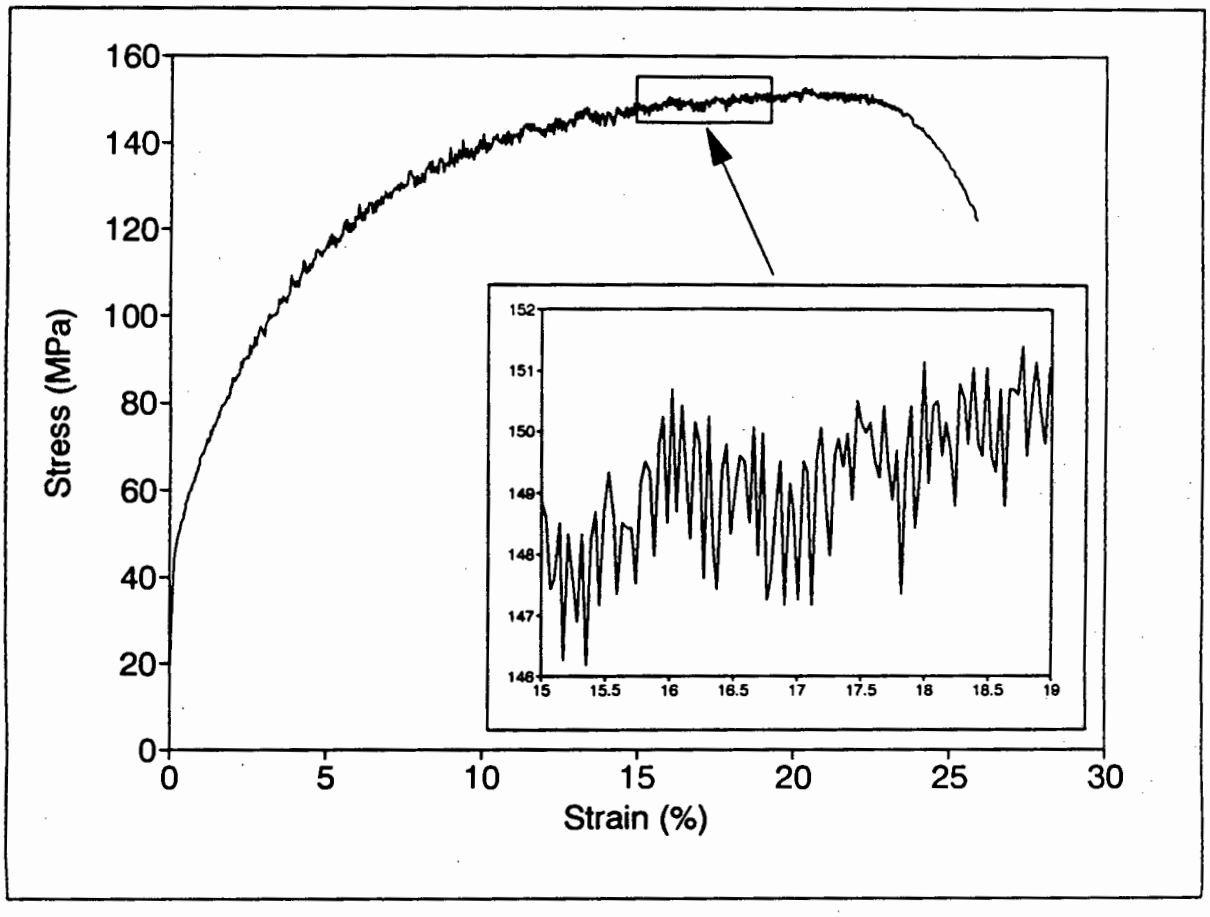

Figure 87: The tensile deformation record of 3 mm thick cold–rolled alloy VF615 (Mg) tested immediately after solution treatment (400°C, 30 mins, WQ).

Upon consideration of the tensile deformation records presented in figures 85, 86 and 87 as well as that of 1070 after the same heat treatment (figure 28, page 91), the following features are significant:

1. 2at.% additions of Zn, Ag and Mg to the base material (1070), produce progressive strength increases from UTS=60.4 MPa in the case of 1070 to 81.3, 115.4 and 152.9 MPa respectively.
2. The transition from elastic to plastic deformation is made more distinct by all three alloying additions.
3. 1070, VF617 (Zn) and VF619 (Ag) all display serrated flow from the onset of plastic deformation, where $\triangle\sigma$ was observed to increase in amplitude during work hardening and stabilise during deformation approaching ideal plasticity.
4. The stress amplitude of serrations ($\triangle\sigma$) was, however, unaffected by the additions of 2at.% Zn or Ag to 1070. $\triangle\sigma$ was observed to be consistent and regular ranging from $\sim$0.2 $\rightarrow$ 0.4 MPa in all 3 cases.
5. In the case of VF615 (Mg), $\triangle\sigma$ is present from the onset of plastic deformation increasing to a maximum of $\sim$4 MPa during work hardening. During the portion of the curve corresponding to ideally plastic deformation (dynamic recovery), where little or no work hardening occurs, $\triangle\sigma$ was consistent and regular with values ranging from 1 $\rightarrow$ 3 MPa.

In summary, therefore, only the addition of Mg was observed to significantly alter the nature of serrated flow. All four materials had been identically treated prior to tensile testing by being cold–rolled to a thickness of 3 mm and subsequently solution treated at 400°C followed by water quenching immediately prior to tensile testing.

An interesting anomaly was observed to occur in the tensile deformation of VF619 (Ag). The solution heat treatment originally given to the 2at.% alloys was at 400°C (10 mins, WQ). This time was, however, insufficient to fully recrystallise 1070 and therefore not subsequently employed as a heat treatment. The tensile deformation record of 3 mm

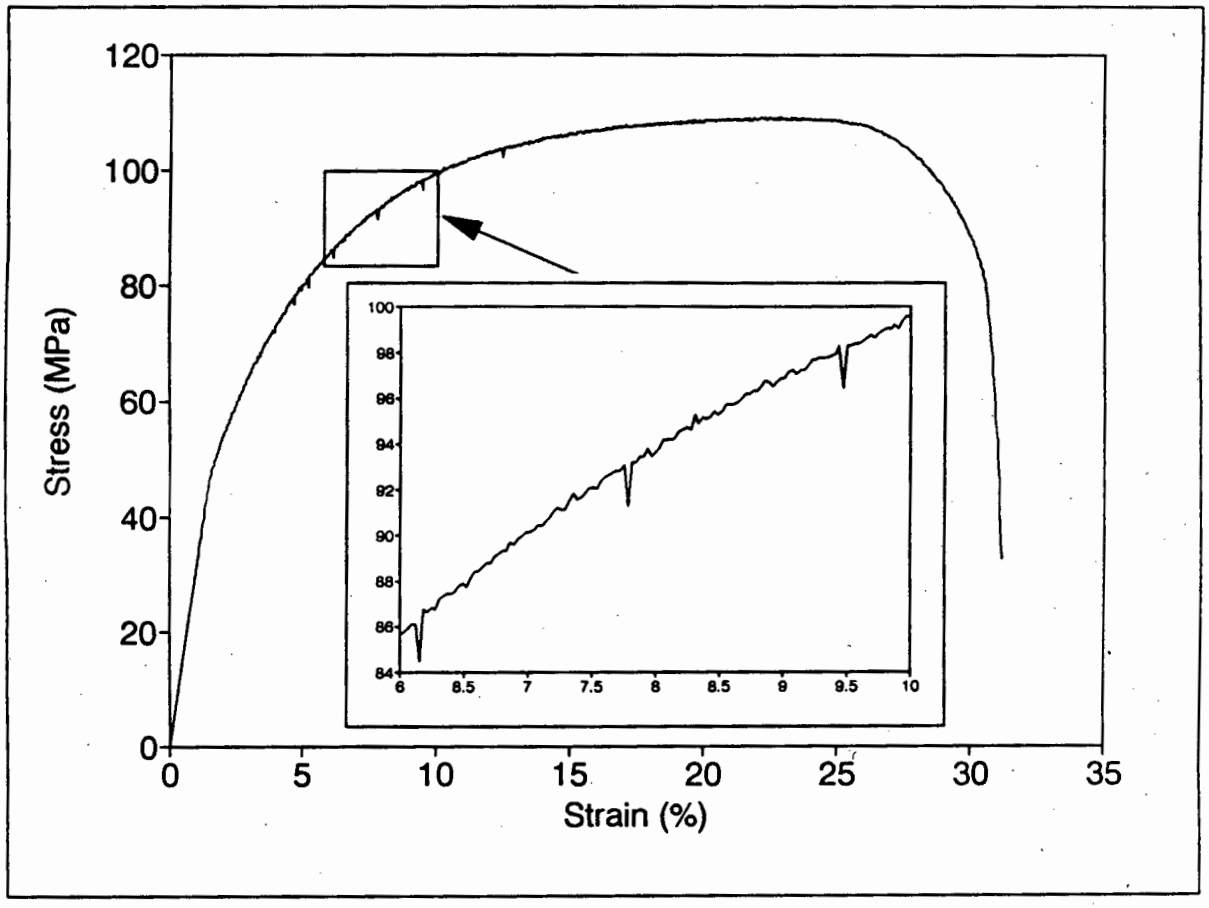

Figure 88: The tensile deformation record 3 mm thick cold-rolled alloy VF619 (Ag) tested immediately after annealing (400°C, 10 mins, WQ).

thick VF619 (Ag), heat treated at 400°C(10 minutes, WQ) is, however, shown in figure 88.

Figure 88 can be compared to figure 89, where the latter shows the deformation curve of the same material, solution treated for the same period at 500°C (10 minutes, WQ).

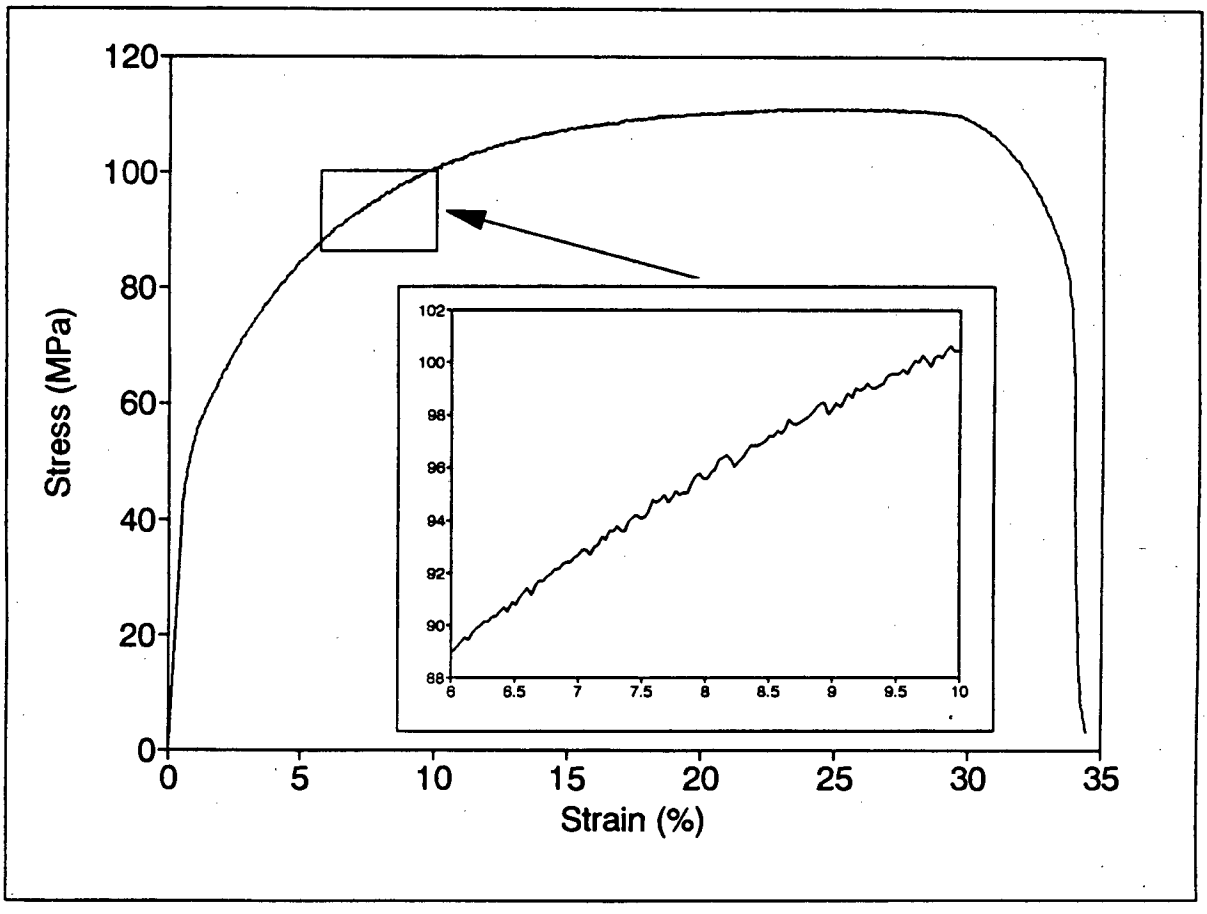

Figure 89: The tensile deformation record 3 mm thick cold–rolled alloy VF619 (Ag) tested immediately after solution treatment (500°C, 10 mins, WQ).

The curves in figure 88 and figure 89 are distinguished by the occurrence of single large isolated stress drops in the case of material treated at 400°C, superimposed on the more regular and frequent serrations. The isolated large serrations are clearly illustrated in the inset of figure 88. The serrations were comparable in terms of their isolated and sudden occurrence to those exhibited by 2014 (see figure 39, page 102).

The occurrence of isolated large stress drops in VF619 (Ag) was attributed to the presence of developed γ' precipitation, apparent after TEM examination of the corresponding

pre–deformation microstructure [215]. A TEM micrograph of the 3 mm cold–rolled material after a 400°C (10 mins, WQ) anneal is shown in figure 90. The microstructure of the same material treated at 500°C (10 mins, WQ) is shown in figure 91.

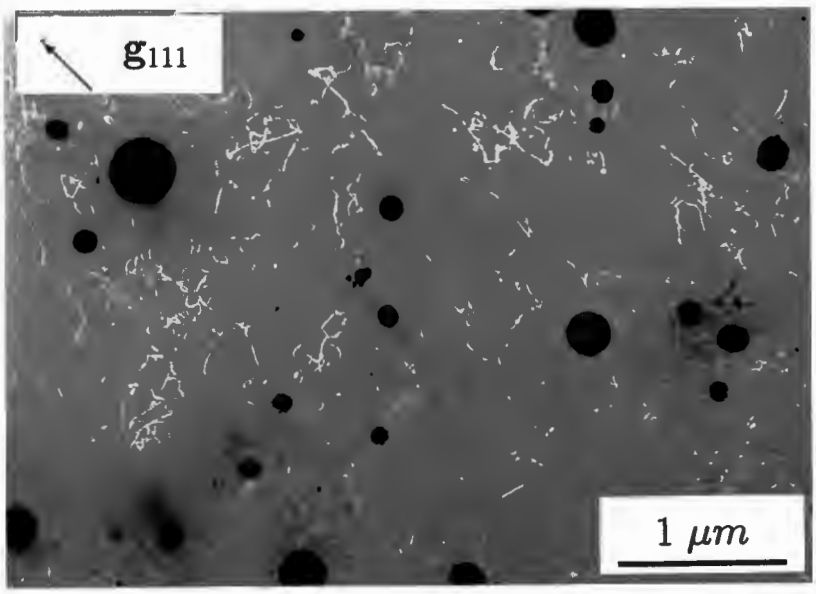

Figure 90: Weak–beam TEM micrograph of 3 mm cold–rolled alloy VF619 (Ag) plate after annealing at 400°C (10 mins, WQ).

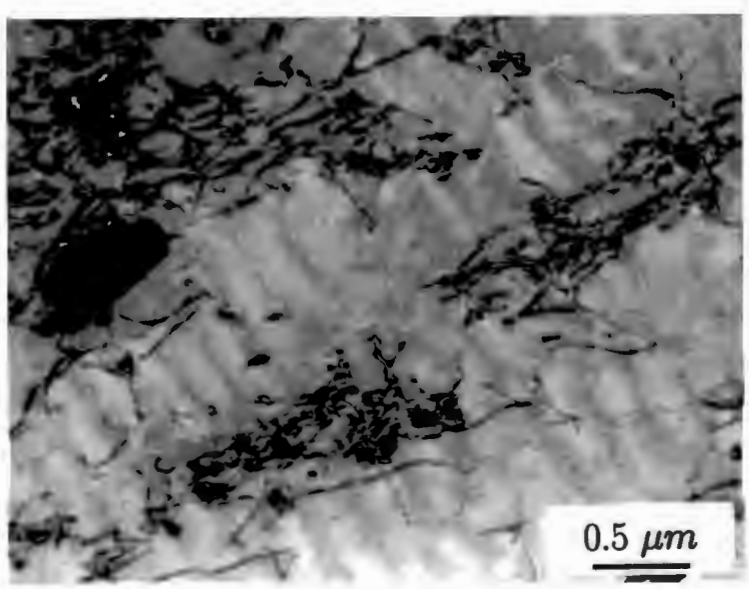

Figure 91: Bright–field TEM micrograph of 3 mm cold–rolled alloy VF619 (Ag) plate after annealing at 500°C (10 mins, WQ).

Full–size Specimens

In addition to testing subsize ASTM B557M specimens machined from the 3 mm thick rolled plate, full–size specimens were also tested. The full–size specimens were stamped from ~0.4 mm thick sheet by HULAMIN. The tensile testing of full–size specimens served two purposes, firstly to examine the effect of cold–rolling deformation on serrated flow characteristics, and secondly to directly test material in the same condition in which it was tested in HVEM in–situ straining experiments.

It was anticipated that material rolled to ~0.4 mm thickness would recrystallise in a shorter time (at the same solution temperature) than that required to recrystallise 3 mm thick plate because of the greater amount of stored energy in the former case. TEM examination confirmed the shorter time necessary for complete recrystallisation, revealing that 20 minutes at solution temperature was sufficient in all cases. Specimens were water quenched from the solution temperature (400°C) immediately prior to tensile testing. The exception was the VF619 (Ag), which was treated at 450°C for 20 minutes to ensure complete solution of the Ag.

4.8.3 The Effect of Strain Rate

In order to test for the occurrence of a macroscopically measurable negative rate sensitivity (SRS) of the flow stress, a set of single tests at a range of constant[15] nominal strain rates were carried out. The nominal strain rates ranged from 1×10^{-6} s^{-1} to 1×10^{-1} s^{-1}, and all tests were at room temperature. Inconclusive results arose from the testing of both 1070 and VF617 (Zn), in that no specific trend could be established, but this was not the case for VF615 (Mg) and VF619 (Ag).

The results from VF615 (Mg) and VF619 (Ag) are presented in figures 92 and 93. Clear trends are visible in that a negative measured rate sensitivity occurs for VF615 (Mg) over most of the strain rates tested except for the higher strain rates where the SRS became sharply positive. In the case of VF619 (Ag), the influence of precipitation of γ' resulted

[15]No facilities (eg. ramp generator) were available for instantaneous strain rate changes during the course of a single test.

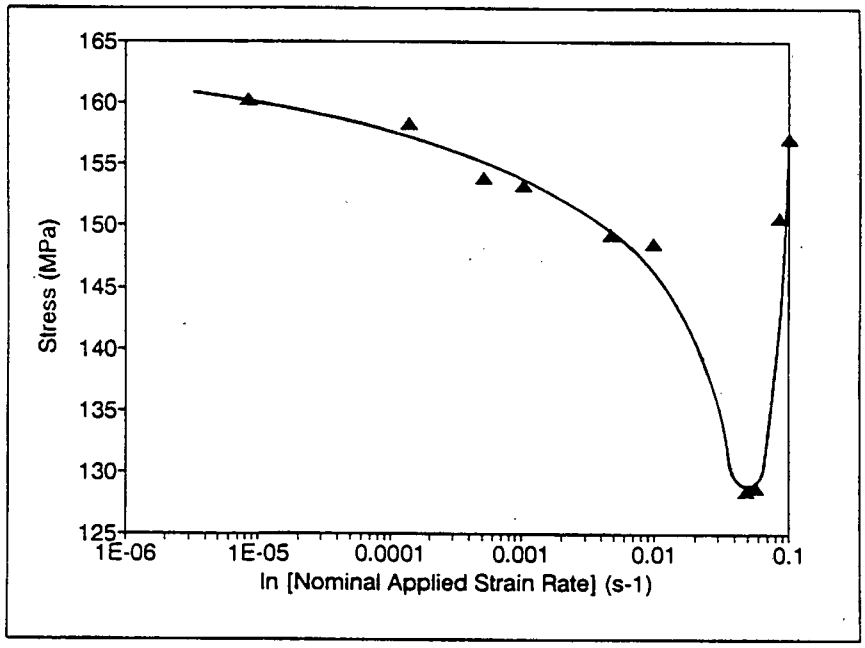

Figure 92: The effect of variations in the nominal strain rate on the flow stress of alloy VF615 (Mg), at a specific value of total strain ($\epsilon \approx 15\%$), during tensile testing at room temperature.

in various regimes of apparent strain rate sensitivity, as is further discussed in chapter 5.

4.8.4 Surface Deformation Observations

Slip line features on the surfaces of the three alloys tested were examined in the SEM. Pre–polished specimen gauge lengths were examined after premature termination of tensile tests. Slip lines, in all cases, were characterised by strongly planar features from the onset of tensile straining. Low strain deformation featured parallel slip traces with features consistent with cross–slip evident in the vicinity of grain boundaries. Cross–slip related slip line features within the grains (i.e. not associated with grain boundary pile–up) readily occurred in 1070 from low values of total strain.

Deformation bands were only observed on the surfaces of specimens of 1070, VF617 (Zn) and VF619 (Ag) *immmediately prior to final failure.* These bands corresponded directly with the orientation of the eventual fracture surfaces of the specimens, and could be described as "attempts to fracture" prior to failure. Deformation bands were, however,

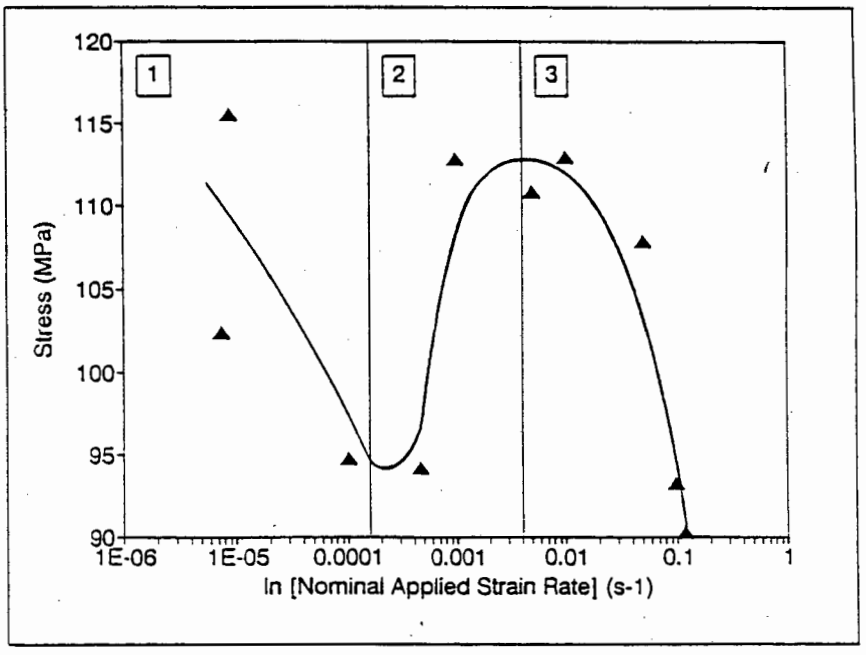

Figure 93: The effect of variations in the nominal strain rate on the flow stress of alloy VF619 (Ag), at a specific value of total strain ($\varepsilon \approx 15\%$), during tensile testing at room temperature.

observed *during the full course of the tensile test* (at the lower end of the strain rate regime tested) on the surface of VF615 (Mg). Bands, in all cases, were only observed on the surfaces of full–size specimens stamped from the ~0.4 mm thick sheet and were oriented at 60° to the tensile axis on the broad specimen face. No band formation occurred on the surfaces of the subsize specimens machined from 3 mm thick plate.

4.8.5 Microstructural Observations (CTEM)

Microstructures of the three alloys were examined after cold–rolling and also after subsequent solution treatment, as well as after the application of various amounts of tensile strain. The cold–rolled microstructures exhibited varying amounts of dynamic recovery, indicated by the occurrence of aligned dislocation arrays, moire fringes and cell–like dislocation arrangements. The most obvious distinction was when the similar microstructures of 1070 and VF617 (Zn), both of which had undergone significant amounts of dynamic recovery, were compared to VF615 (Mg) and VF619 (Ag), which displayed densely accumulated dislocation structures.

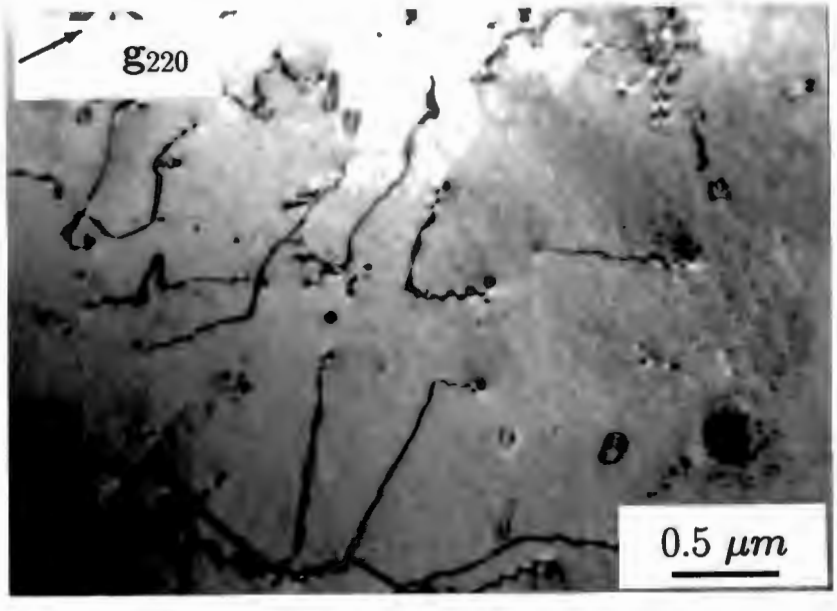

Figure 94: TEM bright–field image of the microstructure of alloy VF617 (Zn), after quenching from solution temperature, showing dislocation loops, elongated loops and a low density of quenched in line dislocations.

Solution treatment and water quenching resulted in microstructures dominated by dislocation loops and small clusters of dislocation tangling. Arrays of adjacent loops were visible in VF617 (Zn). VF619 (Ag) was characterised by the occurrence of both dislocation loops and helices as well as combinations of the two. Segments of dislocations were observed adjacent to some rows of loops. The features described above are illustrated in the micrographs in figures 94, 95 and 96.

Tensile straining of VF617 (Zn) produced an evolution of the microstructure similar to that exhibited by 1070 (section 4.3, page 90). Deformation was characterised by the formation of dislocation tangles which subsequently became organised into cell wall type structures. The development of the microstructure of VF617 (Zn) is illustrated in figures 98 and 99.

CTEM examination of microstructural development of VF619 (Ag) indicated a more rapid accumulation of dislocations than in the case of VF617 (Zn). Dynamic recovery processes had also been apparently restricted by the addition of Ag, compared with Zn, evidenced by less obvious dislocation cell arrangements in the former alloy. Figures 100, 101 and 102 illustrate the microstructure of VF619 (Ag) deformed in tension to total strain levels of 0.1%, 1% and 17.5% respectively.

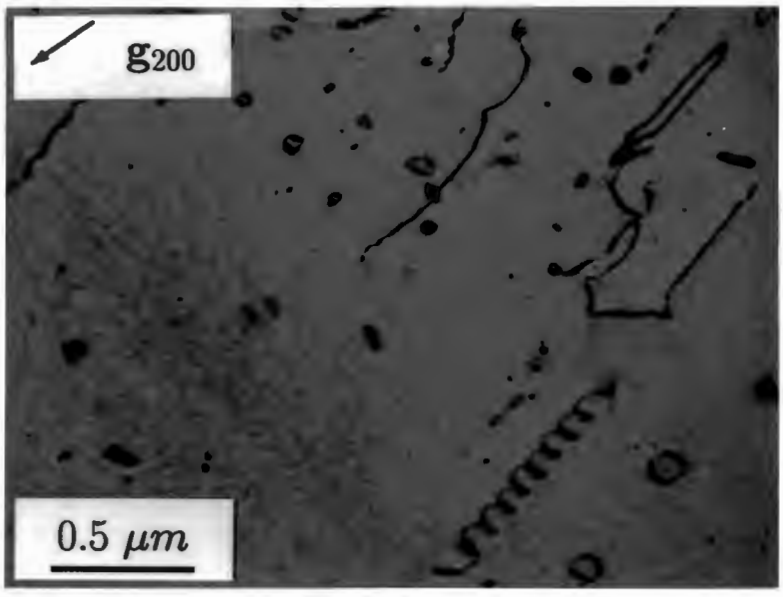

Figure 95: TEM bright–field image of the microstructure of alloy VF619 (Ag), after quenching from solution temperature, showing dislocation loops, extended loops and dislocation helices.

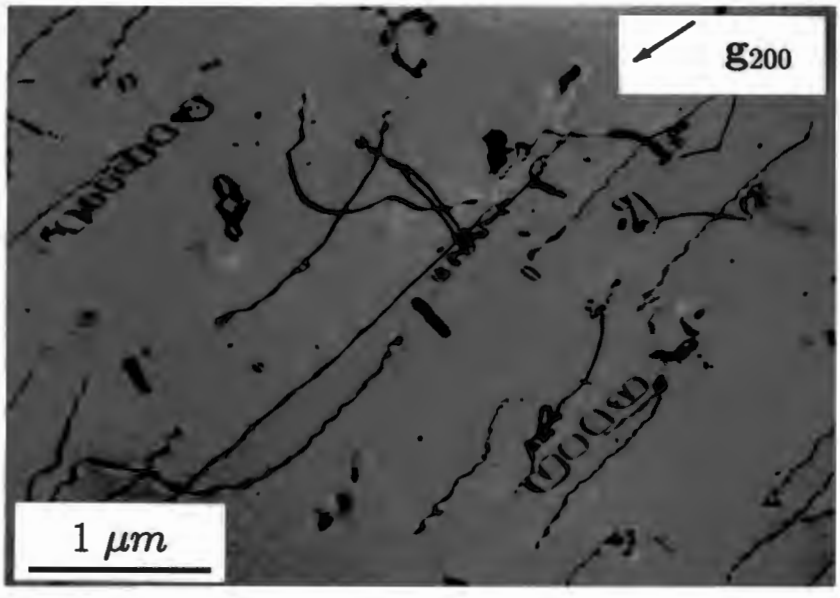

Figure 96: TEM bright–field image of the microstructure of alloy VF619 (Ag), after quenching from solution temperature, showing dislocation loops and rows of loops adjacent to line dislocations. The features are consistent with the condensation of vacancies onto screw dislocations to produce helices [210].

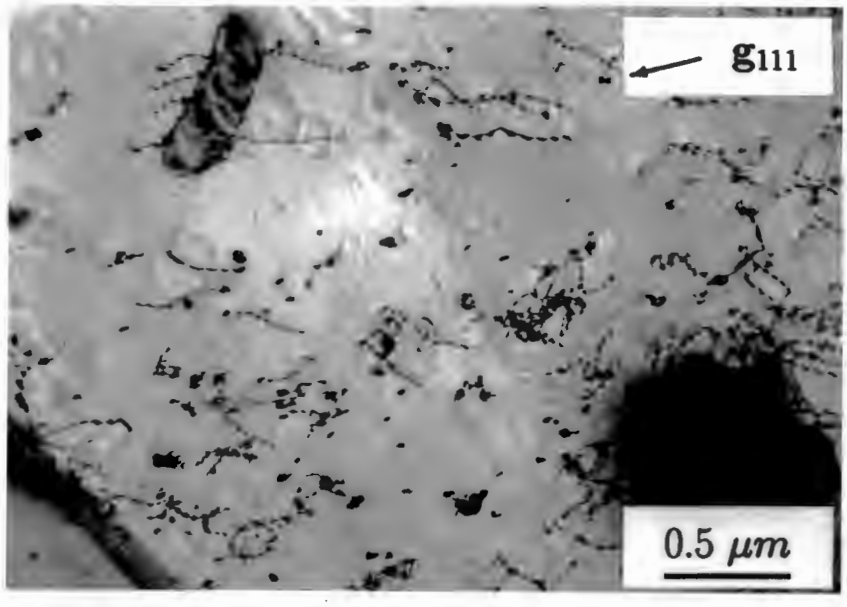

Figure 97: TEM bright–field image of the microstructure of alloy VF615 (Mg), after quenching from solution temperature, illustrating an approximately uniform distribution of line dislocations and loops.

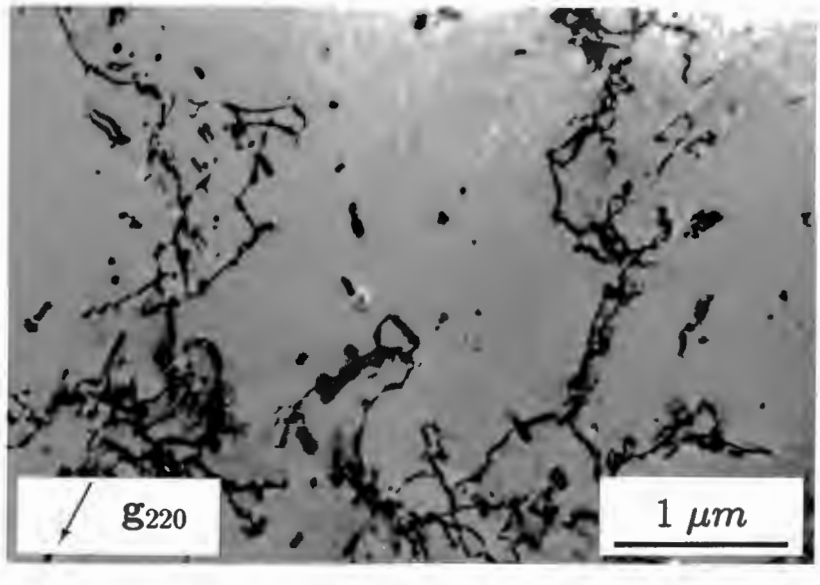

Figure 98: TEM bright–field image of the dislocation structure of quenched alloy VF617 (Zn), after a total tensile strain of 0.3%. The initiation of dislocation arrangement into cell walls is already evident against a background of quench associated loops.

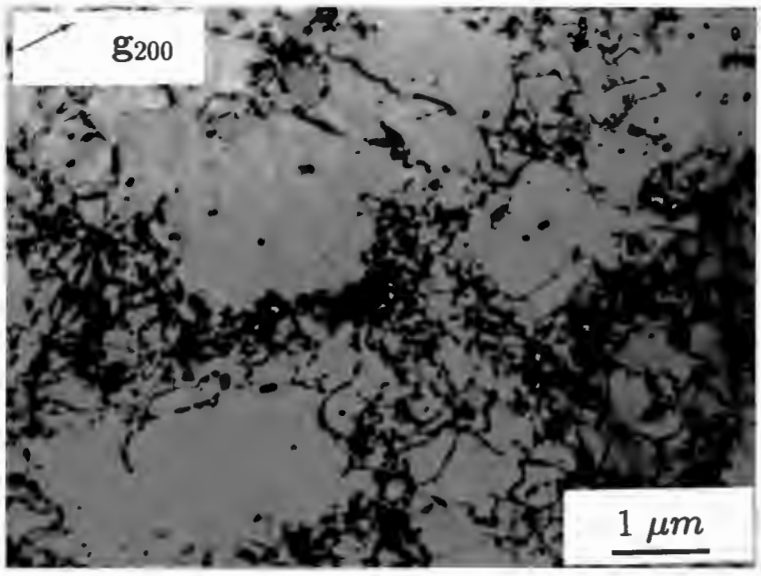

Figure 99: TEM bright–field image of the dislocation structure of quenched alloy VF617 (Zn), after a total tensile strain of 1%. The development of a recovery associated dislocation cell structure is evident.

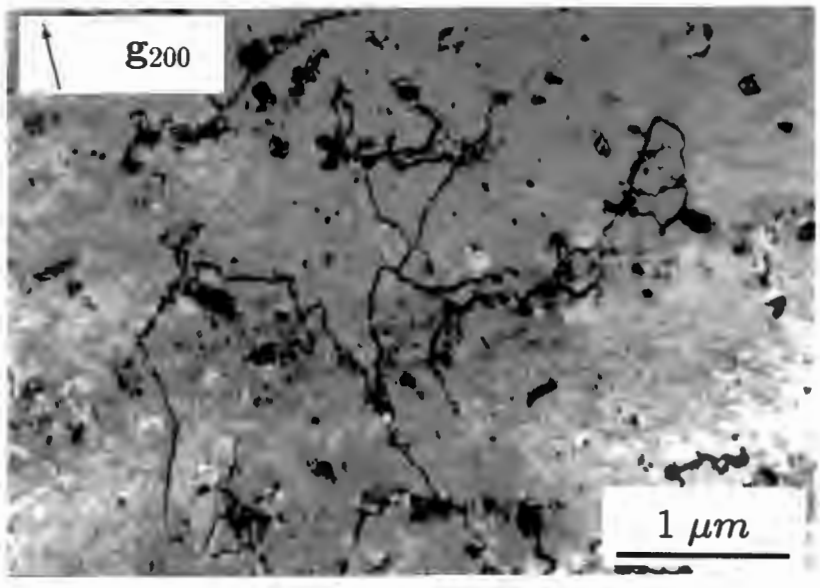

Figure 100: TEM bright–field image of the microstructure of alloy VF619 (Ag), subjected to a total tensile strain of 0.1% after quenching from solution temperature. Initial dislocation tangling is similar to both 1070 and alloy VF617 (Zn).

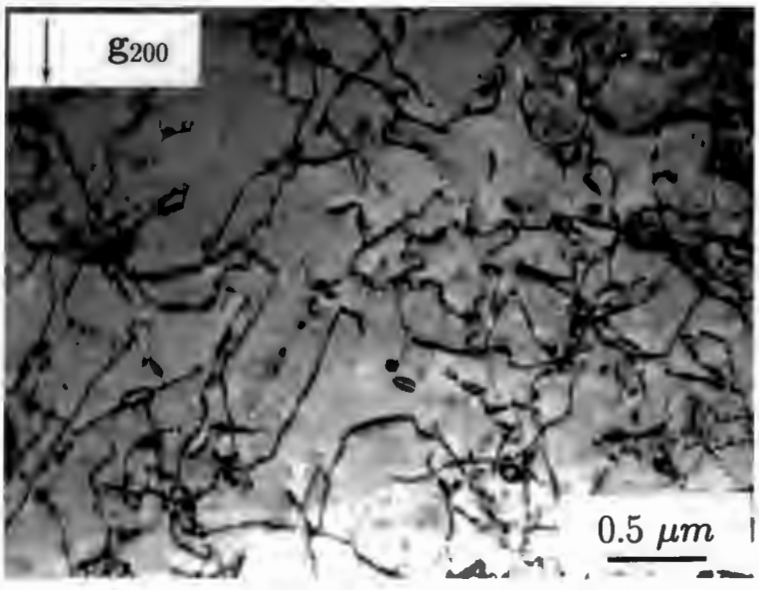

Figure 101: TEM bright–field image of the microstructure of alloy VF619 (Ag), subjected to a total tensile strain of 1% after quenching from solution temperature. Dislocation distribution is relatively uniform.

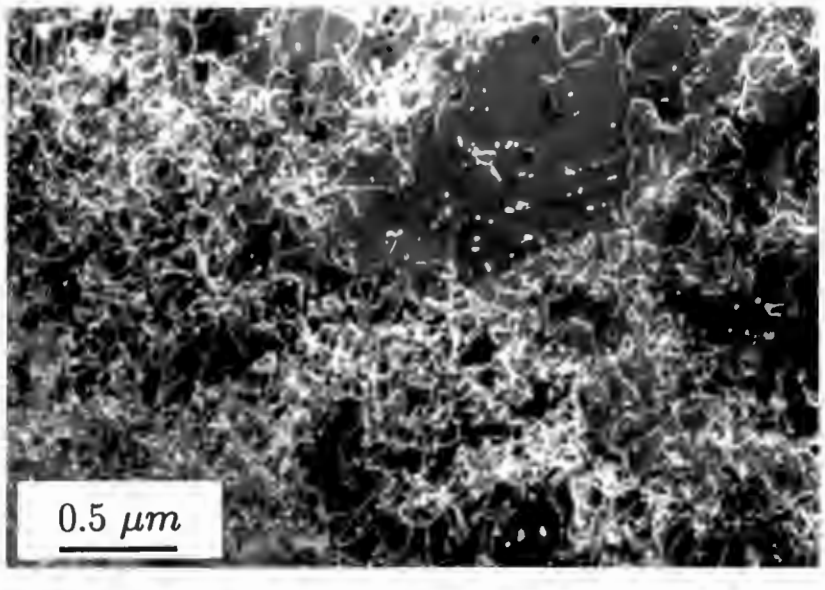

Figure 102: TEM weak–beam image of the microstructure of alloy VF619 (Ag), subjected to a total tensile strain of 17.5% after quenching from solution temperature. Some low dislocation density regions are evident, but generally the accumulation is uniform.

4.8.6 Microstructural Evolution (HVEM)

Two clearly distinct and characteristic deformation modes were observed during in–situ straining experiments in the HVEM. All the alloys deformed by sequential discrete yield events on a microscale, in direct correspondence with the observed features of macroscopic deformation. These, microyield events, were often separated by very little dislocation activity within the deforming grain under observation.

At strains well beyond that required for initial dislocation motion (yield point), no distinction was evident between the collective dislocation behaviour of 1070, VF617 (Zn) and VF619 (Ag). Similarly, no qualitative distinction was observed between the deformation of VF615 (Mg) and alloy 5182. The alloys were therefore able to be divided into two groups according to whether or not they had been alloyed with Mg. A partial exception to this division was the occurrence of some sustained planar dislocation motion in VF619 (Ag), immediately after yielding. The occurrence of planar dislocation arrays and pile–ups was also observed in 5182.

Some examples of this behaviour have already been described in sections 4.3 and 4.5.4. Further examples of the microstructural features reproduced from both video tape and conventional high resolution film are presented in the micrographs following:

Figure 105 illustrates the planar motion of dislocations in VF619 (Ag), observed immediately after the yield point. Two dislocation sources were observed to be responsible for the planar dislocation arrays in figure 105, namely a grain boundary source and an unidentified intragranular source. The latter was responsible for dislocation emission in opposite directions in the same slip plane resulting in pile–ups occurring against two grain boundaries of the actively deforming grain. The operation of the intragranular source (in grain 1) is shown in figure 106.

Propagation of the deformation was observed to occur by the classic mechanism of grain boundary transmission (eg. [203]). Noteworthy, in this case, was the suddenness of yielding in the adjacent grain, the planarity of the observed slip traces and their directional continuity. The rapidly formed slip traces in the adjacent grain are shown in figure 107.

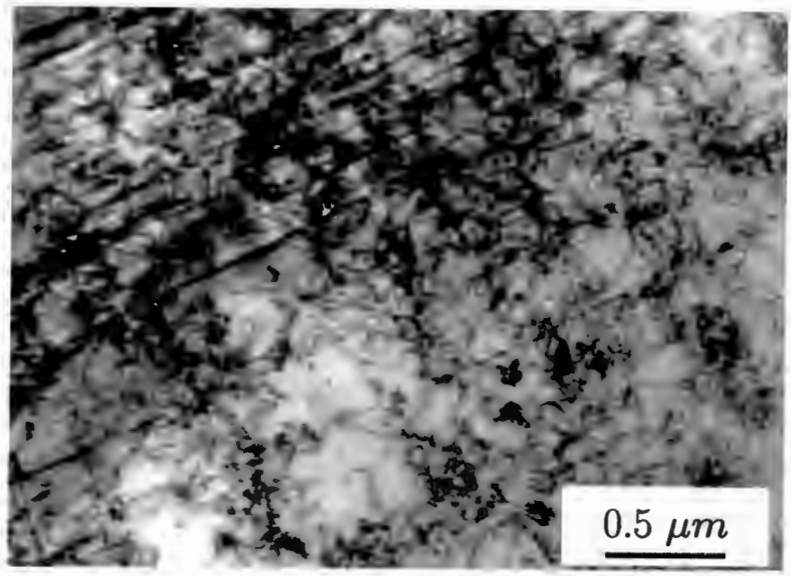

Figure 103: HVEM micrograph of alloy VF615 (Mg) after tensile straining, illustrating dislocations and some straight slip traces.

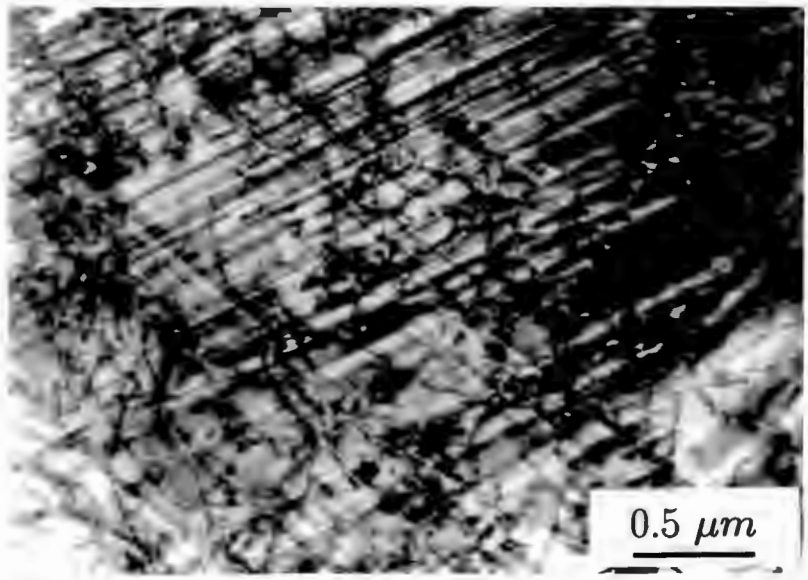

Figure 104: HVEM micrograph of the same region as that illustrated in figure 103 illustrating the rapidly formed intersecting slip traces, with no obvious evidence of cross–slip having occurred.

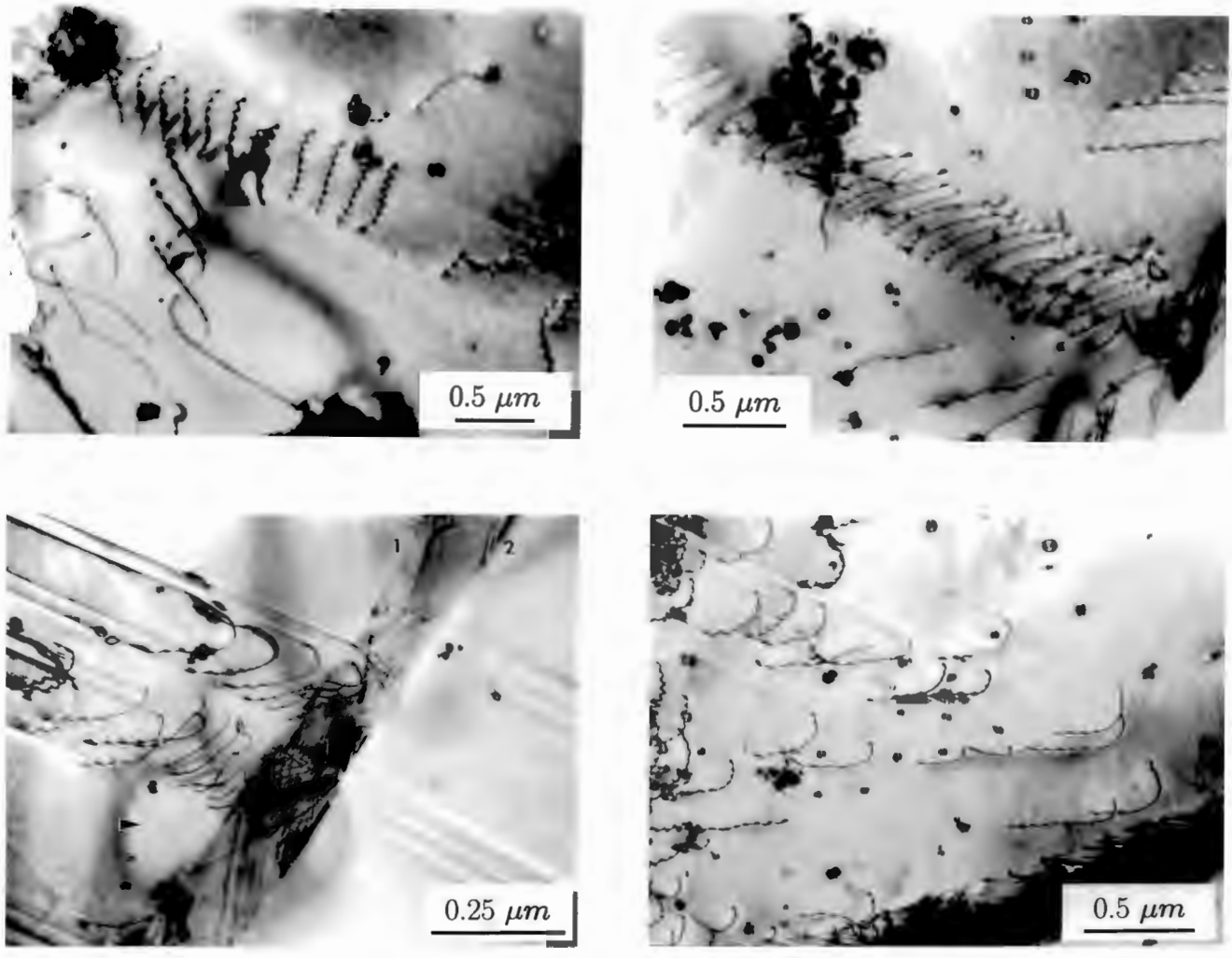

Figure 105: Sequence of micrographs taken from the in–situ deformation of alloy VF619 (Ag), illustrating dislocation motion in planar arrays formed immediately after the yield point. Some grain boundary transmission of slip is evident from grain 1 to 2.

Figure 106: The operation of an intragranular dislocation source responsible for producing a planar dislocation array in grain 1 of the previous figure.

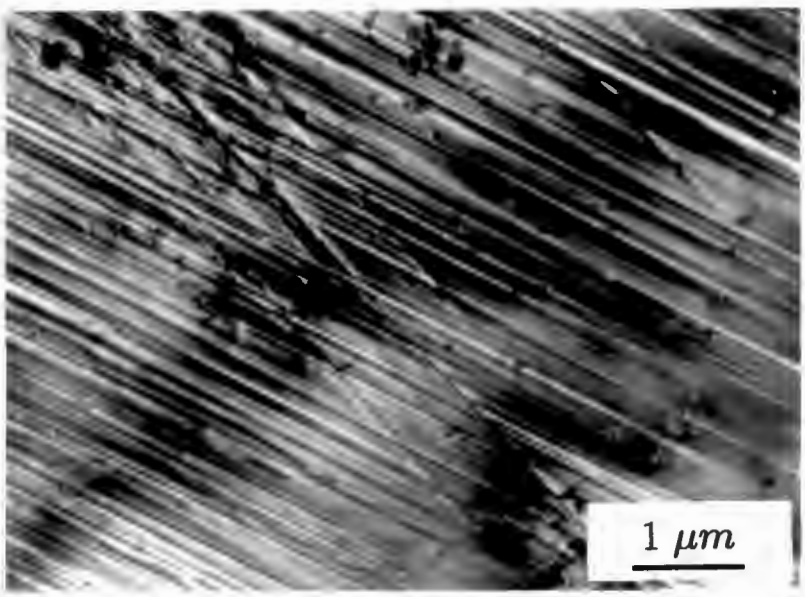

Figure 107: Grain 2 from figure 105, showing a sudden planar yield across the grain resulting from dislocation pile–up against the grain boundary in the adjacent grain (grain 1).

4.8.7 Fracture

The nature of the fracture observed in the 2at.% alloys correlated with the differences observed in their tensile deformation. A distinction can be made between the two different stages of cold rolling deformation as well as the associated specimen geometries.

Subsize Specimens

In the cold worked condition, three failure modes were observed:

1. Plastic instability of a region of the gauge length, followed by tensile overload, in the case of 1070.
2. Plastic instability followed by 45° shear failure through the specimen thickness in the case of both VF617 (Zn) and VF615 (Mg).
3. A combination of plastic instability, shear and delamination in the rolling direction in the case of VF619 (Ag).

After solution treatment and water quenching, however, the fracture mode of all three alloys was similar. Final fracture in all cases was accomplished by 45° shear through the specimen thickness following localised plastic instability (necking) in the gauge length. The size of the reduced area, fractured by ductile shear, correlated with the degree to which dynamic recovery could occur in the alloy. VF615 (Mg), therefore, had the largest shear surface (associated with the least area reduction) and 1070 the smallest.

Full Size Specimens

In the case of full–size specimens, stamped from the ~0.4 mm thick cold–rolled sheet material, the nature of the fracture could again be correlated with the general plastic deformation properties of the alloy.

1070 failed by localised area reduction through the specimen thickness, regardless of the strain rate employed. The orientation of fracture surface was consistently at 90° to the direction of tensile loading with regions of the fracture surface at 60° in some cases. Some deformation banding was observed, but only directly prior to, and in the vicinity of, the final fracture.

Fracture of VF617 (Zn) and VF619 (Ag) was qualitatively similar to 1070, but with a higher proportion of the fracture surfaces at 60° to the tensile axis. No direct correlation was observed between the angle of fracture and the rate of deformation.

In the case of VF619 (Mg), fracture surfaces were consistently oriented at 60°, regardless of the rate of deformation. Deformation band formation, which only occurred at the slower strain rates tested, was not a necessary precursor to this mode of failure. The mode of fracture commonly observed to occur in full–size specimens of the Mg containing alloys is illustrated in figure 108.

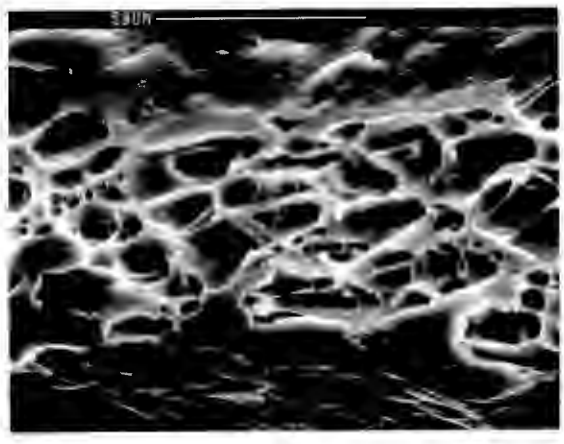

Figure 108: SEM micrograph of the fracture surface of alloy VF615 (Mg) after deformation by the repeated formation of PLC bands. The micrograph indicates the type of fracture surface associated with the deformation band formation in specimens tested under plane stress (W≫T) conditions i.e. a progression of localised necks.

4.8.8 Comment

Only the addition of 2at.%Mg effectively altered the nature of serrated flow exhibited by the experimental alloys, when compared to the base material (1070). The more general characteristics of the tensile deformation were, however, altered by both Ag and Zn

additions. These results can be initially rationalised simply by considering the relatively small solute additions, as well as the small (Zn) and neglible (Ag) atomic radius differences between the solutes and Al.

Tensile test results presented in this section were consistent with both the microstructures observed in the CTEM, as well as their dynamic evolution observed in the HVEM. Finally, features of the surface deformation of macroscopic test specimens correlated well with similar features observed on the surfaces of the HVEM specimens. The SEM surface examination of HVEM specimens is discussed in Chapter 5, section 5.2.4.

Chapter 5

Discussion

5.1 Introduction

This chapter provides a synthesis of the three preceding chapters by discussing both the techniques applied in the course of this work and the associated results. The chapter brings together information on each of the materials under sectional headings based on the presentation of the results in Chapter 4. The experimental techniques are first critically discussed, following which, an examination and discussion of the results of mechanical testing and microscopy is presented.

5.2 Effectiveness of Experiments

5.2.1 General

The emphasis during the course of this work has been placed on comparing the deformation properties of a range of materials. In order to make these comparisons valid, test procedures and experimental variables were standardised throughout. Generally, test temperature, strain rate and specimen geometry were fixed except in two specific cases. The effect of specimen geometry was examined in alloy 5182 (see section 4.5.1) and the effect of strain rate on the flow stress at specific strains was examined in the case of the 2at.% experimental alloys (see section 4.8.3).

5.2.2 Tensile Testing Procedures

Specimen Alignment

It is well established [88] and was further confirmed during the course of this work that inaccurate specimen alignment can affect initial yield point effects. The majority of material tested in tension deformed without a defined yield drop and therefore accurate axial specimen alignment was less critical. In the case of annealed alloy 5182, however, a sharp yield drop was observed to define the onset of macroscopic plastic flow in carefully aligned specimens. Mechanical alignment in this case was achieved by careful positioning of specimens in the grips using a conventional set square.

Surface Polishing

Tensile specimens were mechanical polished utilising standard metallographic grinding discs followed by polishing with diamond impregnated cloths. Caution had to be exercised that this process did not induce damage in the surface layers and alter the subsequent deformation, with specific reference to the initial yielding. Polishing was therefore undertaken prior to any final annealing (where appropriate), in order to ensure that mechanical damage was removed by the annealing process.

Quenching

In all cases, tensile testing followed immediately after the quenching of specimens from the furnace. Where more than one specimen was tested in a set of tests, heat treatments were staggered in order to ensure that specimens were "freshly" quenched prior to mechanical testing. This therefore ensured that natural ageing effects did not result in comparable specimens being tested with varied solid solution solute contents.

5.2.3 CTEM

In the course of Chapter 4 (see eg. figure 34), comment was made on the effect of relative dislocation densities resulting from heat treatments and tensile deformation. No quantitative measurement of dislocation density was made during the course of this work, so such comments are essentially subjective. In order to ensure the validity of comments on relative dislocation densities, however, efforts were made to consider representative regions of TEM foils. Specimens were always examined well away from the foil edge and two or more foils from the same condition were examined in all cases.

5.2.4 HVEM

Experiments in electron microscopes with high accelerating voltages require specific precautions over and above the conventional careful preparation and examination appropriate to CTEM studies. These precautions are detailed in the two sections following, where a division is made between the conventional precautions taken associated with HVEM studies and those specific to the experiments undertaken during the course of this work.

Conventional Considerations

The experimental limitations as well as the practical considerations affecting in–situ deformation experiments in the HVEM have been recently summarised by Butler and Hale [205] and will, therefore, not be discussed in detail here. Generally, however, recognition must be made of the competition between the critical specimen thickness for observing dynamic processes and the radiation damage associated with the necessary accelerating voltages to examine thick specimens. In addition, interactions between dislocations and the foil surfaces should be accounted for specifically when the surface is coated by an oxide or contamination layer [216].

Specific Considerations

All microtensile specimens tested in–situ were annealed and quenched prior to deformation in the HVEM in order to remove any damage produced by specimen manufacture. Also, the time between quenching and testing was minimised by ensuring that heat treatment was carried out immediately prior to jet–polishing and testing in the microscope. Experiments to verify the results obtained were carried out and are discussed at the end of this section.

The alloys tested did not represent the ideal situation of concentrated solid solution FCC alloys approaching the solubility limit [217]. Reasonably high lattice friction forces could be expected, however, given the fact that all material was annealed and quenched prior to testing, thereby maximising the solid solution solute content. In addition, strong obstacles to dislocation motion could be expected in the alloys tested, given the macroscopically observable stress discontinuities present in all cases from the onset of plastic deformation. These factors can be expected to counterbalance the effects of image forces to some extent [216].

In–situ deformation was carried out at room temperature at an accelerating voltage of 1.5 MeV. The temperature was, therefore, at or below the critical temperature for aluminium [217], but the voltage was well above the threshold for radiation damage [178]. The critical temperature (T_V) refers to the temperature threshold above which the steady state vacancy concentration induced by irradiation is lower than the thermodynamic equilibrium concentration [217]. The high accelerating voltage was necessary to ensure observation of specimen thicknesses where the dislocation behaviour approximated that which occurs in bulk specimens [179]. To minimise the effects of working at a high accelerating voltage, microstructural development was largely recorded continuously on video tape via a sensitive transmission tube using a substantially spread beam. Also, observation was often at lower magnifications over a wide region in accordance with the suggestion by Fujita [180]. In addition to being necessary to examine thick areas of the jet–polished regions, the accelerating voltage was similar to that used in comparable work on single crystals of aluminium base alloys (1 MeV [53] and 2 MeV [181]). Tabata and Fujita [181] thoroughly considered the limitations of in–situ deformation and concluded that serrated yielding microprocesses could be observed in thin specimens and closely

related to the behaviour of bulk specimens. Finally, no visible irradiation damage effects [180] were observed during the course of this testing.

Verification of the in–situ deformation observations encompassed various approaches. In addition to comparing the defect microstructures produced in–situ with those produced by bulk deformation (and examined in a CTEM), surface deformation examination and macroscopic tensile tests were also carried out. Macroscopically, full–size ASTM B557M specimens (punched from the same material used for microtensile specimens) were also tested in the same heat treated condition. Further, a comparison was made between the formation of the surface slip–step features of HVEM specimens and bulk specimens. Examples of such features from a jet–polished microtensile specimen, examined in the SEM are shown in figure 109. The commonly observed features of planar slip trace formation, as well as cross–slip associated with grain boundary dislocation pile–ups were seen to occur in–situ in the HVEM and on the surfaces of microtensile specimens as well as on the surfaces of deformed bulk specimens.

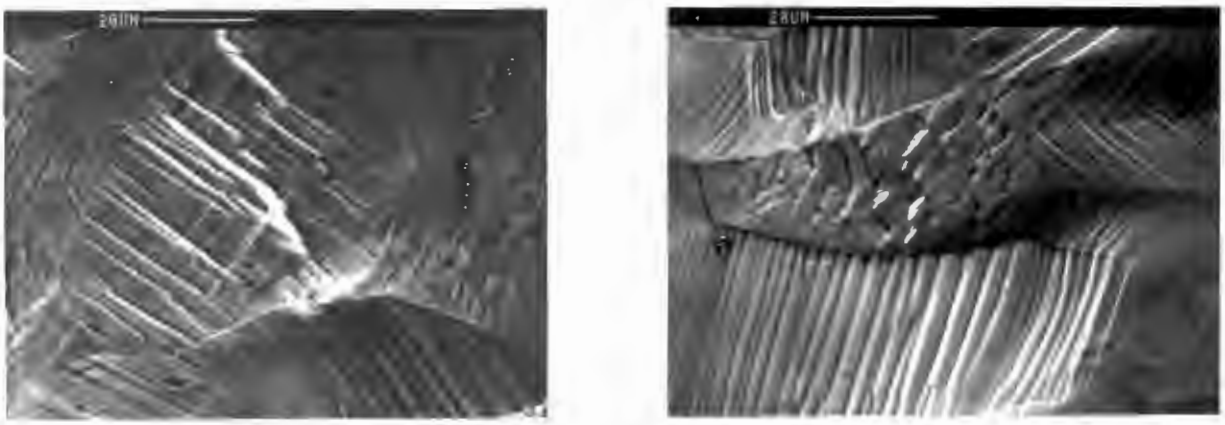

Figure 109: SEM micrographs of the surface deformation of microtensile HVEM specimens (1070) deformed utilising the SEM "straining–stage".

Although bursts of dislocation motion are often observed in in–situ deformation experiments because of the potentially uneven friction of the straining mechanism [181], two distinctions can be considered in the work presented here. Firstly, in terms of the mechanics of the straining, dislocation motion was only recorded during the continuous application of strain using the piezoelectric crystals, which are able to provide very smooth application of tensile strain. The straining stage utilised is reportedly capable of straining with no detectable image blurring at magnifications of up to 150 000 times

[203]. In addition, dislocation burst activity was not immediately concurrent with the application of stress but rather, it was repetitive during the continuous straining of the specimen. Secondly, as has been discussed in Chapter 4 and further in this chapter, dislocation behaviour and specifically collective effects were markedly different between the alloy types investigated. This correlates with macroscopically observable differences as well as previous results and therefore lends credibility to the accuracy of the observed phenomena.

5.3 Tensile Deformation Characteristics

5.3.1 Finite Element Analysis of Specimen Geometry

A finite element mesh was placed on the standard specimen geometry plan and the effect of *elastic* uniaxial loading under both plane stress and plane strain conditions was examined (see also section 4.2.1). Primarily, the aim was to confirm the location of the stress maxima to ascertain the likely location of initial yielding. Type A (flamboyant) deformation markings are known to originate in regions of maximum stress intensity [69]. During the course of testing, the formation of type A markings on the surface of annealed alloy 5182 specimens was primarily in the shouldered regions of the specimen. The maximised pre–yield stress intensity in this region of the specimen was confirmed by the finite element analysis. Yield loci (see figure 24, page 86) indicated that the stress intensity, immediately prior to the onset of plastic deformation, was maximised at the shoulder region and progressively decreased towards the centre of the gauge length. The observed triangular form of type A markings observed (see figure 7, page 15), initiated in the specimen shoulder region, correlated directly with such an analysis.

Type A markings were always formed primarily in the specimen shoulder regions i.e. the regions of macroscopic stress concentrations. Occasionally, however similar markings were also observed to form in other regions of the gauge length. Their existence can be explained by the presence of minor local stress concentrations resulting from roughness of the specimen edges caused by the manufacturing (stamping from sheet) of the plane

stress specimens.

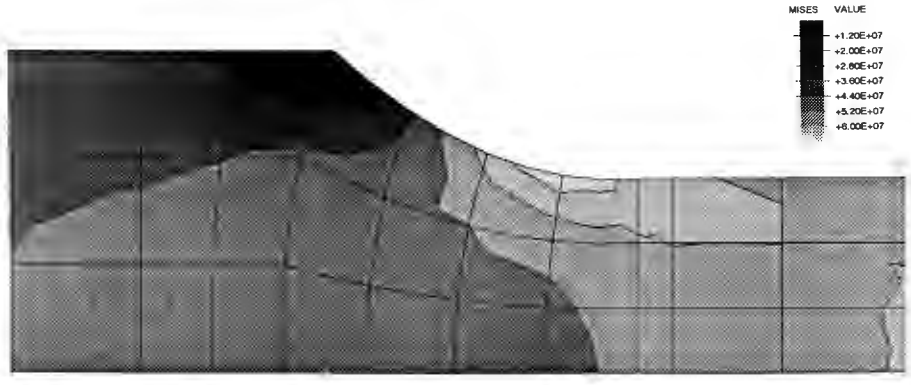

Figure 110: Shading indicating relative stress intensities in an axially loaded ASTM B557M specimen, elastically deformed under *plane strain* loading conditions.

The plane strain analysis which utilised the same mesh as that for plane stress analysis is shown in figure 110. The stress intensity can be seen to be less localised than in the plane stress analysis. This does not preclude the formation of type A markings, but is more likely to induce homogeneous yielding. In this regard, the commercial problem of the undesirable formation of flamboyant markings occurs only during the cold pressing of sheet material, analagous to the plane stress situation. Finally, tensile testing of specimen geometries deformed under plane strain loading conditions was not observed to result in the formation of type A markings. The loading geometry can be considered as one influence on the non–occurrence of type A markings during plane strain deformation. It has, however, also been demonstrated during the course of this work (see section 5.5.4) that the quenched condition (in which the plane strain specimens were tested) suppresses the formation of type A markings. Their suppression results is a result of homogeneous yielding associated with a uniform distribution of dislocations arising from the thermal stresses produced by quenching from solution temperatures.

5.3.2 Comparison of Alloy Types

Commercial Monolithic Alloys

General features of the deformation can be summarised as follows:

1. All the alloys tested (2014, 5182 and 6061) deformed with serrated flow curves consistent with the occurrence of DSA microprocesses. The only exceptions were alloys 2014 and 6061 in the T6 (artificially aged) condition.

2. Only alloy 2014 exhibited discontinuities in the flow stress which could be attributed to a process other than DSA.

3. A defined yield drop was only exhibited by air cooled annealed alloy 5182, but the onset of plastic deformation was markedly more defined in the alloys 2014 and 6061 tested in the T6 condition than in all other cases.

4. The dominant serration type observed at the strain rates tested was regular repetitive load drops preceded by elastic or partially plastic reloading. These are classified as type B or C or serrations respectively.[1]

The existence of small repetitive serrations punctuated by single isolated stress drops in alloy 2014 is consistent with both the composition and surface deformation observations reported for the alloy. Alloy 2014 contains additions of Cu, Mg, Si, Fe, Mn and Zn as shown in table 3, page 68. The deliberate inclusion of any of these solutes may result in a serrated flow curve of the binary alloy in each case (see section 2.5.2). The existence of regular low amplitude serrations in the solution treated condition but not in the artificially aged condition is, therefore, consistent with the alloying additions, but not exclusively attributable to any single addition. Solution treatment can be expected to increase the solid solution content of the alloy, promoting DSA of the mobile dislocations. The removal of the small serrations by artificial ageing suggests that the solutes responsible for DSA are likely to be primarily those required for precipitation hardening, namely Cu and Mg.

The existence of isolated single stress drops in both the solution treated and artificially aged conditions is consistent with the surface deformation observations. The cracked Cu rich inclusions (see figure 40, page 103), readily visible on the gauge lengths of deformed specimens at values of nominal strain above ~5%, were seen to be responsible for extreme deformation localisation. High intensities of slip line formation, consistent with localised plastic flow were regularly observed in the vicinity of the Cu rich inclusions. The EDS composition analysis suggests that the inclusions are $CuAl_2$ particles.

[1]The classification of serration types has been discussed in section 2.3.1, page 10.

The commercial Al–Mg alloy, 5182, exhibited serrated flow in all conditions investigated during the course of this work. Serrated flow in Al alloys has been most extensively discussed in the literature for the case of binary Al–Mg alloys. The 5182 alloy tested in this work produced deformation characteristics largely consistent with the prior work (eg. [79]). In 0.35 mm thick cold–rolled material, deformation was characterised by two successive stress "plateaus" of serrated flow. The first of which, following the critical strain, was accompanied by the single passage of a deformation band front along the gauge length while the second was simply accompanied by the formation of deformation bands at apparently random locations. Serrations were exhibited from the onset of plastic deformation with the occurrence of a distinct critical strain[2] only evident in this and similarly severely cold worked material. The noteworthy condition for the occurrence of a Lüders elongation is discussed separately in section 5.4.2, page 195.

The existence of a second stress plateau suggests that each (randomly located) band is formed in regions of the material in the same state i.e. with approximately the same microstructure. The low work hardening rate, in turn, suggests that some dynamic recovery may be occurring, although CTEM examination shows that alloy 5182 exhibited the lowest capacity, of the alloys tested, to recover during straining. The minimal dynamic recovery is itself consistent with the restricted cross–slip expected as a result of Mg additions [218] and correlates with the lack of cross–slip seen to occur in the HVEM in–situ deformation experiments presented in this work (see section 4.5.4, page 126).

Annealing of alloy 5182 produced tensile deformation characterised by rapid work–hardening after the initial yield, again with very little evidence of dynamic recovery. The increase in serration amplitude during the increase of stress with strain accumulation can be explained on the basis of the increasing strength of dislocation intersections as work–hardening progresses. The increased obstacle strength can be rationalised on the basis of an increasing forest dislocation population [109] and therefore longer waiting times at such obstacles. The mobility of solutes can also be expected to increase with the increased vacancy concentration resulting from plastic deformation. Finally, more effective pinning of mobile dislocations may arise, associated with the enhanced pipe diffusion resulting from the higher forest dislocation densities.

[2]The occurrence of critical strains during the course of this work is discussed further in section 5.3.4, page 191.

The deformation of alloy 6061 only produced a serrated deformation record in the solution treated condition. As in the case of alloy 2014, serrations cannot necessarily be attributed to the presence of a single solute in solid solution. Cu, Mg and Si additions can each be expected to produce a serrated deformation record in the material (see section 2.5.2, page 25.). The general form of the deformation record exhibited in the solution treated condition was similar to that exhibited by hot–rolled alloy 5182, but $\Delta\sigma_{max}$ was approximately 1/3 of that exhibited by alloy 5182. The microstructural processes in alloy 6061 were therefore likely to be comparable to those of alloy 5182 but consistent with the lower total solute content in alloy 6061, specifically the Mg content (approximately 1/5 of that in alloy 5182).

Experimental Monolithic (2at.%) Alloys

Generally, tensile deformation in the experimental alloys, including 1070, was characterised by undefined yield points, some initial work hardening and followed by an extended region comprising a low work hardening rate. Alloy VF615 (Mg) was an exception, which displayed continued work hardening until the end of uniform elongation (onset of plastic instability). The magnitude of $\Delta\sigma$ was similar in all cases except alloy VF615 (Mg) and was observed to increase during regions of work hardening and stabilise during the ideally plastic extension.

A general feature arising from the study is that the addition of 2at.% Ag or Zn to the commercial purity aluminium is insufficient to enhance the serrated flow exhibited by the base material (1070). Either the addition of 2at.% solute (Ag or Zn) is insufficient to cause serrated flow in Al or alternatively the combination of impurity elements present in the material effectively masks the effect deliberate alloy additions. Previous experiments on binary Al–Ag and Al–Zn are both controversial and not conclusive enough to resolve the possibilities (see section 2.5.2, page 25). The general characteristics of the tensile deformation of 1070 was, however, substantially altered by both alloying additions, confirming that the alloys were effectively solution treated. More extended work hardening resulted from both the addition of Ag and Zn to 1070 and the yield stress was substantially raised by the addition of Ag.

Serrated flow was present from the onset of plastic deformation (not preceded by a critical strain) in 1070 as well as in the 2at.% alloys VF617 (Zn) and VF619 (Ag). The serration amplitude was generally observed to increase to a maximum during work hardening, consistent with the expected increase in forest dislocation density during this portion of the deformation [219]. The results, therefore suggest that the dominant operative obstacle, where DSA of dislocations occurs, was the intersection of mobile and forest dislocations. Serration amplitude in all three cases was, however, stable at the same maximum ($\triangle\sigma$) value during the region of low work hardening, suggesting that the operative DSA mechanism was the same. On the basis of the similarities in the deformation, it can be concluded therefore, that the solutes responsible were indeed the impurities initially present in unalloyed 1070 and not a result of the deliberate alloying additions.

Following from the suggestion by Pink et al [55], which was discussed in section 2.5.2, 1070 + 2at.% Zn was quenched from a lower temperature (225°C) in order avoid the effect of vacancy sinks produced by quenching material from higher temperatures. No distinction in the deformation properties between this and material quenched from the standard (400°C) higher temperature was observed. The result therefore again suggests that Zn in isolation is generally not capable of inducing serrated flow in Al or alternatively its effect is masked by the impurity content present in 1070. The reason for this is not entirely resolved but it has been suggested that deformation enhanced precipitation may result in solute depletion of the matrix in Al–Zn alloys [105].

Finally in the case of alloy VF615 (Mg), the high rate of work hardening and increased serration amplitude were consistent with the established role of Mg as the most potent solute for producing DSA effects in Al. The maximum amplitude ($\triangle\sigma_{max} \approx 4$ MPa) in VF615 (2at.%Mg) compared favourably with that of 10 MPa commonly observed in alloy 5182 ($\sim$ 5at.%) confirming the obvious inference that Mg was indeed directly responsible for the enhanced serration amplitude. The generally observed maximum stable value of $\triangle\sigma$ can be rationalised in terms of the expected saturation value of density of mobile dislocations at higher strains [219]. The severe restrictions on dynamic recovery imposed by the addition of Mg, however, is likely to inhibit the saturation of mobile dislocation density to high values of tensile strain, much nearer the rupture strain. The result in Mg alloyed 1070 (and less severely with other alloying additions) is, therefore, the delayed onset of a stable $\triangle\sigma$.

A distinction between the serration amplitude of full and subsize specimens was shown to occur in Chapter 4. For example, in the case of 1070, annealed subsize specimens deformed with $\Delta\sigma \approx 0.3$ MPa whereas the full sized specimens exhibited a serration amplitude of $\sim$3 MPa. The significant difference can be attributed to two factors. Firstly, the smaller thickness (0.4 $\times$ 12.5 mm^2) of the full size specimens could be expected to result in a more dramatic cooling rate when compared to the subsize specimens (3 $\times$ 6 mm^2). A rapid cooling rate would result in an increase in the quenched in defect density, as observed in TEM microstructure examination (see figures 32 and 34 for example). The enhanced defect density could, in turn, be anticipated to provide for more effective pinning of mobile dislocations, and therefore enhanced serrated flow. In addition to the above, annealed $\sim$0.4 mm thick material had a finer grain size after the final anneal. In the case of 1070, the final grain size of the $\sim$0.4 mm thick material was 20 μm as opposed to 75 μm in the case of the 3 mm thick material. The general characteristics of the deformation were, however, similar when the tensile test records of full and subsize specimens were compared.

The effect of strain rate on the flow stress at a constant strain was examined for 1070 and the three experimental alloys. Single full-size specimens were tested at a range of strain rates, between $1 \times 10^{-6}s^{-1}$ and $1 \times 10^{-1}s^{-1}$. This then produced a measure of the apparent SRS rather than the inherent microscopic SRS of dislocations which is not readily accessible to experimental observation (see section 2.2.3, page 7). Taking cognizance of this fact however, the macroscopically measurable flow stress can give an indication of the existence of a negative total SRS and hence the operation of DSA micromechanisms. As outlined in Chapter 4, inconclusive results were achieved from the testing of both 1070 and alloy VF617 (Zn), indicating the relatively mild effect of DSA in these cases. In alloy VF615 (Mg), however, a clear and increasingly negative trend was observed in the flow stress over most of the strain rate range tested (see figure 93, page 161), consistent with the observed intensity of jerky flow in the material. Initially, the measured SRS was close to zero, while at the high end ($\sim 5 \times 10^{-2}s^{-1}$) of the range tested, a sharp increase (positive SRS) was observed, indicating the proximity of the end of the DSA strain rate regime for this alloy. This result is in agreement with current theoretical predictions for the regime of existence of the PLC effect in Al–Mg [109]. The model predicts the strain rate regime of the PLC effect in Al–Mg to be $1.8 \times 10^{-6}s^{-1}$ to $5.8 \times 10^{-2}s^{-1}$.

The result of a similar set of tests (see figure 93, page 161) on alloy VF619 (Ag) confirms the problems associated with applying this type of testing, specifically to precipitation hardenable alloys in the solution treated condition. In section 2.5.3, page 38, the work of Rosen [94] on alloy 2024 was discussed with respect to similar test procedures and the effect of precipitation processes on the resultant stress–strain rate plots. At very slow strain rates, it can be expected that natural ageing will occur during the course of the tensile tests. As the strain rate is increased, less time becomes available for natural ageing during the test, and the strength of the alloy becomes lower at higher strain rates, resulting in an apparent negative SRS. This process would then account for the initial regime of apparent negative SRS observed to result from the constant strain rate testing of VF619. Importantly, this result further highlights the potential inaccuracies which may result from SRS testing at constant strain rates, as opposed to instantaneous strain rate changes in a single test, especially in the case of solution treated material susceptible to rapid natural ageing.

Metal Matrix Composites

MMC materials based on the commercial monolithic alloys 2014 and 6061 were tensile tested in the solution treated (WQ) condition (see section 4.7, page 140). Both sets of materials had additions of 10%, 15% and 20% Al_2O_3 and the alloy 6061 was also tested with the addition of 20% SiC. All reinforcement was in the form of particulate as opposed to whisker additions (size and distribution of particles is indicated in tables 9 and 10).

As shown in table 7, page 140 a progressive strength increase was observed in conjunction with the increasing volume fraction of particulate additions. In addition, alloy 6061 + 20% SiC was more effectively strengthened than the same material containing 20% Al_2O_3. The increased strength of the SiC containing composite can be attributed to the higher strength of the SiC relative to Al_2O_3 [220][3] resulting in a lower likelihood of particle fracture. Particle fracture can be expected to decrease the strengthening effect of the additions as well as aid in initiating premature nominally brittle fracture as discussed in section 5.7.

[3]See page 67 of [220].

In terms of the serrated flow properties of the alloy 6061 based MMC's, $\triangle\sigma$ was observed to be consistent and similar to the monolithic material (0.5–2 MPa), with exception of alloy 6061 + 15% Al_2O_3 (2–5 MPa). This effect can be considered in the context of the mean particle size and spacing in the materials (see table 9).

Table 9: Average particle diameters, calculated interparticle spacing and Vickers hardness for the 6061 based composites.

Reinforcement	Particulate ϕ	Spacing	H_{V20}
Monolithic	–	–	123.8
10%Al_2O_3	14.1 μm	84.5 μm	130.4
15%Al_2O_3	32.2 μm	121.6 μm	151.7
20%Al_2O_3	15.1 μm	40.3 μm	135.3
20%SiC	17.0 μm	45.2 μm	159.6

Particle size can be seen to be similar in all the composites, with the exception of the material containing 15% Al_2O_3. This effect on $\triangle\sigma$ can be understood on the basis of two considerations. Firstly, the addition of a brittle reinforcing phase can generally be expected to plastically constrain the deformation of the matrix [152]. The plastic constraint imposed by all three volume fractions of particulate, in conjunction with the associated stress transfer to the reinforcing phase, are two fundamental bases for the observed strength increases. Secondly, under DSA deformation conditions, the coordination of deformation amongst several grains [96] within a volume of material (after local unpinning of dislocations) can be expected to influence the magnitude of the serrations observed. For a given volume fraction of particulate, the size of the regions of relatively unconstrained material can be expected to increase with increasing particle size. On this basis, the correlation between increased particle size and the observed increase in $\triangle\sigma$ can be rationalised. From table 9, it can be seen that the interparticle spacing and hence the volume of relatively unconstrained material between particulates is maximised in the 15% Al_2O_3 composite. The volume of material available for any single localised yield event (serration) can, therefore, be expected to be similarly maximised and hence produce a larger serration amplitude.

The question that the above rationalisation poses is then, why is the serration amplitude similar in the case of the monolithic material when compared to both the 10% and 20% Al_2O_3 composites? A tentative explanation can be based on the grain size of the composites. A decrease in grain size is known to cause an increase in the serration amplitude [65]. This effect has been explained in terms of the possibility of DSA occurring preferentially at grain boundaries. The particulate inclusions have the effect of pinning the grain boundaries and hence minimising grain growth during the annealing process. The resultant grain size is therefore smaller in all the composite materials relative to the monolithic material and can therefore be expected to offset the decreased serration amplitude associated with the inclusion of particulate reinforcement.

The composites based on alloy 2014 displayed different deformation characteristics to those based on alloy 6061, most notably in terms of a strength *decrease* with increasing volume fractions of particulate. The strength decrease associated with the increasing volume fractions of particulate, in contrast to the material based on alloy 6061, can be rationalised on the basis of the strength differences between the two matrices. The higher strength of alloy 2014 means that the stress transfer required to fracture the Al_2O_3 reinforcement is more readily achieved than in alloy 6061. The net result of this is the premature fracturing of particles. The full reinforcement potential associated with a given volume fraction of (higher strength) particulate is, therefore, not realised. A direct comparison of the fracture surface micrographs in figures 84 (2014 + 20% Al_2O_3) and 78 (6061 + 20% Al_2O_3) shows the greater extent of particle fracture occurring in the stronger (2014) matrix material. In this regard, it can be anticipated that additions of a stronger or more fracture resistant reinforcing phase would reproduce the same trend observed in alloy 6061. Increasing the volume fraction of an appropriate particulate reinforcement could be expected to produce an increase in strength proportional to the volume fraction of such particulates. Limited availability of composite material, however, did not allow for a systematic study of the effects of particle size, strength and volume fraction during the course of this work. Variation of these parameters could be expected to further clarify the suggestions presented in the current analysis.

Serration amplitude in alloy 2014 was generally similar to the monolithic material and consistent at $\sim$1 MPa except for the material containing 20% Al_2O_3, which had an higher average $\triangle\sigma$ higher at $\sim$2 MPA. Again by considering both the measured particle size

Table 10: Average particle diameters, calculated interparticle spacing and Vickers hardness for the alloy 2014 based composites.

Reinforcement	Particulate ϕ	Spacing	H_{V20}
Monolithic	-	-	151.4
10%Al_2O_3	11.4 μm	68.1 μm	162.5
15%Al_2O_3	13.6 μm	51.3 μm	173.8
20%Al_2O_3	27.2 μm	72.5 μm	196.9

and the interparticulate spacing presented in table 10, these results can be understood in a similar way to the case of composites based on alloy 6061. Alloy 2014 containing 20% Al_2O_3 had particles with an average diameter which was more than double that of either the 10% or 15% Al_2O_3 reinforced material, both of which had approximately similar particle sizes.

5.3.3 The Effects of Cold Rolling and Specimen Geometry

Commercial alloy 5182 was tested for the effect of cold–rolling reduction on serrated flow characteristics in both the cold–worked condition as well as cold–worked followed by a solution anneal. Subsize 3 mm thick specimens were tested in all cases except for material cold–rolled to 2 mm and 1 mm thickness, where the specimen thickness corresponded to the initial plate thickness. In addition, the effect of varying specimen thickness was examined on material previously cold–rolled to 3 mm thickness. 3 mm, 2 mm and 1 mm thick specimens, as well as circular cross–section specimens with a diameter of 2.8 mm, were tested in the cold–rolled and also the solution annealed conditions.

The maximum serration amplitude was variable in the purely cold–rolled material, while a consistent increase with prior rolling reduction was observed in material which had been subsequently annealed. An incubation strain was only observed in the cold–rolled material reduced to a thickness of 3 mm or less. All other cases tested exhibited jerky flow from the onset of plastic deformation. The increase in $\Delta\sigma$ (accompanied by an increase in tensile strength) can be attributed to a more refined recrystallised grain

size produced in the more heavily cold–rolled material. In addition, specimen geometry effects also influence the value of $\triangle\sigma$, as discussed below. In the purely cold–worked material, a significant increase in $\triangle\sigma$ was only observed in the specimens machined from 1 mm thick material, which is again attributable to the specimen geometry effect discussed below. The variation in critical strain with prior cold–rolling deformation is not easily understood but it has been recognised that the variation of material or experimental parameters may affect the properties of the critical strain [109].

The effects of cold–work on serrated flow properties are not well defined and contradictions arise in the existing literature. As discussed in chapter 2, cold–rolling deformation has been observed to diminish the range of existence of jerky flow or suppress it completely. These effects may, however, be a result of deformation induced precipitation [105] decreasing the solute concentration in solid solution. Korbel and Dybiec [35] have shown a strength increase and corresponding increase in $\triangle\sigma$ to accompany cold–rolling reductions in binary Al–Mg. This largely corresponds with the observations of the work presented here and suggests that caution must be taken when examining the effects of cold–rolling deformation in alloys where the solid solution solute concentration is unstable under plastic deformation.

The serration amplitude was substantially increased in 3 mm thick material as the specimen thickness was decreased concurrent with the appearance of clearly visible 60° deformation bands on the surface. This was observed for material that had been purely cold–rolled as well as that which had been subsequently annealed. The suggestion from this result is that the change of specimen cross–sectional area results in a different mode of deformation arising from the transition from plane strain to plane stress loading conditions. The value of $\triangle\sigma$ must, therefore, be recognised as being potentially influenced by factors other than microstructural variables. Where comparative remarks or calculations based on the value of $\triangle\sigma$ are made, the test conditions including specimen geometry should, therefore, be accurately documented. The increase in $\triangle\sigma$ associated with the decrease in specimen thickness can be attributed to the constraints on the deformation imposed by the plane stress loading geometry. Deformation can no longer proceed by successive shear band formation but instead relies on the formation of local necks in the gauge length [72]. Circular cross–section specimens deformed with characteristics essentially similar to rectangular section specimens tested under plane strain conditions. In

addition, the fracture mode of the two geometries was similar i.e. rapid ductile shear as discussed in section 5.7.

5.3.4 The Occurrence of a Critical Strain

The majority of tensile deformation testing undertaken during the course of this work was carried out on solution treated and quenched alloys, which were consistently characterised by the onset of jerky flow immediately after the onset of macroscopic yielding. In addition, this was followed by an increasing serration amplitude during periods of work hardening, and a stable amplitude during periods of straining at approximately constant nominal stress (see figure 45).

The occurrence of a classic incubation strain followed by well defined serrated flow was only observed in cold–rolled unannealed 5182. In this case, the incubation strain was initially observed to be absolutely smooth on deformation records produced using a conventional analogue chart recorder. Subsequent deformation records acquired using a computer interfaced to the tensile test machine showed this initial portion of the curve to be lightly serrated (see figure 43). The initial elongation could still be classified, albeit less strictly, as an incubation strain as it was followed (at a definite point in the elongation) by the sudden onset of dramatically larger serrations.[4] In addition, the major serrations were accompanied by the onset of macroscopic strain localisation in the form of a propagating band front.

A simple physical rationalisation of the occurrence of a critical strain in cold–worked 5182, but not in the same material which had been solution treated and quenched, can be based on the microstructures prior to tensile deformation. In the case of quenched 5182 (which does not deform by the initial propagation of a Lüders front), TEM investigations have shown the microstructure to be characterised by an approximately homogeneous and relatively high dislocation density (see figure 52). These dislocations can be expected to act as immediate and effective obstacles to the passage of mobile dislocations, thereby acting as sites for DSA from the onset of plastic deformation. In fact, this argument

[4] A more formal definition of the critical strain relies on the change from positive to negative total SRS of the flow stress.

holds true for the case of all the materials tested in the quenched condition, all of which consistently displayed a high initial density of quench associated defects (see figures 94 and 97). Dynamic studies in the HVEM confirmed the role of quenched in dislocation loops in this regard, as acting as effective pinning points during the passage of mobile dislocations (see figure 105).

In the specific case of heavily cold–rolled alloy 5182, which displayed the incubation strain effect, consideration must be given to the different initial microstructure. TEM examination shows it to be characterised by an extremely high dislocation density with very little evidence of the prior occurrence of dynamic recovery processes (see figure 50). Although a substantial proportion of the mobile dislocations in such a microstructure can be expected to be entangled and aged, some dislocations should be free to glide. The sequence of microstructural events upon tensile straining would then be initiated by the motion of the unpinned dislocations, over relatively short distances compared to the initial motion in material which had not been annealed. Dislocations which were both glissile and free to move would be "used up" relatively quickly as they encountered the strong obstacles resulting from the previous cold working of the material. Subsequent to the motion of these initially unpinned dislocations, breakaway from the well developed tangles would be necessary, resulting in the large stress drops which follow the initial incubation strain. Alternatively, mobile dislocation creation and motion on different operative slip systems to those predominant during cold–rolling may dominate initially, as a result of the different loading geometry. As in the preceding argument, such dislocations would soon be arrested by the high density of forest dislocations resulting from the prior cold–rolling. Ageing of such dislocations, followed by unpinning and associated strain localisation could be expected to ensue.

In all cases described above, the results lend support to the intersection between forest and mobile dislocation obstacles being the predominant sites for the occurrence of DSA effects.

The occurrence of one or more critical strains has recently been extensively discussed and modelled in terms of the evolution of a critical dislocation density [109]. The work concentrated on modelling the effects of changes in strain rate or temperature on the strain range and occurrence of one or more critical strains. Although neither of these variables

was systematically changed during the course of the present work, some comment can be made in the context of the model proposed by Kubin and Estrin [109]. The occurrence of any of the critical strains is not always accessible to experiment, and this may be the case under the specific experimental conditions of the present work. Although the effect of initial microstructural variations in the same material was not explicitly covered by the model, the effect of varying material constants and elementary dislocation mechanisms was acknowledged as potentially affecting both the position and height of the determining parameter, Ω.[5] Furthermore, the variation by several orders of magnitude of the strain rate regimes for the occurrence of jerky flow (and associated critical strains) when material or experimental variables are altered was also acknowledged. Finally, Kubin and Estrin's model covers those cases where the critical strain may be too small to detect and so the lack of incubation strains observed under the very specific conditions of the present work do not necessarily contradict its predictions.

5.4 Surface Deformation

Surface deformation features on the pre–polished gauge lengths of tensile specimens were examined in the SEM at various values of strain (see eg. figure 30). The gauge lengths of MMC tensile specimens were, however, only examined after fracture because of limited material availability.

5.4.1 Comparison of Alloy Types

Sanders [169] examined the microstructure, slip distribution and strain hardening of a range of commercial aluminum alloys, including alloys 5182 and 6061, tested in both uniaxial and biaxial tension. Generally, dispersion strengthened alloys displayed a wavy slip mode together with a resistance to strain localisation. Both precipitation strengthened and solid solution strengthened alloys exhibited more localised deformation and lower capacities for biaxial strain hardening. The alloys tested in the course of the present work

[5]The reader is referred to section 2.7, page 50 for a more comprehensive description of the model discussed here.

all fall into the latter category, with the main distinction between them being the capacity to exhibit macroscopically resolvable surface markings (deformation bands), as discussed in section 5.4.2.

Generally, the observations were self consistent throughout, with no major deviations observed in surface slip characteristics. The current work suggests the effective potential of similar experiments using in–situ deformation in the SEM to analyse the rapidity and ease of formation of characteristic surface slip features. Work of this nature could be expected to compliment existing dynamic studies carried out by Neuhauser et al (eg. [167]).

Observations of the surface deformation features in the experimental alloys (see section 4.8.4) correlated well with the dynamic evolution of microstructures observed in the HVEM. At low strains, planar slip features were regularly observed with features consistent with cross–slip in the vicinity of the grain boundaries. Higher strain deformation produced intensification of the existing slip traces and, finally, cross–slip associated features within the central regions of the grains. Surface features of ruptured specimens demonstrated extensive slip band intersections and a well developed waviness of the slip traces. Finally, continuity of the slip trace direction across grain boundaries was frequently observed indicating the collective effects between deformation in adjacent grains. These observations were verified by examining the surface deformation features of HVEM microtensile specimens in the SEM (see figure 109). In–situ HVEM deformation , discussed in more detail in section 5.6, revealed planar motion of dislocations in the early stages of deformation, followed by cross–slip at grain boundary pile–ups. The higher strain deformation was characterised by dramatic variations in the number of simultaneously active slip systems as well as the amount of cross–slip observed, depending on the alloy being tested.

In the case of the MMC material, the surface deformation associated with the fracture or interface decohesion of the particulate inclusions is an effective to aid in understanding specific features of the tensile deformation characteristics. Limited availability of material meant that surface features of the MMC's were not examined at intermediate strains prior to fracture. The implication is that the surface deformation features are most relevant to fracture and are accordingly discussed in section 5.7 in this chapter.

5.4.2 Occurrence of Band Formation

Three factors determined the occurrence of macroscopically observable band formation. Firstly the alloy type and solute content, as banding was only observed to occur in the alloys which were primarily alloyed with Mg. Secondly, in a solution treated alloy which is susceptible to deformation by the formation of bands, a critical grain size is necessary [97, 98] for band formation and, finally, the specimen geometry determines the nature and orientation of the bands (see section 5.3.1).

5.4.3 The Distinction Between Lüders and PLC Bands

The literature on inhomogeneous deformation contains many references to both Lüders bands and PLC bands (eg. [46]), and occasionally these are used interchangeably [71, 81, 137, 212]. On the basis of observations made in the course of this work, however, the fundamental distinctions between the two can be clarified. Both situations are the result of the mechanical response of the material being tested to the microstructural instability present at different stages of the deformation.

Lüders type deformation is most commonly associated with the inhomogeneous yielding at the onset of plastic deformation in polycrystalline steels [80, 212, 221, 222, 223], but may be observed in other contexts including the deformation of single crystals [123]. The formation of both Lüders and PLC bands is dependent on the macroscopically operative stress system of the specific loading geometry, the most obvious distinction being between plane stress and plane strain loading conditions. The result of this is that Lüders and PLC bands in the same specimen can be expected to have exactly the same orientation and the results of the work on the orientation of Lüders bands [82] can, therefore, be generalised to bands whose microstructural origins lie in DSA phenomena.

Essentially a Lüders band can be defined as a deformation band which initiates and propagates immediately after the onset of plastic deformation. The propagation of such a band then occus at approximately constant stress until uniform deformation of the gauge length (the single passage of a band) has been achieved [46]. Microstructurally, this is

associated with successive yielding of adjacent areas of the gauge length by various mechanisms, eg. predominantly dislocation unpinning from carbon atmospheres in mild steel or the creation of mobile dislocations in annealed Al–Mg (as discussed in the next section of this chapter). Subsequent to the Lüders extension (ε_L), deformation then proceeds homogeneously or inhomogeneously depending on the alloy in question and the conditions of deformation. This is specifically dependent on whether DSA micromechanisms are operative.

PLC bands refer to the repeated formation (and propagation under specific conditions) of deformation bands associated directly with DSA phenomena. PLC bands form repeatedly and are frequently observed to persist until fracture, which invariably occurs in such a band (see also section 5.7). In addition to the above, as has been observed in this work, the formation of shear bands may occur only immediately prior to the final fracture. In this case, band formation may occur prior to fracture without necessarily being preceded by either Lüders or PLC band formation, but they are likely to be associated with serrated flow, as has been observed in the course of this work and by others [43].

A further potentially complicating factor in attempting to clarify the appropriate terminology, is the possibility of the interrupted passage of a Lüders front. This has been observed in the course of this work, as well as in mild steels deformed in the "blue–brittleness" temperature range [4] and on other occasions [137]. The interrupted passage of a Lüders front is associated with the DSA of dislocations at the front [42, 46]. The rate sensitivity of the interrupted band propagation results from the inherent rate sensitivity of DSA [52] or, alternatively, it has been suggested to arise from the time available for dynamic recovery of internal stresses (stress relaxation) at the band front [81, 35].

In conclusion, therefore, this section has attempted to clarify the potentially confusing terminology applied to deformation banding as well as to illustrate the similarities between both PLC (type B) banding and Lüders bands.

Elucidation of the mechanism by which PLC bands, which form in the latter stages of plastic deformation, do or do not propagate was not achieved in the present work. In both annealed and cold–worked material, such bands were observed to initiate at apparently

random locations in the gauge length and then to propagate on some occasions. Propagation of these bands was never observed to occur over the entire gauge length. The most likely explanation of the behaviour described is that successive serrations, accompanied by the formation of single isolated bands, were the result of a combination of internal stress concentrations and DSA microprocesses. Band formation which, on occasions was self propagating, probably initiated at the highest local internal stress concentration [46]. The internal stress concentrations could then provide the impulse for local unpinning of aged dislocations from glide plane obstacles. Material adjacent to that where a band had just formed could be expected to be in a higher state of internal stress than other regions of the gauge length [88], favouring discontinuous band *propagation*. Discontinuous band *propagation* during the latter stages of deformation was, however, not observed at the relatively low strain rates tested. This can be attributed to the relatively long reloading time between successive serrations allowing for localised (in the vicinity of the band) stabilisation of the microstructure. Stabilisation would be likely as a result of internal stress relaxation in material adjacent to a recently formed deformation band [35] caused by dynamic recovery, secondary slip [35, 224] or solute reordering [183, 225].

5.5 Microstructural Observations (CTEM)

The general features of the microstructural evolution recorded during CTEM observations have been incorporated, where appropriate, into various sections of this chapter. Some specific considerations are, however, outlined in the following subsections.

5.5.1 Commercial Monolithic Alloys

The commercial binary Al–Mg alloy, 5182, was extensively examined using CTEM for the evolution of microstructure during tensile straining. Heavily cold–rolled material deformed via the repeated formation of deformation bands on the surface of the specimens during extension at approximately constant stress (see eg. figure 43). The implication of deformation at constant stress is that bands were successively formed in material in an approximately similar microstructural condition [46]. The CTEM observations bear this

out, in that no obvious changes in the microstructure were evident concurrent with the accumulation of tensile strain.

In the case of annealed material, the development of the microstructure is discussed in subsections 5.5.3, 5.5.4 and 5.5.5. The two distinguishing factors were firstly, the rapid accumulation of dislocations with increasing strain and the absence of any dynamic recovery, as has previously been reported for materials deformed under DSA conditions (eg. [175]). Secondly, no direct evidence was found for the existence of micro–banding or micro–shear banding associated with the deformation on a microstructural level.

This fact that no micro–shear banding was observed was unexpected, given previous work which has discussed the role of such features in strain localisation during the cold–rolling of Al–Mg [172] and in the tensile deformation of steel [173]. In this context, it is worth noting that HVEM observations during the present work could be interpreted to suggest that the rapidly formed coarse slip bands (CSB) produced during in–situ deformation may be the precursors to the formation of micro–shear bands. The coordinated penetration of a dislocation substructure (and the associated CSB formation) by the avalanche glide of a group of mobile dislocations has been previously suggested to be the necessary precursor to the formation of micro–shear bands [172, 173]. Finally, polished and etched cross–sections of the fracture surfaces of alloy 5182 specimens, which had failed by rapid ductile shear, showed the presence of grain–scale[6] shear bands oriented parallel to the fracture surface. Grain–scale shear bands formed during the plane strain extension of Al–Mg sheet have been attributed to crystalline slip and associated dislocation avalanches which become coordinated over relatively large distances [135]. These distances may correspond to a few grain diameters in fine grained material [135] and the end result is the formation of sample–scale shear bands [136].

5.5.2 Experimental (2at.%) Alloys

The microstructural evolution in the experimental alloys, observed using CTEM, indicated no obvious features distinct to deformation under DSA conditions. A steady decrease in

[6]Shear bands are termed microscopic [226] or grain–scale [227] when they cross a few grains, or alternatively, macroscopic [228] or sample scale [227] when they have grown to cross a the specimen.

the capacity for dislocations to dynamically recover was observed concurrent with the addition of Zn, Ag and Mg to 1070, in that order. In 1070, the ready formation of a cell structure was observed to begin at low values of tensile strain (see figure 33). VF617 (Zn) was very similar to 1070, whereas VF619 (Ag) only displayed signs of cell formation at much higher strains. The alloy VF615 (Mg), consistent with the commercial Al–Mg alloy 5182, showed no sign of cell formation. As has been previously discussed, these results can be attributed to the general restrictions on dynamic recovery produced by solutes in solid solution, most dramatically in the case of Mg.

5.5.3 Yield Point in 5182

An initial yield point is classically associated with the mass creation or multiplication of dislocations, their unpinning from specific sites or a combination of the three [88, 184]. In the course of testing alloy 5182, a distinct yield drop was observed to sometimes precede the Lüders extension. Also, the formation of type A markings at the yield point, as well as the subsequent passage of the Lüders band, have been shown in Chapter 4 to be associated with a significant increase in the dislocation density.

Prior to yielding, the recrystallised (300°C, 30 mins, AC) alloy 5182 had an extremely low dislocation density (see figure 51), in contrast to that of material *quenched* from 450°C, shown in figure 52. In terms of their deformation properties, the two heat treated conditions were distinguished by the absence of a Lüders extension in the latter case, in spite of their similar grain sizes. The suggestion from these observations is that the high uniform density of dislocations (arising from thermal stresses associated with the quench) is sufficient to remove the yield point inhomogeneities which were observed in the material air cooled from a lower temperature.

In work on fine grained (0.5–20μm) Al–6wt.%Ni, Lloyd [229] observed both a yield drop and the formation of Lüders bands at the finest grain sizes. In this case, the inhomogeneous yielding was not attributed to solute pinning effects, but rather to an initial shortage of mobile dislocations resulting from an absence of easily operated dislocation sources. Microstructural observations in alloy 5182 suggest that mobile dislocations are

readily produced at triple point junctions, grain boundaries and inclusion matrix interfaces (see section 4.5.3). Because of the low thermal stresses associated with air cooling, however, these dislocations have to be created en masse at the yield point and during the subsequent passage of a Lüders band. In contrast to this, the high density of dislocations observed in the quenched material apparently allows for more homogeneous initial yielding.

Finally, the above discussion does not preclude Mg as a possible element for inducing yield drop and Lüders extension effects in Al, as systematic static ageing tests were not conducted. The results do, however, suggest that the major contribution to the observed effects was the mass creation of mobile dislocations. These dislocations are then susceptible to being aged while held up at local obstacles, including grain boundaries [65] during the passage of a Lüders front, thereby causing the discontinuous propagation of such a front.

5.5.4 Stretcher Strain Markings

The formation of type A (random, flamboyant) markings in industrial press–forming operations is aesthetically undesirable. As has been discussed in section 2.4.1, empirically based pre–treatments have been devised to minimise the occurrence of type A surface markings. Briefly, the three methods are as follows:

1. "Pinch–rolling" or "skin passing" entailing a low deformation cold–roll pass.
2. Annealing followed by quenching.
3. Production of material with a large grain size.

The first has been explained in terms of tearing dislocations away from their solute clouds [61] however, no explanation has been put forward for the second method. A large grain size probably decreases the likelyhood of coordinated deformation amongst a group of grains. Large grains are, however, not entirely desirable because of the associated tendency for larger grained material to develop "orange–peel" type surface roughening.

The results discused in the previous section are able to demonstrate the usefulness of the first two methods described above, in removing the occurrence of type A surface markings. In the first case, "pinch–rolling" produces a homogeneous distribution of mobile dislocations, which are then readily able to glide and multiply during subsequent cold–forming. The second method is consistent with the removal (by quenching) of ε_L, in a tensile test, as discussed in the previous section. The thermal stresses associated with quenching are capable of producing sufficient mobile dislocations to homogenise yielding a tensile test and therefore the same is likely in industrial cold–forming operations.

Finally, an interesting observation mentioned in Chapter 4 was the indistinguishability between the microstructures observed in conjunction with the formation of type A deformation markings and the passage of the Lüders front. The conclusion which can be drawn is that both situations represent formerly unyielded material deforming by exactly the same mechanism. The difference between the surface markings observed in each case result from the operative combination of internal and applied stress. Type A markings are known to result from the material response to local stress concentrations [68] and this has been confirmed by the plane–stress based finite element analysis (presented in section on 4.2.1 and discussed in section 5.3.1) in this work. The passage of a Lüders band, then, represents a succession of similar microstructural events to those responsible for the formation of type A markings. The apparently more orderly Lüders front is then simply a mechanical response of the specimen produced by the successive localised formation of necks through the gauge width [72].

5.5.5 Planarity of Dislocation Structure

Martin [183] has suggested that the microscopic heterogeneity associated with the PLC effect is, in part, associated with heterogeneous glide of dislocations confined to specific glide planes. Further, Mg, the solute most commonly associated with the PLC effect in Al alloys, is known to severely inhibit dynamic recovery processes [103], a process commonly associated with restricted cross–slip. The results presented in this thesis bear out these observations.

HVEM observations, discussed in section 5.6, have illustrated the connection between

restricted cross–slip and the severity of occurrence of the PLC effect in Al alloys. In addition, CTEM examination of alloy 5182 has shown that pre–macro yielding prior to the macroscopic passage of a Lüders band is associated with the emission of planar dislocation arrays in select, appropriately oriented, grains throughout the gauge length. This observation confirms the suggestion by Vreeland et al [230], that the pre–yield micro strain is uniformly distributed in materials which subsequently deform by Lüders band propagation. Subsequent deformation, while not strictly achieved by the motion of dislocations in distinct planar arrays, was characterised by yielding on a single dominant slip system. The grounds for this deduction come from the observation of predominantly parallel dislocations observed to occur in recently yielded grains of both alloys 5182 and VF615 (Mg) (see figures 54 and 61).

5.6 Microstructure Evolution (HVEM)

Previous studies utilising in–situ deformation in the HVEM have been discussed in section 2.6.3. In brief, single crystals of Al–Mg have been investigated on two occasions [53, 181]. Tabata et al [181] compared the results of in–situ deformation of Al–Mg single crystals to pure Al single crystals of the same orientation and confirmed that the microstructural heterogeneity associated with PLC type deformation was accessible to experiment under in–situ deformation conditions.

Nohara et al [53] investigated the effect of temperature on dislocation motion in Al–3.3at.%Mg single crystals at an accelerating voltage of 1 MeV. At temperatures corresponding to macroscopic manifestations of the PLC effect, rapid and simultaneous formation of slip bands was observed. Below the PLC temperature regime, pinning and bowing of dislocations was observed. At temperatures above the same regime, smooth, viscous and simultaneous motion of dislocations took place. In the work of Tabata et al, Al–0.3wt.%Mg single crystals were deformed at both -80°C and room temperature at an accelerating voltage of 2 MeV. The PLC effect was attributed to sudden bursts of dislocation motion after dislocation pile–up at obstacles in the glide plane. Dislocations were observed to suddenly cross–slip and multiply followed by the ready formation of coarse slip bands. Waiting time at dislocation tangles was reduced at -80°C and dislocation

motion was observed to become more smooth and homogeneous, corresponding to that observed in pure Al.

In the present work, the results of which have been presented Chapter 4, polycrystalline alloy 5182, 1070 and three experimental alloys consisting of 1070 + 2at.% additions of Zn, Ag and Mg were deformed in–situ in the HVEM. All testing was at room temperature and at an accelerating voltage of 1.5 MeV. All material was tested as soon as possible after quenching from the annealing temperature.

The observed deformation characteristics could be divided into two cases depending on whether or not the metals had been deliberately alloyed with Mg. The distinction correlated directly with macroscopic features of the deformation, where only the addition 2at.% Mg altered the serration amplitude observed in annealed and quenched 1070. Alloy 5182 and 1070 + 2at.%Mg were observed to deform macroscopically via the repeated formation of PLC deformation bands.

An exception to the above was the formation of distinct planar dislocation arrays in the alloy containing 2at.%Ag during the initial stages of in–situ deformation. This effect can be rationalised in terms of the precipitation characteristics of the alloy and the formation of pre–precipitation solute clusters [231]. Of the five materials tested in the HVEM, only the 2at.%Ag alloy was readily susceptible to room temperature age hardening.

5.6.1 Al–Mg Alloys

Deformation was characterised by the rapid formation of parallel slip bands consistent with the activation of a particular slip system in each isolated yield event. The major yield events, probably corresponding to the initiation of a single serration at a macroscopic level, were interspersed with significantly lower velocity (viscous) motion of dislocations. The slower motion of a few dislocations, therefore, preceded the more dramatic and catastrophic mass motion motion of dislocations. During the events prior to sudden collective motion, dislocation segments were observed to rotate about a single pinning point or alternatively to slowly move between pinning points in a single glide plane. An example of the viscous motion is shown in figure 111.

The catastrophic formation of planar parallel slip traces was observed to occur from low strain levels and persist until fracture of the microtensile specimen. Frequently, only a minimum of isolated dislocation motion interspersed such events, which can be interpreted to correlate with the elastic loading commonly observed between macroscopically recorded serrations in the tensile deformation record. The sudden microyielding observed was, therefore, able to penetrate the existing dislocation substructure after mass movement of the dislocations, initiated by local breakaway. The observations lend support to current interpretations of DSA which emphasise the waiting time at local obstacles in the glide plane [17]. Waiting time at local obstacles, although not recorded in the course of this work, can be expected to increase in conjunction with increasing strength of such obstacles as forest dislocations and local tangles.

Deformation in grains adjacent to those in which a catastrophic yield event had occurred, was often observed to propagate by maintaining the continuity of the observed slip trace. This observation suggests that the role of factors such as cold–rolled texture and the associated preferred orientation of annealed microstructures is important in determining the nature of macroscopically observed serration features [73]. Crystallographic microband formation as well as their coordination into macroscopic shear bands has been associated with deformation heterogeneities in Al–Mg [172]. While no microband formation was observed in this investigation, the coordinated coarse slip band formation observed may be the origin of microband or micro–shear band formation.

5.6.2 Alloys Without Mg

In–situ deformation in this group of alloys was similarly characterised by successive dramatic yield events, which were sometimes punctuated by isolated viscous dislocation motion. The coordination of slip was, however, dramatically different to that observed in the Mg containing alloys. Deformation was characterised by the simultaneous activation of many intersecting slip systems and the frequent observation of cross–slip events. The net effect was a dispersion of deformation onto various slip systems. It must be stressed, however, that these micro–yield events were similarly sudden and dramatic when compared to their occurrence in Mg containing alloys. The discontinuities observed during

in–situ deformation therefore correspond with the fact that discontinuities were observed in the flow stress, during macroscopic tensile deformation, of the same material.

5.6.3 Al–2at.%Ag

The alloy VF619 (Ag), warrants isolated discussion to rationalise the existence of the planar dislocation arrays observed during in–situ deformation at very low strains. Planar dislocation motion producing piled–up dislocations in distinct arrays was most obviously observed in alloy VF619. The deformation characteristics at higher strains, however, were indistinguishable from those of the alloys discussed in the preceding subsection and were therefore consistent with their similar serrated flow features.

Silver is unique as an alloying element in Al because of the negligible difference in atomic radius between Ag and Al (~0.7%) [80, 92, 116]. In terms of the Cotterell theory [127], elastic interaction between dislocations and solutes is due to a size effect. Silver, in solid solution in aluminium, would therefore not be expected to initiate a PLC effect in Al. As discussed in Chapter 2, the PLC effect has been observed to "persistently" occur in binary Al–Ag [92, 116], and this has been attributed to solute cluster formation. The cause of the PLC effect in this case (and other alloy systems discussed) was proposed to be due to local softening of glide planes associated with destruction of clusters or SRO regions. In addition, recent work [231] has questioned the validity of SFE as a sole parameter in determining the occurrence of planar slip in FCC alloys. In fact, Gerold and Karnthaler attributed the sole origin of planar slip features to the local destruction of SRO or ordered precipitates, which in turn result in glide plane softening.

No evidence has been found during the current experiments to support the suggestion that silver (as a solute in Al) is capable of initiating or enhancing serrated flow by any mechanism. The results of microstructural investigations do, however, lend support to the proposed mechanisms, discussed above. The planar arrays of dislocations observed in the HVEM can be considered in terms of the probable existence of pre–precipitation solute clusters. In this context it is important to emphasise that alloy VF619 (Ag) displayed rapid natural ageing after quenching, a phenomenon which was not exhibited by 1070 or the alloys VF617 (Zn) and VF615 (Mg). Disruption of the pre–precipitation solute

clusters, by the initial passage of dislocations, could be expected to result in glide plane softening and the associated easier passage of subsequent dislocations in the same glide plane.

Piled up dislocations at the head of arrays (arrested at grain boundaries) were observed to move under the stress produced by further dislocation motion in the same slip plane. Spacing between such dislocations was reduced to the point where internal stresses completely restricted motion in the same plane. After this, cross–slip onto an adjacent parallel slip plane was observed to take place. The pile–up motion and subsequent cross–slip as illustrated in the two sets of sequential micrographs shown in figure 112. These results correlate with the surface deformation features observed in the SEM, where planar slip traces were observed to display features consistent with cross–slip in the vicinity of grain boundaries. The micrographs shown in figure 112 were photographed from the same grains as the micrographs presented in figure 105, page 169.

Planar dislocation arrays were not observed in samples from bulk specimens which were examined (after tensile straining) in the CTEM. The bulk samples had been subjected to identical heat treatments to those used on the HVEM microtensile specimens. On the basis of this, the observations should be more carefully considered. Firstly, the mean free path of dislocations is known to be larger during the initial stages of deformation in an annealed alloy, prior to the formation of developed dislocation tangles [232]. This has consequences in terms of in–situ deformation, where the mean free path of defects may exceed the specimen thickness and therefore produce results which are essentially HVEM artifacts at low strains. A second consideration is that the local heating resulting from the exposure of the specimen to the electron beam in the HVEM may have accelerated any pre–precipitation phenomena and resulted in premature solute clustering relative to the bulk sample. In this regard, no evidence of SRO was detected in long exposure diffraction patterns produced in the CTEM from solution treated VF619. These considerations are, however, largely negated by the support for the HVEM observations produced by examination of surface deformation features in the SEM. Slip line features on the surface of bulk specimens were indeed consistent with the deformation mechanisms observed in the HVEM. The correlation suggests that the planar arrays observed were therefore not simply a result of testing under the unique conditions experienced during in–situ deformation experiments.

5.6.4 Summary

On a macroscopic level, two features distinguish the behaviour of the two alloy types discussed in preceding sections. Firstly, the serration amplitude of the one group (1070, 1070 + 2at.%Ag or Zn) was very similar to one another and no macroscopic band formation was observed. Secondly, in the case of alloys primarily alloyed with Mg, serration amplitude was markedly higher than in the first group of alloys and band formation was regularly observed to occur.

The difference in macroscopically observed serration amplitude can therefore be explained by considering two aspects.

1. The stress required to unpin dislocations, thereby initiating the sudden yield events, is likely to be much higher in the case of the Mg containing material. This consideration can be justified by examining the atomic radius differences between Al and the various alloying elements under consideration [80]. Hydrostatic effects on edge dislocations can be expected to be much higher when the interaction between dislocations and Mg in Al is considered relative to the same parameter applied to Zn or Ag in Al and therefore the result is likelt to be stronger pinning effects.

2. The observed difference between the number of simultaneously active slip planes and the extent of cross–slip in the two alloy groups has implications for the net effect of any single yield event. In the Mg containing alloys, the parallel glide planes activated in each yield event can be expected to produce far more effective propagation of deformation between adjacent grains. The coordinated and directional nature of such avalanche slip events can be expected to be more effective in penetrating the existing substructure than the more dispersed multiple slip events in the alloys which do not contain Mg. The net result of such events would be the coordination of yielding between several adjacent grains as proposed by Fujita [96], as well as its possible coordination into a deformation band. Also, the extent of deformation localisation initiated by slip on a single system would be necessarily much greater than a similar event whose effect was dispersed by cross–slip and the simultaneous activation of numerous slip systems.

5.7 Fracture

The fracture mode regularly observed during the course of this work was rapid, "catastrophic" [43] ductile failure, often accompanied by shear. Also, both the orientation of the fracture surface and the rapidity of final failure (i.e. the extent to which plastic instability developed prior to failure) could be correlated with the characteristics of the tensile deformation. In general, the final failure of a specimen results from either material or geometric instability [139] or a combination of the two. The dominance of either one of these factors in the eventual failure mode was observed to account for failure on different occasions during the course of this work and they are therefore discussed in detail below.

5.7.1 Fracture Types

Although rapid ductile shear failure was frequently observed, the occurrence of a range of fracture surface types warrants further discussion.

Under *plane stress* ($W \gg T$) conditions, three fracture types occurred:

1. Ductile rupture in the direction of tensile loading, preceded by extensive plastic instability, with the fracture surface oriented at 90° to the tensile axis. e.g. annealed 1070.
2. Sudden ductile rupture following the formation of a localised neck (deformation band) in the gauge length. Fracture was preceded by minimal plastic instability and through such a deformation band i.e. at 60° to the tensile axis. eg. alloys 5182 and VF615 (Mg)
3. A combination of the above two modes where tensile deformation was not necessarily accompanied by deformation band formation, but some localised banding preceded fracture. eg. alloys VF617 (Zn), VF619 (Ag)

Under *plane strain* ($W \approx T$) conditions, three fracture types occurred:

1. Rapid premature shear failure, through the specimen thickness at 45° to the tensile axis, usually preceded minimal plastic instability (diffuse necking). eg. in alloys 5182 and 2014

2. As for (1), but far less common, with the fracture at 45° to the tensile axis through the specimen width.

3. Ductile rupture by tensile overload, prior to the formation of a localised neck (nominally brittle). MMC material only.

Circular section specimens were only manufactured from alloy 5182, and consistently failed by 45° shear.

5.7.2 The Relationship Between DSA and Fracture Mode

It is clear from the discussion in Chapter 2 that DSA is strongly correlated with both a negative microscopic (intrinsic) strain rate sensitivity (SRS) as well as the high probability of a negative measurable SRS. A direct consequence of this is the possibility of spontaneous strain localisation resulting from any fluctuation in the strain rate [58].

The influence of the above material conditions on fracture is that if deformation is localised, by a structural heterogeneity for example, the strain rate may then be appreciably raised [3]. A modification of the more conventional "diffuse" necking arises and a more localised and rapid failure results. The relationship between serrated yielding and localised shear failure in tension was examined in two quenched commercial Al–Zn–Mg alloys by King et al [43]. No PLC band propagation was reported but fracture occurred in one of several parallel shear bands which formed, distinctly in the vicinity of the neck, immediately prior to failure.

The dominance of a ductile shear failure mode in the course of this work confirms the results of both King et al [43] and the unstable shear mode reported to occur in Al–Zn–Mg by Chung et al [139]. Distinctions can be made, however, between the operative fracture mechanisms of the different alloys examined in the course of this work.

Commercial Monolithic Alloys

When tested under plane strain conditions, the alloys 2014, 6061 and 5182 all failed consistently by rapid ductile shear, but differences were observed in each case. The type of strain localisation producing the shear strains necessary for this type of failure requires either strain softening or a negative SRS [139].[7] The resulting fracture condition is such that material instability may be obtained prior to any geometric instability [139] and is therefore different to the usual *Considéré* condition [233].

In the case of alloy 2014, material instability was potentially present in two forms. Firstly, the time from quenching until eventual failure allowed for deformation enhanced natural ageing and hence the formation of GP zones. In addition, alloy 2014 was shown to exhibit strain localisation arising from the cracking of $CuAl_2$ inclusion particles, concurrent with audible acoustic emission (a.e.). It is likely in this case, therefore, that major deformation localisation was initiated by the breakdown of $CuAl_2$ inclusions. The potential then exists for the magnification of such strain localisation to occur because of the inherent instability of the GP zones under the passage of dislocations [209]. Destruction of the zones by dislocations potentially initiates glide plane softening which in turn may enhance the potential for slip localisation.

The occurrence of isolated major serrations was reduced but not removed by natural ageing and some such serrations were still present after artificial ageing to the T6 (peak hardness) condition. This suggests that the relative stability of the aged microstructure was sufficient to more readily resist the occurrence of strain bursts.

A further consideration, is the existence of small amplitude ($\triangle\sigma_{max} \approx 1$ MPa) serrations in the quenched condition, which occurred between the isolated stress drops. These serrations, typically resulting from DSA effects, arose from the increased solute concentration in solid solution produced by quenching from solution temperature. The amplitude of the serrations observed in alloy 2014 was similar to that in annealed (quenched) commercially pure Al (1070), which was not observed to fail in the same mode. It is therefore doubtful whether the extent of DSA occurring in alloy 2014 was sufficient to be solely

[7] The consideration here does not account for adiabatic shear effects which may be operative in testing at low temperatures.

responsible for the "catastrophic" shear failure mode regularly observed. In addition to the a.e. heard in conjunction with the appearance of the isolated stress drops, alloy 2014 was consistently observed to fail with the emission of a powerful a.e. burst.

In the case of alloy 6061, a comparison can be made with alloy 2014, by considering the capacity of the alloys to withstand the onset of localised deformation (necking) in the gauge length. Table 11 shows data from both alloys indicating both the area reduction of the gauge length and the area reduction in the vicinity of the fracture surface.

Table 11: Summary of the general and localised (fracture surface) area reduction data for alloys 2014 and 6061. Original cross–section in all cases was 6×3 mm^2.

Alloy	Condition	% Reduction in area	
		Gauge Length	Fracture Surface
6061	Soln.	14.4	46.1
6061	T6	2.2	36.7
2014	Soln.	16.1	27.8
2014	T4	16.1	23.6
2014	T6	13.3	23.3

When considering the solution treated conditions of both alloys, it can be seen that while the ductility (% RA[8] of the gauge length) of the alloys is similar, the final area reduction at the fracture surface is not. A similar, but less severe, condition holds true for the aged material. The table illustrates a distinction between the fracture types, which is not evident in the SEM micrographs presented in Chapter 4. In both cases, eventual failure was by rapid ductile shear and therefore characterised by dimple elongation in the direction of shear [206].

The schematic construction of a failure surface in $\sigma - \varepsilon - T$ was used as an illustration of different fracture modes by Chung et al [139]. One use of such a concept is the illustration of the continuity between different competing mechanisms, and the potential for a mixture of modes to occur. Insight can be gained by considering the final region of a

[8]The area reduction of the gauge length (% RA) is defined as: % RA = $\frac{A_o - A}{A_o} \times 100$
A_o = original cross–sectional area
A = reduced area

tensile deformation curve from alloy 6061 in the solution treated condition, presented in figure 113. The serrations in the flow stress can be seen to cease concurrent with the onset of plastic instability. While the micromechanics of the situation are not self–evident, it is clear that an increase in local strain rate must accompany the onset of plastic instability. The increased strain rate potentially results in deformation of the material in a regime outside of that in which DSA is dominant.

In spite of the lack of serrated flow during the region of plastic instability in alloy 6061, the final failure was shear assisted. Serrated flow is a single manifestation of underlying DSA phenomena and therefore, the fact that serrations are not present does not necessarily imply that DSA of dislocations is no longer occurring. If DSA is indeed still active during the period of plastic instability, then the net effect may well be the maintenance of a negative SRS. The result of such a situation, would be the retained possibility of material instability assisted shear fracture, albeit after some local area reduction in the gauge length.

Finally, an interesting feature of the fracture surface of alloy 6061, shown in figure 69, is the bimodal shear of the specimen at failure. In contrast to the commonly observed single shear plane, the micrograph illustrates failure on two shear planes corresponding to two principle shearing stresses whose normals bisect the (90°) angles between the operative principle stresses [234].

In the case of alloy 5182 tested in plane strain, fracture surface orientation was consistently at 45° to the tensile axis, regardless of the microstructural state of the material. The only variation observed was in terms of the amount of area reduction preceding final fracture, which was limited in all cases. Prior to the full development of geometric plastic instability, material was always observed to fail by rapid ductile shear directly resulting from material instability associated with DSA. A clear example of this effect is shown in figure 114 taken from the final region of the tensile deformation curve presented in figure 46. The figure shows that the onset of plastic instability is accompanied by the occurrence of serrated flow until specimen fracture.

For comparison, data from alloy 5182 corresponding to that presented in table 11, is shown in table 12.

Table 12: Summary of the area reduction data from alloy 5182 specimens after tensile testing to failure. Original cross–sections are indicated.

X–section	Condition	% Reduction in area	
		Gauge Length	Fracture Surface
6×6 mm^2	7.4 mm HR	16.7	31.7
6×3 mm^2	3 mm CR (annealed)	20.0	32.0
ϕ=2.8 mm	3 mm CR	3.5	17.7
ϕ=2.8 mm	3 mm CR (annealed)	12.9	30.6
6×2 mm^2	2 mm CR	2.3	10.1
6×2 mm^2	2 mm CR (annealed)	13.9	19.8

Clearly, the important consideration in both table 11 and table 12 is the difference between the final area reduction at the fracture surface and the area reduction of the gauge length. The difference between the two indicates the degree to which plastic instability was able to develop prior to failure. Alloy 2014 shows the least difference, indicating the extreme nature of material instability in the alloy as it was tested. Secondly, alloy 5182 shows a similarly small difference, in most cases, also as a result of material instability, but related directly to DSA effects. The greatest difference between the two sets of data, in the case of alloy 6061, does not preclude DSA influences but indicates a less significant contribution of material instability to the failure mode than in the case of either alloy 2014 or 5182.

Experimental Monolithic (2at.%) Alloys

The 2at.% experimental alloys are discussed here in conjunction with the commercial purity Al (1070) on which they were based. In the cold–rolled condition, all except 1070 failed by a combined mechanism of plastic instability followed by shear. In the annealed condition, however, only VF615 (Mg) failed by the DSA associated limited area reduction and shear.

The occurrence of shear fracture in cold–worked subsize specimens, but not in identical annealed material, suggests that DSA is not the sole microstructural prerequisite for

Table 13: Summary of the area reduction from the 2at.% experimental alloys after tensile testing to failure. Original cross–section is 6×3 mm^2.

Material	Condition	% Reduction in area	
		Gauge Length	Fracture Surface
1070	Annealed	37.8	60.0
VF617 (Zn)	Annealed	20.6	64.4
VF619 (Ag)	Annealed	18.3	49.1
VF615 (Mg)	Annealed	13.3	49.4

failure by ductile shear. Similarities between the fracture surfaces of the cold–rolled materials are clearly illustrated by the SEM micrographs illustrated in figure 115.

The annealed and quenched 1070 as well as solution treated 2at.% material can be expected to have a higher solute content in solid solution than similar material which has only been cold worked and not solution treated immediately prior to testing. Consideration of CTEM electron micrographs presented in Chapter 4 shows that 1070 and the 2at.% alloys had varying abilities to dynamically recover during cold–rolling. The ease of dynamic recovery is illustrated by the extent of formation of dislocation cell structures and other recovery associated microstructural features. Recovery processes are partially associated with the cross–slip of dislocations (eg. [235]) and therefore restricted recovery can be expected to imply the restriction of glide to specific planes. The restricted dynamic recovery can be expected to be manifest in both the slope of the stress–strain curve and the extent to which a high rate of work hardening persists. It can be seen from sections 4.3.1 and 4.8.2 that 1070 and the 2at.% experimental alloys do indeed demonstrate a progressively decreasing ability to undergo dynamic recovery in conjunction with the addition of Zn, Ag and Mg respectively.

The consequence of restricted dynamic recovery is then shown by the ability of an alloy to withstand non–uniform plastic deformation (plastic instability) as well as the extent to which uniform plastic elongation persists. These traits are clearly exhibited in table 13 and correlate with the extent to which final fracture was shear assisted in the various alloys. In summary, therefore, the correlation between restricted dynamic recovery processes and the occurrence of DSA phenomena must also be considered in the

final analysis of fracture surface formation and orientation to the tensile axis.

5.7.3 Metal Matrix Composites

The addition of particulate reinforcement to Al–based MMC's results in both a decrease in strain to fracture as well as a change in the failure mode [154]. As the reinforcement volume fraction is increased, the failure mode in composites based on alloy 6061 was observed by McDanels to change from a ductile 45° "chisel–point" shear to a more brittle flat and granular fracture. The hydrostatic stresses arising from constrained plastic flow in MMC's generally limits the strain to failure [236]. The constraint arising from particulate reinforcement is, however, much less than for whisker reinforcement. As a result, strains large enough to induce void nucleation can occur in significant volumes of the matrix. The sources of dimples observed on the fracture surfaces have been variously attributed to fracture or decohesion of the particles, as well as inclusions, precipitates and grain boundaries [237].

All composite material tested during the course of this work failed with no localised area reduction (nominally brittle) in the gauge length, but with extensively dimpled fracture surfaces. The ductility reduction and relative ease of fracture was clearly illustrated in the case of the alloy 2014 + 10% Al_2O_3 composite. As a result of axial inhomogeneity (banding in the extrusion direction) of the Al_2O_3 particles, premature formation of fracture surfaces occurred in these regions (see figure 81). Preferential crack initiation has previously been reported to initiate in clustered regions of SiC particles in Al based MMC's [237]. In addition, the premature failure of such regions was further evidenced by the small dimple size in relation to adjacent particle rich regions (see figure 82). The small dimple size and relatively smooth overall appearance of the particle free regions suggests that void coalescence was pre–empted by rapid final fracture originating in the particle rich regions. The relatively smooth appearance correlates with similar observations of the rapidly (and prematurely) formed fracture surfaces associated with the "catastrophic" ductile shear, discussed in the preceding sections.

Smooth planar particle interfaces commonly observed in the larger dimples on the fracture surfaces (see eg. figure 80) suggest that the particles were fractured rather than

decohered [238]. The particle matrix interfaces, exposed by decohesion (see eg. figure 78), can be easily distinguished because of the presence of reaction products between the particle and the matrix, produced in processing. The observed particle fracture resulted largely, if not completely, from tensile deformation (not prior processing), evidenced by the absence of such features on the surfaces of undeformed specimens. Acoustic microscopy of similarly produced composite material [239] found less than 2% of particle fracture was associated with processing.

The dominant occurrence of particle fracture as opposed to interface decohesion confirms that interface chemistry in MMC's is sufficiently developed to ensure adequate stress transfer and associated elastic loading [240] of the particulate inclusions. In addition, however, fracture of the particles, associated with their relative brittleness, was observed to enhance deformation localisation. Deformation localisation in the vicinity of particle inclusions can therefore be expected to aid in premature microvoid formation and the associated ductility decrease. The observed features lend support to the Brown/Embury deformation model [241] which predicts that for high volume percentages of reinforcement ($\geq$15%), void growth provides an insignificant contribution to ductility

Finally, it has previously been shown that the microstructural condition of the matrix affects the micromechanisms of fracture [154] and that the under–aged condition favours internal cracking of particulates [237]. Further, an increase in volume fraction of particulates influences the transition of fracture initiation from interface decohesion to particulate cracking [239]. The relative roles of interface decohesion and particle fracture in the overall deformation and fracture process in this case are, however, difficult to asses because samples were only examined for surface deformation features after final fracture. Surface deformation of pre–polished specimens, where deformation had been terminated prior to fracture can be expected to provide this clarification.

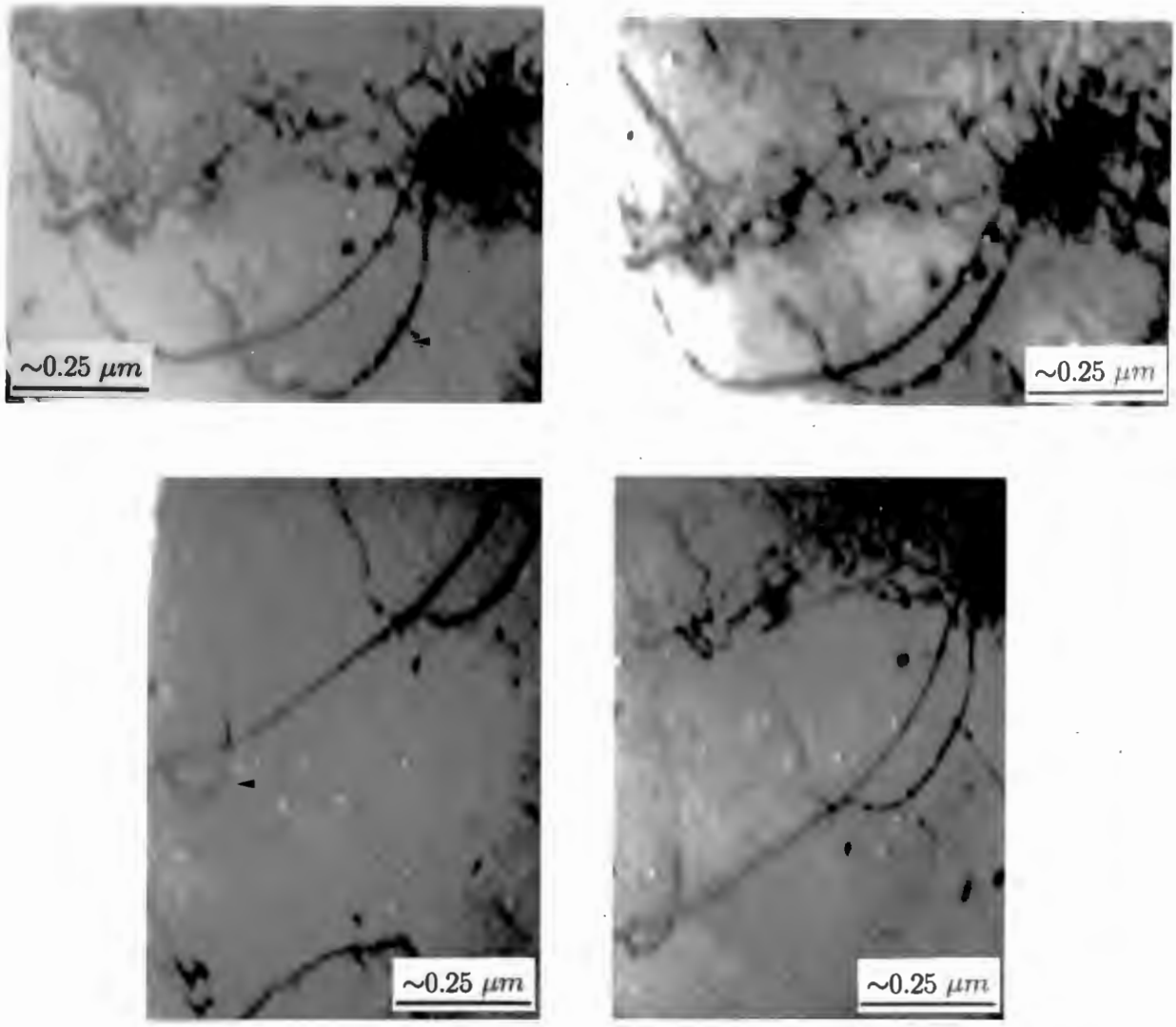

Figure 111: Bright–field HVEM micrograph sequence (digitally reproduced from video tape) illustrating the viscous motion of dislocation segments in alloy 5182, preceding a more dramatic microyield event.

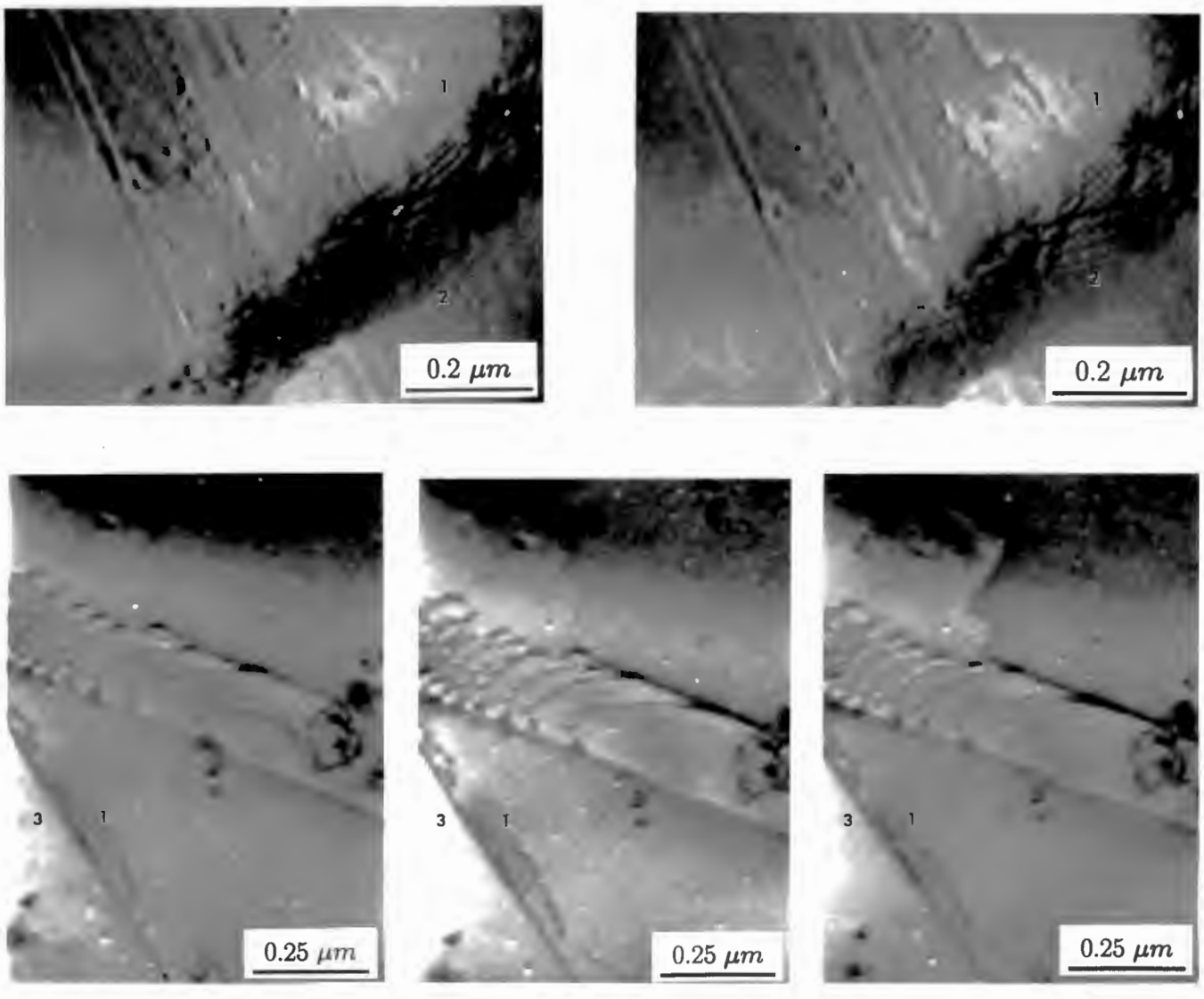

Figure 112: Bright–field HVEM micrograph sequence (digitally reproduced from video tape) illustrating the planar pile–up of dislocations at grain boundaries in VF619, followed by planar cross–slip on to adjacent slip–planes.

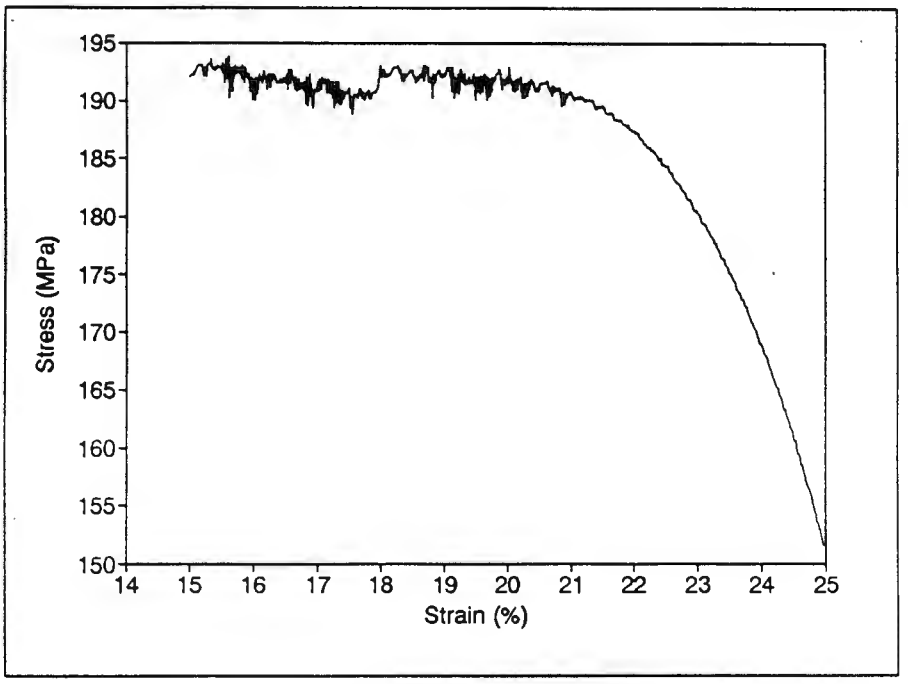

Figure 113: Final portion of a tensile deformation record from solution treated alloy 6061, showing the lack of serrations associated with the final region of plastic instability.

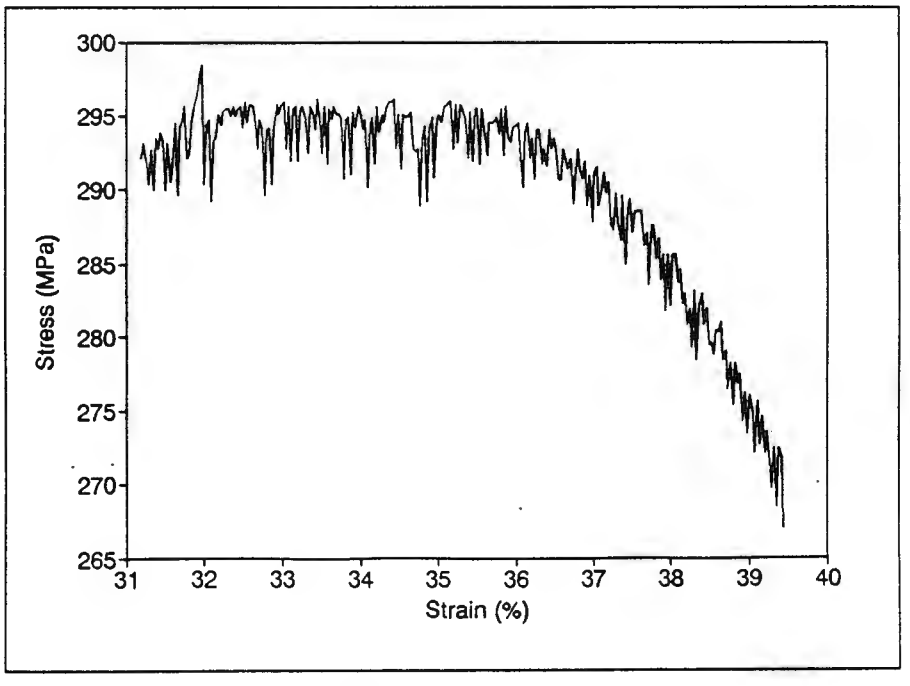

Figure 114: Final portion of a tensile deformation record from alloy 5182 (Hot rolled to 7.4 mm), showing the persistence of serrated flow until specimen failure (by ductile shear).

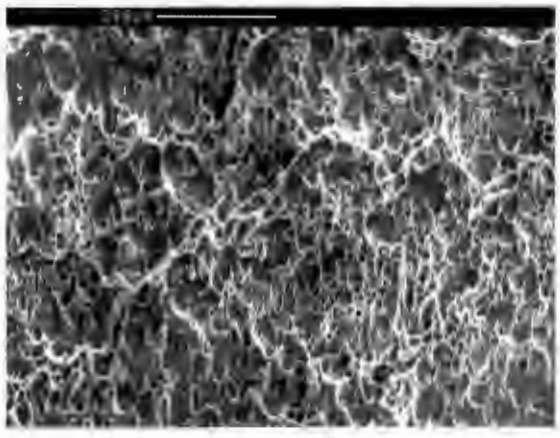

(a)

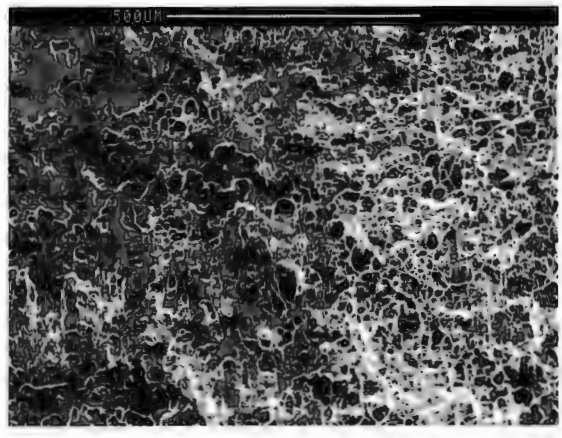

(b)

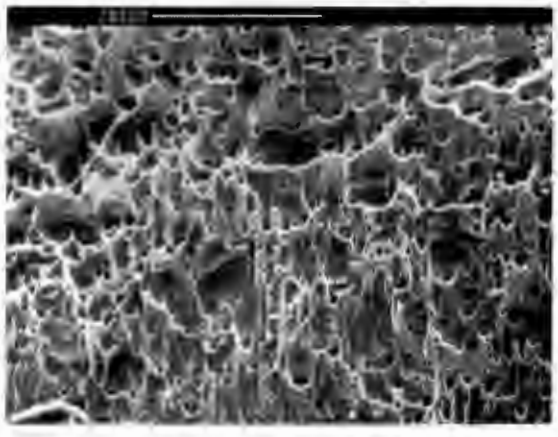

(c)

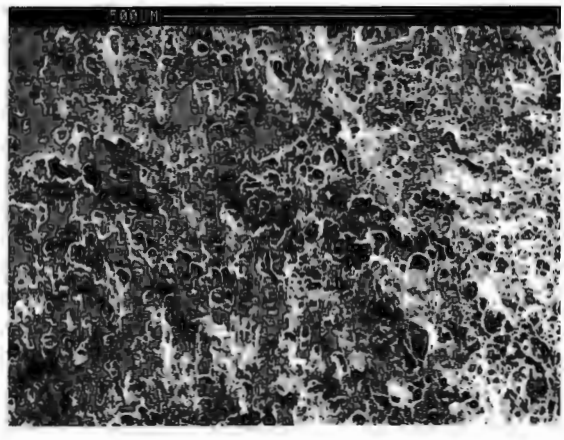

(d)

Figure 115: SEM micrographs of the fracture surfaces of 3 mm thick cold–rolled commercially pure 1070 as well as alloys VF617, VF619 and VF615 illustrated respectively in (a) – (d).

Chapter 6

Conclusions

6.1 Introduction

This chapter serves to present a summary of the significant findings presented during the course of this thesis. Although these are not all encompassing, the conclusions presented in this chapter represent a significant contribution to the current state of understanding of the inhomogeneous deformation of aluminium alloys.

6.2 List of Conclusions

1. Commercially pure (99.7%) aluminium contains sufficient impurities to exhibit room temperature serrated flow. A smaller grain size results in an increased serration amplitude, consistent with previously reported results.

2. The addition of 2at.% Zn or Ag to commercially pure aluminium is insufficient to enhance or alter the serration amplitude, in spite of altering the general characteristics of the deformation.

3. The addition of 2at.% Mg to commercially pure aluminium results in a marked increase in the serration amplitude and produces sufficient microstructural instability to allow for the formation of PLC type deformation bands during tensile deformation.

4. Single isolated stress drops during the tensile deformation may occur coincident with the formation of developed precipitation in commercially pure aluminium, alloyed with 2at.% Ag.

5. In the case of commercial quaternary Al–Cu–Mn–Si (2014), single isolated stress drops arise from the internal cracking of $CuAl_2$ inclusions in the microstructure. The associated deformation localisation is enhanced by the general instability of the microstructure.

6. Low stress amplitude serrations in the commercial alloys 2014 and 6061 arise from the combined effect of the deliberate addition of various alloying elements. The existence of these discontinuities cannot be attributed to a single alloying addition.

7. The pre–macro yield phase of the deformation of 5182 is characterised by the emission of planar dislocation arrays from grain boundary and triple point junction sources in select grains.

8. The characteristic yield drop in annealed 5182 arises from the mass creation of dislocations in an initially very low dislocation density microstructure. Dislocation motion is predominantly on a single slip system in any particular grain.

9. Type A (flamboyant) surface markings arise from localised deformation at the yield point arising from macroscopic stress concentrations, predominantly at the specimen shoulders.

10. The subsequent passage of a Lüders front arises from a succession of microstructurally indistinguishable events similar to the initial formation of type A surface markings.

11. The suppression of initial deformation inhomogeneities (yield drop, type A surface markings and the passage of a Lüders front) in annealed 5182 can be achieved by quenching from the solution temperature. This is the result of the uniform creation of dislocations generated by thermal stresses associated with quenching. The net effect is similar to the commercially applied pre–treatments known as pinch rolling or skin passing.

12. Previous results on the orientation of Lüders bands can be generalised to the case of PLC band formation and propagation. The orientation of PLC deformation bands is a direct result of the macroscopic stress system.

13. The formation of PLC bands originates in microscale heterogeneities and the macroscopic coordination of these events is a direct result both the microscopic severity of such events as well as the operative loading geometry.

14. Where serrated flow is not accompanied by the formation of visually detectable PLC bands, the geometry of the test specimen does not affect the record of deformation. Where such band formation occurs, altering the specimen geometry affects the nature of the serrated flow which occurs, the orientation of the deformation bands and the mode of final fracture.

15. Pronounced PLC type deformation in aluminium alloys is characterised by a rapid and continuously increasing dislocation density accompanied by minimal dynamic recovery.

16. The occurrence of an incubation strain prior to the onset of PLC type instabilities is most marked in previously cold–worked material which has not been annealed prior to tensile testing. The microstructural condition of any specific alloy is, therefore, a significant determinant in the extent and occurrence of a critical strain.

17. Planar slip traces and features consistent with cross–slip, predominantly at grain boundaries are regularly observed on the surfaces of pre–polished tensile specimens of aluminium alloys which exhibit jerky tensile deformation.

18. The existence of serrated flow in MMC material is directly affected by the addition of particulate reinforcement. The type, size, volume fraction and distribution of such particulate inclusions influence the general tensile deformation characteristics including final fracture as well as the nature of the serrated flow.

19. The addition of Mg to aluminium alloys is a primary determinant in affecting the type of microscale deformation heterogeneity observed during in–situ HVEM deformation experiments. Deformation in alloys containing deliberated Mg additions is characterised by sudden activation and collective motion of multiple dislocations,

predominantly on a single slip system. In contrast, alloys not containing Mg exhibit less severely serrated curves and extensive cross–slip in conjunction with the operation of multiple active slip systems.

20. CTEM examination of the microstructures of deformed alloys indicate that a pronounced PLC effect is coincident with a rapid accumulation of dislocations. Strong suppression of dynamic recovery processes occurs concurrent with a pronounced PLC effect, as has been previously reported, but it is are not a prerequisite for the occurrence of jerky flow.

6.3 Potential for Future Work

The scope of the present work has been broad, given the both the range of materials examined, as well as the techniques employed. As was pointed out in the introduction, this was intentional in order to provide a comparative approach to a phenomenon which is manifest in a range of materials. In addition, it must be emphasised that the PLC effect results in macroscopic discontinuities of deformation whose origin lies in microscopic defect interactions. As such it is suited to an approach which examines a range of levels of the deformation sequence. An effect of this approach, however, is to both stimulate further questions as prompt detailed enquiry of pertinent issues which this thesis has examined less specifically.

A quantitative approach to the dynamic evolution of microstructure in polycrystals exhibiting the PLC effect utilising HVEM techniques would be appropriate. Such an examination could be expected to elucidate more clearly the origin and operation of dislocation sources in the microyield events. More importantly, clarification of the mechanisms of the coordination of deformation arising from the microscopic discontinuities could result from a detailed examination of aspects such as dislocation interactions with grain boundaries.

The potential exists for in–situ dynamic straining experiments within the SEM where the propagation of deformation between several grains could be examined. Factors such as the observed continuity of slip traces between adjacent grains could be examined in

more detail by utilising such an approach. Quantification of the mechanisms could be achieved by measuring the rapidity of formation of slip traces and their propagation into adjacent grains.

On a macroscopic level, measurements of deformation band volume and propagation velocity have not been made. Analysis of these parameters could be expected to provide data such as the true strain rates occurring during discontinuous deformation which would provide useful support to current modeling approaches. In addition, it has been suggested [242] that near–periodic type A serrations may not occur without the occurrence of propagating deformation bands. The lack of visually detectable deformation bands in some such cases during the course of this work, therefore requires additional precautions to be taken in the course of future testing. Visual detection methods should be accompanied by strain–time measurements utilising a clip–on extensometer covering only a small portion of the gauge length in order to accurately determine the existence of propagating deformation bands.

A comparative study of high purity binary alloys could be expected to clarify the role of select elements in the discontinuous deformation process. This approach could be expected to allow for a quantitative understanding of the relative contributions of the different elements to jerky flow in more complex alloy systems. Caution would be necessary to minimise extraneous variable such as grain size and the occurrence of precipitation phenomena.

Appendix A

ASTMB557M Tensile Test Standards

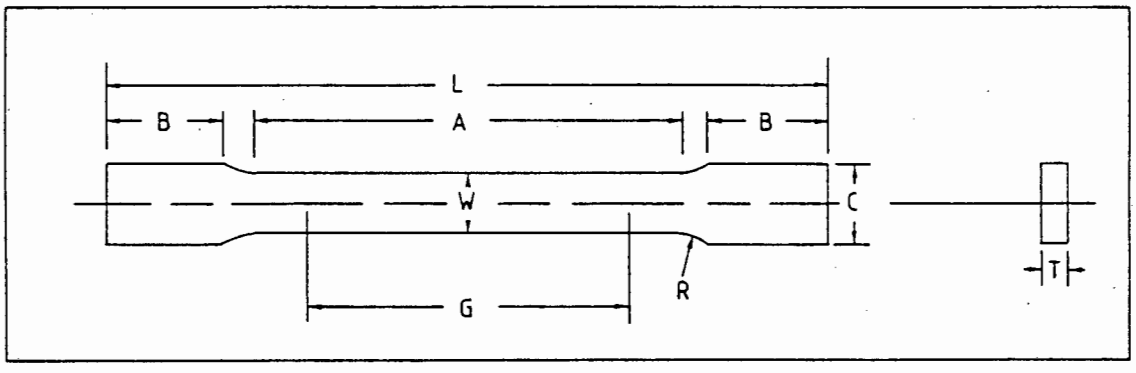

Figure 116: Rectangular Tension Test Specimens

	Dimensions (mm)	
	Standard Specimen (12.5 mm Wide)	Subsize Specimen (6 mm Wide)
G—Gage length	50.00 ± 0.10	25.00 ± 0.10
W—Width (Notes 1 and 2)	50.00 ± 0.10	6.00 ± 0.10
T—Thickness (Note 3)	Thickness of material	
R—Radius of fillet, min	12.5	6
L—Over-all length, min (Note 4)	200	100
A—Length of reduced section, min	57	32
B—Length of grip section, min (Note 5)	50	30
C—Width of section, approximately (Notes 2 and 6)	20	10

Note 1: The ends of the reduced sections shall not differ in width by more than 0.06 mm or 0.025 mm, respectively. Also, there may be a gradual decrease in width from the ends to center, but the width at either end shall not be more than 1% larger than the width at the center.

Note 2: For each of the specimens, narrower widths (W and C) may be used when nescessary. In such cases, the width of the reduced section should be as large as the width of the material being tested permits: however, unless stated specifically, the requirements for elongation in a product specification shall not apply when these narrower specimens are used. If the width of the material is less than W, the sides may be parallel throughout the length of the specimen.

Note 3: The dimension T is the thickness of the specimen as stated in the applicable material specifications. Maximum nominal thickness of 12.5 mm and 6 mm wide specimens shall be 12.5 mm and 6 mm respectively.

Note 4: To aid in obtainig axial loading during testing of 6 mm specimens, the overall length should be as large as the material will permit, up to 200 mm.

Note 5: It is desirable, if possible, to make the length of the grip section large enough to allow the specimen to extend into the grips a distance equal to two thirds or more of the length of the grips. If the thickness of the 12.5 mm wide specimens is over 9 mm, longer grips and correspondingly longer grip sections of the specimens may be nescessary to prevent failure in the grip section.

Note 6: The ends of the specimen shall be symmetrical with the center line of the reduced section within 0.2 mm and 0.1 mm respectively.

Appendix B

Proprietry Product List and Sources

HULAMIN : Hulett Aluminium (Pty) Ltd.

MINTEK : Council for Mineral Technology

CSIR : Council for Scientific and Industrial Research

NCEM : National Center for Electron Microscopy

DURAL : Dural Aluminium Composites Corporation

MSNW : Materials Science (North West) Ltd.

LEYBOLD–HERAEUS : Leybold–Heraeus GmbH and Co.

STRUERS : Struers Denmark

TENUPOL : Struers commercial twin–jet TEM specimen polisher.

ZWICK : Zwick GmbH and Co.

ZWICK 7005 : Zwick software : "Tensile, Compression and Bend Testing."

QUATTRO PRO : Borland International Inc. Spreadsheet.

MATROX : Matrox Electronic Systems Limited

ASTM : American Society for Testing Materials

CAMBRIDGE : Cambridge Instruments Ltd.

BORLAND : Borland International Inc.

References

[1] R. W. Cahn (editor). *Encyclopedia of Materials Science and Engineering*, Volume 1 (Supp.), pp. 504–508. Pergamon Press, Oxford, 1988.

[2] R. B. Schwarz and L. L. Funk. *Acta metall.*, **33**, 295, 1985.

[3] E. Pink. *Aluminium*, **60**, E646, 1984.

[4] R. E. Smallman. *Modern Physical Metallurgy.* Butterworth and Co., 1985.

[5] A. Wijler, J. Schade Van Westrum, and A. Van Den Beukel. *Acta metall.*, **20**, 355, 1972.

[6] R. A. Mulford and U. F. Kocks. *Acta metall.*, **27**, 1125, 1979.

[7] J. C. Haung and G. T. Gray. *Scripta metall. mater.*, **24**, 85, 1990.

[8] G. J. Lopriore and P. G. McCormick. In R. C. Gifkins (editor), *Strength of Metals and Alloys (ICSMA 6)*, pp. 419–423, Melbourne, Australia, 1982.

[9] L. P. Kubin and J. Poirier. *Solid State Phenomena*, **3/4**, 473, 1988.

[10] F. Le Chatelier. *Rev. Metall.*, **6**, 914, 1909.

[11] A. Portevin and F. Le Chatelier. *C. R. Acad. Sci.*, **176**, 507, 1923.

[12] A. Portevin and F. Le Chatelier. *Trans. ASST*, **530**, 457, 1924.

[13] I. J. Polmear. *Light Alloys : Metallurgy of the Light Metals.* Edward Arnold, 1981.

[14] L. P. Kubin, K. Chihab, and Y. Estrin. *Acta metall.*, **36**, 2707, 1988.

[15] A. H. Cottrell. *Phil. Mag.*, **44**, 829, 1953.

[16] J. Friedel. *Dislocations.* Pergamon Press, London, second edition, 1964.

[17] A. van den Beukel. *Acta metall.*, **28**, 965, 1980.

[18] A. van den Beukel and U. F. Kocks. *Acta metall.*, **30**, 1027, 1982.

[19] U. F. Kocks, A. S. Argon, and M. F. Ashby. *Prog. Mater. Sci.*, **19**, 1, 1975.

[20] A. W. Sleeswyk. *Acta metall.*, **6**, 598, 1958.

[21] A. S. Keh and Y. Nakada. *Acta metall.*, **18**, 437, 1970.

[22] P. J. Worthington and B. J. Brindley. *Phil. Mag.*, **19**, 1175, 1969.

[23] F. R. N. Nabarro. Report on the strengths of solids. *London : Physical Society*, p. 38, 1948.

[24] R. W. Hayes. *Acta metall.*, **31**, 365, 1983.

[25] V. K. Garg and M. N. Shetty. *Metals Sci.*, **14**, 193, 1980.

[26] B. A. Wilcox and G. C. Smith. *Acta metall.*, **12**, 371, 1964.

[27] A. M. Weinstein, P. Ferraglio, and A. K. Mukhergee. *Mater. Sci. Engng.*, **8**, 198, 1971.

[28] B. Russel. *Phil. Mag.*, **8**, 615, 1963.

[29] T. Takagaki and A. K. Mukherjee. In P. Haasen et al. (editors), *Strength of Metals and Alloys (ICSMA 5)*, Volume 1, pp. 589–593, Aachen, W. Germany, 1979.

[30] M. Mayer, D. Vohringer, and E. Macherauch. In P. Haasen et al. (editors), *Strength of Metals and Alloys (ICSMA 5)*, Volume 2, pp. 807–812, Aachen, W. Germany, 1979.

[31] M. Jovanovic and B. Djuric. *Scripta metall.*, **15**, 469, 1981.

[32] K. W. Qian and R. E. Reed-Hill. *Acta metall.*, **31**, 87, 1983.

[33] H. Era, N. Ohura, R. Onodera, and M. Shimizu. *Scripta metall.*, **18**, 1041, 1984.

[34] X. Lingang. *Scripta metall.*, **22**, 179, 1988.

[35] A. Korbel and H. Dybiec. *Acta metall.*, **29**, 89, 1981.

[36] P. G. McCormick and Y. Estrin. *Scripta metall.*, **23**, 1231, 1989.

[37] A. Wijler and J. Schade van Westrum. *Scripta metall.*, **5**, 159, 1971.

[38] S. H. van den Brink, A. van den Beukel, and P. G. McCormick. *Phys. stat. sol. (a)*, **30**, 469, 1975.

[39] H. Yoshinaga and S. Morozumi. *Phil. Mag.*, **23**, 1387, 1971.

[40] L. J. Cuddy and W. C. Leslie. *Acta metall.*, **20**, 1157, 1972.

[41] J. D. Cambell, R. H. Cooper, and T. J. Fischhof. In A. R. Rosenfield et al. (editors), *Dislocation Dynamics*, pp. 723–746. McGraw Hill, 1968.

[42] D. J. Lloyd and K. Tangri. *Mater. Sci. Engng.*, **10**, 75, 1972.

[43] J. E. King, C. P. You, and J. F. Knott. *Acta metall.*, **29**, 1553, 1981.

[44] P. Rodriguez. *Bull. Mater. Sci.*, **6**, 653, 1984.

[45] K. Chihab, Y. Estrin, L. P. Kubin, and J. Vergnol. *Scripta metall.*, **21**, 203, 1987.

[46] C. H. Caceres and A. H. Rodriguez. *Acta metall.*, **35**, 2851, 1987.

[47] C. B. Scruby, H. N. G. Wadley, and J. E. Sinclair. *Phil. Mag.*, **44**, 249, 1981.

[48] H. N. G. Wadley, C. B. Scruby, and J. H. Speake. *Int. Met. Rev.*, **2**, 41, 1980.

[49] C. R. Heiple, S. H. Carpenter, and M. J. Carr. *Metals Sci.*, **15**, 587, 1981.

[50] R. Pascual. *Scripta metall.*, **8**, 1461, 1974.

[51] C. H. Caceres and H. R. Bertorello. *Scripta metall.*, **17**, 1115, 1983.

[52] L. P. Kubin and Y. Estrin. *Scripta metall.*, **23**, 815, 1989.

[53] A. Nohara, Y. Muramoto, N. Yukawa, and T. Imura. In *Proc. Fifth Int. Conf. on HVEM*, pp. 443–446, Kyoto, Japan, 1977.

[54] J. G. Morris. *Mater. Sci. Engng.*, **13**, 101, 1974.

[55] E. Pink and J. Krol. *Mater. Sci. Engng.*, **75**, 87, 1985.

[56] Y. Estrin and L. P. Kubin. Collective dislocation behaviour in dilute alloys and the plc efect. Submitted for publication 1990.

[57] C. P. Ling and P. G. McCormick. *Acta metall. mater.*, **38**, 2631, 1990.

[58] L. P. Kubin and Y. Estrin. In *Proc. Conf on Mechanisms of Deformation and Strength of Advanced Materials*, Aussois, France, March 1990.

[59] P. Penning. *Acta metall.*, **20**, 1169, 1972.

[60] L. P. Kubin and Y. Estrin. *Acta metall.*, **33**, 397, 1985.

[61] E. Pink. *Aluminium*, **60**, E601, 1984.

[62] E. Pink and A. Grinberg. In R. C. Gifkins (editor), *Strength of Metals and Alloys (ICSMA 6)*, Volume 1, pp. 83–88, Melbourne, Australia, 1982.

[63] M. Teresa Correia and M. A. Fortes. *Scripta metall.*, **15**, 369, 1981.

[64] P. G. McCormick. *Acta metall.*, **19**, 463, 1971.

[65] S. L. Mannan, K. G. Samuel, and P. Rodriguez. In R. C. Gifkins (editor), *Strength of Metals and Alloys (ICSMA 6)*, Volume 2, pp. 637–642, Melbourne, Australia, 1982.

[66] E. Pink and A. Grinberg. *Mater. Sci. Engng.*, **51**, 18, 1981.

[67] R. Eborall, M. Lack, and V. A. Phillips. *Bull. Inst. Metals*, **1**, 58, 1952.

[68] V. A. Phillips, A. J. Swain, and R. Eborall. *J. Inst. Metals*, **81**, 369, 1952/53.

[69] V. A. Phillips. *J. Inst. Metals*, **81**, 751, 1952/53.

[70] W. H. L. Hooper and J. Holden. *Bull. Inst. Met.*, **1**, 161, 1952.

[71] J. G. Morris. *Mater. Sci. Engng.*, **5**, 299, 1969/70.

[72] R. Hill. *J. Mech. Phys. Solids*, **1**, 19, 1952.

[73] W. M. Webernig, J. Krol, and E. Pink. *Mater. Sci. Engng.*, **80**, L16, 1986.

[74] A. T. Thomas. *Acta metall.*, **14**, 1363, 1966.

[75] E. W. Fell. *J. Inst. Metals*, **80**, 689, 1951/52.

[76] B. A. Parker. In P. Haasen et al. (editors), *Strength of Metals and Alloys (ICSMA 5)*, Volume 2, pp. 899–904, Aachen, W. Germany, 1979.

[77] D. Hull (editor). *Introduction to Dislocations.* Pergammon Press, Oxford, second, revised edition, 1975.

[78] R.Iricibar, J.Mazza, and A.Cabo. *Scripta metall.*, **9**, 1051, 1975.

[79] D. J. Lloyd. *Metall. Trans.*, **11A**, 1287, 1980.

[80] E. O. Hall. *Yield Point Phenomena in Metals and Alloys.* MacMillan, 1970.

[81] I. S. Kim amd M. C. Chaturvedi. *Mater. Sci. Engng.*, **37**, 165, 1979.

[82] D. E. Delwiche and D. W. Moon. *Mater. Sci. Engng.*, **7**, 203, 1971.

[83] C. S. Barret and T. B. Massalski. *The Structure of Metals.* Pergamon Press, third edition, 1980.

[84] B. Jaoul. *J. Mech. Phys. Solids*, **9**, 69, 1961.

[85] W. M. Lomer. *J. Mech. Phys. Solids*, **1**, 64, 1952.

[86] E. O. Hall. *Proc. Phys. Soc. (London)*, **B63**, 724, 1950.

[87] J. F. Butler. *J. Mech. Phys. Solids*, **10**, 313, 1962.

[88] G. T. Van Rooyen. *Mater. Sci. Engng.*, **3**, 105, 1968/69.

[89] E. O. Hall. *Proc. Phys. Soc. (London)*, **B64**, 742, 1951.

[90] A. Nadai (editor). *Theory of Flow and Fracture in Solids.* Mc Graw–Hill, New York, 1950.

[91] D. W. Moon and T. Vreeland. *J. Appl. Phys.*, **39**, 1766, 1968.

[92] R. Onodera, T. Ishibashi, M. Koga, and M. Shimizu. *Acta metall.*, **31**, 535, 1983.

[93] D. M. Riley and P. G. McCormick. *Acta metall.*, **25**, 181, 1977.

[94] A. Rosen and S. R. Bodner. *Mater. Sci. Engng.*, **4**, 115, 1969.

[95] S. Miura. In *Proc. Int. Conf. on Mech. Behaviour of Mat.*, Volume 1, pp. 128–139, Kyoto, Japan, 1971.

[96] H.Fujita and T.Tabata. *Acta metall.*, **25**, 793, 1977.

[97] R. Chadwick. *J. Inst. Metals*, **51**, 120, 1933.

[98] G. A. Knight and G. Murray. *Sheet Metal Ind.*, **23**, 1741, 1946.

[99] H. H. Rossig, G. Ibe, and W. Gruhl. *Metall.*, **28**, 232, 1974.

[100] E. Pink. *Acta metall.*, **37**, 1773, 1989.

[101] R. Chadwick and W. H. L. Hooper. *J. Inst. Metals*, **80**, 17, 1951/52.

[102] A. Korbel, H. Dybiec, and A. Pawelek. In *Polish–French Colloquium on Strain Localisation and Recrystallisation*, Krakow, 1979.

[103] B. J. Roopchand and J. G. Morris. *Scripta metall.*, **7**, 839, 1973.

[104] G. G. Saha, P. G. McCormick, and P. Rama Rao. *Mater. Sci. Engng.*, **62**, 187, 1984.

[105] E. Pink. In P. O. Kettunen et al. (editors), *Strength of Metals and Alloys (ICSMA 8)*, Volume 1, pp. 495–500, Tampere, Finland, 1988.

[106] U. F. Kocks. *Metall. Trans.*, **16A**, 2109, 1985.

[107] J. Guillot and T. Grilhe. *Acta metall.*, **20**, 291, 1972.

[108] R. W. Hayes and W. C. Hayes. *Acta metall.*, **32**, 259, 1984.

[109] L. P. Kubin and Y. Estrin. *Acta metall. mater.*, **38**, 697, 1990.

[110] B. A. Parker and R. G. O'Donnell. In R. C. Gifkins (editor), *Strength of Metals and Alloys (ICSMA 6)*, pp. 437–442, Melbourne, Australia, 1982.

[111] P. G. McCormick. *Scripta metall.*, **15**, 441, 1981.

[112] J. Wood and P. G. McCormick. *Acta metall.*, **35**, 247, 1987.

[113] D. Dew-Hughes and W. D. Robertson. *Acta metall.*, **8**, 156, 1960.

[114] G. Lutjering and S. Weissmann. *Acta metall.*, **18**, 785, 1970.

[115] M. Niinomi, T. Kobayashi, and K. Ikeda. *J. Mater. Sci. Lett.*, **5**, 847, 1986.

[116] R. Onodera, H. Era, T. Ishibash, and M. Shimizu. *Acta metall.*, **31**, 1589, 1983.

[117] M. Jovanovic, M. Gujicic, and D. Drobnjak. In P. O. Kettunen et al. (editors), *Strength of Metals and Alloys (ICSMA 8)*, Volume 1, pp. 337–341, Tampere, Finland, 1988.

[118] W. H. L. Hooper. *J. Inst. Metals*, **81**, 563, 1952.

[119] N. Kruprik and N. Ford. *J. Inst. Metals*, **81**, 601, 1952.

[120] A. Rosen. *Mater. Sci. Engng.*, **7**, 91, 1971.

[121] R. B. Schwarz and L. L. Funk. *Acta metall.*, **31**, 299, 1983.

[122] C. P. Hinesly and J. G. Morris. *Mater. Sci. Engng.*, **6**, 48, 1970.

[123] T. Tabata, H. Fujita, and N. Ueda. *Mater. Sci. Engng.*, **44**, 81, 1980.

[124] H. Chossat. *Rev. Metall.*, **47**, 167, 1950.

[125] H. Chossat. *Rev. Metall.*, **47**, 343, 1950.

[126] E. Bouchaud, L. Kubin, and H. Octor. *Metall. Trans.*, **22A**, 1021, 1991.

[127] A. H. Cottrell. *Dislocations and Plastic Flow in Crystals.* Clarendon Press, Oxford, first edition, 1952.

[128] R. J. Price and A. Kelly. *Acta metall.*, **12**, 159, 1964.

[129] E. Pink, W. M. Webernig, and J. Krol. *Mater. Sci. Engng.*, **93**, L1, 1987.

[130] E. Pink and W. M. Webernig. *Acta metall.*, **35**, 127, 1987.

[131] H. P. Degischer, Ch. Y. Zahra, and A. Zahra. *Z. Metallkd.*, **82**, 635, 1973.

[132] S. F. Malan and A. E. Paterson (editors). *Introduction to Aluminium.* Aluminium Federation of South Africa, Isando, South Africa, first edition, 1989.

[133] A. W. McReynolds. *Trans. A.I.M.E.*, **185**, 32, 1949.

[134] J. E. Hatch (editor). *Aluminium : Properties and Physical Metallurgy.* ASM, Metals Park, Ohio, first edition, 1988.

[135] J. E. Bird, K. E. Newman, and K. Narasimhan. In *Proc. Int. Conf. on Aluminium Technology '86*, pp. 604–612, London, 1986.

[136] J. E. Bird, K. E. Newman, J. M. Carlson, and K. Narasimhan. In *Proc. Int. Conf. on Aluminium Technology '86*, pp. 597–603, London, 1986.

[137] P. R. Cetlin, A. S. Gulec, and R. E. Reed-Hill. *Metall. Trans.*, **4**, 513, 1973.

[138] H. J. Harun and P. G. McCormick. *Acta metall.*, **27**, 155, 1979.

[139] N. Chung, T. Embury, R. G. Hoagland, and C. M. Sargent. *Acta metall.*, **25**, 377, 1977.

[140] E. Nes. *Z. Metallk.*, **69**, 35, 1978.

[141] B. Andersson. *Scripta metall.*, **77**, 69, 1980.

[142] K. Matsuura, T. Nishiyama, and S. Koda. *Trans. Jap. Inst. Metals*, **10**, 429, 1969.

[143] M. Chaturvedi, D. J. Lloyd, and K. Tangri. *Metals Sci.*, **6**, 16, 1972.

[144] R. W. Hayes and W. C. Hayes. *Acta metall.*, **30**, 1295, 1982.

[145] R. Onodera, T. Ishibashi, H. Era, and M. Shimizu. *Acta metall.*, **31**, 817, 1984.

[146] J. A. Wert and P. A. Wycliffe. *Scripta metall.*, **19**, 463, 1985.

[147] J. T. Evans. *Scripta metall.*, **21**, 1435, 1987.

[148] P. J. Gregson, D. S. McDarmaid, and E. Hunt. *Mater. Sci. and Tech.*, **4**, 713, 1988.

[149] M. Tamura, T. Mori, and T. Nakamura. *Trans. Jap. Inst. Metals*, **14**, 355, 1973.

[150] C. R. Heiple, S. H. Carpenter, and S. S. Christiansen. *Acta metall. mater.*, **38**, 611, 1990.

[151] R. J. Arsenault. *Mater. Sci. Engng.*, **68**, 171, 1984.

[152] W. J. Clegg. *Acta metall.*, **36**, 2141, 1988.

[153] W. J. Clegg, I. Horsfall, J. F. Mason, and I. Edwards. *Acta metall.*, **36**, 2151, 1988.

[154] D. L. McDanels. *Metall. Trans.*, **16A**, 1105, 1985.

[155] R. J. Arsenault and N. Shi. *Mater. Sci. Engng.*, **81**, 175, 1986.

[156] I. Dutta and D. L. Bourell. *Mater. Sci. Engng.*, **A112**, 67, 1989.

[157] M. P. Shaw and J. M. Robinson. In T. Chandra (editor), *Proc. Int. Conf. on Recrystallization in Metallic Materials*, pp. 699–704, Wollongong, Australia, 1990.

[158] Sun Ig Hong and C. Laird. *Acta metall. mater.*, **38**, 1581, 1990.

[159] M. Von Heimendahl. *Electron Microscopy of Materials.* Academic Press, 1980.

[160] V. Gerold and P. Karnthaler. *Acta metall.*, **37**, 2177, 1989.

[161] U. F. Kocks. *Acta metall.*, **33**, 623, 1985.

[162] H. Mughrabi. In G. C. Sih and H. Zorski (editors), *Proc. First Int. Symp. on 'Defects and Fracture'*, p. 15, Nijhoff, The Hague, 1982.

[163] H. Neuhauser, O. B. Arkan, and H. H. Potthoff. *Mater. Sci. Engng.*, **81**, 201, 1986.

[164] T. Steffens, C. Schwink, A. Corner, , and H. P. Karnthaler. *Phil. Mag.*, **A 56**, 161, 1987.

[165] L. P. Kubin and J. Lepinoux. In P. O. Kettunen et al. (editors), *Strength of Metals and Alloys (ICSMA 8)*, Volume 1, pp. 35–59, Tampere, Finland, 1988.

[166] H. Heuhauser. In F. R. N. Nabarro (editor), *Dislocations in Solids*, Volume 6, pp. 319–340, North–Holland, 1989. North–Holland.

[167] H. Neuhauser, J. Plessing, and M. Schulke. *J. Mech. Behaviour of Materials*, **2**, 231, 1990.

[168] H. Traub, H. Neuhauser, and Ch. Schwink. *Acta metall.*, **25**, 437, 1977.

[169] R. E. Sanders. In *Formability of Metallic Materials–2000 A. D.*, Volume ASTM STP 753, pp. 35–39, 1982.

[170] C. J. Schmidt and A. K. Miller. *Acta metall.*, **30**, 615, 1982.

[171] O. D. Sherby, R. A. Anderson, and J. E. Dorn. *Trans. A.I.M.E.*, **3**, 643, 1951.

[172] A. Korbel, J. D. Embury, M. Hatherly, P. L. Martin, and H. W. Erbsloh. *Acta metall.*, **34**, 1999, 1986.

[173] A. Korbel and P. Martin. *Acta metall.*, **34**, 1905, 1986.

[174] J. D. Baird and C. R. MacKenzie. *JISI*, **202**, 427, 1964.

[175] A. S. Keh, Y. Nekada, and W. C. Leslie. In *Dislocation Dynamics*, pp. 381–408. McGraw Hill, 1968.

[176] A. Korbel and P. L. Martin. *Acta metall.*, **36**, 2575, 1988.

[177] Sun Ig Hong. *Mater. Sci. Engng.*, **79**, 1, 1986.

[178] T. Imura. In *Proc. 6th Int. Conf. on HVEM (HVEM 80)*, pp. 280–287, Antwerp, Belgium, 1980.

[179] H. Fujita. *Journal of Electron Microscopy Technique*, **3**, 243, 1986.

[180] H. Fujita. In *International Symposium on In Situ Experiments with HVEM*, pp. 1–23, Osaka Univ., 1985.

[181] T. Tabata, H. Fujita, and Y. Nakajima. *Acta metall.*, **28**, 795, 1980.

[182] T. Tabata, S. Yamanaka, and H. Fujita. *Acta metall.*, **26**, 405, 1978.

[183] J. L. Martin. *Revue Phys. Appl.*, **15**, 853, 1980.

[184] J. J. Gilman. In A. R. Rosenfield et al. (editors), *Dislocation Dynamics*, p. 3, New York, 1968. McGraw–Hill.

[185] H. Neuhauser, R. Rodloff, H. Flor, and C. Schwink. In *Strength of Metals and Alloys (ICSMA 4)*, Volume 1, pp. 100–104, Nancy, France, 1976.

[186] H. Neuhauser, H. Fiebiger, , and N. Himstedt. In P. Haasen et al. (editors), *Strength of Metals and Alloys (ICSMA 5)*, p. 1531, Aachen, W. Germany, 1979.

[187] P. G. McCormick. *Acta metall.*, **20**, 351, 1972.

[188] A. Korbel, J. Zasadzinski, and Z. Sieklucka. *Acta metall.*, **24**, 919, 1976.

[189] G. Schoek. *Acta metall.*, **32**, 1229, 1984.

[190] G. Ananthakrishna and M. C. Valasakumar. *J. Phys. D*, **15**, L171, 1982.

[191] P. G. McCormick. *Acta metall.*, **36**, 2575, 1988.

[192] K. T. Hong and S. W. Nam. *Acta metall.*, **37**, 31, 1989.

[193] K. Neelakantan and G. Venkatamaran. *Acta metall.*, **31**, 77, 1983.

[194] P. G. McCormick. In P. O. Kettunen et al. (editors), *Strength of Metals and Alloys (ICSMA 8)*, Volume 1, pp. 409–414, Tampere, Finland, 1988.

[195] Y. Estrin. In G. Martin and L. Kubin (editors), *Int. Conf. on Non Linear Phenomena in Materials Science*, pp. 417–428, Aussois, France, 1988.

[196] U. F. Kocks. *Prog. Mater. Sci., Chalmers Anniv. Vol.* Pergammon Press, 1981.

[197] A. H. Cottrell and M. A. Jawson. *Proc. RSA*, **199**, 104, 1949.

[198] A. van den Beukel. *Phys. stat. sol. (a)*, **30**, 197, 1975.

[199] R. K. Ham and D. Jaffrey. *Phil. Mag.*, **15**, 247, 1967.

[200] P. Wycliffe, U. F. Kocks, and J. D. Embury. *Scripta metall.*, **14**, 1349, 1980.

[201] N. Louat. *Scripta metall.*, **15**, 1167, 1981.

[202] P. J. Goodhew. *Thin Foil Preparation for Electron Microscopy*, Volume 11 of *Practical Methods in Electron Microscopy.* Elsevier, Amsterdam, 1985.

[203] W. A. T. Clark et al. *Ultramicroscopy*, **30**, 76, 1989.

[204] W. A. T. Clark, B. Hardiman, and R. H. Wagoner. In J. C. Bravman et al. (editors), *MRS Symp. Proc. Vol. 115 : Spec. Prep. for TEM of Materials*, pp. 99–102, 1988.

[205] E. P. Butler and K. F. Hale. *Dynamic Experiments in the Electron Microscope*, Volume 9 of *Practical Methods in Electron Microscopy.* North–Holland, Amsterdam, 1981.

[206] H. Liebowitz (editor). *Fracture*, Volume 2. Academic Press, 1968.

[207] D. Fahr. *Metall. Trans.*, **2**, 1883, 1971.

[208] J. A. Hall, V. F. Zackay, and E. R. Parker. *Trans. ASM*, **62**, 965, 1969.

[209] R. B. Nicholson, G. Thomas, and G. Nutting. *J. Inst. Metals*, **87**, 429, 1958/59.

[210] R. E. Smallman and K. H. Westmacott. *Mater. Sci. Engng.*, **9**, 249, 1972.

[211] D. W. Moon. *Mater. Sci. Engng.*, **8**, 235, 1971.

[212] H. Fujita and S. Miyazaki. *Acta metall.*, **26**, 1273, 1978.

[213] P. Cotterill and P. R. Mould. *Recrystallization and Grain Growth in Metals.* Surrey University Press, London, 1976.

[214] T. Lyman et al. (editors). *Metallography, Structures and Phase Diagrams*, Volume 8 of *Metals Handbook.* ASM, Metals Park, Ohio, eighth edition, 1973.

[215] J. M. Robinson and M. P. Shaw. In *Electron Microscopy Society of Southern Africa : Communications*, Volume 20, p. 37, Grahamstown, RSA, 1990.

[216] J. L. Martin and L. P. Kubin. *Ultramicroscopy*, **3**, 215, 1978.

[217] J. L. Martin and L. P. Kubin. *Phys. Stat. Sol. (a)*, **56**, 487, 1979.

[218] J. G. Morris. *Mater. Sci. Engng.*, **4**, 220, 1968/69.

[219] Y. Estrin and L. P. Kubin. *Acta metall.*, **34**, 2455, 1986.

[220] I. J. McColm. *Ceramic Science for Materials Technologists.* Leornard Hill, 1983.

[221] V. S. Ananthan and E. O. Hall. *Scripta metall.*, **21**, 1699, 1987.

[222] V. S. Ananthan and E. O. Hall. *Scripta metall.*, **23**, 1075, 1989.

[223] R. Iricibar and J. Mazza. *Scripta metall.*, **10**, 289, 1976.

[224] A. Korbel and A. Pawelek. In *Proc. Acta/Scripta Metallurgica Conf. on Dislocation Modelling in Physical Systems*, pp. 193–196, Gainesville, Florida, 1980.

[225] N. Clement, D. Caillard, and J. L. Martin. *Acta metall.*, **32**, 961, 1984.

[224] A. Korbel and A. Pawelek. In *Proc. Acta/Scripta Metallurgica Conf. on Dislocation Modelling in Physical Systems*, pp. 193–196, Gainesville, Florida, 1980.

[225] N. Clement, D. Caillard, and J. L. Martin. *Acta metall.*, **32**, 961, 1984.

[226] M. Hatherly. In R. C. Gifkins (editor), *Strength of Metals and Alloys (ICSMA 6)*, pp. 1181–1195, Melbourne, Australia, 1982.

[227] G. Canova, U. F. Kocks, and M. Stout. *Scripta metall.*, **18**, 437, 1984.

[228] R. Asaro and A. Needleman. *Scripta metall.*, **18**, 429, 1984.

[229] D. J. Lloyd. *Metals Sci.*, **14**, 193, 1980.

[230] T. Vreeland, D. S. Wood, and D. S. Clark. *Trans. ASM*, **45**, 620, 1953.

[231] V. 0. Gerold and H. P. Karnthaler. *Acta metall.*, **37**, 2177, 1989.

[232] H. Fujita and S. Kimura. In *Proc. Int. Conf. on HVEM*, pp. 333–336, Berkeley, USA, 1983.

[233] P. F. Thomason. *Ductile Frcature Of Metals.* Pergamon Press, Exeter, U.K., 1990.

[234] J. F. Knott. *Fundamentals of Fracture Mechanics.* Butterworths, London, 1973.

[235] R. W. K. Honeycombe. *The Plastic Deformation of Metals.* Edward Arnold, second edition, 1984.

[236] J. Llorca, A. Needleman, and S. Suresh. *Acta metall. mater.*, **39**, 2317, 1990.

[237] J.J. Lewandowski, C. Liu, and W.H. Hunt. *Mater. Sci. Engng.*, **A107**, 241, 1989.

[238] S.V. Kamat, J.P. Hirth, and R. Mehrabian. *Acta metall.*, **37**, 2395, 1989.

[239] P. Mummery and B. Derby. *Mater. Sci. Engng.*, **A135**, 221, 1991.

[240] Y. Brechet, J.D. Embury, S. Tao, and L. Luo. *Acta metall. mater.*, **39**, 1781, 1991.

[241] L.M. Brown and J.D. Embury. In *Strength of Metals and Alloys (ICSMA 3)*, p. 161, London, 1975.

[242] P. G. McCormick. Private communication. 1992.